8-2013

The Effect of Processing Parameters on Barrier Properties of Polymers

Russell Louis Hallman Jr.
rlhjr@icx.net

To the Graduate Council:

I am submitting herewith a dissertation written by Russell Louis Hallman Jr. entitled "The Effect of Processing Parameters on Barrier Properties of Polymers." I have examined the final electronic copy of this dissertation for form and content and recommend that it be accepted in partial fulfillment of the requirements for the degree of Doctor of Philosophy, with a major in Polymer Engineering.

Roberto Benson, Major Professor

We have read this dissertation and recommend its acceptance:

Kevin Kit, David Joy, Christopher P. Stephens

Accepted for the Council:

Carolyn R. Hodges

Vice Provost and Dean of the Graduate School

(Original signatures are on file with official student records.)

The Effects of Processing Parameters on Barrier Properties of Polymers

A Dissertation Presented for
the Doctor of Philosophy Degree
The University of Tennessee, Knoxville

Russell Louis Hallman, Jr.
August 2013

Dedication

The single greatest piece of knowledge I have learned during this pursuit is that the attainment of knowledge is a result of a group effort. I suppose that there are those who can say they attained their degree all on their own, but I cannot. From the help of librarians to those who offer encouragement during times of dismay your path is made smoother by the aid of others. The acquisition of knowledge does not isolate a person with the privilege of education but obligates them to serve and return the kindness to others with vigor. Who should be mentioned first is my late mother and father Margaret and Russell Hallman. I wished they could have lived to see the fruits of their labor. Although they did not have the benefit of a higher education, they desired it for me and encouraged me to persevere.

Acknowledgments

I would like to thank many people for their assistance in my pursuit of this degree. Let me start with my doctoral committee members Roberto Benson, Ph.D.; Kevin M. Kit, Ph.D.; David C. Joy, Ph.D.; and Christopher P. Stephens, Ph.D., for their willingness to guide me through this process. Thanks to my laboratory group Ryan Hammonds, Kaan Serpersu, Pelagie Favi, William Gazzola, and Andrew Wills. I appreciate the financial support received from the Y-12 National Security Complex through the educational assistance program. Also, I want to express my appreciation to the administrative staff Sandy Maples, Carla Lawrence, and Susan Seymour of the Material Science office. Thanks also to the Material Science and Engineering machine shop staff Doug Fielding, Larry Smith, and Dan Hackworth and to Dr. Rajen Patel and Dow Corporation for supplying the polymer. Many thanks to Linda Kathryn Shaw for her many hours of patient editing and continued encouragement. Dr. Jonathan Morrell and Dr. Patrick Moehlen provided valuable technical advice and suggestions critical in the development of kinetic model.

Thank you all for your help.

Abstract

The intent of this work was to learn if polyethylene could be made with predictable water transfer rates by control of the microstructure. A series of films were formed from three different polyethylenes with a range crystallinities using melt pressing, a controlled cooling rate, and subsequent heat treatments. The samples were tested on a novel device called the polymer characterization device that measures the water transfer flux as a function of temperature. The samples' morphology was examined using differential gradient column, differential scanning calorimetry, Fourier transform infrared microscopy, wide-angle X-ray diffractions, small-angle X-ray scattering, and small angle light scattering, and scanning electron microscopy. When the water transfer flux was expressed as the frost point of a dry carrier gas the results showed a remarkable sensitivity that allows for analysis of subtle distinction in rates due to changes in morphology. Analysis showed that the water transfer flux is a function of the polymer, conditions of the samples preparation from the melt, and any subsequent heat treatment. Another interesting finding was that the time for the sample to reach a steady state water transfer flux is a function of morphology. A free volume model was developed to that simulates the response of the polymer as a function of morphology, presence of water, and thermal cycling. The conclusion of this work is that the water transfer flux is a function of the specific polymer, the initial formation conditions, and later heat treatments and with this knowledge the polymer could be made with a specific water transfer flux.

Table of Contents

List of Tables

List of Figures

Introduction

By their very nature containers are constructed to confine a material for later use or transport without losses. A container's design and materials of construction limit its effectiveness. A container is designed strong enough to avoid breakage under the load of its contents with a lid that fits snugly to prevent evaporation or spillage. The only path in which the contents can leave is through the wall of the container. When the passage of gases, liquids, and vapors through the wall of a container is described it is often generically called permeation. In the common vernacular permeation has become a catchall term meaning the passage of a fluid through an otherwise solid object. In fact, permeation is one very specific technique which is part of a much broader field of study that measures the mass transport flux (MTF) or lose of the container's contents. The term permeation is often incorrectly used because it is not only a function of the area and thickness of the container's wall but also the difference in partial pressures of the migrating species on each side of the wall. Many materials are to be evaluated under environments such as liquid contact that are inappropriate for the permeation testing method.

In ceramics the MTF is modeled as gas flow through small pores and voids forming interconnected channels. The processing of ceramics from slurries, solution, or pressed-and-sintered powders leads to void space within the solid structure. These randomly dispersed, microscopically interconnected pores create an orifice effect to the flow of gases and vapors. As with flow through pipes, the flow then becomes regulated by the applied pressure, the size of the channel, the number of twist and turns (tortuosity), and fluid viscosity. These effects can be seen in non-glazed clay planter pots; when a plant is watered, the water can be seen flowing through the wall of the pot. The porosity of ceramics has been commercially exploited and used to create robust filters for water purification acting as a fine sieve.

Gases, liquids, and vapors are known to migrate across polymers, although the process by which it occurs is different. As opposed to ceramics in which there is a definite solid phase with void, in polymers there is an ordered crystal phase and disordered amorphous phase. The crystals act much like the solid particles of the ceramic, and the amorphous region acts much like the voids permitting movement of the migrating species. These two phases are a result of the nature of polymers and thermal treatment.

Polymers are macromolecules with a chain of one or more types of repeat units up to tens of thousands in length. In the molten state they have been compared to a bowl of spaghetti or randomly arranged filaments that slip past one another under stress. During this author's development of laboratory instruments called moisture blending systems (MBSs), it was discovered that each piece of polymer used had a unique MTF characteristic, irrespective of the fact that the vendor had stated that they all had the same properties.[1] This caused each MBS to have slightly different performance characteristics. During an investigation of this inconsistence in MTF from one polymer to a chemically identically tube it was surmised that the rate is a function of the morphology of a polymer, and in thermoplastics the morphology is in large part due to the thermal history.

This dissertation documents the results of an investigation of the morphological changes in polyethylene sheets as a function of thermal history during formation and subsequent heat treatment and its effects on MTF. More specifically this study focuses on the MTF of liquid water in contact with one side of a polymer film to vapor on the other and this specific measurement is being called the water transport flux (WTF). This work was undertaken to determine the effects of changes in density and morphology on barrier properties of polyethylene to water. Morphology is a term that broadly refers to the various forms or structures that can occur in a material, and in polymers it generally refers to either a crystalline structure, highly ordered and aligned, or an amorphous structure. When thermoplastics cool and solidify they form a semi-crystalline solid. They do not form a single monolith of highly uniform crystalline phase but instead form a multitude of crystallites, crystalline regions of different sizes, and orientations. The remaining portion of the polymer matrix is amorphous, or non-crystalline, as shown in Figure 1, inspired by a similar image from Mandelkern.[2] The figure also depicts techniques that may be used to analyze each respective region.

[1] "Method and Apparatus for Providing a Precise Amount of Gas at a Precise Humidity," Patent No.: US 6,182,951 B1, Feb. 6, 2001.

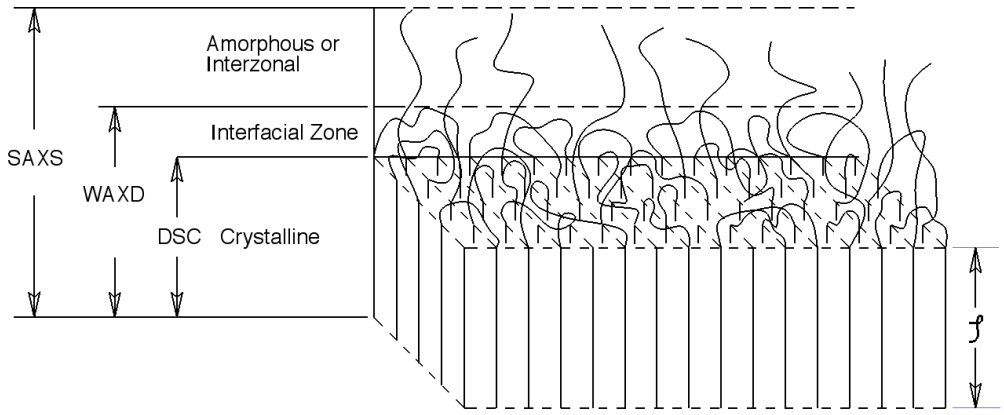

Figure 1. Schematic different regions of polymer crystal labeled with detection methods.[2]

The WTF through the polymer is governed by its structure. How the structure controls the WTF may be understood in the general sense that gases do not move through the crystalline phase; thus, only the amorphous region provides a path for the transport. Upon cooling, polymers rearrange by a number of different mechanisms to form crystals of a given size if enough time is provided. Slow cooling from the melt of low under cooling favors the formation of a solid with a high degree of crystallinity; conversely, quick cooling, as in quenching, yield the structure in an amorphous, or disordered, state. These differences in structure also manifest themselves in the performance of the polymers in other ways. For example, as the degree of crystallinity increases, polymers generally become stiffer, more opaque, and less ductile. 7

As mentioned previously, the differences in WTF between otherwise chemically identical polymer tubes were first seen when they were used in the MBS. The manifold configuration used in the MBS provided a very stable and reproducible set of conditions from which subtle differences in the transport rate between different polymer tubes can be observed. The MBS manifold was further modified to enhance the MTF control and is the basis of the WTF

[2] L. Mandelkern, "The Crystalline State," *American Chemical Society* Physical Properties of Polymers.

measurement in this study.[3] This new instrument is called the Polymer Characterization Device (PCD).[4]

[3] "Controlled Differential Pressure System for an Enhanced Fluid Blending Apparatus," Patent No.: US 7,494,114 B1, Feb. 24, 2009.
[4] "Fluid Permeability Measurement System and Method," Patent No.: US 7,325,439 B2, Feb. 5, 2008.

Chapter 2
Background

The earliest known record of a fluid transport across a barrier was by Jean-Antoine Nollet, a French physicist who lived from 1700 to 1770. Nollet was born of peasant parents who sent him to study at Clermont and Beauvais.[5] He became a clergyman and a leading member of the Paris Academy of Science, where he was an experimental physicist. The account of the discovery of fluid transport is found in his original work entitled "Recherches sur les causes du Bouillonnement des Liquides" ("Investigations on the Causes for the Ebullition of Liquids"), J. A. (Abbe') Nollet, *Histoire de l'Acade'mie Royale des Sciences*, Anne'e MDCCXLVIII, (Paris, 1752), pages 57–104.[6] An English translation of pages 101 to 104 and plate containing sketches 10 and 11 from the original work can be found as part of a retrospective in the *Journal of Membrane Science*.[7]

In Nollet's own words he acknowledges the "discovery by chance." Nollet wanted to see if ethanol would spontaneously form bubbles if it was first degassed and stored in a manner that no air could reenter the container. He prepared the sample by first degassing ethanol contained in a flask with a vacuum until it stopped bubbling. He then sealed the top of the flask using a wet pig bladder in such a manner that the flask was filled with ethanol to the top to expel all air; afterward he stored the seal flask beneath water in a large vase. As the account goes, he was surprised to see that, after only 5 to 6 hours, the flask contained more liquid than it had started with. The addition of liquid to the flask was evident because the pig-bladder seal on the flask had a convex bulge. He went on to note that not only had the water migrated across the pig-bladder seal but also the water's addition to the flask overcame an ever-increasing pressure within the flask. When the pig bladder was pricked with a pin to relieve the pressure, a stream rose to a height more than 1 foot.

To confirm that it was the movement of water across the pig bladder and not ethanol that caused the increase in volume, Nollet repeated the experiment with a small change. He reversed the order

---

[5] Incredible People information about the famous people from around the world, http://profiles.incredible-people.com/jean-antoine-nollet/

[6] J.A. Nollet, "Recherches sur les causes du Bouillonnement des Liquides (Investigations on the Causes for the Ebullition of Liquids)," *Histoire de l'Académie Royale des Sciences* (1752).

[7] K. W. Boddeker, "COMMENTARY - TRACING MEMBRANE SCIENCE," *Journal of Membrane Science* 100, no. 1 (1995).

of the fluids; this time he placed water inside the flask sealed with a pig bladder and stored it beneath ethanol. As expected, the water left the flask, evident by the concaved deflection of the pig bladder at the mouth of the flask.

To further investigate the particulars of this observation he conducted the experiment a third time, but this time he filled the flask only halfway with ethanol before sealing it with the wet pig bladder. The flask was stored beneath the water for two days, and after its retrieval, no significant change was detected. The flask was then inverted in order to bring the inside of the pig bladder into contact with the ethanol and submerged back into the water. When the ethanol was in contact with the pig bladder, the water penetrated the pig bladder and began to fill the flask. Additional testing showed that the pig bladder favored the permeation of water over that of ethanol.

What Nollet had shown was that liquids can cross an otherwise impervious barrier; that two chemicals can interact across a barrier to affect each other's behavior; and that a barrier, the pig bladder in this case, can selectively allow for the permeation of one liquid species preferentially to another. These behaviors have been given names in these modern times. *Permeation* is now used to describe the transport of gases or vapors with a difference in partial pressure across a barrier generally without interference from other factors. When two fluids are placed on opposite sides of a barrier and they influence each other's chemical potential for migration across the barrier, it is called *osmosis*; and when a barrier permits one liquid and rejects the other, the barrier is said to be *selective*.

In another of Jean-Antoine Nollet's laboratory records he begins the section with an account of how all matter appears to have open space within it.[8] He notes that when a sponge or porous stone is submerged in water, the air is expelled and water replaces it. Conversely, when the stone or sponge is dried, it becomes lighter, indicating the evaporation of the water. Nollet refers to minute divisions of water that move into and out of the open spaces within the sponge and stone as corpuscles, which in the nomenclature of the time meant smallest discrete division of matter. This was at a time that the concept of atoms had not been proved. He further elaborated on the theory

[8] Nollet and John Colson, *Lectures in experimental philosophy* (London: Printed for J. Wren ... 1752).

of space within matter by noting how light passes through material that water will not and concludes “pores of another order” exist but could not be proved. Nollet states it this way:

> “Therefore excepting only the simple and primary parts of bodies, we shall fix it as a general proposition, that whatever is composed of material parts is porous; hard bodies as well as liquids, those that are organized as well as others. And if there is any difference among them, tis only as to the magnitude, the number, the figure, or situation of the pores.”[9]

Boddeker[10] also givens a number of other early researchers credit for advancing the field of mass transport through membranes. They include Dutrochet,[11] Graham,[12] Mitchell,[13] Knudsen,[14] Fick,[15] Van ‘t Hoff,[16] Donnan,[17] Bigelow and Gemberling,[18] Kober,[19] and Barrer.[20] Contributions important to this work will be reviewed.

---

[9] Ibid.
[10] Boddeker, "COMMENTARY - TRACING MEMBRANE SCIENCE."
[11] R.J.H. Dutrochet, "Nouvelles Observations sur l"Endomose et l"Exosmose et sur la cause de ce double phénomène (New Observations on Endosmosis and Exosmosis, and on the Cause of this Dual Phenomenon)," *Annnales de Chimie et de Physique* 35(1827).
[12] T. Graham, "Notice of the Singular Inflation of a Bladder," *Quarterly Journal of Science,* no. II (1829).
[13] J.K. Mitchell, "On the Penetrativeness of Fluids," *The Journal of the Royal Institution of Great Britian,* no. IV (1831).
[14] M. Knudsen, "Die Gesetze der Molekularströmung und der inneren Reibungsströmung der Gase durch Röhren (The Laws of Molecular Flow and of Inner Friction Flow of Gases Through Tubes)," *Annalen der Physik* 28(1909).
[15] A. Fick, "Über Diffusion, Poggendorff's Annalen der Physik und Chemie," *The London, Edinburgh, and Dublin Philosophcal Magazine and Journal of Science* X(1855).
[16] J.H. van 't Hoff, "Die Rolle des osmotishcen Druckes in der Analogie zwischen Lösungen und Gasen (The Role of Osmotic Pressure in the Analogy Between Solutions and Gases)," *Zeitschrift für Physikalische Chemie* 1(1887).
[17] F.G. Donnan, "Theorie der Membranegleichgewichte und Membranpotentiale bei Vorhandensein von nicht dialysierenden Elektorlyten. Eing Beitrag zur physikalisch-chemischen Physiologie (Theory of Membrane-Equilibria and Membrane Potentials in the Presence of Non-Dialysing Electrolytes. A Contribution to Physical-Chemical Physiology)," *Zeitschrift für Elektrochemie und angewandte physikalishche Chemie* 17(1911).
[18] S. Lawrence Bigelow and Adelaide Gemberling, "COLLODION MEMBRANES," *Journal of the American Chemical Society* 29, no. 11 (1907).
[19] Philip Adolph Kober, "PERVAPORATION, PERSTILLATION AND PERCRYSTALLIZATION.1," *Journal of the American Chemical Society* 39, no. 5 (1917).
[20] Richard M. Barrer, *Diffusion in and Through Solids*, The Cambridge Series of Physical Chemistry (London: Cambridge University Press, 1941).

Henri Dutrochet explored liquid transport across organic and inorganic membranes and coined the terms *endosmosis* and *exosmosis*, from which we have osmosis. Up to that time the rate of mass transport was believed to be relative to the rise of a liquid in a capillary. The capillary was used to characterize a fluid because the theory of the day was that the fluid transport was due to this capillary action through the membrane. "Endosmosis and exosmosis" is the passage of fluid across a membrane from fluid A into B and conversely from B to A. Other descriptions for endosmosis include the movement of less dense liquid through a membrane to the more dense fluid, or the movement of fluid from the lower concentration to the higher concentration. Conversely, the exosmosis is the movement in the opposing direction.

Thomas Graham was a chemist who lived from 1805 to 1869.[21] Educated at the University of Glasgow, and later a Fellow of the Royal Society, he is known for his work in the study of diffusion and dialysis. Graham studied the rates that gases of different molar masses pass through porous plugs and small holes. The relationship of these rates is expressed as Graham's Law, which states that the rate of two competing gases is inversely proportional to the square root of the molecular weights, as Equation 1 shows:

Equation 1.

$$\frac{Rate_1}{Rate_2} = \sqrt{\frac{M_2}{M_1}}$$

This relationship is often used as a basis upon which multi-gas mass transport is modeled. Some materials are characterized as porous and thus owe their mass transport properties to the size and quantity of pores within their structure. In addition, Graham studied the separation of gases through membranes looking at the interactions of these gases in combination with water.

Richard Barrer was a researcher who worked in the field of zeolite development and diffusion. The Barrer unit is named in his honor for the technical contribution of his work. He produced a

[21] http://www.britannica.com/EBchecked/topic/240743/Thomas-Graham

classic text "Diffusion in and Through Solids," which remains today a classic technical reference. Barrer is given credit for establishing a common unit of measure for transport rates through materials.[22] Martin Knudsen showed how the flows of gases through small narrow openings change from friction flow (Poisseuille's law) to molecular flow. Adolph Fick, after reviewing a number of works from other researchers, developed a mathematical approach to describe the flow. The model he built was patterned after Fourier's theory of heat flow and Ohm's law for electrical flow. Two of these equations have come to be known as Fick's First and Second laws of diffusion. The first law applies to steady state flows, and the second law applies to non-steady state flow. Donnan, and Bigelow and Gemberling performed most of their work in the field of dialysis.

Since the first reported observations by Nollet in 1752, membrane development has remained an active field of study. The implications and potential applications of this work were not obvious at first. Some may have viewed these discoveries as shortcomings of a material to hold a liquid or gas. Others may have just been curious as to how the transport occurs from a purely scientific basis. Since that time, ongoing membrane development has shaped products in modern society in indispensible ways. This knowledge routinely affects scientific and engineering approaches to problem solving and product design on a daily basis. Some examples include applications of these techniques to biological studies of fluid migration across cell walls, time-released drug devices, blood purification, chemical separation, hydrogen migration in weld joints, design of polymer fuel storage containers, and land fill liners, to name a few.

One practical application where permeation is used in the design of a product is in the field of personal chemical monitors. SKC Inc. has a line of personal monitors that are worn like a badge by workers who must go into areas with potentially high chemical concentrations of organic vapors.[23] The device is shown in Figure 2. This device captures a sample of the organic vapors and retains the vapors for later analysis to determine the employee's exposure to hazardous chemical. It works by having a permeable barrier that the organic vapors pass through at a predetermined rate based on concentration and is stored in a sorbent chosen on the basis of the chemical of interest. Some of the chemicals routinely monitored include toluene,

[22] S. A. Stern, "The "barrer" permeability unit," *Journal of Polymer Science Part A-2: Polymer Physics* 6, no. 11 (1968).
[23] http://www.skcinc.com/prod/575-001.asp

tetrachloroethylene, trichloroethylene, xylenes, ethylbenzene, 2-Butanone (MEK), hexane, benzene, butyl acetates, and styrene.

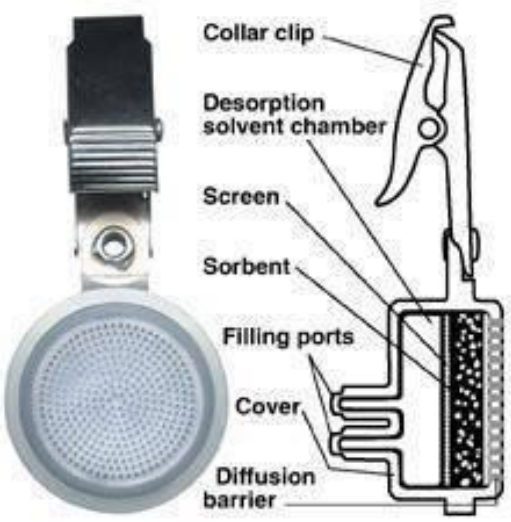

Figure 2. Passive diffusion samplers for parts per million-level organic vapors monitoring.

A more mundane but no less important application of the fundamentals of barriers is in the design of protective gloves. A critical consideration during the design of the glove is the material of construction that must match the application. If the application is for use in nonhazardous aqueous solutions, then the major consideration may only be comfort and durability with minimal concern for the penetration of chemical gases and vapors. However, if the application is for use with acid plating solution, where there is a hazard in contact with acids and a potential for skin absorption, then the gas and vapor transport properties must be carefully chosen.

Another application of controlled mass transport is in water filtration. One such system is the reverse osmosis system. Culligan, along with a number of other manufacturers, is a distributor of water purification systems based on the reverse osmosis principal for use in the home and industry.[24] These systems range in size from a few gallons per day to hundreds of gallons per minute. The principle by which these systems work is analogous to Nollet's pig-bladder-covered

[24] http://www.culliganmatrixsolutions.com/industrial/products/membranes/reverse_osmosis/

flask. Recall that Nollet noted that when the flask was filled with ethanol, covered with the pig bladder, and stored beneath water, the water migrated across the membrane and built pressure within the flask. In the reverse osmosis system the water and other components are already mixed. The pressure that results from the mixing is overcome by increasing the pressure and thus reversing the migration of water back through the membrane to separate the mixed components. This method results in a cost-effective, highly efficient method of purification.

Transport properties are a concern for designers of landfills. Landfills are governed by a number of Environmental Protection Agency regulations and laws such as the Hazardous Waste Act. It is well documented that landfills leach contaminants into the groundwater and air, and thus new landfills must provide barriers to limit spread of contamination. As part of the design of landfills the liners must be selected for compliance with federal law. The function of these barriers is to stop the flow of fluids through the debris from rain and entrained fluids and to limit migration of hazardous chemicals into the groundwater and air. One such liner is a heavy, typically 0.100-inch-thick polyethylene sheet called high-density polyethylene (HDPE) geomembranes.[25]

This material provides the physical strength to limit tearing as the landfill is filled with debris and is deformed due to settling. Other considerations are the migration of volatile liquids and vapors through the film. In this particular study testing was performed on these geomembranes to determine the transport rate of a number of chemical species including benzene, chloroform, ethylbenzene, methylene chloride, tetrachloroethylene, 1,1,1-trichloroethane, trichloroethylene, toluene, o-xylene, and p-xylene. As the study shows, accounting for mass transport rate in a product for a specific effect or as an unintended consequence of a material selection can impact a product's performance. [26]

Many industries make products with qualities that depend on the control of moisture during production. Everyday products such as natural gas, industrial acid gases, microelectronics, pharmaceutics, metallic welds, and refinement of reactive metals are severally degraded if moisture is not monitored and controlled. Devices used for monitoring moisture are called

[25] J. C. Joo, K. Nam, and J. Y. Kim, "Estimation of mass transport parameters of organic compounds through high density polyethylene geomembranes using a modifield double-compartment apparatus," *Journal of Environmental Engineering-Asce* 131, no. 5 (2005).
[26] Ibid.

hygrometers. The very nature of these moisture-monitoring devices is their sensitivity and, consequently, they are susceptible to malfunction due to process contaminates, sensor depletions, electronic drift, or other interferences that will affect the accuracy, sensitivity, and response rate of the device. As such these devices require routine calibration to ensure their reliability. Historically, moisture standards used for calibrating hygrometers have been sophisticated laboratory instruments requiring a high degree of environmental control. Calibration of hygrometers often requires the removal of the instrument from service, shipment to a calibration lab where the moisture standard resides, calibration, and subsequent reinstallation. During calibration a second device has to be substituted for the unit being calibrated or the process may require shutdown. Either of these choices constitutes a substantial operating expense. Until recently there were few choices for field deployable moisture standards. Novices to the field of moisture monitoring and calibration recommend the purchase of a premixed gas standard with a prescribed moisture content.

Inquiry at any major industrial gas supplier will reveal that the supplier is unable to supply industrial gases such as air, argon, and nitrogen with specified moisture content. Moisture is not an ideal gas but a vapor formed from a condensable. Moisture also has a phenomenal tendency to form condensed layers on any surface it contacts. The equilibrium between the vapor phase and condensed phase is thermally and pressure driven and almost never in a steady state equilibrium. Shifts between the vapor and condensate are promoted because of changes in temperature and pressures. Small changes in room temperature or local process temperatures cause the vapor to condense or be liberated from the surface back into the vapor phase. The dynamic interaction between the vapor and surface makes pre-blended moisture with other gases impossible.

Several devices have been developed for field calibration of hygrometers. One moisture source that has been tried is based in a successive dilution process. A stream of dry gas is bubbled through water to saturate the gas stream and then diluted from saturation back down to the desired moisture content. To ensure accuracy this process requires a series of gas control valves, heat control on the water source and the manifold piping, an inline moisture sensor, and a feedback loop to a proportional-integral-differential (PID) controller to control the blend ratio of moist and dry gases. This is an energy- and equipment-intensive method. Experience has shown that this method is cost effective only for large stationary installations, and although it has been used as a

mobile moisture source, it is not suitable. Figure 3 shows a general schematic of the successive dilution process. Figure 4 shows the flow diagram of a GE commercially available model. Any moisture source based on this technology is only as good as the embedded moisture monitor that controls its operation.

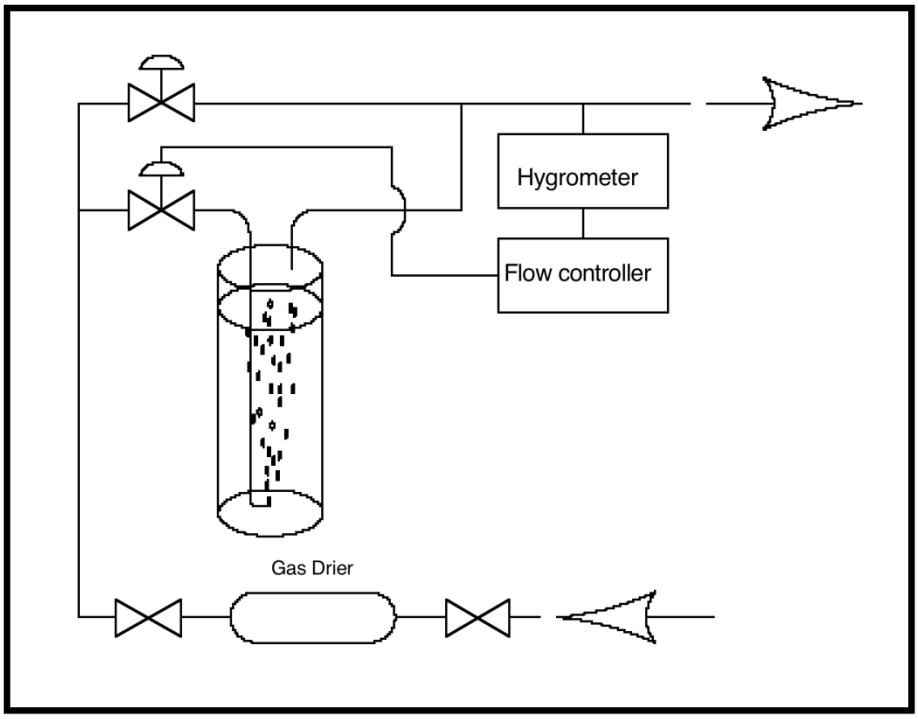

Figure 3. Successive dilution process.

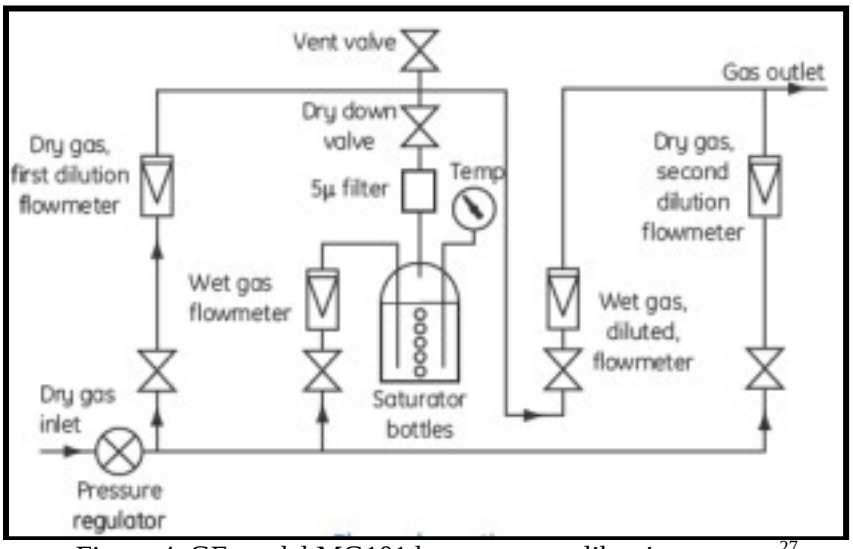

Figure 4. GE model MG101 hygrometer calibration system.[27]

A second field-deployable moisture source is known as a *paired-saturated tower*, Figure 5. It uses a pair of magnesium perchlorate columns, one as a dry desiccant, magnesium perchlorate trihydrate ($Mg(ClO_4)_2 \cdot 3H_2O$) and the second is a fully moisture saturated column of magnesium perchlorate hexahydrate ($Mg(ClO_4)_2 \cdot 6H_2O$). The first salt column provides a dry gas to set a zero moisture point for the instrument calibration, and the second column provides a single moisture content point based on dry gas flow rate and temperature. This method has a high degree of variability and drift. Of recent times it is most often used only to verify that an instrument is operating by providing a lower limit of detection value and a saturated flow value.[28]

[27] http://pdf.directindustry.com/pdf/ge-sensing-inspection-technologies/mg101-moisture-generator/7233-130943-_2.html

[28] C.D. Montgomery, J.M. Googin, and L.R. Phillips, "MOISTURE MONITOR TESTING AND CALIBRATION," in *Other Information: Orig. Receipt Date: 31-DEC-63* (1963).

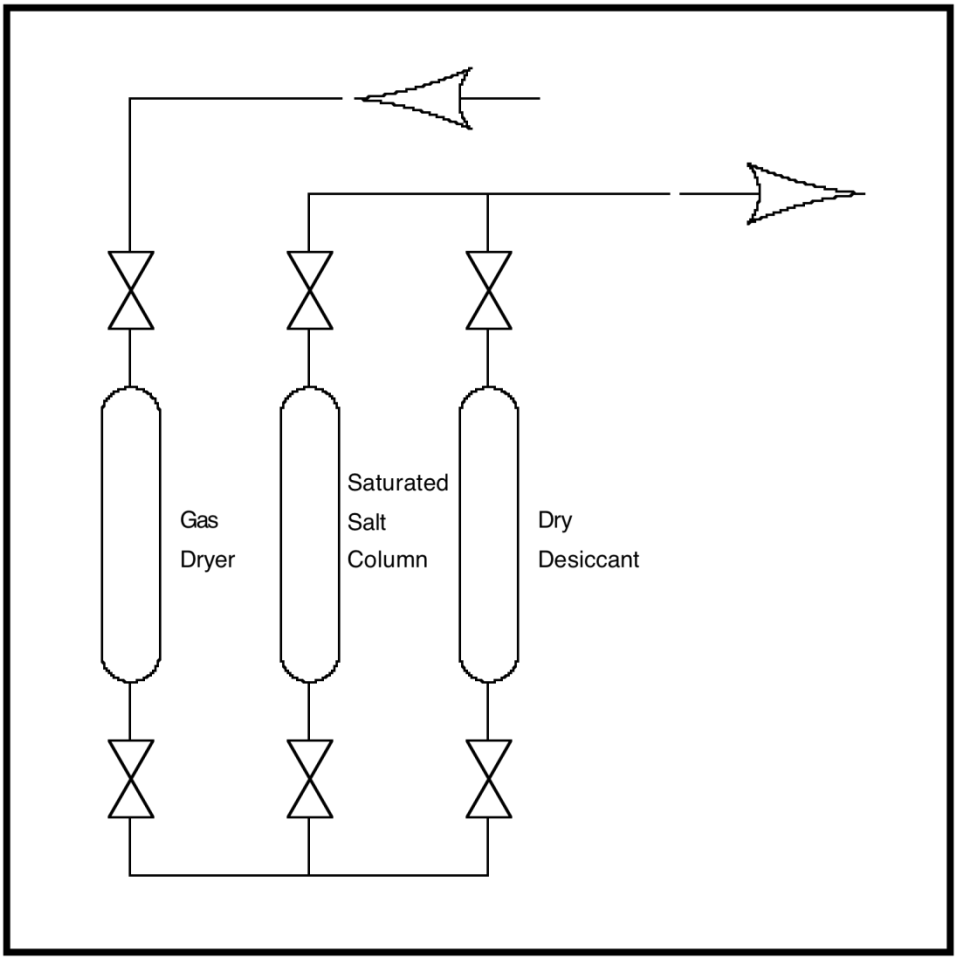

Figure 5. Saturation tower.

A third type of device is made by KIN-TEX®, as shown in Figure 6. It uses water sealed in a Teflon tube that is placed in a temperature-controlled metal gas manifold. The moisture content of the hydrated gas is a function of the mass transport rate of the water through the Teflon tube, the flow rate of the dry gas streams, and temperature of the permeation tube.

Inspection of Figure 6 shows that the gas flow is divided into two streams. One stream is passed through a flow controller at 200 cc/min to the temperature-controlled oven containing the permeation tube, and the second stream is passed through a flow controller at up to 5 L/min as the dilution gas stream. As the manufacturer describes, the oven is held at a constant temperature.

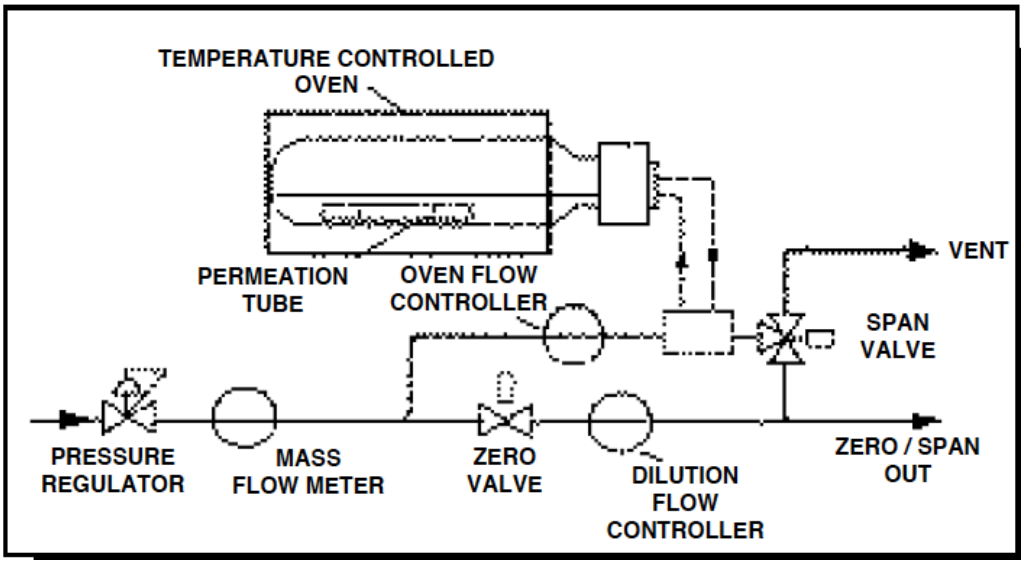

Figure 6. KIN-TEX® moisture delivery device model Span Pac™ H_2O Generator.[29]

As this short history shows, the need for highly reproducible and stable moisture sources existed, and this was the motivation for the development of the moisture blending system (MBS) illustrated in Figure 7. The MBS is a device for the precise blending of water vapor with a dry gas such as argon or nitrogen. The MBS was based on three simple rules. In order to provide a gas with a precise amount of moisture there must be a precise amount of dry bulk gas, a precise amount of water in a vapor form, and a means to mix the two and maintain the mixture until delivery. In this day and time of digital controllers engineers' first choice to control gases is a mass flow controller. That device is expensive, prone to drift, and slow to respond to changing pressure conditions. In contrast, the MBS controls the bulk gas flow rate using a conventional pressure regulator and capillary tube. Once the pressure is set and the length and diameter of the capillary tube are chosen, a bulk gas flow rate with great stability and reproducibility is established. If necessary, the flow rate can be changed either by adjustment of the pressure or by a change in the length or diameter of the capillary tube. Once a change is made, the system is

[29]http://www.kin-tek.com/brochures.html.

stable at the new configuration. Introduction of moisture into the gas is provided by mass transport through the tube wall. This system was designed and built by the author and patented.[30]

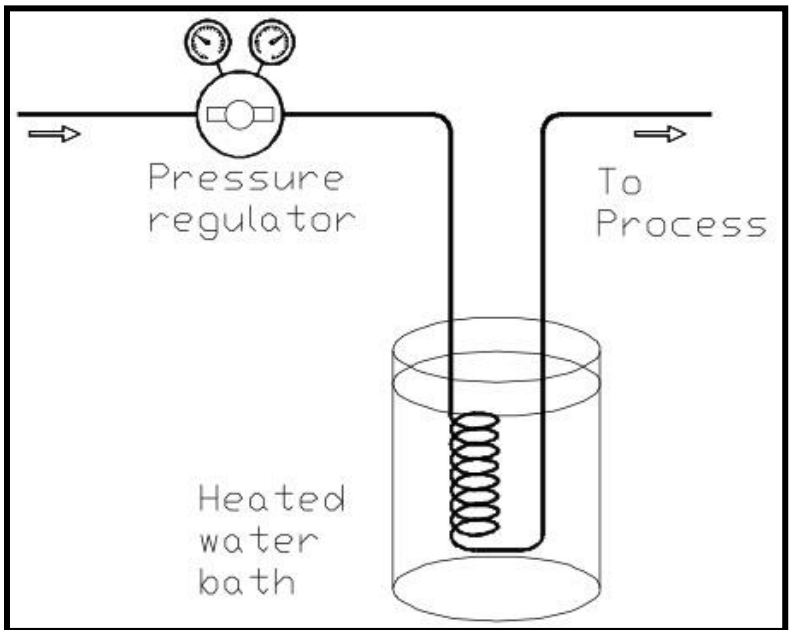

Figure 7. Basic moisture blending system.

The capillary tube, Figure 8, can be made of many permeable materials (e.g., polymers) that provide a nice range for moisture delivery. When the tube is submerged in a constant-temperature water bath, the water dissolves into the polymer and diffuses through to the internal bore. The dry gas is traveling at a relatively high velocity and shears the water vapor off the internal wall of the tube. The high shear rate provides the mixing.

[30] "*Method and Apparatus for providing a Precise Amount of Gas at a Precise Humidity*", US patent number US006182951B1, Feb 5, 2001, Russell L. Hallman, Jr. James C. Truett

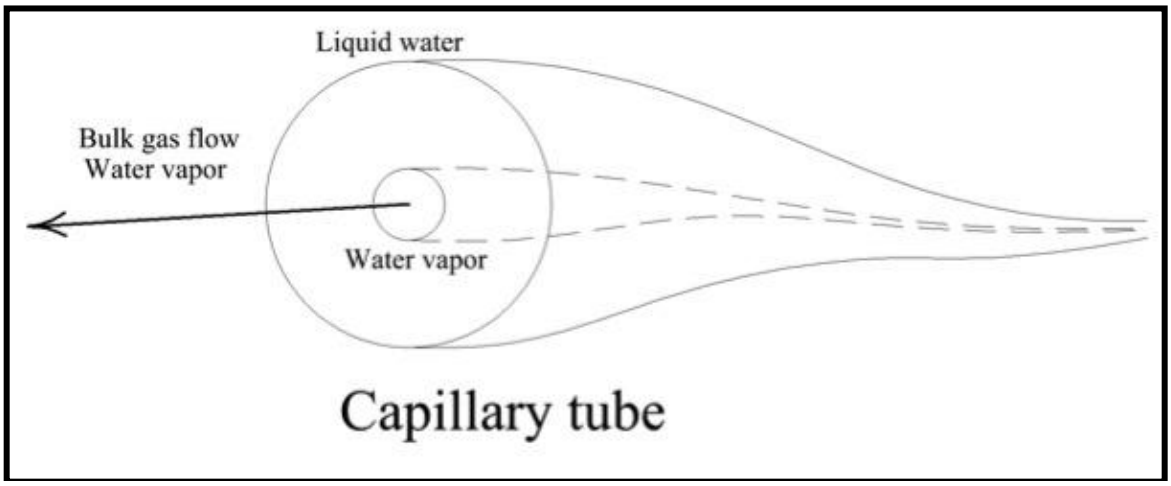

Figure 8. Flow profile of permeable capillary tube.

The configuration shown in Figure 7 establishes some interesting operating conditions that translate into a high degree of stability in the instrument's operation. First, the flow rate of the gas is physically fixed by the pressure difference between the tube's entrance and exit and by the tube's diameter and length. The moisture delivery rate is fixed by the concentration difference between the inside and outside of the tube, the tube's surface areas based on its diameter and length, the mass transport rate of the moisture through the polymer, and temperature of the water bath. Since a capillary tube has a high length-to-diameter ratio, it inherently provides continuous mixing.

The MBS system described is readily reproducible and controls all factors influencing the introduction of moisture into the dry gas, with the exception of changes in moisture transport rate between pieces of polymer. This is where the device began to reveal its sensitive nature to show how differences in transport flux is due to the polymer. Thus, the water transport flux (WTF) of any given tube is described by Equation 2:

Equation 2

$$WTF(T) = \frac{F_r \times M_c}{A}$$

where
WTF(T) is the water transport flux as a function of temperature,

F_r is the flow rate of dry bulk gas entering the tube,
M_c is the moisture content of the exiting gas, and
A is the area of sample.

The water delivery rate can then be further characterized by defining the specific material of the tube, its length and inner diameter, the tube's wall thickness, and the temperature or temperature range at which the test was conducted.

Later improvements to the system included the incorporation of a backpressure control valve, Figure 9, which increases its sensitivity and stability to changes in WTF.

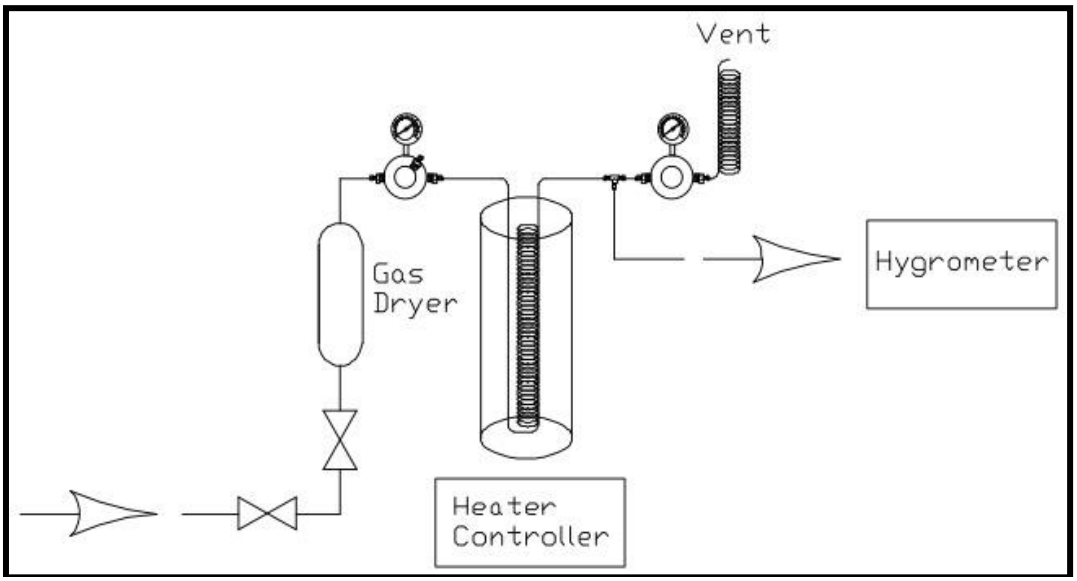

Figure 9. MBS equipped with backpressure control valve.

This new manifold design allows for investigation of the WTF of multiple samples at identical conditions of pressure and temperature. In order to accommodate polymer samples in other forms, several adaptors have been made; and one of specific interest to this study is a film clamp. The film is trapped between two polished metal flanges held within a clamp (Figure 10). Figure 10 (A) shows the polished metal sealing surface and film support grill, (B) showing the cell assembled, and (C) the clamping frame to apply sealing pressure. This novel test cell is used exclusively for the evaluation of all samples in this study.

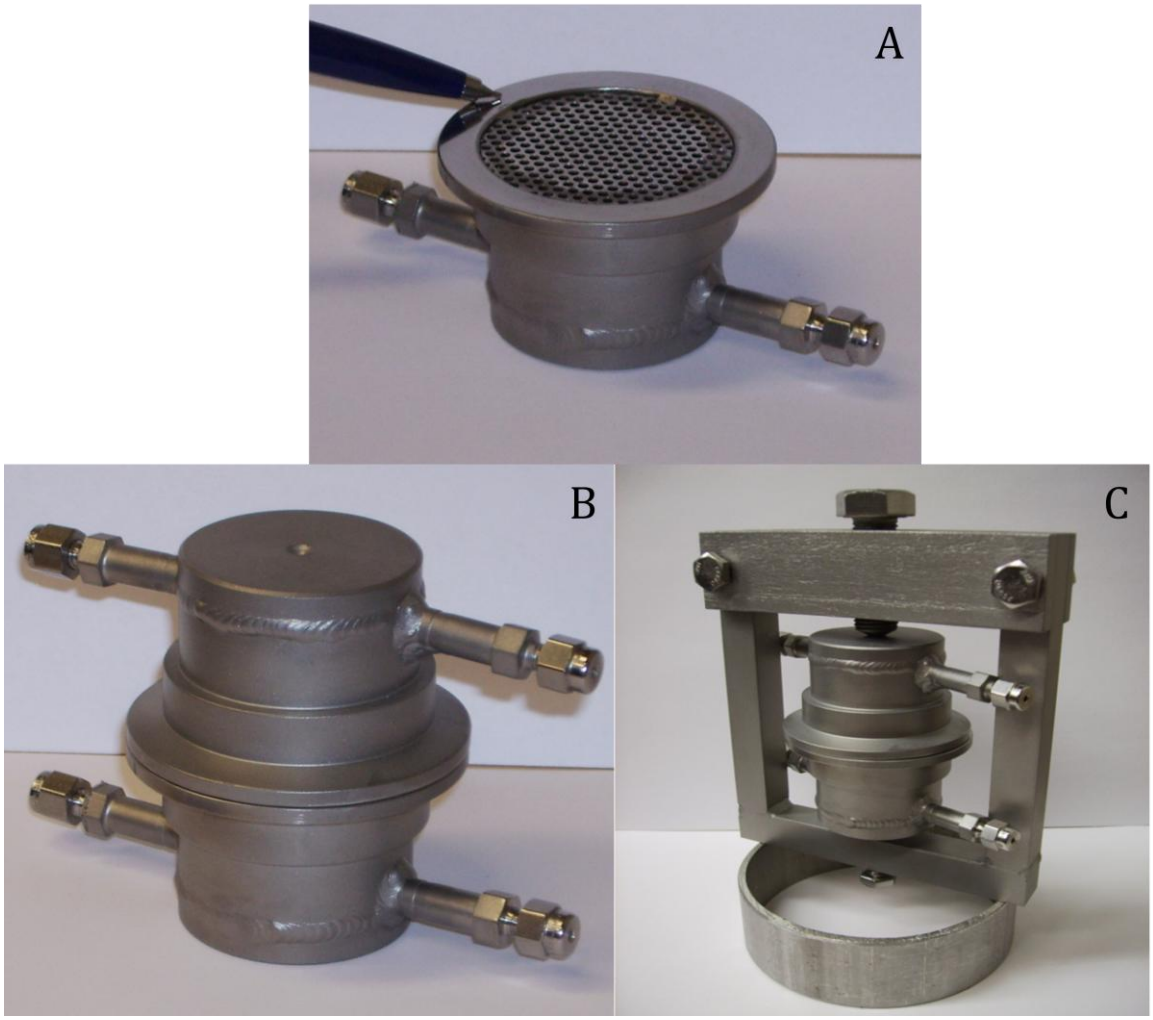

Figure 10. Film clamp mass transport flux cell.

This custom-built flange set is equipped with a support grill to keep the film from being deflected in the event of an imbalance in pressure during testing. The support grill is recessed from the clamping surface so the film is free floating under normal conditions. Figure 11 shows the manifold modified to accommodate the film clamping system. A non-permeable capillary tube for bulk gas flow control has been substituted for the permeable capillary tube. The new manifold also includes a gas drier and a hygrometer to precisely measure the moisture content of the exiting humidified gas stream. The bottom half of the film clamp contains liquid water as a source for the water. Once assembled, the film clamp is submerged in a temperature-controlled bath. Figure 12 shows the flow pattern of the bulk dry gas through the film testing cell. It should

be noted that a baffle is placed in the middle of the gas flow path to deflect the flow over the film surface.

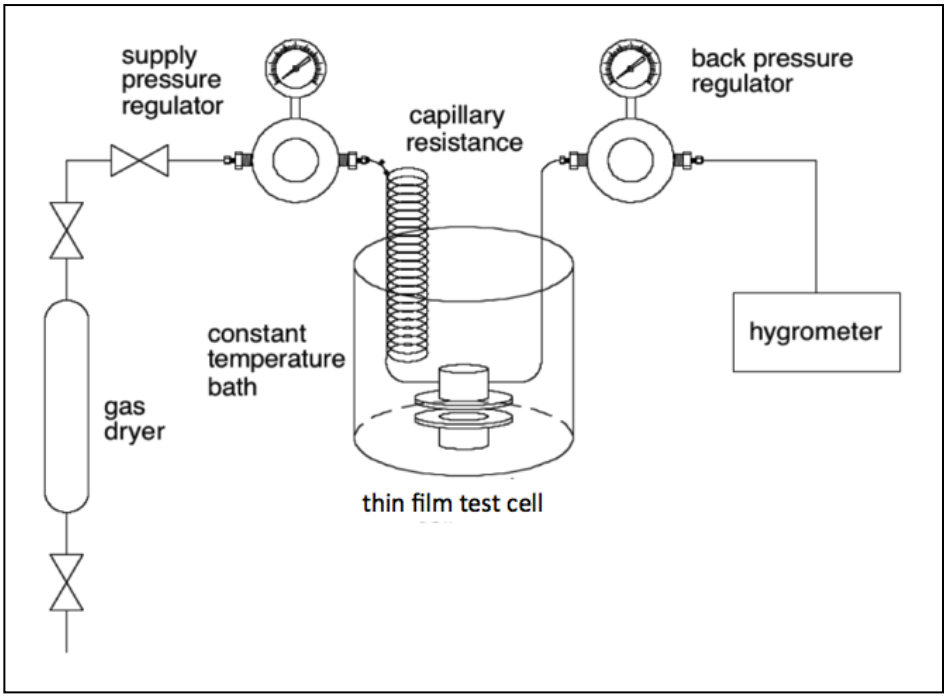

Figure 11. Film test cell with enhanced differential pressure manifold.[31]

It will be shown later that this technique produces precise measurements of the WTF of films to the point that the effects of subtle heat treatments become evident in the materials' behavior. Water transport rates are measured over a range of temperatures in order to more fully characterize the behavior. Figure 13 is a sample of the data collected. Often the temperature must be cycled several times before a constant rate is achieved.

[31] Jr Russell Louis Hallman and Michael John Renner. Fluid permeability measurement system and method. Patent US7325439B2, 2008.

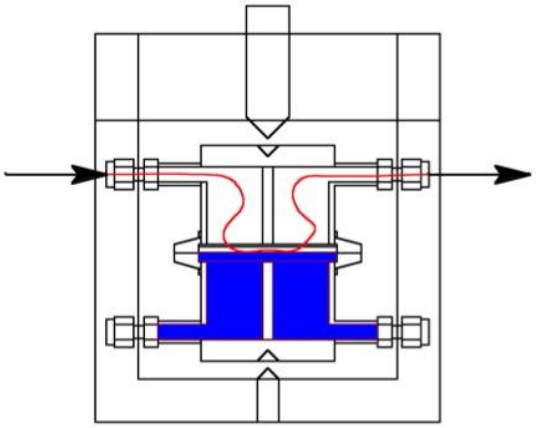

Figure 12. Flow pattern through film test cell.[32]

It will be shown that once a polymer has reached an steady state transport flux, and if the transport flux is measured as the frost point of the bulk gas at constant flow rate, then the data forms a linear relationship versus sample temperature, as Figure 14 shows.

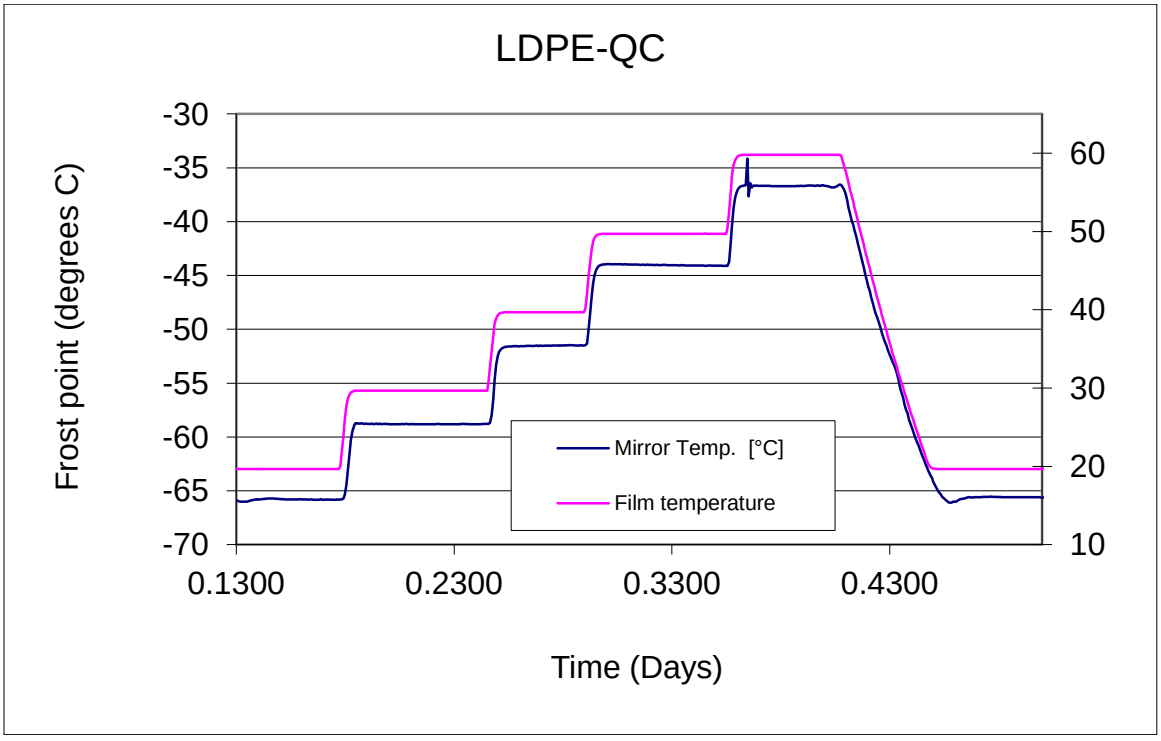

Figure 13. Frost point and sample temperature as function of time.

[32] Ibid.

As Figure 13 illustrates, the new instrumentation provides an enhanced method for characterizing the WTF of polymers not at a single temperature but over a range of temperatures while maintaining all other operating parameters exactly the same. This permits the side-by-side comparison of polymers that are otherwise identical except for variations of processing parameters of interest.

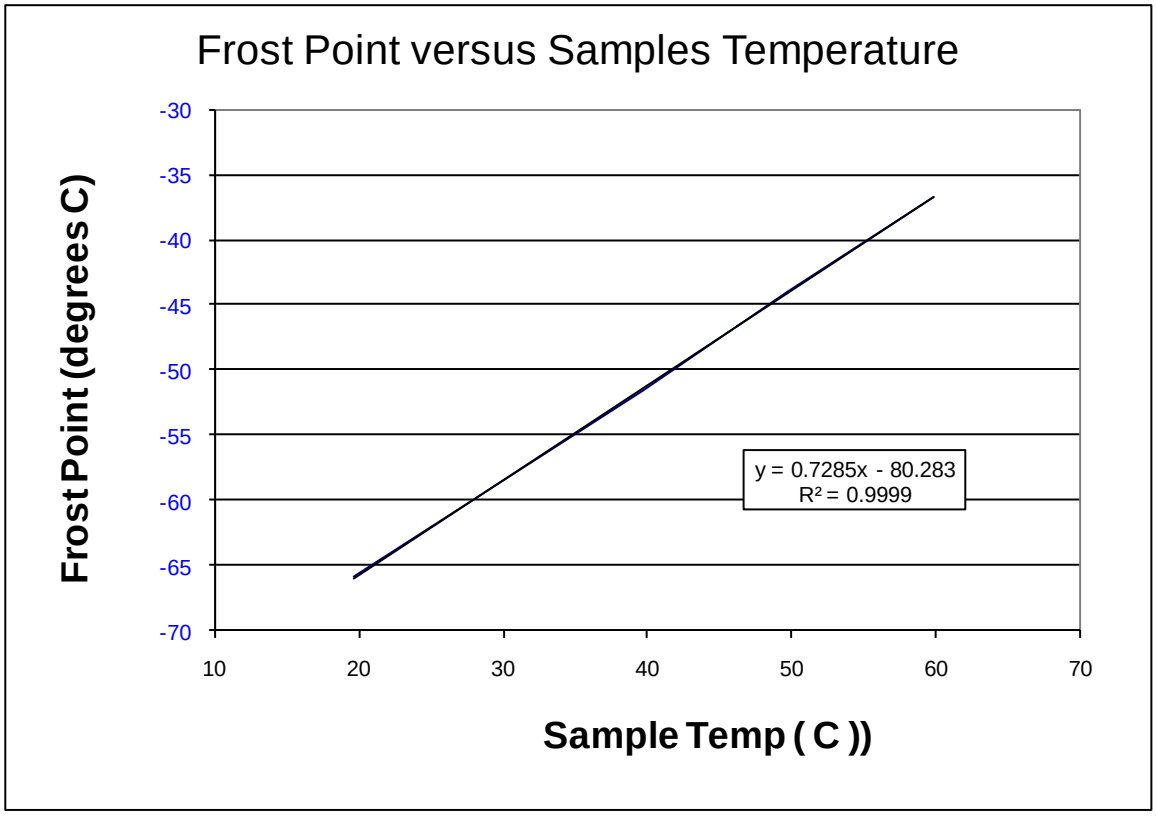

Figure 14. Frost point as function of sample temperature, LDPE-QC.

2.1 Determination of the concentration of water

In the processes shown in Figure 3, Figure 9, and Figure 11 an instrument called a hygrometer is used to determine the moisture content. A quick survey of the literature shows that there are many different technologies employed to measure the moisture content in air and other gases. These include three physical response methods known as the salt impregnated paper-coil method, the hair tension method, and wet bulb-dry bulb method. A number of electrically powered methods exist such as the capacitance, resistance, electrolytic, thermal conductivity, infrared spectrometry, and the chilled mirror method. Although all of these instruments report to measure the moisture

content they each do it by a different method and do not measure the same phenomena and thus provide different information with different implications. What is ultimately needed is a first principals method that provides the most reliable and reproducible indication of the water content irrespective of other process changes.

Before there can be a discussion of the various types of hygrometers and the principals by which these instruments operate, an understanding of the nature of water must be developed. Water is unique in that it can exist in 3 states within the temperature and pressure ranges of human existence. Depending on the temperature, pressure, and energy content water can exist as a solid, liquid, or vapor and in nature it most often exists in more than one state simultaneously causing the determination of its presence challenging. For instance in the environment we often come in contact with water existing simultaneously as solid ice and a vapor at temperatures below 0°C (32°F). Above 0°C the same water can exist simultaneously as a liquid and a vapor. In both of these two instances if the conditions remain constant then the vapor above the ice or water will become saturated based on the temperature of the ice or water. There also is one point where water exist simultaneously in all three states. This is called the triple point and it occurs at 611.73 Pa (0.00603 atm) and 0.01°C. The best way to understand the behavior of water is to realize that water as either ice or liquid exerts a vapor pressure above it that is a function of temperature and the melting of ice into water is a also function a function of temperature.

There are a number of sources in the literature and government organizations that tabulate a variety of thermodynamic properties of water in its various states. One such source from the literature is *"Thermodynamic properties in SI"* by Reynolds.[33] A handy way to show the relationship between the multitude of thermodynamic properties related to water in an informative way is through the use of a psychrometric chart often complied using 1 atmosphere total pressure as the reference pressure. Psychrometric charts present the water vapor that exist above ice and liquid water as functions of temperature. In the chart provided by Reynolds the X-axis is dry-bulb temperature °C, and the Y-axis is vapor pressure P_{water} (kPa). Other useful information included on the chart is wet-bulb temperature °C (also known as dew point above

[33] William C. Reynolds, *Thermodynamic properties in SI : graphs, tables, and computational equations for forty substances* (Stanford, CA: Dept. of Mechanical Engineering, Stanford University, 1979).

0°C and frost point below 0°C), mixture enthalpy (kJ/Kg_{air}), air content (kg_{air}/m^3), relative humidity (or degree of saturation), and γ (kg_{water}/kg_{air}). The point of interest to be understood from this graph is if any two values are defined such as dry-bulb temperature and wet-bulb temperature then all other values are fixed. The chart provided in Reynolds work shows one rendition of the psychrometric chart. Many other version of the chart exists depending on the relationships needing to be associated.

With this basic understanding of the relationship between water, ice, and water vapor a discussion of hygrometers and their method of operation can be conducted. The salt impregnated paper-coil method is used in dial type home units. A salt impregnated paper sheet is formed into a coil with a metal sheet and movement is generated by the differences in expansion between the two coils. The salt impregnated paper sheet expands when it absorbs moisture but the metal sheet does not. This is analogous to a bi-metal heat spring. Paper-coil hygrometers are of limited accuracy on the order of ±10% and do not responding to actual moisture content but to changes in relative humidity.[34] Relative humidity is a term often heard during weather forecast along with the term dew point. Relative humidity refers to the amount of moisture in the air relative to its saturation. The absolute amount of water vapor in saturated air depends on the temperature of the water source. At saturation air holds less water vapor when it is cool and more when it is hot. It is possible for the amount of water in the air to increase at the same time the temperature increases and the relative humidity not change. The paper-coil hygrometer does not measure the absolute amount of water in the air but its relative saturation.

The hair tension hygrometer is made from either human hair or horse hair. It indicates moisture by using the expansion and contraction of the hair with changes in moisture content. This device is also a relative humidity hygrometer. It does not measure absolute humidity. New models of these instruments are available that use synthetic hair and claim greater accuracy and reliability.[35]

There are a number of variation on the wet-bulb / dry-bulb hygrometer. This instrument uses two thermometers. A common stream of air is passed over both thermometers while one is maintained dry and the other has a cotton sock stretched over the thermometer bulb and wetted with water.

[34] http://www.innovateus.net/climate/what-hygrometer
[35] Spectrum Chemical website, http://spectrumchemical.com /

The dry bulb thermometer give the ambient temperature and the wet bulb thermometer gives the saturated dew point. Using these to values and a psychrometric chart the degree all of the other thermodynamic properties of the moisture in the air stream can be obtained. This was the first rigorous method. The wet bulb / dry bulb method is frequently used in industrial application such as heat and ventilation of building and manufacturing and food facilities. More precise method have since been developed.

Capacitance and resistance hygrometers are similar in their fundamental operation. Their sensors are coated with a moisture absorbing material and as they absorbs and desorbs water vapor the corresponding capacitance or resistance changes.[36] The absorbing layers are reported to be made of polymer films, lithium chloride, aqueous solutions of hygroscopic salts, carbon-powder suspension in gelatinous cellulose, aluminum oxide. From the available information these devices are vapor pressure dependent. The are prone to drift and foiling depending on other gases species and vapors that may condense on the active sensor producing a permanent offset or insensitivity. Often delays are seen during measurement with low concentration changes called wet-up and dry-down times.

One type instrument that has been in use for many years is know as a P_2O_5 meter which is based on Faraday's law of electrolysis. The instrument has a cell constructed with a platinum wire coated with P_2O_5 which electrolyzes the water contained in a 100 cc/min air stream.[37] [38] [39][40] [41] The accuracy of the instrument is highly dependent on the regulation of the air stream and is in essence a mass flow meter that discriminates on water although alcohols can cause false readings. The calculation of the moisture content also assumes that the ambient pressure is 1 atmosphere and has no means to accommodate other pressure. Common problems with the instrument is the limited sensing range and coating of the cell is either depleted over time or fouled with vapors.

---

[36] National Instruments website, http://zone.ni.com/devzone/cda/ph/p/id/214
[37] Ametek Instruments website, http://www.ametekpi.com/products/Model-303B.aspx
[38] CMC Instruments website, http://www.cmc-instruments.de/tma_overview.php
[39] Edge Technologies moisture and Humidity website, http://www.edgetech.com/moisture-humidity/gallery/item/oxymaster-16tdp-oxygen-dew-point-analyzer
[40] Meeco website, http://meeco.com/meeco/news-events/awards
[41] Systech Illinois website, http://www.systechillinois.com/en/water-vapor-permeation-analyzer-7000_22.html

Thermal conductivity hygrometers use two negative temperature coefficient thermistor element. There are placed in an electrical bridge circuit. One of the sensors are hermetically sealed in dry nitrogen and the other exposed to the ambient air. When electric power is applied to the two thermistors one will heat faster than the other due to the difference in the heat capacity of humidified air, This instrument is an absolute humidity sensor. It is noted that other gases and vapors with different heat capacities can cause error in the reading. The accuracy is reported to be ±0.5% relative humidity.[42]

Hygrometers based on infrared spectroscopy uses Beer-Lambert Law which is presented in Equation 3. A light source which is tuned to the absorption frequency of water is passed through the gas and the light is absorbed proportionally as a function of the concentration of the water.

Equation 3

$$A = \log_{10} \frac{P_o}{P} = ebc$$

where:

P_o = intensity of incident light beam

P = intensity of transmitted light beam

e = molar absorbtivity with units of L mol^{-1} cm^{-1}

b = path length of the sample cell, expressed in cm

c = concentration of the compound in solution, expressed in mol L^{-1}

A recent article American Meteorological Society online journal by Foskett outlined the procedure.[43] They used a 1 meter gas cell at 1.37 μ for the absorption band and 1.24 μ for the reference band. This method is considered an absolution concentration method. It is equipment intensive and does not accommodate pressures other than atmospheric.

---

[42] Choosing a Humidity Sensor: A Review of Three Technologies
July 1, 2001 By: Denes K. Roveti, website,
http://www.sensorsmag.com/sensors/humidity-moisture/choosing-a-humidity-sensor-a-review-three-technologies-840

[43] Laurence W. Foskett et al., "INFRARED ABSORPTION HYGROMETER," *Monthly Weather Review* 81, no. 9 (1953).

The last method that will be discussed is the chilled mirror method which is used in this work. The stream of gas to be analyzed is passed over a small mirror which is affixed to a sophisticated refrigeration system for cooling the mirror until a water layer forms on its surface.[44] The surface of the mirror is optically monitored to detect the formation of this layer. If the water vapor precipitates out on the mirror at temperatures above 0°C then the precipitate formed is called dew and the temperature at which it occurs is called the dew point. Likewise if the water vapor precipitates out on the mirror at temperatures below 0°C then the precipitate formed is called frost and the temperature at which it occurs is called the frost point. The formation of this layer occurs when the water vapor is cooled to the point at which it is saturated and it changes phase from a gas to a liquid or gas to a solid. Referring back to the discussion of the psychrometric chart it was stated that by knowing two independent points on the chart all other pertinent data about the water vapor can be obtained. The two points that the chilled mirror provides is namely the saturation line and a temperature.

The chilled mirror method is a first principles direct measurement that utilizes the phase transformation on the water itself. With the exception of the IR method, the chilled mirror is the only technique that does not have to refer the moisture content from a secondary measurement or phenomena but measures the phase change temperature directly. The chilled mirror technique is normally very reproducible sensing water vapor typically from -100°C to 20°C. Errors can occur if the mirror is contaminated with salts, organic vapors, or other condensable that may be in the gas stream. These errors can be minimized through proper maintenance and routine cleaning of the mirror. Some instruments are equipped with a automatic cycle that builds up a thick layer and quickly defrost to wash away contaminants.

[44] R H Systems website, http://www.rhs.com/index.php

Chapter 3
Theory

Mass transport across a barrier has been described in many ways for many purposes. If the pursuit was to simply ascertain the total loss of a fluid from a container over a period of time then a very general approach may be taken to obtain the needed results. For instance, a container to be filled could be weighed empty, its contents added and reweighed, stored under desired testing conditions followed by a series of weightings made at prescribed intervals. The results would show the rate at which the container's contents was lost. In this approach the complete container system is tested as a whole including the materials of construction of the container's walls, the integrity of any seams, seals, lids, and valves. If the rate of loss is unacceptable each component must be tested individually.

Depending on what component of the container is discussed it may simultaneously see multiple sets of conditions. If the argument is confined to a bottle half filled with liquid then the bottom half of the bottle is subjected to contact with the liquid on the inside and air on the outside, whereas the top half of the bottle is exposed to vapor at the vapor pressure of the liquid at the current temperature on the inside and air on the outside. If the rate of transport through the wall is a function of concentration, and concentration is defined as the number of molecules per unit volume, then the liquid is clearly more concentrated than the vapor. Thus different testing methods have been developed to evaluate each set of conditions.

The most general term used to describe the quantity of a migrating gas, vapor, or liquid is mass transfer flux (MTF) and if water is migrating then it is referred to water transfer flux (WTF). These terms are being used to remove any ambiguity or confusion that may arise. The definition of a flux is a flow through a cross sectional area in a period of time. Often fluxes are expressed in mass per unit area per unit time, e.g. $g/(cm^2\ s)$ and is represented as the letter J. Sometimes additional parameters are required to describe the transport of a gas, vapor, or liquid through an otherwise solid medium such as thickness of the medium and partial pressures on the supply and exiting sides.

One such description of MTF that is in the common technical vernacular is permeation. The term permeation has been taken to have the general meaning as MTF and is often defined that way. For instance in the ASTM standard F739-12 “Standard test method for permeation of liquids and gases through protective clothing and materials under conditions of continuous contact” the reporting units for permeation is $\mu g/(cm^2\ min)$. Other units also listed in the standard are $mg/(m^2\ s)$ and $mg/(m^2\ min)$. Other organizations define permeation with additional specificity. The Journal of Polymer Science requires permeation rates to be reported as $(kg\ m) / (m^2\ s^1\ Pa^1)$ which includes the mass transport across the barrier, the barrier’s thickness, and the vapor pressure difference from the high concentration supply side to the low concentration collection side.

Mass transfer flux is commonly understood as being the transfer of a fluid, gas or liquid across a solid barrier and is often confused with or used interchangeably with other terms such as permeation as shown in the previous discussion. Other terms used interchangeably include percolation, diffusion, and osmosis. Although these terms do refer to the movement of a mobile species across, through, or within a material matrix, they are technically different.

Percolation is the movement of a fluid through a porous media or barrier to either filter the fluid or allow the fluid to dissolve or leach a component contained within the media for transport. For many years coffee was brewed in a coffee pot called a percolator, in which the ground coffee beans were contained in a perforated basket and hot water was cycled through the ground coffee to extract the flavor.

Diffusion, on the other hand, is the random movement of the dissolved fluid within a material caused by molecular vibration. If the fluid concentration is uniform throughout the material, the fluid molecules have the same likelihood to move up or down, right or left, and in or out; but there is no net change in concentration or preferred flow. If there is a supply of fluid at one surface and a method of removal at the opposing surface, a concentration difference is established and the diffusing molecules have a net flow from the high concentration region to the low region.

Osmosis generally refers to the movement of a solvent across a barrier or membrane in an effort to dilute a highly concentrated solute found on one side of the barrier. This is an entropy-driven behavior.

What differentiates MTF from these other terms is that MTF describes the total flux or material transfer across a barrier, as Figure 15 illustrates. It should be noted that there is a supply of the migrating species on one side of the barrier that is feeding the process and a means of removal on the exiting side that is supporting a dynamic flow. One description of the MTF is known as permeation which describes the flux as the product of diffusion and solubility. Permeation is mathematically described in Equation 4:

Equation 4

$$P = S' D$$

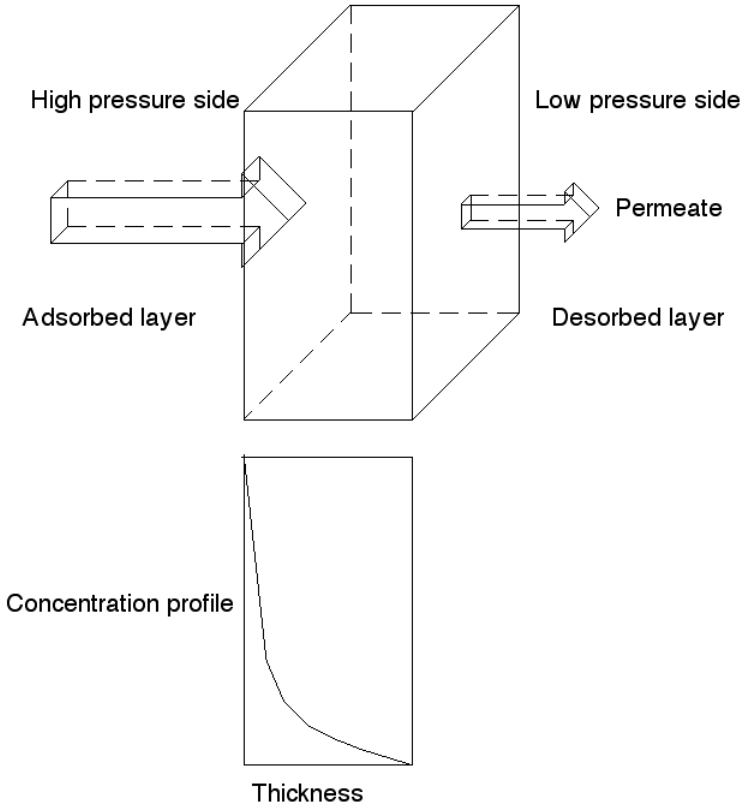

Figure 15. Mass Transfer Rate.[45]

[45] R. P. Campion and Industries Materials Technology Institute of the Chemical Process, *Permeation through polymers for process industry applications* (St. Louis; [Great Britain]: Materials Technology Institute of the Chemical Process Industries, 2000).

Before a discussion of MTF through the material that is of interest to this study can be done, a technical basis needs to be built. The approach used to describe permeation is a convenient place to start. Permeation is defined as the product of solubility and diffusion, a discussion of these two is a natural place to start. Solubility is the ability of one substance to be absorbed by another substance. When sugar is added to water, the sugar dissolves, making a solution. Solubility may be extended to solid substances as well. For the solid object above, solubility may be thought of as a two-step process in which the migrating species first contacts the surface of the solid and forms a thin adsorbed layer. This adsorbed layer is in contact only with the surface. If the adsorbed migrating species then begins to move into the structure of the material, it becomes absorbed or dissolved into the bulk matrix. Please note the difference between *ad*sorption and *ab*sorption. The quantity of the migrating species that is adsorbed and then absorbed is a function of several factors and is dependent on each component making contact. The dominant governing factor of the adsorption process is the free energy of each phase. Other factors include surface roughness, contaminates, pressure, viscosity, and rate of replenishment at the surface. The concentration or amount of permeate that can be dissolved into the matrix can have a broad range from infinitely small to infinitely large. It is all a function of how the matrix accommodates the migrating species within its structure. Examples will be shown later as to how different molecules can be accommodated within a structure and the effects of different size molecules on the structure.

Diffusion is the movement of atoms through a matrix caused by the vibration of the molecules of both the migrating species and the matrix. Diffusion through metals were some of the first materials studied and frequently used to describe the process and will be used here as the substrate. Since molecules are always vibrating and the intensity of the vibration is proportional to the energy they possess from heating, as the temperature increases, the molecular vibration increases. With the vibration of both the migrating species and the matrix, if the vibrations within the matrix coincide, a hole within the structure can momentarily appear, allowing a vibrating migrating molecule to jump into the available position. Since these vibrations are purely random, the is a probability of any given molecule to move in any given direction. Only when the probability is skewed as a result of differences in the availability of holes from one region to another is there a net movement of the migrating species in a given direction. For instance, if within a given region of a matrix many of the holes are filled with migrating molecules, then the

next neighboring region of the matrix would have a higher probability of having a hole, since it possessed fewer migrating molecules. Thus, the net movement of migrating molecules would favor the region with the highest probability of holes.

To illustrate what diffusion may look like, an idealized barrier or material matrix has been created, as shown in Figure 16.

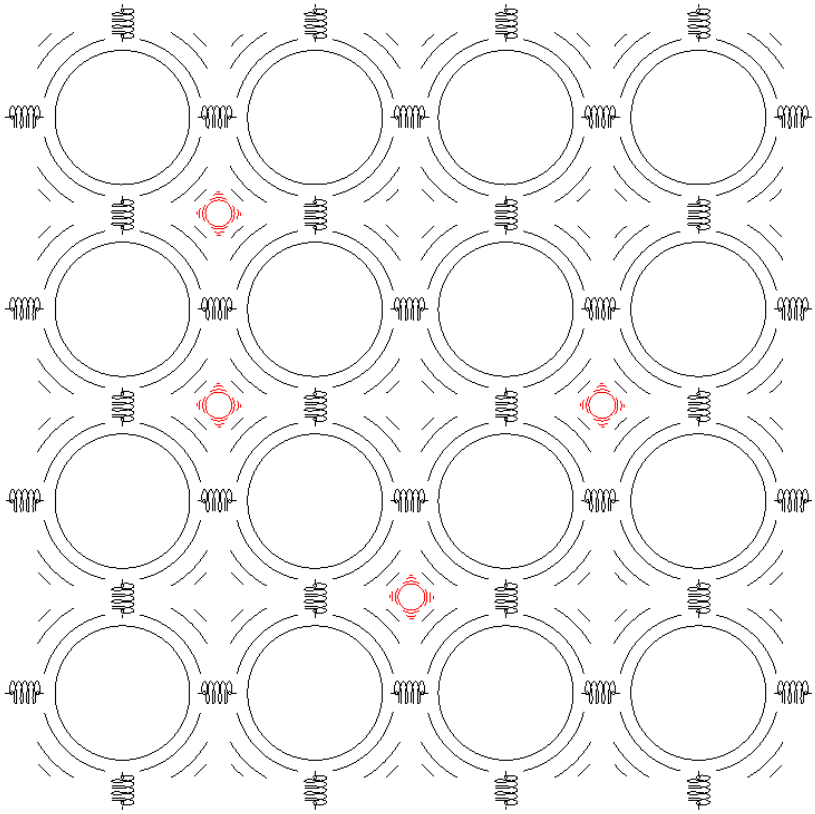

Figure 16. Typical two-dimensional depiction of cubic lattice with small interstitial atoms.

The matrix shows each atom belonging to the matrix of equal-size hard spheres with bonds connecting them to their neighbors. The bonds are like elastic springs that allow for atoms to vibrate. *Interstitial spaces*, where there are no atoms or bonds, are shown. The size of these interstitial spaces varies as the atoms vibrate in three dimensions. If the vibrations of matrix atoms common to an interstitial space moves simultaneously in opposite directions, the void

space may expand sufficiently to allow for the admittance of the migrating atom. These migrating atoms are shown in the interstitial spaces in red.

The previous example is very simplistic and makes many assumptions, such as all atoms in the matrix are identical, all bonds are identical, and the atomic spacing is not distorted by residual stresses caused by outside influences. This type of depiction is often used to represent highly crystalline materials like metals. Elements that are small enough to be found in the interstitial space of a common metal like iron include carbon (C), hydrogen (H), oxygen (O), nitrogen (N), and boron (B). The model depicted in Figure 16 is idealized to explain the basic concept of diffusion. The size of the migrating molecules can influence the behavior of the matrix to accept or permit passage of other migrating molecules due to strain induced into the structure. Figure 17 shows the distortion that may result as a consequence of larger interstitial atoms.

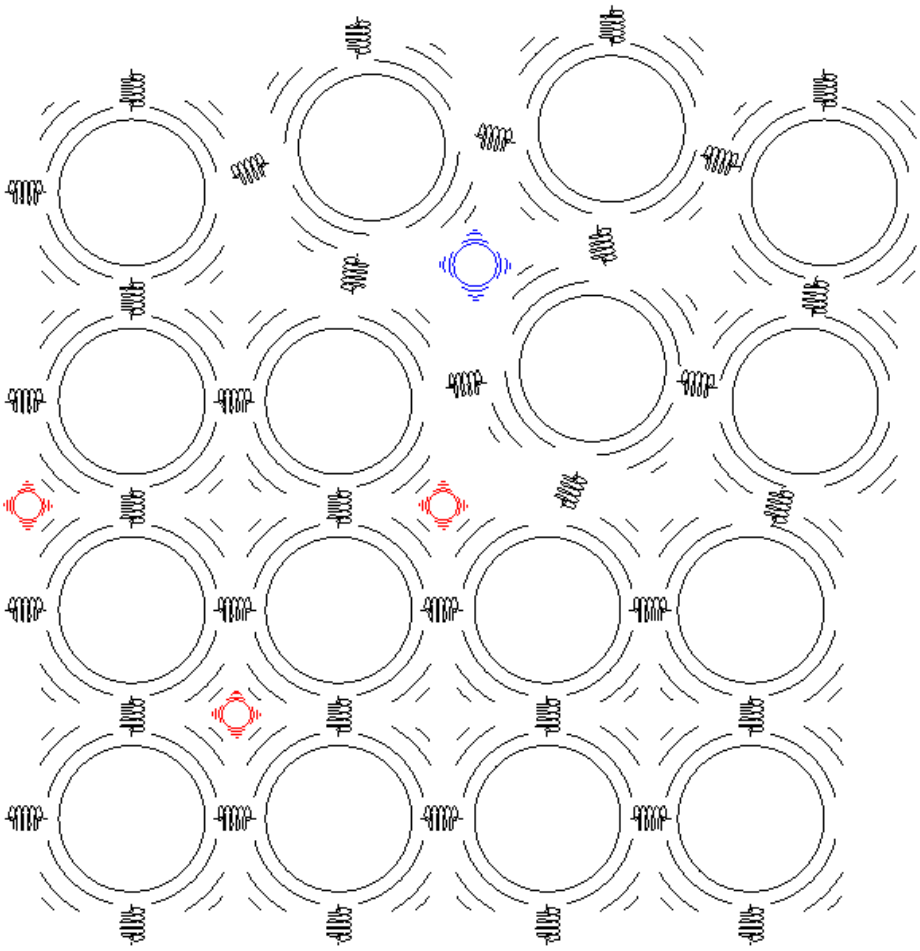

Figure 17. Two-dimensional lattice showing strain due to large interstitial atom.

The large interstitial atom causes distortion in the lattice alignment that may extend into several adjacent rows. The distortion causes crowding of the matrix atoms, possibly hindering the migration of other atoms in the vicinity.

As Figure 16 and Figure 17 show, the number of atoms that could be accommodated within a given structure is a function of the interatomic spacing of the lattice, the size of the interstitial space, and the size and number of the diffusing molecules. A real-world example could be constructed as follows: A transparent box is filled with ping-pong balls glued together at their contact points to represent the lattice structure, and small steel spheres are poured into the ping-

pong balls to represent the interstitial atoms. Obviously, the small steel spheres would easily pass through the void spaces left by the ping-pong balls. But if the small steel spheres were replaced with marbles just small enough to squeeze through the void spaces with a gentle push, the rate of transport and total number of marbles that could be accommodated within the structure and passed through to the other side would be considerably smaller.

This example helps illustrate both concepts that govern permeation: solubility and diffusion. In this case, solubility is the capacity of the ping-pong ball matrix to store either large numbers of small steel spheres or smaller numbers of marbles within the void spaces of the structure. Differences in transfer rate, or diffusion, can be thought of as either the small steel spheres pouring through the ping-pong ball matrix or the marbles having to be pushed. It now becomes obvious that by adjusting the structure of the lattice and the migrating species, both the solubility and rate of diffusion can be affected and so to MTF or permeation.

3.1 Fundamentals of permeation and diffusion

Permeation has been described mathematically in terms of diffusion and solubility. Paul Shewmon described Fick's first law of diffusion for the simplest case as a mass transfer or flux, *J*, which is the quantity of diffusing species, *q*, that occurs through an area, *A*, over time, *t*, as Equation 5 shows:[46]

Equation 5

$$J = \frac{q}{At} \quad .$$

The flux may also be described using the system parameters of concentration difference and thickness through the barrier, as presented in Equation 6:

[46] Paul Shewmon, *Diffusion in solids* (Warrendale, Pa: TMS, 1989).

Equation 6

$$J_1 = -D\left[\frac{\partial c_1}{\partial x}\right]_t$$

D is known as the diffusion coefficient, or diffusivity, which is a scaling factor that describes the flux in terms of the ratio of concentration difference and length. Often when different materials are tested under the same conditions, only the diffusivity is quoted as a measure to compare different transmission rates. The higher the diffusivity, the higher the corresponding flux for a standard set of conditions. For clarity the equation, Equation 7, has been rewritten with units:

Equation 7

$$J_1\left(\frac{mass}{L^2 t}\right) = -D\left(\frac{L^2}{t}\right)\left[\frac{\partial c}{\partial x}\right]\left(\frac{mass/L^3}{L}\right)$$

In this form of Fick's equation it is assumed that the diffusivity is independent of the concentration gradient. Shewmon makes an analogy of constant diffusivity with respect to concentration differences to that of constant electrical resistance of a wire with respect to voltage difference. Both concepts show that resistance and diffusivity remain constant as the potential difference changes.

When diffusivity does change as a function of concentration, Fick developed his second law as Equation 8 presents:

Equation 8

$$\frac{\partial c}{\partial t} = \frac{\partial}{\partial x}\left[D\frac{\partial c}{\partial x}\right]$$

In Equation 8, *D* becomes part of the partial differential, and thus differences in diffusivity can be accounted for along with concentration differences.

In the experimental evaluation of diffusional processes one typical method is to first establish a steady state flux across the barrier and then analytically determine the concentration of the diffusing species at incremental distances through the barrier in the direction of the flux movement. In Figure 18, the flux entering, J_1, is equal to the flux leaving, J_2. If this were not true, there would be a buildup or depletion of the diffusing species over time. If the diffusion is abruptly halted by some means like quenching, the concentration of each differential element can be determined analytically.

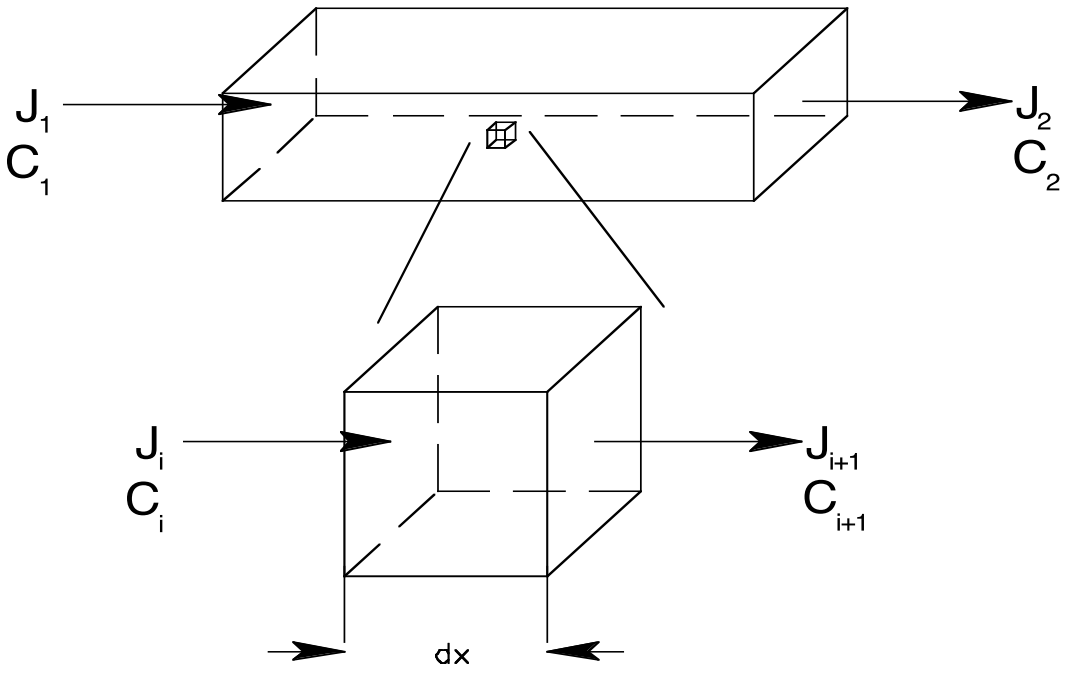

Figure 18. Diffusion flux model showing individual element.

By plotting the concentration versus the distance through the barrier, Shewmon shows that the diffusion coefficient is the slope of the line. For permeation studies of gases through thin films in which the film is too thin to measure the dissolved concentration at differential intervals, the

procedure requires the measurements of the overall steady state flux through the film, the concentration drop across the barrier, and the barrier's thickness. The concentration at each of the two surfaces of the film is taken as an equilibrium concentration with the supply source concentration.

Typically before a barrier is subjected to testing, the concentration of the diffusing species is zero everywhere within the material. The barrier is then mounted in a test apparatus and a known concentration of the diffusing species is brought into contact with the barrier on the supply side. Very often the test incorporates a method to remove the diffusing species as it exits the barrier, thus maintaining its concentration on the exiting side at essentially zero. At the start of the test, the diffusing species begins to build up just within the surface of the barrier and then, driven by the concentration gradient, migrates through its thickness. The concentration initially takes on a profile that looks like t_0 in Figure 19. At this point the diffusing species is beginning to fill the available sites within the structure of the barrier to establish a dynamic movement from the high-concentration supply side to the low-concentration removal side. As time elapses, the concentration moves to a more linear profile throughout the thickness.

By examination of the graph in light of Fick's first law, it can be seen that the slope of the concentration gradient of the linear steady state portion is the diffusion coefficient, *D*. This is assuming that the diffusion coefficient is independent of the concentration gradient. The same diffusion coefficient is applicable to the non-linear curves, but it must be understood that the slopes are changing over the length of the barrier because of accumulation within the material while trying to establish steady state.

If steady state diffusion is achieved without establishment of a linear behavior, the diffusivity must be changing as a function of concentration, and Fick's second law applies.

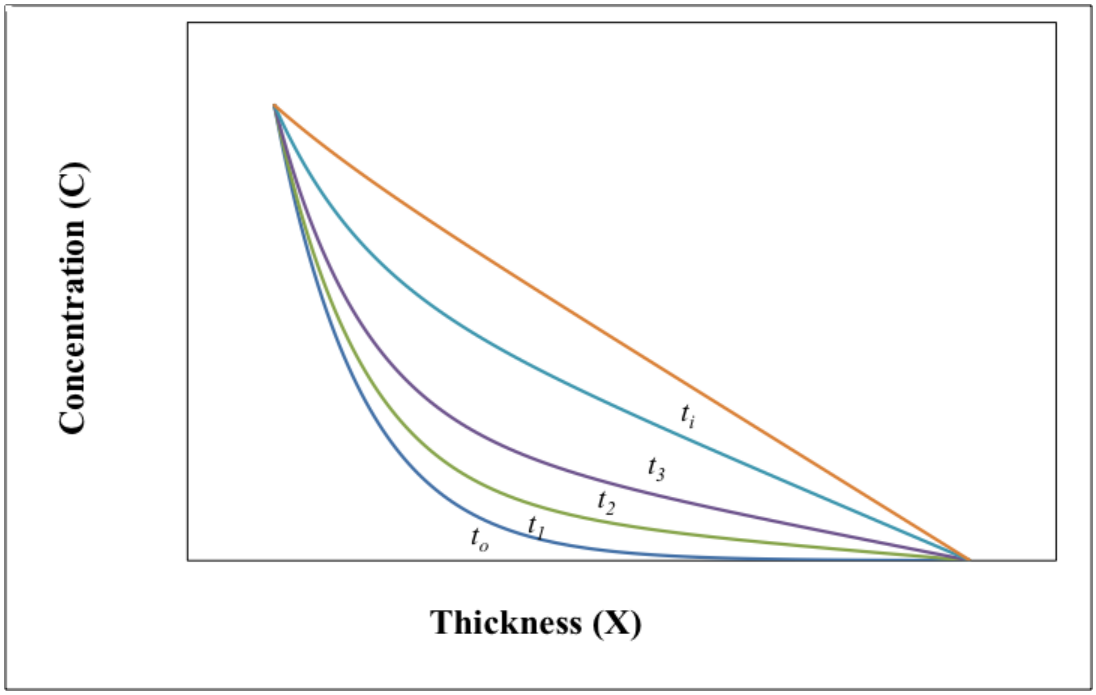

Figure 19. Progression of concentration profiles of diffusing species.

If the concentration of the diffusing species through the barrier cannot be analytically determined — because the barrier is too thin to section, for example — then other means must be used to determine the flux, diffusivity, and concentration gradient through the barrier. One such method is called the *time-lag method*. In that method the barrier is placed in the test apparatus with a zero concentration of the diffusing species within the material, a zero concentration on the supply side, and a zero concentration on the exiting side. The test begins by rapidly increasing the concentration on the supply side of the barrier from zero to the desired testing condition. If the diffusing species is a pure gas, for example, then on the supply side the pressure can be raised very rapidly from a pressure of zero to the testing conditions by a valve opening. On the exiting side of the barrier all material that passes through the barrier is collected in a closed chamber and the pressure rise is recorded. When the volume of the collection chamber and the pressure of the exiting gas are known, the flux can be determined. Figure 20 presents a typical profile of such a test.

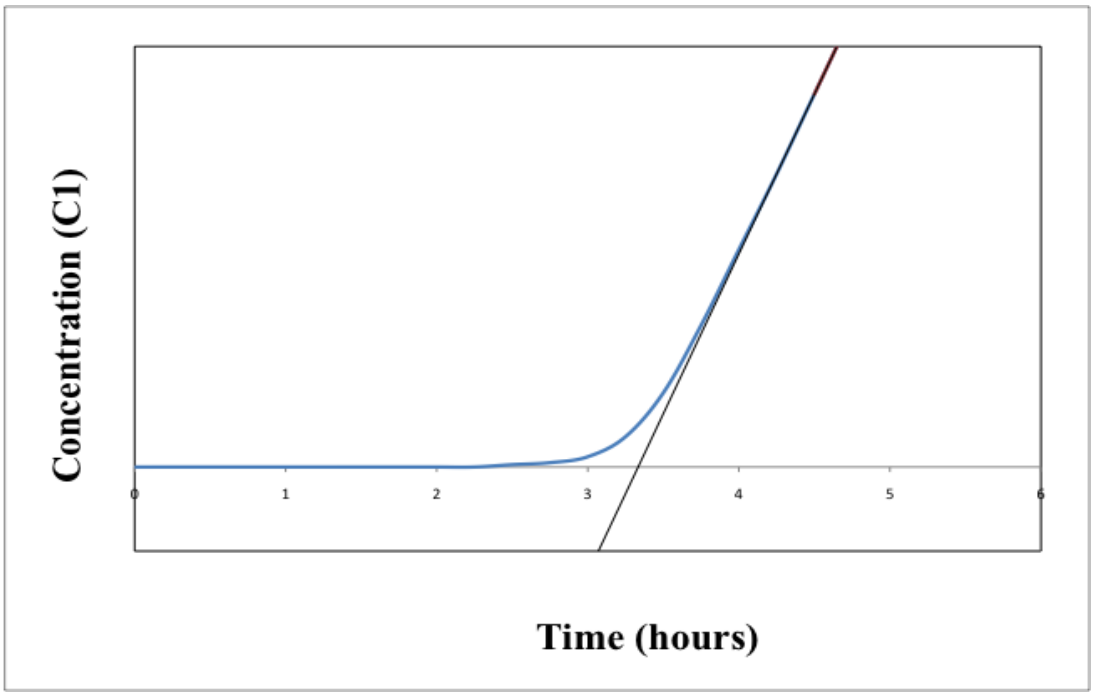

Figure 20. Time-lag diffusion testing profile.

Cussler describes the mathematics used in the time-lag method.[47] Equation 9 shows concentration C_o as the supply side concentration, C_1 as the exiting side concentration, P as the permeability, A as the area of the sample, V as the volume of the sample, l as the sample thickness, t as time, and D as diffusivity:

Equation 9

$$C_1 = \frac{C_o PA}{Vl}\left(t - \frac{l^2}{6D}\right)$$

Examination of the equation shows that at the beginning of the test all factors are constants with the exception of the exiting concentration, the time, and diffusivity. When the test begins, the gas starts migrating into the sample, but it is not until a steady state is reached that the diffusivity

[47] E. L. Cussler, "Diffusion Barriers," *Diffusion Fundimentals* 6(2007).

stabilizes. Once the diffusivity is stable, the pressure assumes a constant pressure rise, and the two remaining variables are exiting concentration and time. The intersection of the linear section of the curve to the x-axis yields the time that the diffusion coefficient becomes stable. The diffusion coefficient is now related to time and is determined using the following, in Equation 10

Equation 10

$$D = \frac{l^2}{6t}.$$

In the aforementioned example, the concentration of the diffusing species was measured as pressure, but it could be mole fraction or a number of other conventional concentration measures, depending on the diffusing species.

When samples need to be tested at relatively low temperatures or the material's responses make the time lag method inappropriate to determine diffusional parameters, a continuous steady state test can be used. In this testing methodology the material is mounted in the testing device as described before and the supply concentration is initiated. As the permeate passes through the barrier, it is continuously removed by a purge gas, and the mixture is passed through a high-resolution detector. The diffusion cell containing the sample is maintained at a constant temperature often submerged in a water bath. The sample cell is then systematically stepped through a series of temperatures. The sample is held at each of these temperatures for a predetermined interval to evaluate the sample's tendency toward equilibrium. Data collected during the test include time, *t*, the flux of permeate, *J*, and sample temperature, *T*. It has been shown that the diffusivity is a function of temperature, as shown by Equation 11 .[48]

Equation 11

$$D = D_0 \exp\left(\frac{E}{RT}\right).$$

[48] Campion and Materials Technology Institute of the Chemical Process, *Permeation through polymers for process industry applications.*

In Equation 11, D_0 is the diffusivity at standard conditions and R is the gas constant, T is the process temperature, D is the diffusivity, and E is the activation energy. Thus D, D_0, and E are the only unknowns; and since there are multiple sets of data collected at different temperatures, the unknowns can be found from the solution to a set of simultaneous equations. Permeation data are typically collected at five discrete temperatures providing abundant data sets. With the measured permeation flux and the determined diffusivity the solubility can be easily obtained.

3.2 Effect of polymer structure on barrier properties

In the earlier example using ping-pong balls, each was bonded to its six closest neighbors. If the atom represented by the ping-pong ball was not able to accommodate six bonds but instead four or eight bonds, as is the case with most metals, then the structures that could be formed would be rather different. These are called *valence states*, which describe the number and types of bonding the atoms can make.

As mentioned earlier, the depictions of molecular structure in Figure 16 and Figure 17 are idealized metal structures used for establishing a basis from which the structure and behavior of more complex materials can be developed. In the metal structure each atom is attached to its neighbor through metallic sharing of non-localized electron bonding represented by springs. For clarity the figures show the structure in two dimensions, but in fact the bonding extends in all three dimensions. Thus, each atom shares six bonds with its neighbors: one above, below, right, left, in front, and behind. The material of interest in this study, polyethylene, has a more complex structure due to its bonding and thus forms different structures, resulting in the formation of different paths for WTF.

Polyethylene is primarily made up of carbon and hydrogen; thus, it is one of many hydrocarbons. Carbon's available valence state is 4, and hydrogen's is 1. In polymer chains of polyethylene the majority of bonds are sigma bonds with either another carbon or hydrogen. Through carbon's ability to form multiple bonds it forms the molecule's backbone populated with hydrogen as shown below, Figure 21.

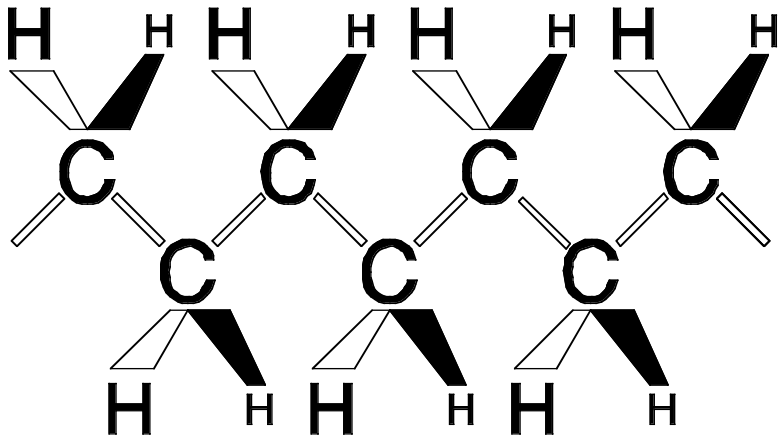

Figure 21. Basic polyethylene structure.

The backbone may extend for tens of thousands of repeat units forming what are known as a polymer or *macromolecules*. Polyethylene can also have branches forming side chains, or the branches may form linkages with another chain or the same chain, forming a cross-linked structure, Figure 22, Figure 23.

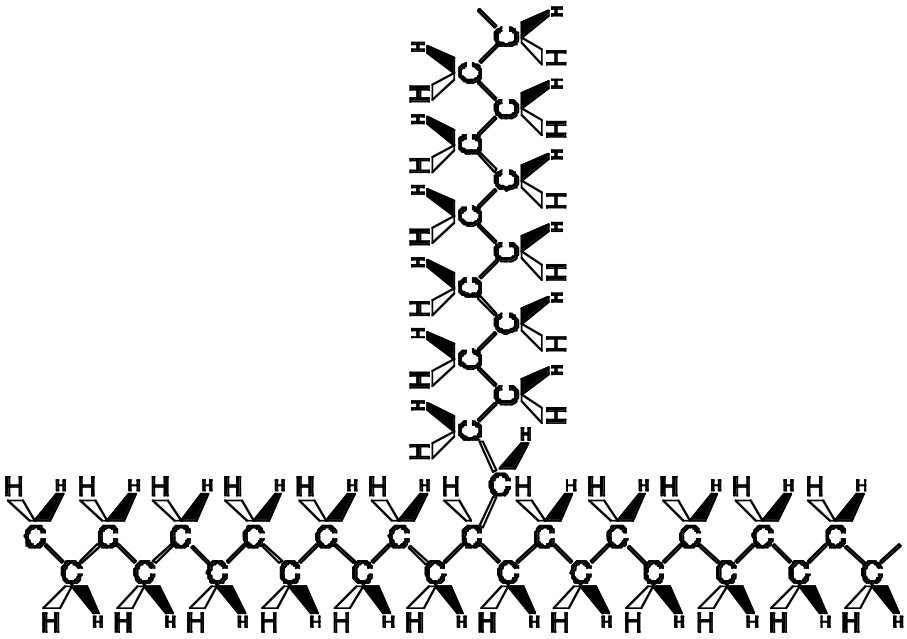

Figure 22. Branched polyethylene structure.

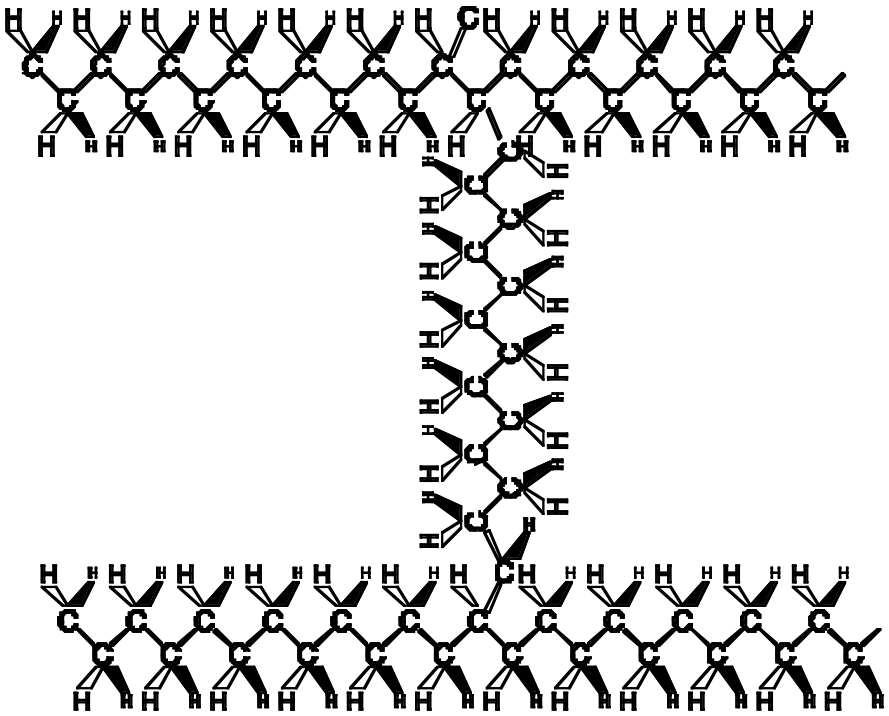

Figure 23. Cross-linked polyethylene chain.

The MTF of gases and liquids through polymers is a broad field and has been described as a function of many parameters throughout literature. This is due in part to researchers' desire to find the relationship between a specific material's properties of interest and moisture transport rate at the time. For example, the property of interest may be the ratio of copolymers, degree of cross-linking within the structure, fillers used during processing, and type of gas or liquid being studied. The present work focuses on the WTF of moisture through semi-crystalline polyethylene polymers. The polyethylene polymers of interest are high density, low density, and linear low density. The degree of crystallinity in these materials is adjusted through the cooling rate from the melt and a post processing annealing. The resulting morphology is assumed to control the WTF. With a command of these three pieces of information — namely, processing parameters, resulting morphology, and WTF — predictions as to how a polymer may be manufactured with a desired WTF is possible. An additional benefit is a foreknowledge of change in WTF that might be

expected if a process change is made. This knowledge will help the process engineer control the product's characteristics instead of simply accepting the resulting consequences.

Unlike the majority of molecules of any given chemical, which are relatively small, discrete, and indistinguishable from one another (e.g., ethylene $CH_2=CH_2$), polymers are macromolecules or long chain molecules made up of the linkage of these fundamental repeat units known as *mers* i.e., -CH2-CH2-. Depending on the method of polymerization these mers can link together to form linear chains of various lengths, such as in linear or branched polyethylene or they can cross-link to form complex networks. As a consequence of these extremely large molecules, they behave different in both their molten and solid states. In the molten state they often form viscous fluids that have complex flow properties that respond to both compressive and tensile forces due to the extremely long chemical chains. These polymer chains behave in a similar fashion to strings that have to slide over one another when a force is applied. The shorter these strings are, the more the molecules behave like hard spheres, as viewed in many classical chemical perspectives. If the strings are long, they become entangled with one another and, thus, increase the resistance to deformation and flow, which is the primary cause for the increase in viscosity.

As they cool into a solid state, these long chain molecules form amorphous and crystalline phases. The crystalline phase is highly ordered, aligned, and denser. The amorphous phase is a random disordered chain devoid of any discernable repeating pattern in the solid cooled form. Because of the random disordered nature of these structures, the amorphous phase is less dense than the highly ordered crystalline forms because it is not as tightly packed. Consequently, these two phases coexist, and under the appropriate chemical and/or physical influences they can be converted from one to the other. The process by which these two phases are formed and converted from one to the other will be explained.

At this point it should be pointed out that two general categories of polymers exist: *thermoplastics* and *thermoset polymers*. *Thermoplastics*, like polyethylene, are ones that melt upon heating, form viscoelastic fluids, solidify upon cooling, and can be reheated to re-melt. *Thermoset polymers*, like epoxy, form a solid by chemical reactions causing linkages to form between the individual chains of polymers or to form with itself at another location, creating a network structure. The thermoplastics will re-melt upon heating, whereas the thermoset polymers

will degrade through chemical linkage destruction instead of melting. Obviously, these two materials respond differently to the application of heat. This difference in response to heating provides a means to control the thermoplastics morphology that may be used to probe the effects of structure of the material in the solid state on WTF. Therefore, thermoplastics can be heated to erase their structure and through controlled cooling can be re-formed into shapes with differing degrees of crystallinity.

The application of heat results in molecular thermal motion. This motion can be manifested as vibrational, translational, or rotational movement. These energized modes of motion allow the chains of molecules to have main chain and segmental motion and slide over one another. An alternate understanding is that these chains can occupy states requiring higher energy levels. As heat is added, the hindrance to movement is overcome and the solid becomes a fluid when the chains are permitted to assume all possible modes. If the polymer is cross-linked, the chain is not completely free to move. If the degree of cross-link is high, as in thermoset polymers, the addition of heat does not lead to additional mobility but to bond destruction and degradation.

Since the focus of this work is to evaluate the relationship between morphological structures as a result of processing parameters and the effect on the WTF, three polyethylenes have been chosen as materials of study. These polyethylenes are low density, linear low density, and high-density polyethylene. These polymers are thermoplastics that are well behaved and known to form semi-crystalline structures from their melted form. The two categories, thermoplastics and thermoset polymers, were used to show how the difference in structure results in how heat has different effects because of their structures upon heating. These three polyethylenes will also be used to show how small modifications to the backbone of the chain effects their tendencies to form crystalline structures that control the WTF.

High-density polyethylene (HDPE) is a linear molecular chain, i.e. with the fewest branches, and upon cooling tends to form (lamella) structures with a high degree of crystallinity, or order. In the literature *molten polymer* is often described as an amorphous coil. Each polymer chain may be thought of as a single amorphous coil that, when pulled easily, slides past all of the other coils. In the molten state the amorphous coil is randomly distributed and is free to assume any shape and move in any direction it is pushed or pulled. The molten random amorphous coil takes up more

space than it would in its solidified state which becomes more ordered. Upon cooling the amorphous coils become ordered and randomly arrange into crystals. The crystalline phase obtains its higher density by eliminating the free space that exists in the amorphous coil.

If this analogy holds true to thermoplastics, then the lowest-energy, highest-density packing arrangement for the polymer would be in the form of polymer chains aligned parallel to one another. The question then becomes, How does a mass of randomly distributed polymer chains become aligned into an ordered structure? First, the polymer chains became disordered by adding heat that provided sufficient energy for the segments of polymer chains to begin to assume higher energy states (i.e., to begin to move in ways they earlier could not, thus increasing disorder). This new mobility allows the segments to become randomly distributed. Conversely, as energy is removed, the randomly moving chains move through all possible orientations and get trapped in the lowest energy configurations. Polymer chains are almost infinite in length relative to their diameter, so the chains tends to find local low-energy traps that segments of the whole chains assume. This produces the affiliation of one chain with many parallel ordered alignments. These parallel ordered alignments are known as *lamella*, and if the energy is removed slowly, the chains have sufficient time to slide past one another to reorder into very large crystallite islands.[49]

As Figure 24 shows, the chains align into crystallites, and they continue to grow until the chain becomes energetically favorable to fold back on itself. If the polymer is cooled from the melt very slowly, the chains have sufficient energy to move and align with a crystallite, which then tends to grow very large in size. The larger the crystallite, the lower the energy states and the higher the degree of crystallinity. Mandelkern has reported lamella thicknesses up to 1000 angstroms with a density approximately 0.99 g/cm^3 for low molecular weight fractions which is approaching the theoretical unit cell density of 1 g/cm^3.[50] This sample was crystallized at 130°C for long periods of time. As a corollary, a high molecular weight fractions was rapidly cooled producing a density of just 0.92 g/cm^3 showing insufficient time and energy for rearrangement. The low molecular

[49] B. Wunderlich, *Macromolecular Physics: Crystal nucleation, growth, annealing* (Academic Press, 1976).
[50] "Morphology of Semicrystalline Polymers," Leo Mandelkern, Characterization of Materials in Research, Ceramics and Polymers, Syracuse University Press, Syracuse, NY, 1975

weight slow cooled sample also possess the highest heat of fusion 69 cal/g, nearly the theoretical maximum, whereas the high molecular weight sample heat of fusion was 37.5 cal/g.

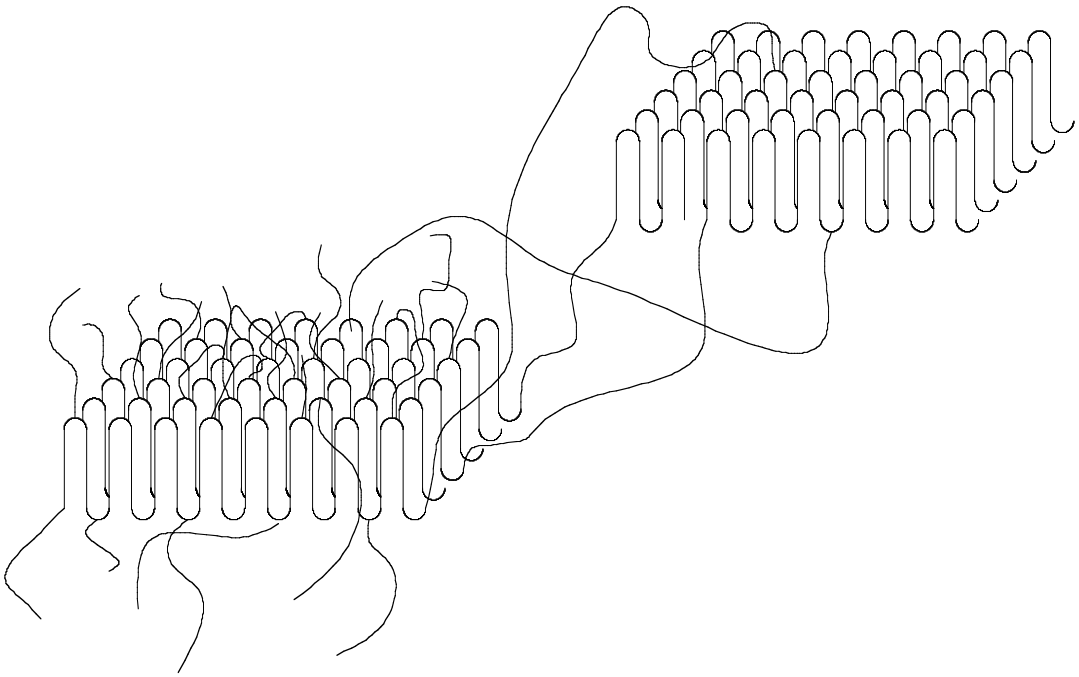

Figure 24. Crystallite formation showing amorphous region and excluded side branches.

Figure 24 shows the folded crystallite, note that the side branches are excluded at the folds of the chains, and the tie chains connecting individual crystallites that constitute the amorphous region. It should be noted that there are several key factors that control the formation of crystallites. These factors include the temperature below the melting temperature at which the polymer is solidified from the melt (i.e., under cooling), the critical sequence length, and length of side chains. By controlling these factors it is possible to control the crystallinity.

The structure of Low Density Polyethylene (LDPE) and Linear Low Density Polyethylene (LLDEP) differ from that of HDPE because of the sequence length of the molecule's backbone and the length of the side branches. Figure 25 shows the structure of LDPE on the left and LLDPE on the right. During the polymerization process side branches are formed and in the

LDPE the spacing on the backbone and the length of the side branch are small. In the LLDPE the size of the side branches are fixed by the copolymer and spacing on the backbone more regular.[51]

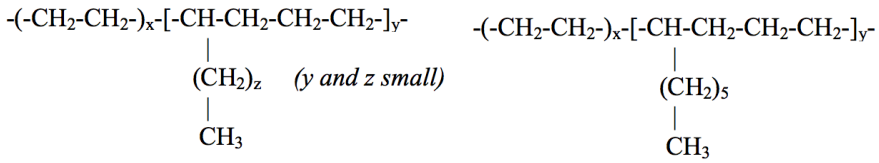

Figure 25. Structure of LDPE (left) and LLDPE (right)

Although random defects can occur during polymerization causing branching, most branched polymers result from the combination of two or more monomers. Wunderlich points out that the monomers may differ by chemistry, configuration, structure, or position.[52] The order of the repeat units can be regular, block, or random. He notes that the inclusion of a different monomers within the chain can disrupts the crystals formation and often is rejected at the interface or causes defects within the forming crystal. When the defect is within the crystal it can be a simple point defect or the cause for the start of an amorphous region. Wunderlich describes Flory's two-phase equilibrium theory of crystallization as a simplistic model but a good basis for understanding the thermodynamic driving force for crystallization.

The two-phase model consist of A and B units and the A units occur in sequences with various lengths. These A sequences are what combines to form the basic crystal. When a B unit occurs the crystal must be terminated. Equilibrium is reached when the sequence length of repeat A units match a minimum sequence length ζ. These basic crystal formation are know as micellar. Once all of the A units with minimial sequence length have been incorporated into crystals the B units are rejected to the interface. This is a simplistic model but serves the purpose of showing a systematic approach to crystal formation.

It is important to understand the relationship between controlling the crystallinity and WTF rate. The ratio of the crystalline and amorphous phases changes with crystallization temperature. Since water migration occurs in the amorphous phase, the nature and amount of the amorphous phase

[51] http://www.steinwall.com/ART-polyethylene.html
[52] Wunderlich, *Macromolecular Physics: Crystal nucleation, growth, annealing*.

affect the WTF. Now with an understanding of the basic crystal formation the effects of different cooling rates will be explored.

Mandelkern showed that when polyethylene is crystallized at high temperatures, ~130°C, over extended periods of time more dense structures with higher degrees of crystallinities are formed.[53] When the samples were quenched lower densities were formed. Higher densities correspond to higher degree of crystallinities. For a given crystallization temperature the low molecular weight fractions produce the highest densities. Thus the degree of crystallinity is proportional to the crystallization temperature and inversely proportional to the molecular weight.

3.2.1 Effect of cooling rate and heat treatments on morphology

It has been stated that when polymers are heated above their melting points, sufficient energy is supplied to allow the chains to assume higher energy states that translate into greater freedom of movement. Conversely, when the energy is removed, the chains tend to be limited to fewer modes of movement and align forming crystals. If a unit volume of polymer is heated just above the melting point and cooled infinitely slowly, it would possess enough energy and have enough time to rearrange and form a nearly perfect crystal. It would first begin at a single point, where a critical number of chains would align and form a nucleus, giving up its energy to the rest of the chains. As energy was further removed from the system infinitely slowly, the chains would have time and energy to move to the lowest possible energy state and be incorporated into the single nucleus. Over time all of the chains would be combined into a massive crystal grown from just one nucleus. It could be said that the degree of crystallinity was nearly 100%. In other words, the polymer was almost crystalline with little amorphous region. Now assume the melted polymer was cooled infinitely fast. If heat could be removed from all chains at the same instance, all of the chains would have insufficient energy and time to rearrange and would be frozen in their current random position. Now in its cooled state it could be said that the material was 100% amorphous. It possessed no resemblance of order within its structure.

---

[53] L. Mandelkern, "Morphology of Semicrystalline Polymers, Characterization of materials in research — ceramics and polymers, J. J. Burke and V. Weiss, Eds., Syracuse University Press, Syracuse, N. Y., 1975," *Journal of Polymer Science: Polymer Letters Edition* 15, no. 10 (1977).

The concept of a perfect crystal and perfect amorphous phase has been introduced to illustrate the point that the polymer can be solidified to produce a range of crystallinities. It is theoretically possible to create a polymer that is 50% crystalline and 50% amorphous phase. The 50% crystalline phase could be one large crystal, or it could be divided into many small crystals, the sum of which equals 50%. As the crystals are fragmented into smaller units, so is the amorphous phase.

One means to create small discrete crystals is to change the cooling parameters. One such cooling process would be to cool the melt to a temperature below the melting point sufficient to more rapidly initiate nucleation and hold that temperature to allow for crystal growth. Once 50% crystallinity was achieved, quenching could halt the crystal's growth. The larger the under cooling, the higher the number of nucleation sites, each with a proportionally smaller volume.[54] This would likewise fragment the amorphous region into smaller volumes. If the cooling regime was made more radical by increasing the under cooling, an even large number of even small nucleation sites would be formed. Ultimately, this scheme provides a means to control the degree of crystallinity and the crystal size distribution.

Another cooling regime that could be used is a postprocessing heat treatment. Postprocessing heat treatment is the reheating of materials that include crystallized and amorphous regions to promote the growth of the nuclei at the expense of the amorphous region. The way this process would work is that the polymer would be cooled to a predetermined under cooling to initiate crystallization and grow a specific number of crystallites and then be quenched to stop the process. This would result in a polymer with a specific number of nuclei but with a less than desirable degree of crystallinity. The polymer would then be reheated to a temperature just below the crystallization temperature that would promote the additional incorporation of the amorphous phase into the existing crystalline phase. This temperature would be held for a specific period of time until the desired degree of crystallinity was achieved.

---

[54] Leo Mandelkern, *Crystallization of polymers. Vol 2, Vol 2* (Cambridge: Cambridge University Press, 2004).

3.2.2 Influence of degree of crystallinity and crystal size distribution on barrier properties

When water passes through a polymer, it seeks the path of least resistance. In semi-crystalline polymers that path is through the amorphous phase found in between crystallites. The amorphous phase consists of interfacial and interzonal regions, as Figure 1 shows. The interface is that region adjacent to the crystal made up of loose loops and tie chains excluded from the crystallite. The interzonal region primarily consists of tie chains connecting crystallites. If the polymer were 100% amorphous, the flow would have the least resistance passing around the individual chains, as if passing through a highly porous media. If some of the chains are aligned to form crystallites, the dense packing of the crystallites prohibits the passage of water, and they act as obstacles.[55]

Resistance to flow is a function of two factors, degree of crystallinity and crystal size distribution. By adjustment of these two factors it is possible to have two polymer samples that are chemically identical but have vastly different WTFs. Changes in the flow properties can be attributed to differences in flow pathway or *tortuosity*. Tortuosity is the introduction of objects into the flow pathway, requiring the flow to change directions, alter its velocity, travel longer distance, and squeeze through narrow passages, increasing flow resistance.

Let's consider two polymer samples, each composed of a unit volume of polymer and each having 50% crystallinity. If it is assumed that the first sample contained one single large crystal, Figure 26, the amorphous phase would have a large, almost unobstructed path around the crystal, and the flow would not be appreciably changed. But if the second sample contained tens of thousands of small, uniformly distributed crystals, the amorphous phase would also be divided into many small channels with many twists and narrow passages greatly increasing resistance to flow, Figure 27. Thus, if the degree of crystallinity and crystal size distribution can be controlled, so too can the WTF.

[55] Campion and Materials Technology Institute of the Chemical Process, *Permeation through polymers for process industry applications*.

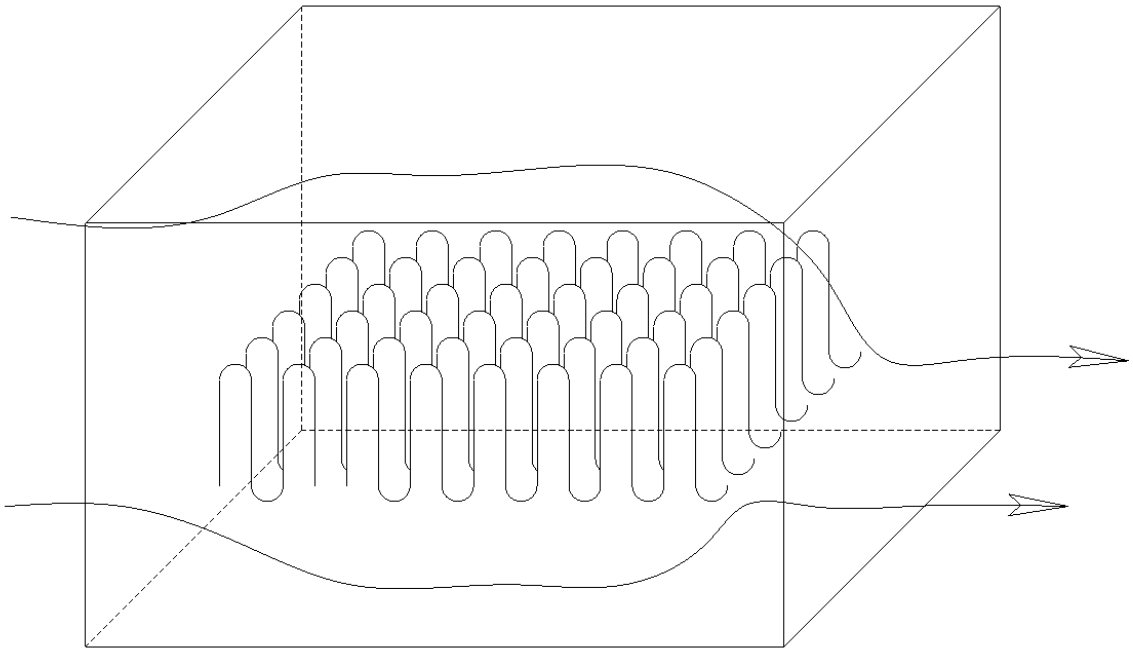

Figure 26. Flow past single crystal with minimal resistance.

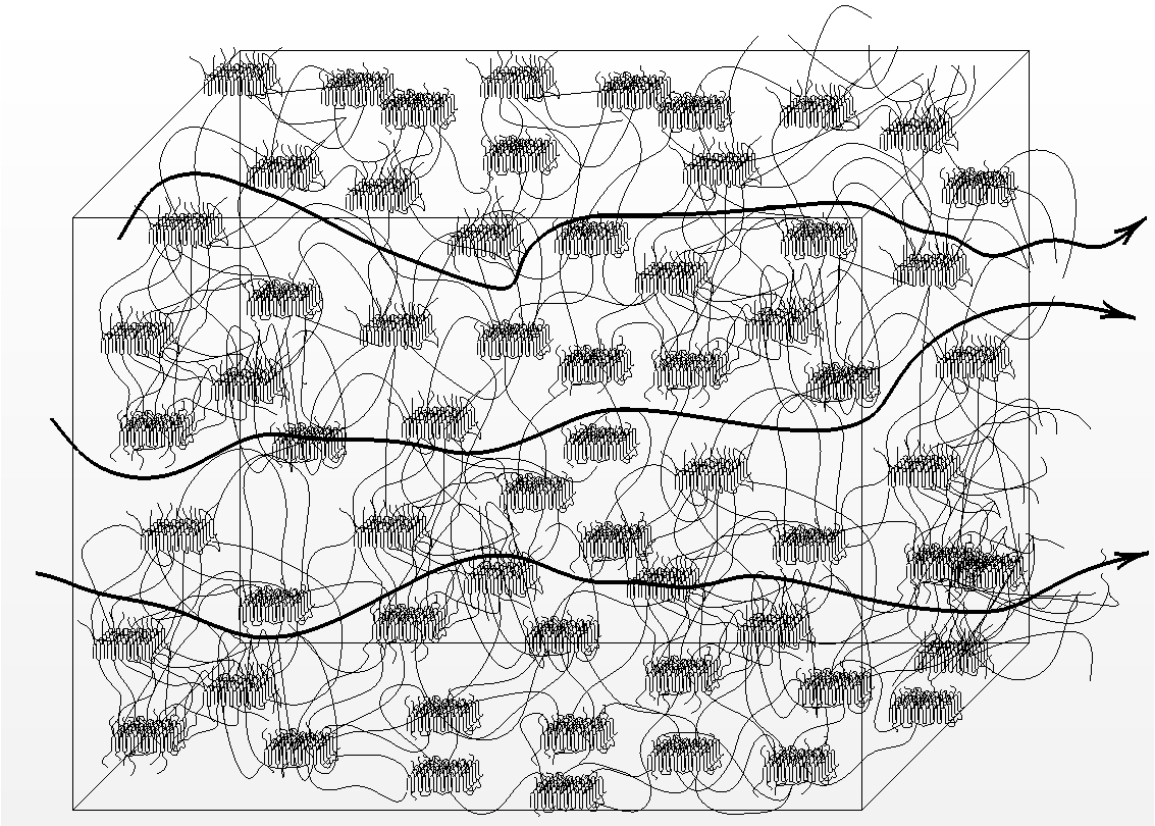

Figure 27. Flow through polycrystalline materials with high tortuosity.

If the free volume of a polymer sample is reduced as crystallinity is increased as a result of increased chain packing, the total capacity of the unit volume to absorb water is reduced along with its mobility. The capacity of almost all absorbing materials is increased with increasing temperature. This may be attributed to an increase in thermal expansion, higher modes of motion of the chains in the amorphous phase, thermal vibration of the chains and water, and other factors. This multitude of influences is thought to work together to cause water transport in some semi-crystalline polymer to have a unique response to temperature changes. As described earlier, water transport in semi-crystalline polymers is through the amorphous phase, and as the temperature is increased, the amorphous region chains can assume higher modes of motion, making transport easier because of increased free volume. These higher modes allow for increased solubility within the matrix and higher diffusion rates through the matrix. As a response to the new steady state flux at the new higher temperature, local concentration of water is also increased. It should be noted that the temperature can be changed quickly, and there is an observable time lag between the temperature increase and the corresponding increase in flux. Now with increased amorphous

region volume expansion, additional water molecules can be accommodated. If the temperature is abruptly reduced, the amorphous phase becomes unable to accommodate the additional water, segregating it into clusters isolated within the amorphous structure. Fukuda et al. showed in simulation how water clustering as described could occur.[56] [57] [58] Figure 28 and Figure 29 show water clusters causing a strain on the amorphous tie chains, forcing them to align and become denser, inhibiting water transport when returned to the former temperature. In some polymer structures with a high degree of crystallinity, thermal cycling has resulted in lower water-transport rates attributed to strain.

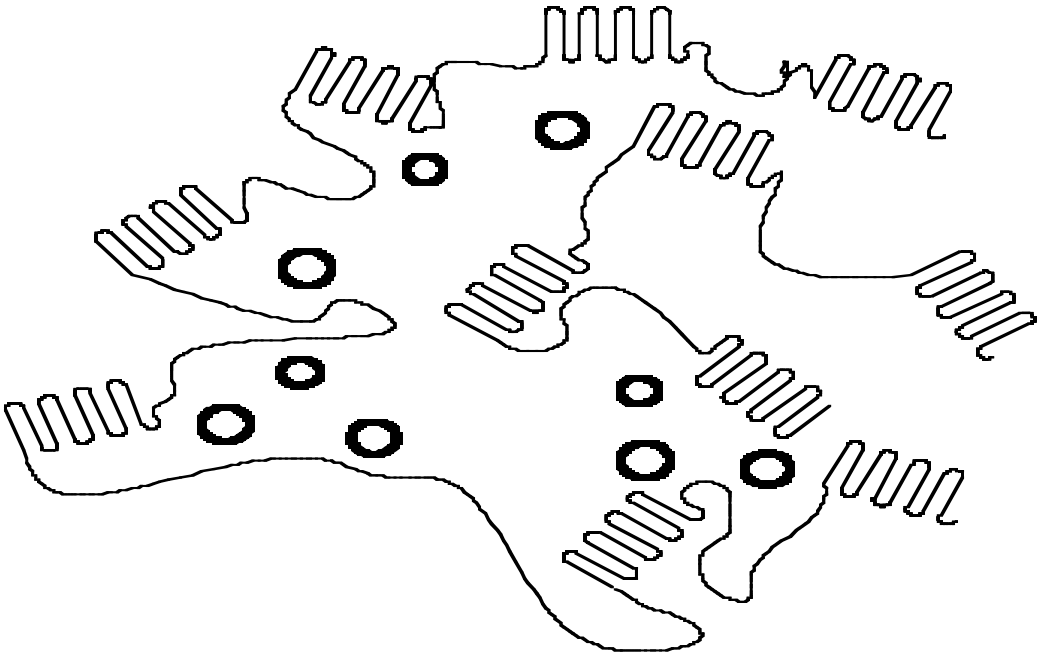

Figure 28. Water dispersed throughout matrix at elevated temperatures.

[56] Mitsuhiro Fukuda and Satoru Kuwajima, "Molecular-dynamics simulation of moisture diffusion in polyethylene beyond 10 ns duration," *The Journal of Chemical Physics* 107, no. 6 (1997).
[57] Mitsuhiro Fukuda, "Clustering of water in polyethylene: A molecular-dynamics simulation," *The Journal of Chemical Physics* 109, no. 15 (1998).
[58] Mitsuhiro Fukuda, "Solubilities of small molecules in polyethylene evaluated by a test-particle-insertion method," *The Journal of Chemical Physics* 112, no. 1 (2000).

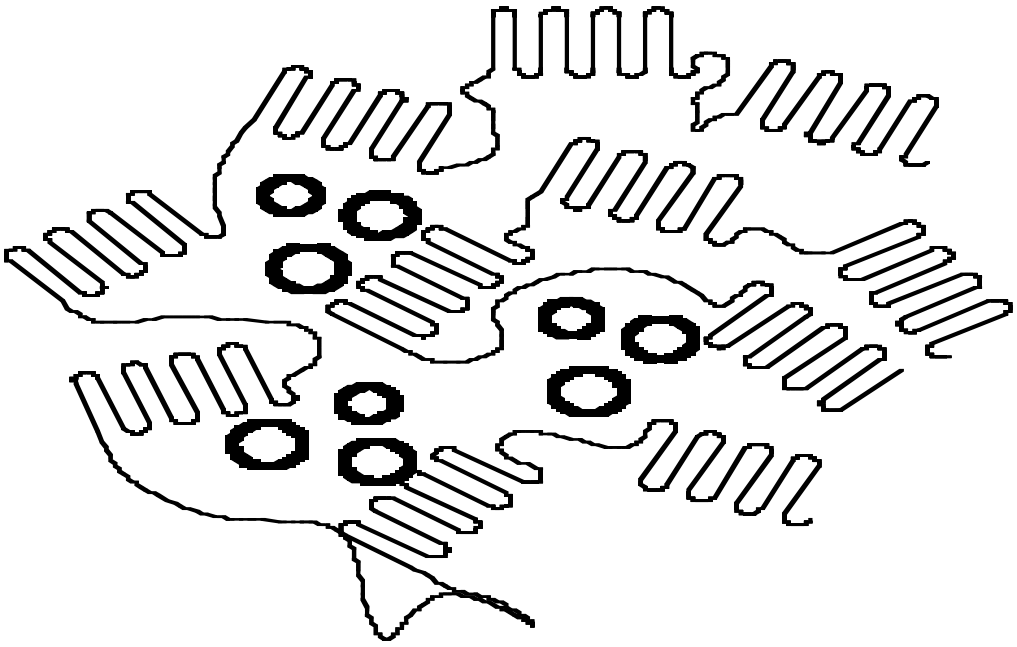

Figure 29. Water clusters formed at lower temperatures causing strain in matrix.

As the previous discussion shows, WTF does not just happen by random chance, but it moves through polymers by a somewhat orderly and predictable manner. Apparently the control of major features of crystallinity can be used to governed the WTF.

3.2.3 Effect of annealing on crystal morphology

Annealing is one of many different heat treatment processes used in material processing. Annealing is conducted after a materials is formed to shape but at temperatures below the melting point. In general this promotes molecular motion within the structure of the material. Depending on the material being annealed the goal and structural effects of annealing differs.

One of the oldest applications of annealing is in the fabrication of glass products. Glass is an amorphous material and during its formation internal stresses can build up often due to uneven heating and or cooling causing the component to have reduced strength promoting premature failure often due to shock sensitivity. Glass workers often inspect their work by backlighting the part and viewing it using a polarized viewing lens called a polariscope to reveal internal bands of

stress.[59] Glasses typically have a broad melting range and to relieve these stress the part is uniformly heated to soften but not melt the material allowing for its rearrangement and in the process relieve the stress. Annealing is usually performed through slowly heating the part to the desired temperature (usually approximately 450°C), holding it there for a predetermine period of time to allow for rearrangement before slowly cooling back to room temperature. Slow cooling is required due to poor thermal conductivity of glasses to avoid reintroducing stress in the part.

In metals annealing is a term often confused with or incorrectly used in place of descriptions of other heat treatment processes such as tempering, normalizing, and hardening. Annealing in metal is performed in a similar fashion to that of glasses but for different structural reasons. With few exceptions, metals are highly crystalline, usually alloyed, and often forms multiple phases and structures upon solidification from the melt. These castings can be machined to final shape or used as a billet to feed subsequent metal forming processes. These semi-finished billets are often formed into shapes such as rod, bar, and sheet through processes such as rolling, hammering, extrusion, and stamping, either at room temperature (cold work) or elevated temperatures (hot work) causing grain fragmentation and increasing stress.

Some of the various annealing processes are process annealing (500-1400°F), also known as subcritical or intermediate annealing, intercritical annealing (1335-1600°F), recovery annealing (300-1000°F), recrystallization annealing (300-1450°F), isothermal annealing (1300-1650°F), spheroidized annealing (1200-1400°F), full annealing (650-1650°F), and solution annealing (900-2250°F).[60] Depending on the metal and specific alloy being treated the temperatures and duration of soaking are refined based on the phase diagram using the lower and upper critical temperatures. Benefits obtained through these annealing processes include, stress reduction, improved machinability or formability, minimization of distortion, restore ductility between forming operations, new grain formation, and in preparation for age hardening.

---

[59] Corning museum of glass, website http://www.cmog.org/article/annealing-glass#.UUGppxkobek

[60] Rhode Island Heat Treatment Services, website http://www.riheattreating.com/heat-treating-specialties.html

Same as there is a difference between annealing glasses and metals due to the fundamental nature of the material and desired effect, there is a difference in the annealing process of polymers because of the fundamental nature of the material and desired effect. As previously mentioned, in both metals and glasses annealing is often used to relieve stress. As opposed to glasses which are amorphous, annealing of metals can be used to refine grain size. Polymers occupy a unique placed between amorphous glasses and crystalline metals, they are often semi crystalline. Polymers are not a discrete single molecular weight or molecular architecture but fall within a range of weights and the molecules can very from linear to branched and even crosslinked to form networks. When speaking of polymers one does not typically refer to molecular weights of 10's or 100's of atomic mass units but often 1,000's to 1,000,000's of AMU. With such an array of molecular sizes and architectures it is not surprising that the solidified structures can be complex and diverse. The transition between molten and solid presents an almost endless possibility of crystalline arrangements and even coalescences of multiple crystals into super molecular structures sometimes visible to the naked eye. An additional consequence of the shear size of polymer molecules is the incorporation of a given molecule into multiple regions of crystalline and amorphous formation.

Wunderlich explored the effects of annealing of polymers. He describes polymer annealing as analogous to metallurgical annealing producing changes to the crystalline structure including the growth of crystalline areas, with the formation of more perfect crystals, and the stabilization of crystal structures.[61] These structural changes result in improved heat resistance, dimensional stability, improved impact strength, and prevention of crazing and cracking. He sums up annealing as recrystallization with the molten or dissolved material using the remaining crystalline materials as a substrate for new crystal formation. The thermal dynamic effect of annealing provides a path to a lower free enthalpy. He lists the nearest-neighbor interactions within the structure that leads to the lowest free enthalpy in the order of covalent bond, rotational isomers, close packing, crystal defects, nonequalibrium crystal defects, larger grain size conformation including crystal size and shape. He states that changes may occur to any of these upon annealing.

---

[61] Bernhard Wunderlich, "CHAPTER VII - The Annealing of Crystals," in *Macromolecular Physics* (Academic Press, 1976).

In broader terms Wunderlich describes most macromolecular structure as starting far from an equilibrium structure and annealing allows them to move closer to the equilibrium but never achieving equilibrium. Of specific interest is changes that occur to the crystal's shape, macroconformation, defect concentration, and polymorphic. He states that the first morphology to form from the mobile state is a chain folded lamellae macroconformation. The length of the folds vary from fifty to several hundred angstroms. These are metastable structures due to the large lateral dimensions since the frequent folding provides large fold surfaces increasing free energy and reducing melting temperature. If the molecular mobility is insufficient for the chain folding small fringed micellar structures form. The micellar structures are more defective than the lamellae. These structures are susceptible to change during annealing. The surface free energy of these crystals is divided between the surfaces parallel to the chain direction and those cutting across the chain direction. Those surfaces cutting across the chain direction includes chain folds, tie molecules, ends, and loops. Experimental data shows that the surface free energy of the surface cutting across the chain direction is five to forty times the surface free energy of the surfaces parallel to the chain direction. Tests have shown that annealing of fractured surfaces of extended chain crystals leads to less extended chain crystals which is attributed to recrystallization. In some tests large lamella have broken up into smaller lamellae but with increased thickness which was though to be more stable due to elimination of defects.

As mentioned earlier Wunderlich proposes that changes are though to also occur in the macroconformation of the lamellae by major mass transport along the molecules instead of by recrystallization. Upon annealing the folded chains in a lamellae could slide past one another to ultimately cause a doubling or quadrupling of the lamellae thickness and eliminating a potential defect and reducing surface free energy of the fold surface

Changes have been seen in several types of defects as results of annealing. Wunderlich described the defects as kinks, edge dislocations, and screw dislocations. Some of the data was unclear whether the defects were eliminated or relocated to lower energy states. Misfit angle between adjacent planes were evident at low temperature annealing.

3.2.4 Theoretical basis of small angle light scattering (SALS)

Small-angle light scattering (SALS) has been used to probe the crystalline structure of polymers since the late 1950s.[62] A number of researchers have used this technique to identify structures formed as a function of chemical changes, heat treatments, or processing methods.[63] [64] [65] [66] Benson concisely described the basis of SALS in terms of the physics and showed how some crystal size could be determined from the image. [67] Although a number of different instrument designs may be found in the literature, a schematic of the system used for imaging in this work is shown in Figure 30.

SALS uses polarized laser light to detect various morphological features such as spherulites, rods, or random crystalline patterns, which shifts the light. Ordinarily, if laser light is passed through a polarizer, only one orientation of the electric vector of the laser light is allowed to proceed. If that same light beam is then passed through a second polarizer turned at a right angle to the first, all of the light is blocked. If a sample of polymer film is placed between the two polarizers, the rotation of the light caused by the structure in the polymer will pass through the second polarizer, causing a pattern when impinged on a screen.

There are several different configurations of the SALS apparatus. Plaza and Stein showed an early version using a ruby red laser and later refined the design incorporating

---

[62] Alphonse Plaza and Richard S. Stein, "The scattering of light from polyethylene films at low angles," *Journal of Polymer Science* 40, no. 136 (1959).
[63] Richard S. Stein and Marion B. Rhodes, "Photographic Light Scattering by Polyethylene Films," *Journal of Applied Physics* 31, no. 11 (1960).
[64] Marion B. Rhodes, Daniel A. Keedy, and Richard S. Stein, "The use of a laser as a light source for photographic light scattering from polymer films," *Journal of Polymer Science* 62, no. 174 (1962).
[65] Leo Mandelkern, "Relation between properties and molecular morphology of semicrystalline polymers," *Faraday Discussions of the Chemical Society* 68(1979).
[66] M. D. Failla, J. C. Lucas, and L. Mandelkern, "Supermolecular Structure of Random Copolymers of Ethylene," *Macromolecules* 27, no. 6 (1994).
[67] Roberto Benson, dissertation, 1978, Florida State University, Tallahassee, Fl.

polarizers .[68] Two polarizers were employed in the design. The polarizer immediately after the laser polarized the beam vertically before the beam passed through the sample and then through a second polarizer, called an *analyzer*, which could be placed in the same orientation or rotated 90 degrees. The image is then projected onto a screen for recording by a camera. It should be noticed that the laser used in the apparatus employed in this work produces polarized light and does not require a polarizer before the sample; only the analyzer is required.

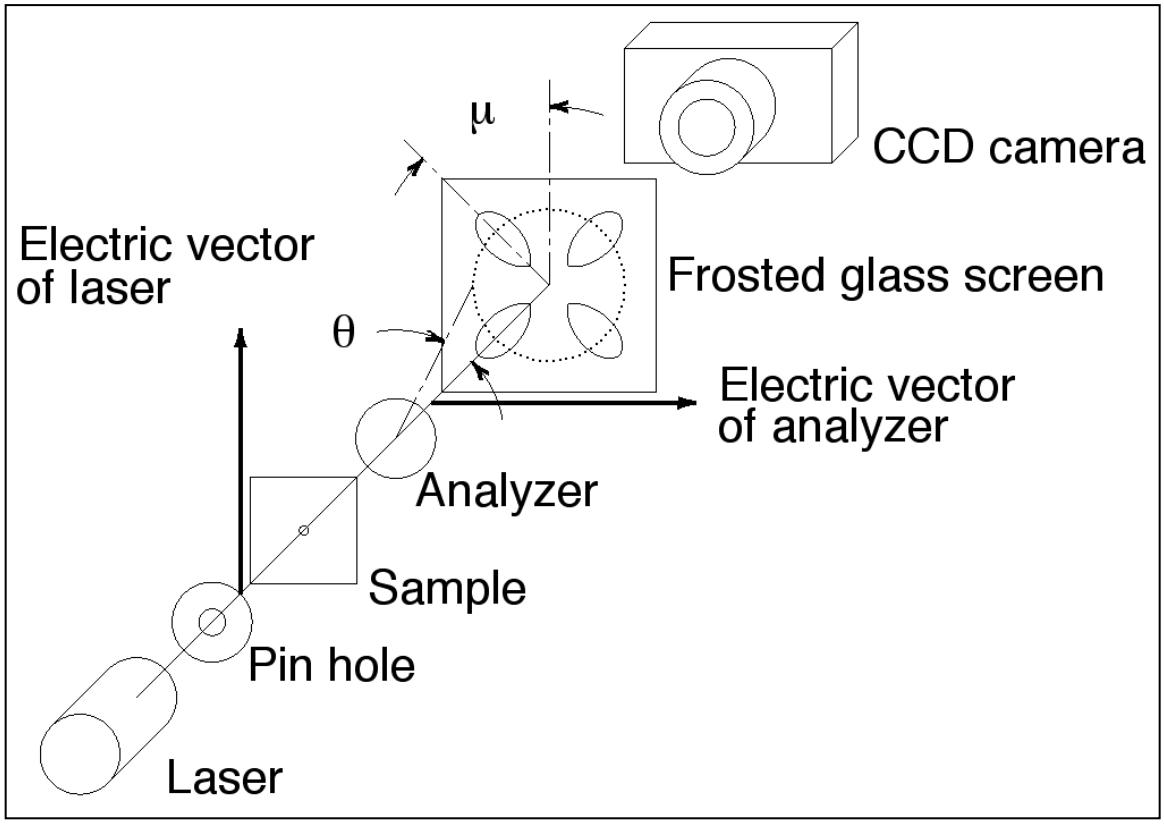

Figure 30. Small-angle light scattering (SALS) apparatus.

The scattered patterns are first classified with respect to the orientation of the polarizer and analyzer. If the two are both oriented in the vertical plane, the pattern is designated as a Vv pattern. If the two are turned 90 degrees to each other, the pattern is designated as an Hv pattern.

[68] Plaza and Stein, "The scattering of light from polyethylene films at low angles."

Expressions for the intensity of both the Vv and Hv patterns follow in Equation 12 and Equation 13.

Equation 12

$$I_{H_v} = C_3 V^2 \left\{ 3/U^3 \left(a_t - a_r\right) Cos^2\left(f/2\right) Sinm Cosm X \left(4SinU - UCosU - 3(Si)U\right) \right\}^2$$

Equation 13

$$I_{V_v} = C_3 V^2 \left\{ \begin{array}{l} \left(3/U^3\right)\left(a_t - a_s\right)\left(2SinU - UCosU - SiU\right) + \left(a_r - a_s\right)\left(SiU - SinU\right) - \\ \left(a_t - a_r\right) Cos^2\left(q/2\right) Cos^2 m \left(4SinU - UCosU - 3SiU\right) \end{array} \right\}^2$$

where

V = volume of spherulites,

U = reduced angle [$(4\pi R/\lambda)$ Sin $\theta/2$],

R = radius of spherulites,

μ = asimulthal scattering angle,

α_r = parallel component of polarizability,

α_t = perpendicular components of polarizability, and

(Si)U = $\int_0^U (\mathrm{SinX/X})dx$.

Only Equation 12 will be used in this work. Spherulites are often seen when polymers are examined. They result because of the anisotrophy in the polarizability ($\alpha_r - \alpha_t$) of the spherulites. A maximum is found at $\mu = \pi/4 + n\pi/2$ and in θ when μ=45° as shown in Equation 14.

Equation 14

$$U_{\max} = \left(4pR/l\right) Sin\left(q/2\right) = 4.1$$

U_{max} is the point of maximum intensity from the center.

Spherulites have been found in the present work, and Equation 14 will be used later to find their sizes.

There are five distinct structures revealed by SALS images that require further discussion: three spherulitic and two non-spherulitic shown in Figure 31. The most distinct pattern is that of a high θ angle well-defined spherulite. It has the appearance of a four-leaf clover or is sometimes referred to as a tennis racket and is designated as a type A pattern. As the θ angle is reduced, the lobes merge at the center, known as a type B pattern. Further degeneration of the θ angle produces a less defined lobed pattern that resembles a box pattern known as a type C pattern.

Two non-spherulitic structures are also seen; they are rod-like and random. The rod-like structure is described as lamellae in a fibrillar arrangement that assumes a random assembly of anisotropic orientation to the optical axis. The incline of the plane made up by the bundles of fibrils is defined as angle ω_o and is fixed in a plane defined with an azimuthal angle δ. The second non-spherulitic structure is a purely random arrangement of lamellae. Both of these non-spherulitic structures produce a SALS image that is a spot. Artist renderings of these A, B, C, and H patterns are shown in Figure 31. Since the H pattern may represent either the rod-like or random structure, differentiation of the two structures is sometimes made using polarized optical microscopy.

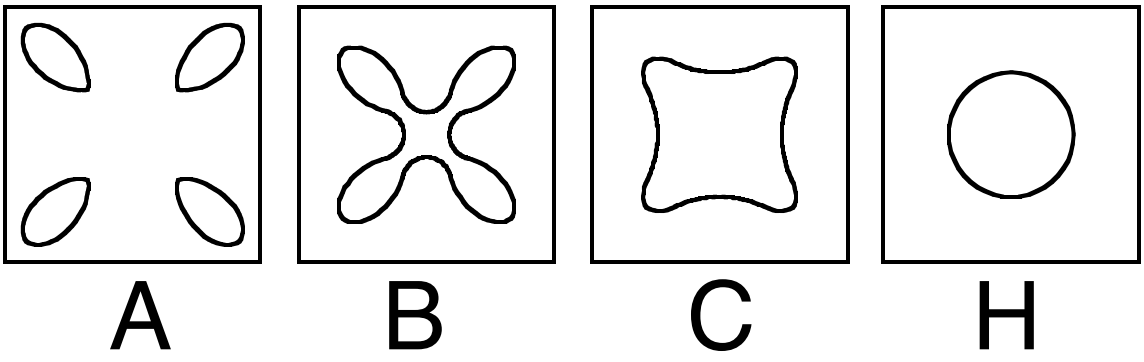

Figure 31. A, B, C, and H SALS patterns.

Equation 15, the equation for the intensity of the non-spherulitic pattern, is more complex.

Equation 15

$$I_{H_V} = K_1\left\{\left[a(q)Sin^2 m Cos^2 m + b(q)\right]P_4(Cos w_o)A(U) + d(q)P_2(Cos w_o)B(U) + C(U)\right\}$$

where

K_1 = constant,

$a(q) = 420Cos^2(q/2)$,

$B(q) = 12 - 60Cos^2(q/2)$,

$d(q) = 60Cos^2(q/2) - 40$,

$A(U) = (1/U^5)\left\{\left[U^3/6\right] - \left[\left(2U^{2-1}\right)/8\right]Sin2U - (U/4)Cos2U\right\}$,

$B(U) = \left(U^2/2\right)\left(1 - [Sin2U/2U]\right)$,

$C(U) = 28[Sin2U/U]\left([1 - Cos2U]/2U^2\right)$, and

$U = (2pL/l)Sinq/2$.

It should be noted that Equation 15 also has a fourfold symmetric about μ, but the scattering is dependent on P4(Cosω_o), the fourth Legendre function in ω_o. Therefore, random lamellae and rods may be treated the same with respect to this equation since and thus Equation 15 is this:

Equation 16

$$\left\langle P_2(Cos w_o)\right\rangle = \left\langle P_4(Cos w_o)\right\rangle = 0$$

The scattering from these structures is therefore circularly symmetric, and the pattern is referred to as an H. To differentiate between the two structures the materials must be examined under a polarized light microscope.

Chapter 4 Experimental Method

The goal is to produce samples from three different polyethylenes with a range of crystal morphologies for each material. These polymers include high-density polyethylene (HDPE), low-density polyethylene (LDPE), and linear-low density polyethylene (LLDPE). The LLDPE was made using 2.3% 1-octene co-monomer which yields a 23 branches / 1000 carbons. There are three stages to this experimental method. In stage one, *sample preparation*, thin films are made by melt pressing the as-received polymer in pellet form to form thin sheets, and controlling the heating to produce samples with a range of crystallinities for each material. In stage two, *sample analysis*, these samples are characterized by various analytical techniques to determine their degree of crystallinity and other morphological features. In stage three, *the water transfer flux* are measured. In each of these three stages there are many steps, the details of which follow. It should be made clear that these three stages may operate concurrently and in concert. For example, analysis by *differential scanning calorimetry*, DSC, of each film provides one measure of the degree of crystallinity critically important as to the effect of adjustments to processing parameters and for post-processing (annealing) is required as post-processing inputs.

4.1 Sample Preparation

4.1.1 Thin Film Formation by Melt Pressing

Each of the three polymers was used to make a set of 12 samples. From each polymer four samples were made. The polymers start off as pellets and are formed into thin sheets by melt pressing. Each set of films is formed simultaneously to experience the same thermal history. The melt pressing process begins by placing ¼-in.-thick aluminum plates into a Wabash press for heating to 180°C. These ¼-in.-thick plates act to uniformly distribute the pressing force over each film. While the plates are being heated, the polymer pellets are placed between two sheets of Kapton® film. The Kapton® sheets with the pellets are placed between the heated ¼-in. aluminum plates and pressed with a force of 10 tons. The amount of polymer used results in films with a diameter of approximately 5 in. corresponding to an area of approximately 20 in.^{2} and distributes the force to 0.5 tons/in^2. Four films from each polymer were melted and pressed.

During the melt pressing process two films from each polymer were removed from the heated press and quenched in a chilled water bath, and the remaining two films were left in the press under pressure and allowed to slow cool to room temperature over a duration of 8 hours. This cooling rate produced two distinct sets of films with different morphologies. The quenched films have a higher percentage of the amorphous phase and a low percentage of the crystalline phase, whereas the slow-cooled films have a low percentage of the amorphous phase and a higher percentage of the crystalline phase.

4.1.2 Annealing of thin films

At this point there are four films from each of the three polyethylene samples: two quenched and two slow-cooled, for a total of 12 samples. One film from each sample set, six films in total, was annealed to increase degree of crystallinity. This process sacrifices smaller, less perfect crystals, and the amorphous phase for the growth of larger, more perfect crystals. The effect is also evident by an increase in density and a reduction in volume.

The annealing temperatures were 129°C for HDPE , 111°C for LDPE, and 123°C for LLDPE. These temperatures were determined by use of a Mettler DSC. This method was developed after consideration of an article by Peterlin, "Secondary Crystallization and Annealing of Polyethylene." [69] In the article, recrystallization of polyethylene was measured as a function of time and temperature above the original crystallization temperature. The higher the annealing temperature, the longer it took before the specific volume to drop, indicating the occurrence of recrystallization. It was reasoned that at higher temperatures approaching the melting temperature of the infinite size crystals, only the lowest-energy most-perfect crystals remained unmelted, and only low-energy crystals will subsequently form, growing epitaxially off these remaining crystals.

Because each sample is either a unique polymer or has a unique crystallization temperature, each sample to be annealed was examined using the DSC. The thermograms of HDPE quick-cooled and slow-cooled are shown in Figure 32 and Figure 33, respectively.

[69] A. Peterlin, "Secondary Crystallization and Annealing of Polyethylene," *Journal of Applied Physics*, Vol. 35, No. 1, January 1964.

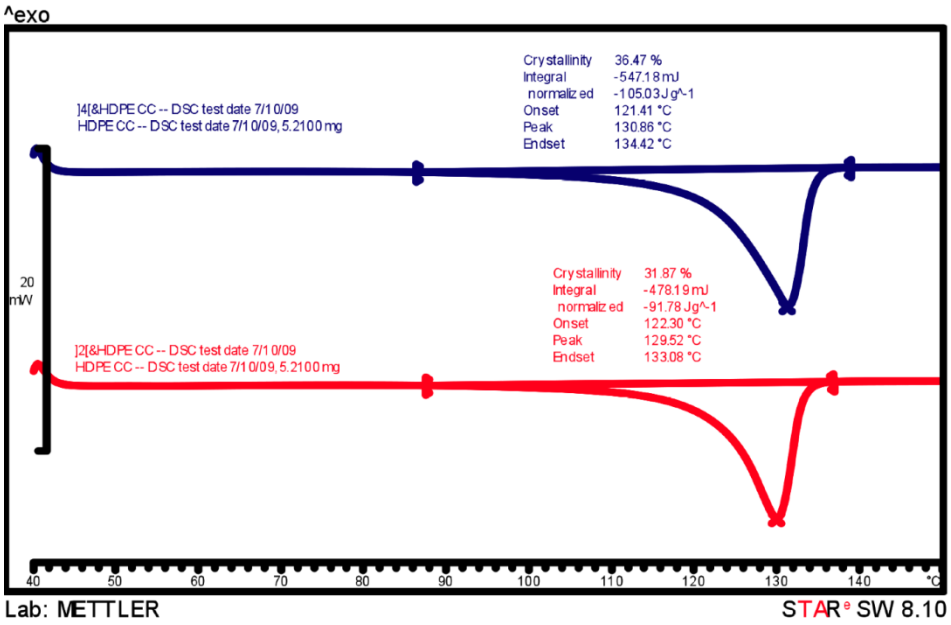

Figure 32. DSC analysis of quick-cooled HDPE.

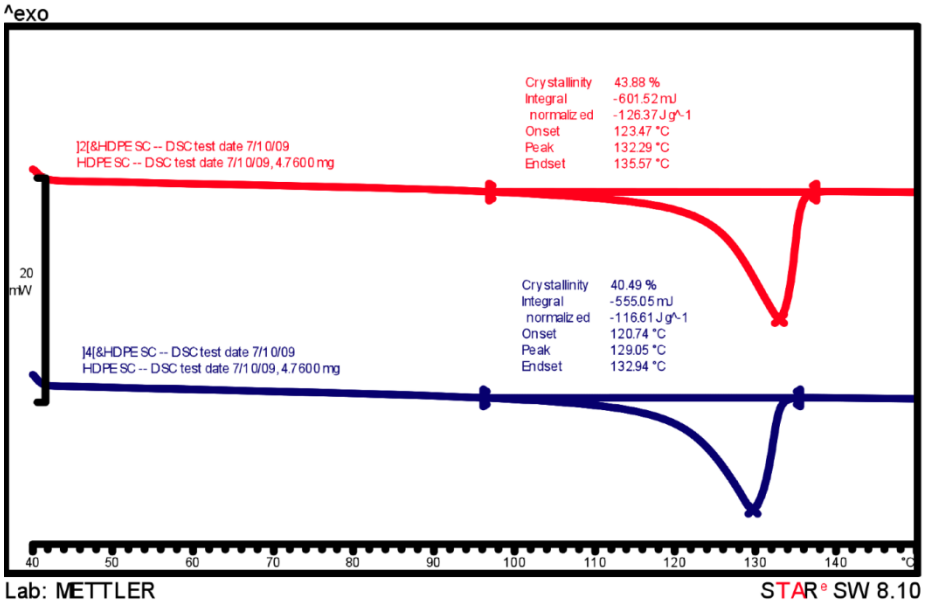

Figure 33. DSC analysis of slow-cooled HDPE.

In each of these figures there are two graphs, with the first pass in red and the second pass in blue. This refers to the DSC heating cycle. These materials were heated to 40.0°C and held for 5.0 min before heating from 40.0 to 150.0°C at a rate of 10.00°C/min. This heating cycle is repeated a

second time. What is shown in the above graphs is the dynamic portion of these cycles with the 5-minute hold eliminated. The annealing temperatures were chosen as 129°C for HDPE, 111°C for LDPE, and 123°C for LLDPE. If one refers to the previous HDPE DSC thermograms, the bottom of the trough on the first pass of each run is 130 and 133°C, respectively. The temperature for the annealing was chosen to be 1° below the lowest peak temperature of the two graphs. This temperature will permit the most energetic crystals to melt and rearrange and combine with the larger lower energy crystals to promote crystal growth.

4.2 Analytical Techniques

In this section various methods of measuring properties of the sample will be presented. The relationships that are being investigated are those between processing parameters, resulting morphologies, and their effects on WTF of moisture vapor.

4.3 Gel Permeation Chromatography

The molecular weight of the base materials from which all of the WTF samples were made was determined by gel permeation chromatography (GPC). Two samples of each base material were tested. From these tests the number average molecular weight, Mn, and weight average molecular weight, Mw, were determined.

The tests begin by dissolving the samples in 1,2,4 trichlorobenzene to a concentration of 1.50 mg/mL and injecting 200 µl into a Polymer Lab-GPC 220 High Temperature Chromatograph. The instrument was calibrated using five polyethylene standards with molecular weight of 196400, 119600, 8700, 32100, and 6280. Once the test was started, a solvent flow rate of 1.0 mL/min was used, and the test was conducted at a temperature of 145ºC.

4.4 Density Gradient Column (DGC)

A DGC was made using isopropanol and water with a density range from 0.87 to 0.98 at an operational temperature of 20°C. Calibration density beads were placed in the column and allowed to equilibrate. Samples were cut from each polyethylene material and gently placed in the column to determine their density. Each sample was dipped and sturred in isopropanol to break the column's and sample's surface tension before it was placed in the column. If the surface tension was not broken, some samples would tend to float on the surface after

introduction into the column. The samples were allowed to equilibrate for 12 to 24 hours before their position relative to the calibration beads was read. The density of the samples was determined by averaging the location of all samples within a group of seven and interpolating their average position between the calibration beads above and below their position using a curve fitted to all of the calibration beads. Figure 34 shows an example of a graph of the column with calibration beads and polymer samples.

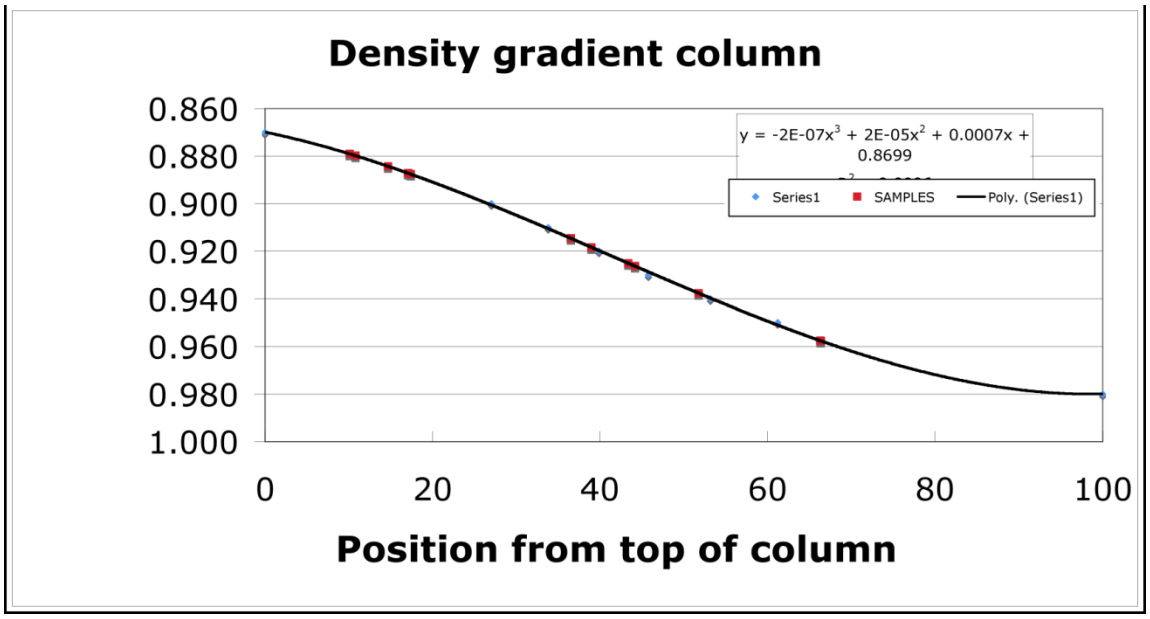

Figure 34. Density of polymer samples with calibration beads.

Figure 35 shows a schematic of the DGC with the stirred filling cylinder. The DGC is filled from the bottom up. The densest fluid is introduced first in the bottom of the column, and subsequent lighter layers of fluid are added on top. To avoid splashing, the fluid is run down the inside of the column. The density of the fluid is continuously varied through the mixing of the most dense fluid found at the bottom of the column and the lighter fluid to be found at the top. This variation in density is achieved by the use of the concentric filling cylinder. The denser fluid is placed in the inner-most cylinder, and the lighter fluid is placed in the outer-most cylinder at approximately the same height. As the fluid is drained from the inner-most cylinder, the fluid from the outer cylinder is siphoned in to maintain a uniform height between the two cylinders. A magnetic mixing bar is placed in the inner-most cylinder to continuously stir the solutions as they are

combined. Determination of the ratios of alcohol and water to attain the proper densities and detailed instruction for the setup and operation of the column are presented in Appendix A.

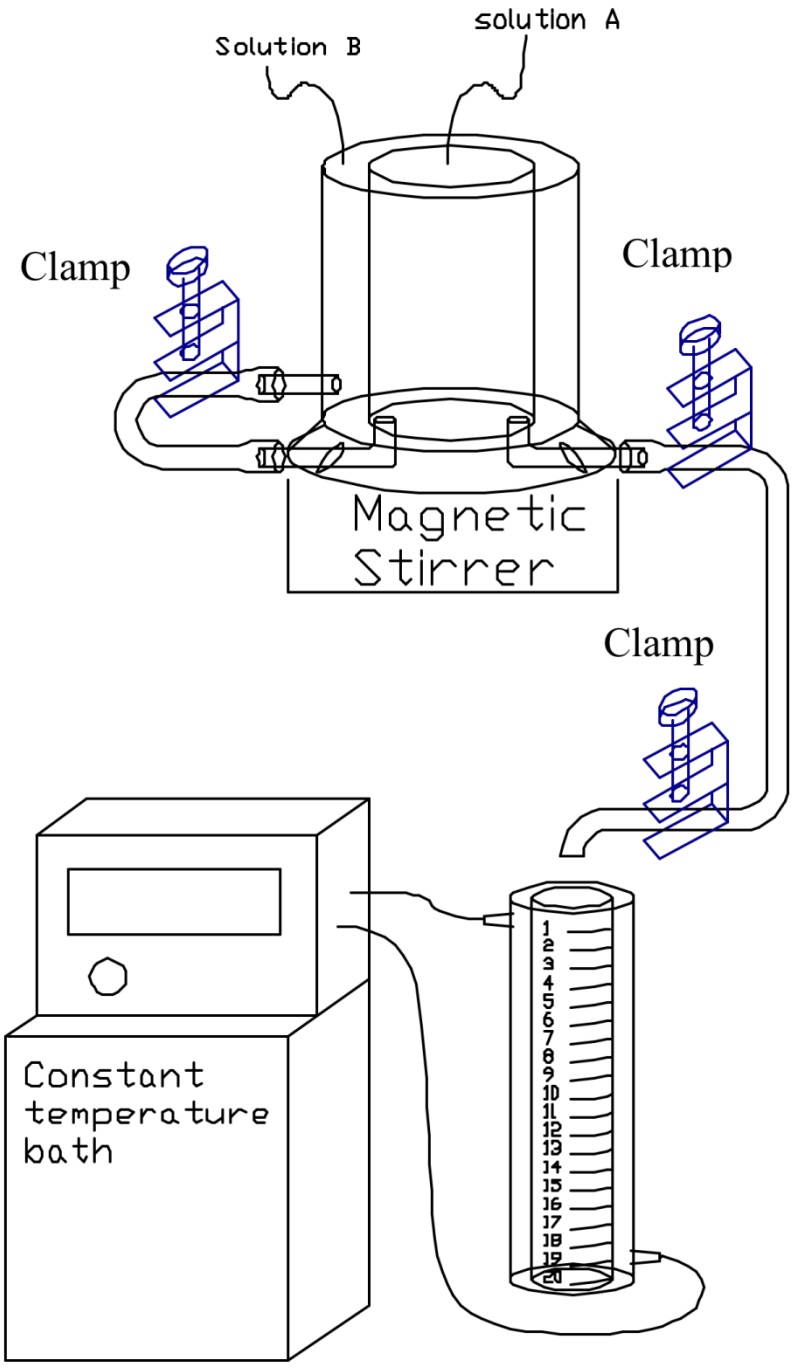

Figure 35. Density gradient column with double-walled mixer and constant temperature bath.

4.5 Variable Temperature Density Gradient Column (VT-DGC)

A more rigorous density measurement method, the *variable temperature/density gradient column (VT-DGC)*, was also used. This method is similar to the DGC previously discussed, but instead of the column's being operated at one temperature, 20°C, which is a standard reference temperature, the temperature of the column is varied slowly at 5°C intervals and allowed to equilibrate for 12 hours in order to determine the samples' densities as a function of temperature. The column is varied in temperature from 20 to 60°C. The utility of this information is that densities can be determined as a function of temperature in the VT-DGC. As mentioned earlier, the polymer samples have two different phases: a crystalline phase and amorphous phase. Information obtained from this method may be used to determine if the two phases expand uniformly with temperature by comparing the change in density with temperature as a function of crystalline content. The density change would include any water absorbed into the amorphous phase by virtue of equilibrium solubility.

Construction and operation of this column are considerably different from the constant temperature standard DGC, and Appendix B provides a full description. The column was constructed with an initial density range of 0.90 to 0.97.

Modifications must be made to the setup instruction used for the standard DGC to account for the change in density of the column's fluid as the temperature is varied. In the standard DGC the density range over the column's length remains constant for the duration of the testing period, but in the VT-DGC the density changes with temperature; therefore, the calibration beads must be selected that will be applicable for the prevailing density. As the temperature rises, the overall density range of the column is lowered; thus, the density beads will progressively move down the column. Ones that start near the bottom when the temperature is near 20°C will soon settle at the bottom of the column, and the ones that start near the top of the column will move down, leaving the top of the column without a calibration reference. With this in mind, the column must be built with the anticipated density changes taken into consideration when bead selection occurs. Additional calibration beads were added to ensure complete calibration of the column as density varies with temperature. The samples were added as before and allowed to equilibrate.

4.6 Fourier Transform Infrared (FTIR) Spectroscopy

A BioRad FTS 6000 FTIR was used to characterize the polymer films after pressing to check for oxidation. Oxidation in polyethylene occurs at ~1735 cm^{-1}.

4.7 Differential Scanning Calorimetry

Polymers' degree of crystallinity is also measured by differential scanning calorimetry (DSC). A Mettler-Toldeo DSC822e with STARe software was used to collect the thermograms. This technique measures the heat required to change the sample's temperature through a range. The heat flow required to change the sample's temperature is indicative of the heat capacity of the sample. The heat of fusion of a 100% crystalline polyethylene sample is 288 J/g. Each sample was run through a temperature profile that consisted of an initial isothermal mode at 40.0°C for 5.0 minutes, then a constant heating rate from 40.0°C to 150.0°C at a rate of 10.00°C/min. The sample was then cooled at a rate of 10.00°C/min from 150.0°C to 40.0°C. This profile was repeated a second time. The first pass through the profile shows the morphology that resulted from the film forming method, and the second pass shows the reestablishment of a baseline behavior since it is the same for each sample. To prevent oxidation and to provide cooling to the process, nitrogen gas was used with a flow rate of 80.0 mL/min. The DSC allows determination of the degree of crystallinity on the basis of the comparison of the heat of fusion of 288 J/g, and the heat of fusion of each sample.

4.8 Wide-Angle X-ray Diffraction (WAXD)

The degree of polymer crystallinity may also be determined by *wide-angle X-ray diffraction* (WAXD). All spectrums were recorded on image plates using a Rigaku molecular metrology x-ray diffractometer with monochromatic CuKα radiation at 40kV and 40ma. The images are retrieved from the image plates using a Fuji BAS 1800 and digitized and azimuthally averaged using ImagePro and Matlab followed by deconvolution with Gaussian-Lorentz routine in PeakFit® software.

The WAXD spectra consist of crystalline and amorphous peaks. The peaks of the spectra have to be deconvoluted using MS Excel, Peakfit, or other software, Figure 36. The ratio of areas of these peaks can be used to determine the degree of crystallinity. Equation 17 shows this:

Equation 17

$$\text{Degree of crystallinity} = \frac{I_{c1} + I_{c2}}{I_{c1} + I_{c2} + I_{amorphous}},$$

I_{c1} and I_{c2} represent the intensity of the 110 and 200 crystallographic planes of the crystalline regions. $I_{amorphous}$ represents the amorphous region. Depending on the polymer and the heat treatment, additional crystalline peaks may be observed. The equation should be adjusted accordingly.

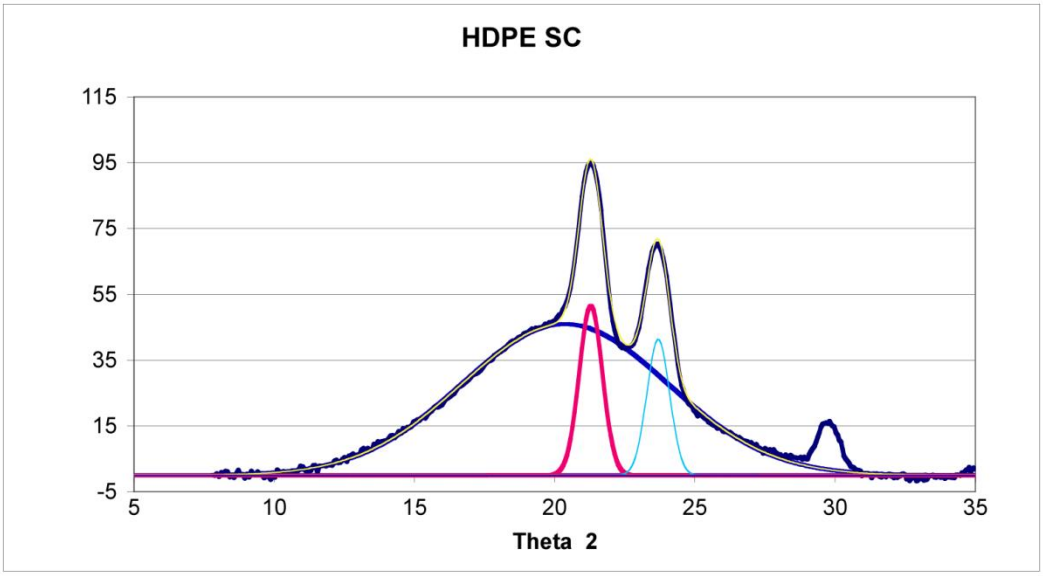

Figure 36. Deconvoluted WAXD spectra of HDPE slow-cooled from melt.

4.9 Small-Angle X-ray Scattering (SAXS)

Small-angle X-ray scattering (SAXS) provides a means to measure the long period of the polymer crystal. SAXS was performed using a Rigaku Molecular Metrology x-ray diffractometer. Monochromatic CuKα radiation at 40 kV and 0.66 mA was exposed to each sample. The diffractometer is equipped with a two-dimensional position sensitive detector. The data is digitally recorded using Matlab. This is also known as the repeat unit length, or periodicity. It is the distance from a common point in one cell to the same point in another. The spectra are inspected, and the relevant hump just before the cutoff caused by the beam stop is used in Equation 18 to determine the long period:

Equation 18

$$L = \frac{2p}{Q_{\max}}.$$

The SAXS spectrum for slow-cooled LLDPE is given in Figure 37.

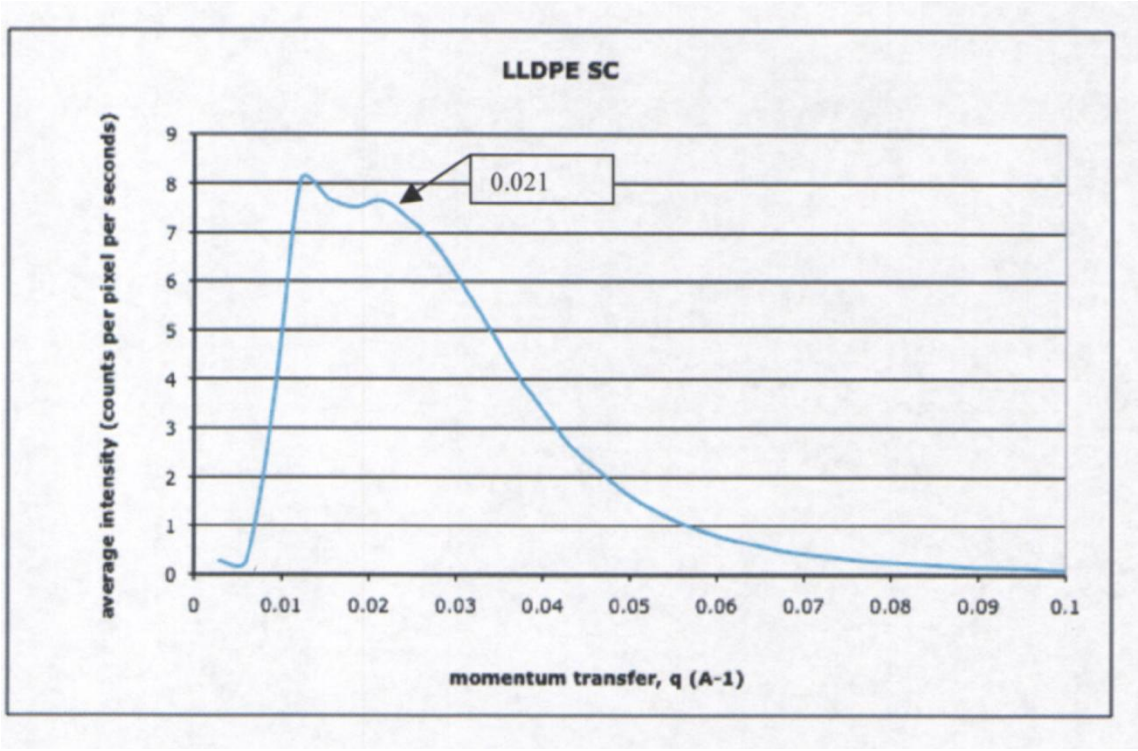

Figure 37. SAXS spectra of LLDPE slow-cooled from melt.

4.10 Determination of Water Transport Flux (WTF)

Once the films were formed and characterized using differential gradient column, differential scanning calorimetry, FTIR, wide-angle X-ray diffractions, and small-angle X-ray scattering, they were then tested to determine their WTF. WTF testing was carried out using thin film test cell shown in Figure 10. The thin film test cell is a key component in the polymer characterization device shown in Figure 11, which holds the film during testing. The cell was constructed of all stainless steel components that trapped the film sample between two polished flange surfaces. One benefit of this cell design is the film forms a gasket between the two polished surfaces eliminating interfering outgassing. This design is also applicable for testing other polymers or elastomers often used as gaskets in other designs.

Before loading the sample in the cell the bottom half of the cell is filled with liquid water which is continuously in contact with the sample throughout the duration of testing as the water source. With the sample loaded in the cell, the cell is connected to the gas manifold of the test apparatus where a precisely controlled 300 cc/min constant flow rate of dry gas is passed over the top of the film. The gas stream enters the cell dry, mixes with the water vapor that has migrated through the film, and carries the moisture to the detector. An RH Systems hygrometer equipped with MKS flow controllers determine the moisture content. Figure 38 presents a schematic of the cell design showing the flow of the carrier gas over the sample. Temperature control of the sample during testing is achieved by placing the thin film test cell containing the sample in a temperature controlled water bath. The water bath is equipped with a programmable controller that permits precise reproduction of temperature profiles necessary to determine WTF as a function of temperature.

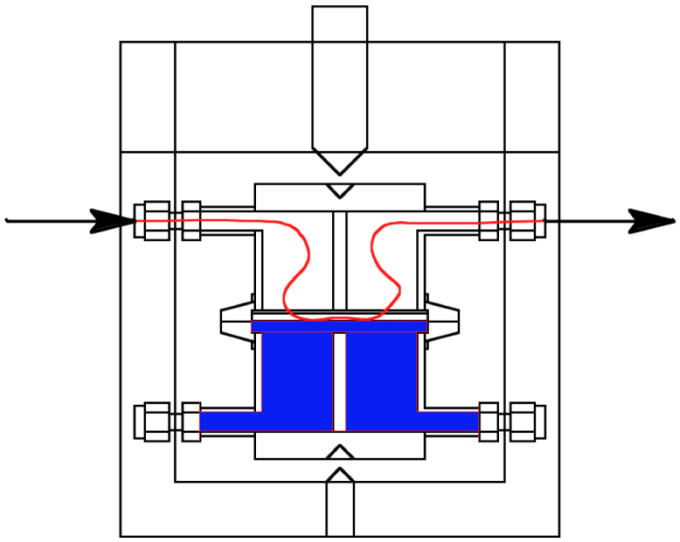

Figure 38. Thin film WTF cell design.

Once the film is loaded into the thin film test cell, it is put inline with the control manifold, which provides a constant flow rate of dry gas is shown in Figure 39.

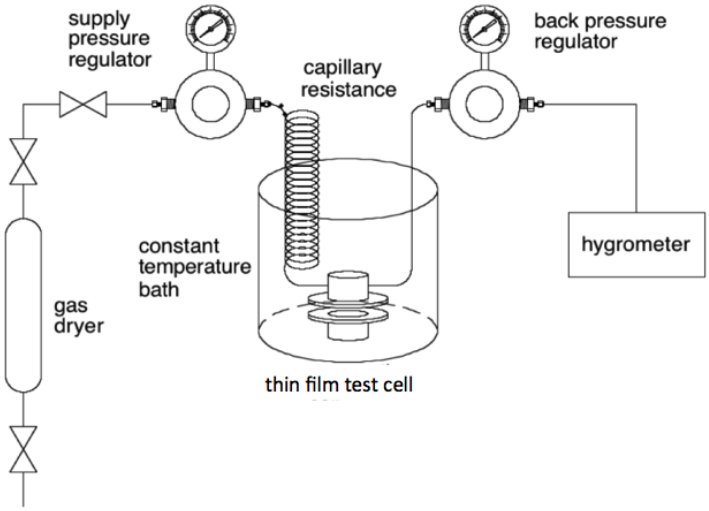

Figure 39. Balance pressure control manifold.

A typical change in WTF of a polymeric film as a function of temperature change in the sample is shown in Figure 40.

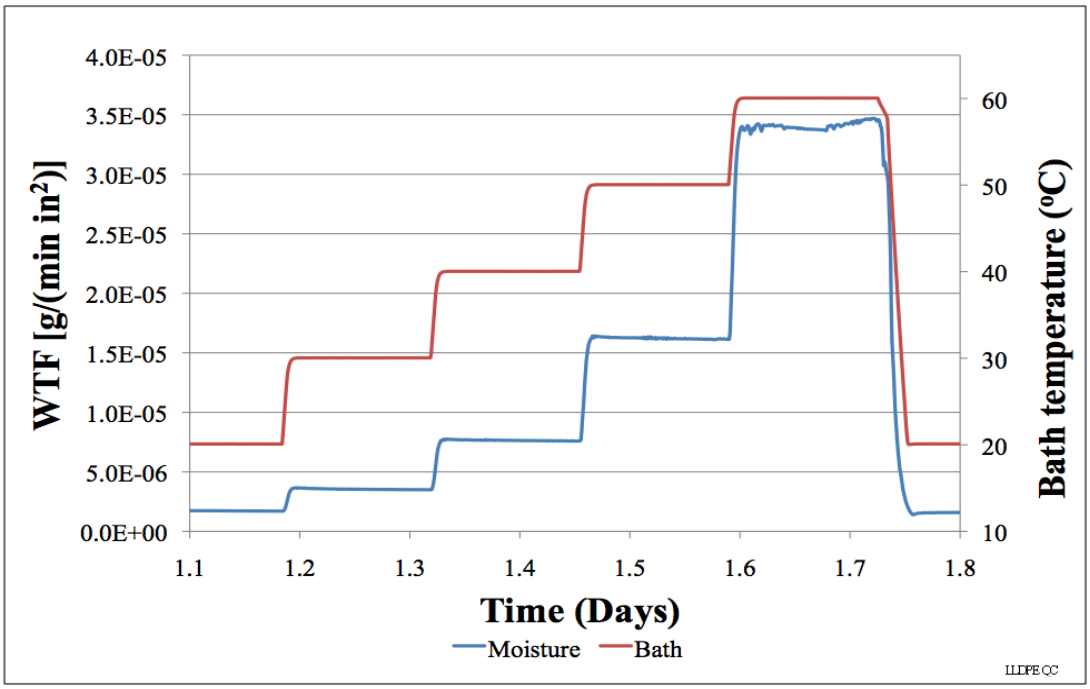

Figure 40. WTF response as a function of temperature.

4.11 Small-Angle Light Scattering (SALS)

In the apparatus used for collection of the current images shown in Figure 30, a 20-mw polarized HeNe JDS Uniphase red laser model 106-1 operating at 632.8 nm was used, eliminating the need for the first polarizer. The beam was passed through an adjustable pinhole, then the sample and an analyzer before being projected onto a frosted-glass screen. The image was recorded using a DVC CCD high-resolution camera, Model 1412AM-T1-TW, with 1380 × 1035 pixel resolution equipped with a Nikkoer 35-70, f/3.3 zoom lens and stored digitally.

4.12 Scanning Electron Microscopy (SEM)

Sample disk approximately 3/16 in. in diameter were punched out of the polymer films and etched using a potassium permanganate in sulfuric acid solution in preparation for imaging by

SEM. The dried samples were mounted on carbon tape and sputtered with gold on a Spi Module Sputter Coater (Spi Supplies: Westchester, PA, USA) at 20 mA for 10 s. They were then analyzed on a LEO 1525 Scanning Electron Microscope (Zeiss: Oberkochen, Germany). The samples were imaged with a 2-kV accelerating voltage and various magnifications from 10KX to 50KX and stored as tiff files for later examination. The images were analyzed with the use of ImageJ® (NIH: Bethesda, MD).

Several etching solution were described by Olley and Bassett.[70] The etching solutions found to work best was a mixture of 2 parts sulfuric acid in water with 0.4% potassium permanganate. The polymer films were cut into small disk and placed in test tubes. The etchant was added and let stand for 1, 2, or 4 hours and the optimal image was used in the document. Following etching Naylor and Phillips found that washing the samples with a series of rinses produces deposit free etched surfaces.[71] Rinsing of the etchant was a 4 step process.

1. 90 s in 10 ml of 2 parts H_2SO_4 to 7 parts H_2O solution at 20°C, followed by
2. 90 s in 10 ml of a 30% hydrogen peroxide, followed by
3. 90 s in 10 ml of H_2O, followed by
4. 90 s in 10 ml of acetone.

The samples were then dried and mounted on SEM post for examination.

[70] R. H. Olley and D. C. Bassett, "An improved permanganic etchant for polyolefines," *Polymer* 23, no. 12 (1982).
[71] K. L. Naylor and P. J. Phillips, "Optimization of permanganic etching of polyethylenes for scanning electron microscopy," *Journal of Polymer Science: Polymer Physics Edition* 21, no. 10 (1983).

Chapter 5 Results

As a consequence of the many tests that have been run on these materials, a large quantity of data has been generated. These data will be used to describe the structural features of the materials and the interplay of these features in governing the resulting water transport flux (WTF) properties. Because of the complexity of this topic no one test fully describes the sample's structure as it relates to its transport performance. Where appropriate, representative examples of the raw data will be presented along with the rest of the data consolidated in tabular form.

5.1 Gel Permeation Chromatography

Gel permeation chromatography was used to determine the weight average and number average molecular weight and these values, as Table 1 lists, were then used to calculate the polydispersity index, or PDI.

Table 1. Molecular weight and polydispersity of HDPE, LDPE, and LLDPE

Sample	**Injection**	**Mw**	**Mn**	**Mw/Mn**
LLDPE	1st	190,936	27,457	6.954
LLDPE	2nd	183,355	35,464	5.170
LDPE	1st	199,730	26,020	7.676
LDPE	2nd	167,769	22,580	7.430
HDPE	1st	166,797	16,355	10.199
HDPE	2nd	209,125	16,056	13.025

It should be noticed that the molecular weights are similar across all three materials. This helps minimize differences among samples to make processing differences clearer.

5.2 Fourier Transform Infrared Spectroscopy

Scans were taken of the polymer films by Fourier transform infrared spectroscopy (FTIR) to characterize the films for oxidation. A collection of scans for all materials from 500 to 4000 wave numbers is shown in Figure 41. Oxidation shows up as a carboxylic acid group at approximately 1735 cm^{-1} wave numbers in the FTIR spectra. Figure 42 shows the FTIR scans for all samples

from 1500 to 2000 wave numbers. No carbonyl absorption is present indicating that oxidation did not occur during the melt pressing operation or the annealing operation.

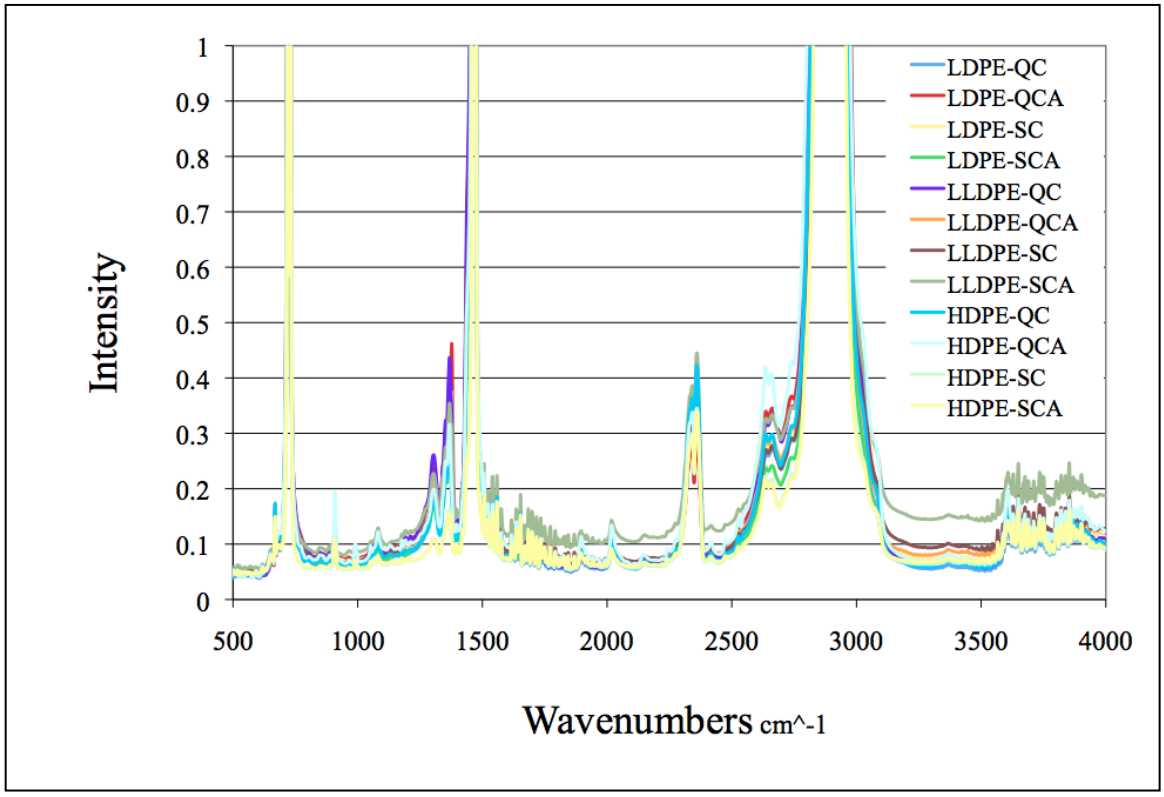

Figure 41, FTIR Spectra of polyethylene samples 500 – 4000 wave numbers

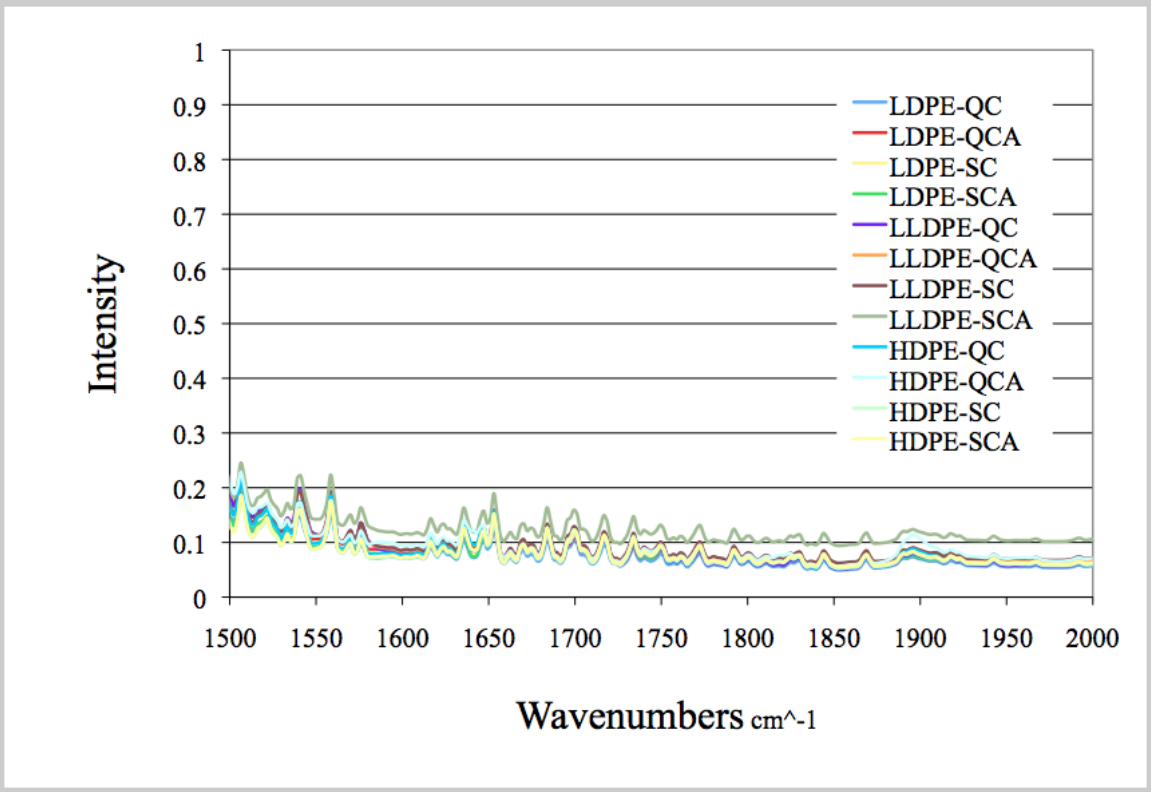

Figure 42. FTIR Spectra of polyethylene samples.

General Characteristics of Water Transport Flux Testing as Opposed to Permeation

WTF data represents the quantity of water that migrates across the polymer film. Most of this type of data up to this point in time has been collected using the time delay method, describe earlier, and has been performed using a vapor-to-vapor testing method as developed by Barrer and others. In their method a high concentration water vapor is placed on the supply side of the film and the migrating water vapor is captured on the exiting side in a closed volume where the pressure rise is monitored. Their data in general describes an unstable induction period followed by a steady state behavior from which the water transport properties are derived, often referred to as permeation. These tests are typically conducted at one temperature and thus determines the rate at only one temperature and provides no information of the material's response to temperature changes.

The previous method does not provide the sensitivity to detect changes in the WTF at key stages of testing needed to identify morphologically based governing factors. The new method used in these tests is believed to produce the highest water transfer flux possible. This higher WTF results in an increase in the signal-to-noise ratio necessary to probe subtle rate changes due to material changes. The new testing method was based on Fick's law which shows that the transmission rate is a function of the concentration difference across the film at a temperature. Thus to have the highest possible transmission rate several design changes were used. First, the thin film test cell maintains the polymer film in contact with liquid water, its most concentrated form, on the supply side instead of vapor. Secondly, to increase the transmission rate the water vapor emerges from the polymer film into a volume that is maintained at a very low water vapor concentration by a dry carrier gas that continuously purges the volume. Thirdly, the temperature of the test cell is programmatically stepped to generate the WTF as a function of temperature not just at one temperature. Fourthly, water contact with the sample provides for conductive heating as opposed to convective heating used in the other method. It is plausible that the evaporation rate on the exit side in the other method potentially cools the sample below the claimed testing temperature thus causing an artificially low reported permeation rate. If the true temperature was used the rate may be reported higher.

In the former method the permeating moisture is measured as a pressure rise whereas in this new method the moisture is measured as the frost point of the water vapor in the carrier gas. The frost point data can be presented in the more traditional units of the mass of water vapor per area per time or it may be represented in the units in which it was measured, frost point. Both of these units have their own strengths. The mass per area per time units are traditional and widely recognized while the frost point representation provides insight into the changing response of the polymer over extended testing periods and temperature ranges.

Collection of the WTF data using this new method allows for analysis of the data in new ways. When the frost point data and sample temperatures are plotted as a function of time it is evident that over time a linear relationship exist between the frost point and sample temperature. When the frost point is plotted versus the sample temperature WTF changes as a function of thermal cycles becomes evident. As these changes progress and the material stabilizes a linear

relationship evolves. The sensitivity of this new system and data analysis method shows how heat treatments effect the material's performance.

The moisture content of the 300 cc/min gas stream is analyzed using an R. H. Systems chilled mirror hygrometer model 373LX. This instrument has an accuracy of ±0.1°C, reproducibility of ±0.05°C, and a measurement range from -95°C to +20°C. The 373LX physically measures the moisture content as the dew point or frost point on a mirror and the user can chose to have the data provided in a number of different units. Knowing the flow rate of the dry gas, its moisture, and the area of the sample the WTF can be determined in mass per area per time.

WTF of LLDPE

Test results from the LLDPE-QC is shown in Figure 43 which contains two plots of data. One plot is of the mass based WTF and the other is the sample's temperature both plotted versus time. The change in WTF is in response to the temperature change. As the data shows the test begins at 20°C and is heated to 60°C for 24 hours. This provides and initial examination of the sample's performance while drying the thin film test cell and metal tubing which may have picked up some ambient moisture while being open to the air during sample loading. The WTF response during the initial 60°C 24 hour period shows any instability in the WTF as a noisy signal and gross change in rate. Comparison of the two plots shows that the step size of mass based WTF data has a non-uniform increase in response to uniform temperature increases. When the mass based WTF is plotted versus the sample temperature the data always produces a curve.

Historically, the WTF has been expressed using a number of different units and is sometimes referred to as permeation although permeation may be defined differently depending on the source. As with most testing each time a test is conducted the researcher is looking for an answer specific to the problem and thus they conduct their test to produce an appropriate answer. To make their work relative to others work and to validate their results it has become convention to put the results in a universal form. Permeation is typically listed at only one temperature, e.g. 20°C, and given in units of mass of moisture per time per area. Other references list the value including partial pressure differences across the film and normalize for film thickness.

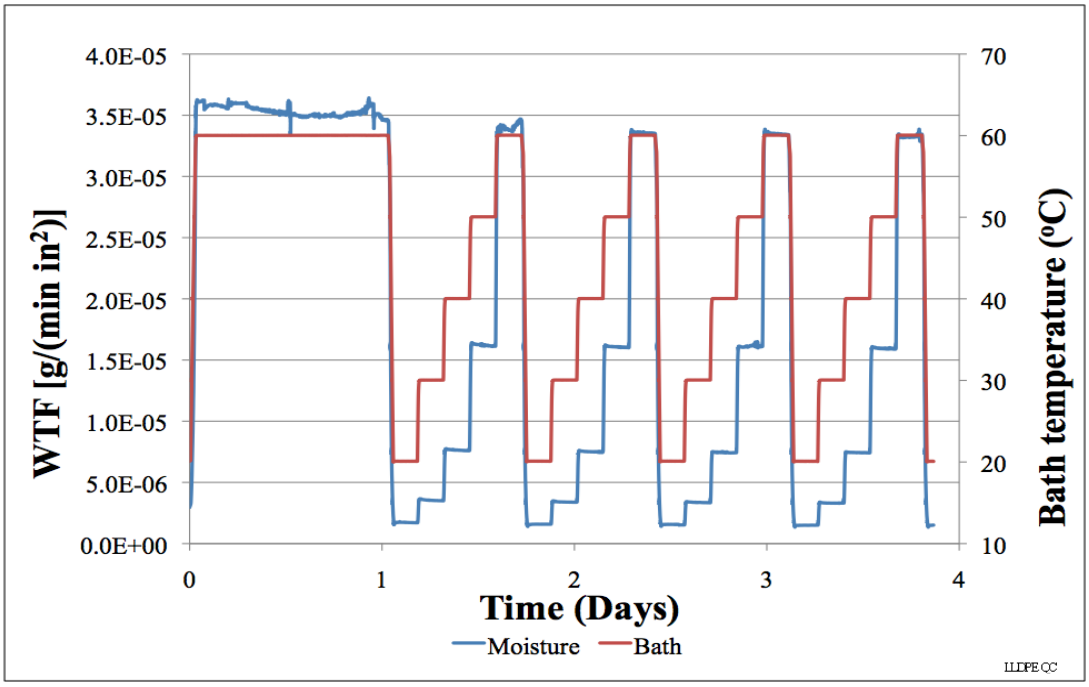

Figure 43. Mass based WTF of LLDPE-QC [g/(min in^2)] and temperature as function of time.

An alternate representation of the WTF data is as the frost point of the water vapor contained in the constant flow rate of dried carrier gas instead of the mass flux as shown in Figure 44. This is exactly the same data set as presented in Figure 43 just expressed as the frost point instead of the mass rate. The frost point is the physical measurement that is made by the chilled mirror hygrometer. The hygrometer uses the frost point and an algorithm to determine the partial pressure of the water vapor which is used to determine the mass water vapor in the carrier gas stream. The main benefit of expressing the moisture transport in this manner is that once the WTF has reached a steady state rate the frost point data has uniform step sizes in response to uniform sample temperature step sizes. When the frost point based WTF is plotted versus the sample temperature the data produces a straight line as shown in Figure 45. In addition to becoming linear as the sample approaches a stable and reproducible WTF, the plot typically will move from a positive curved line to a straight line and decrease in WTF. This will become more prominent in later samples. This is believed to be the first time that WTF data has been presented in this manner and has been named the ultimate linear behavior (ULB). This linear behavior allows for the determination of when the sample has reached a steady state WTF. An alternate method of presenting the data is to plot the frost point at each temperature as a function of thermal cycles.

This representation shows the rate at which the material achieves steady state over time that is evident by the approach to a horizontal, equally spaced behavior, as seen in Figure 46. As described earlier if the WTF is expressed as mass the set size is non-uniform with respect to the sample temperature step size and when the mass basses WTF is plotted as versus sample temperature a curve is produced even once the sample has reached it steady state flux.

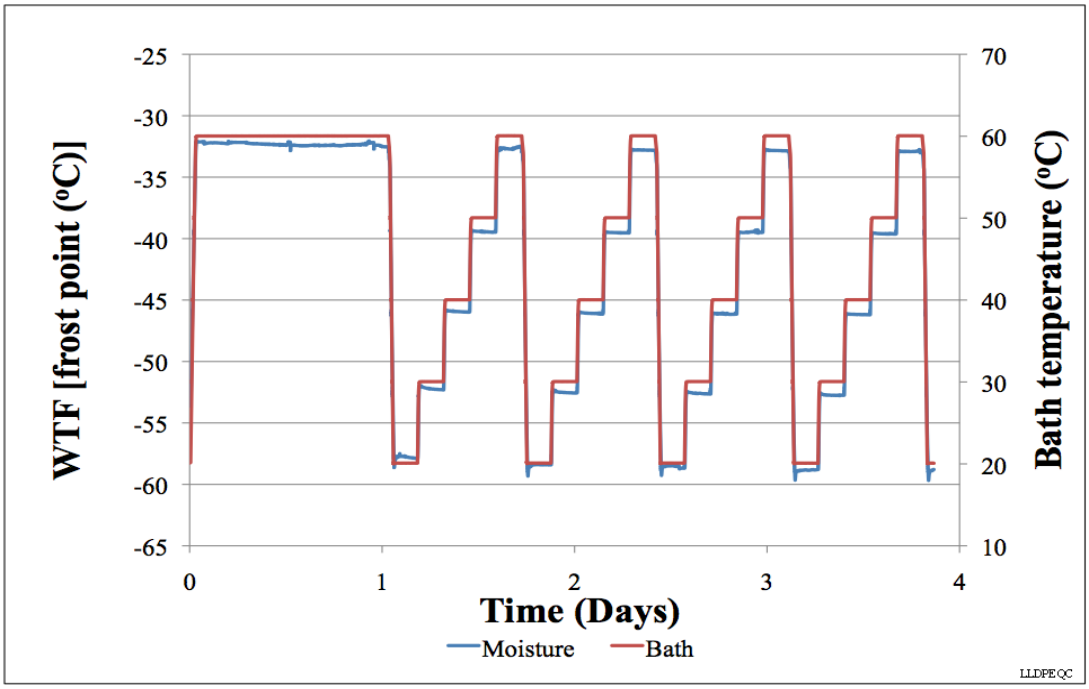

Figure 44. Frost point based WTF of LLDPE-QC [frost point(°C)] and temperature as function of time.

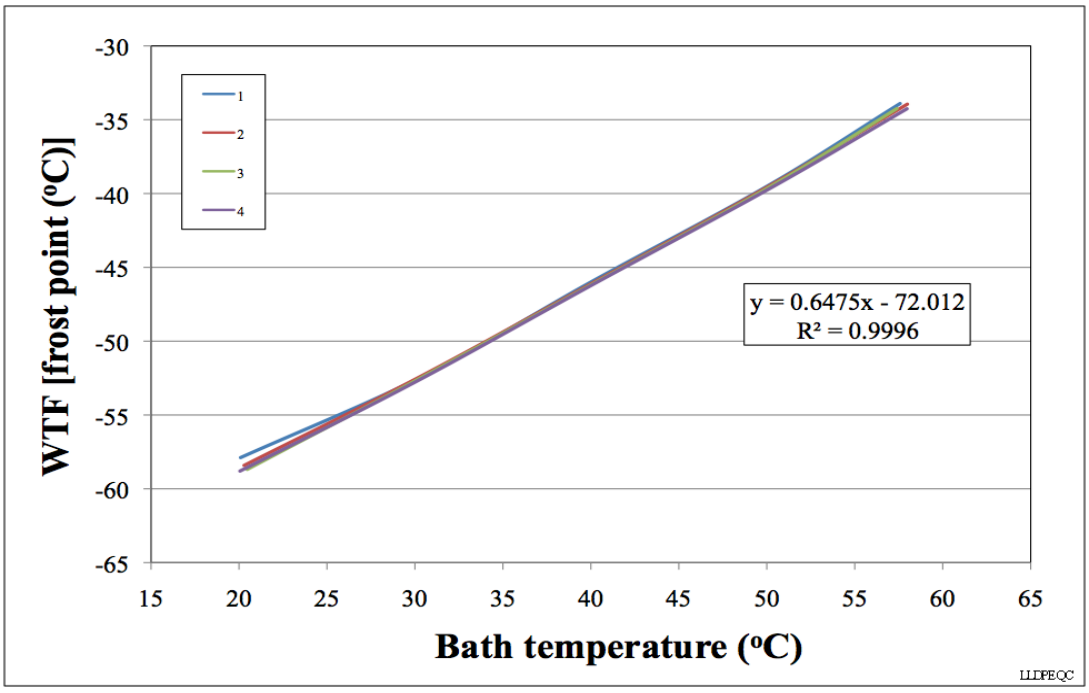

Figure 45. Linear WTF of LLDPE-QC [frost point (°C)] behavior versus temperature.

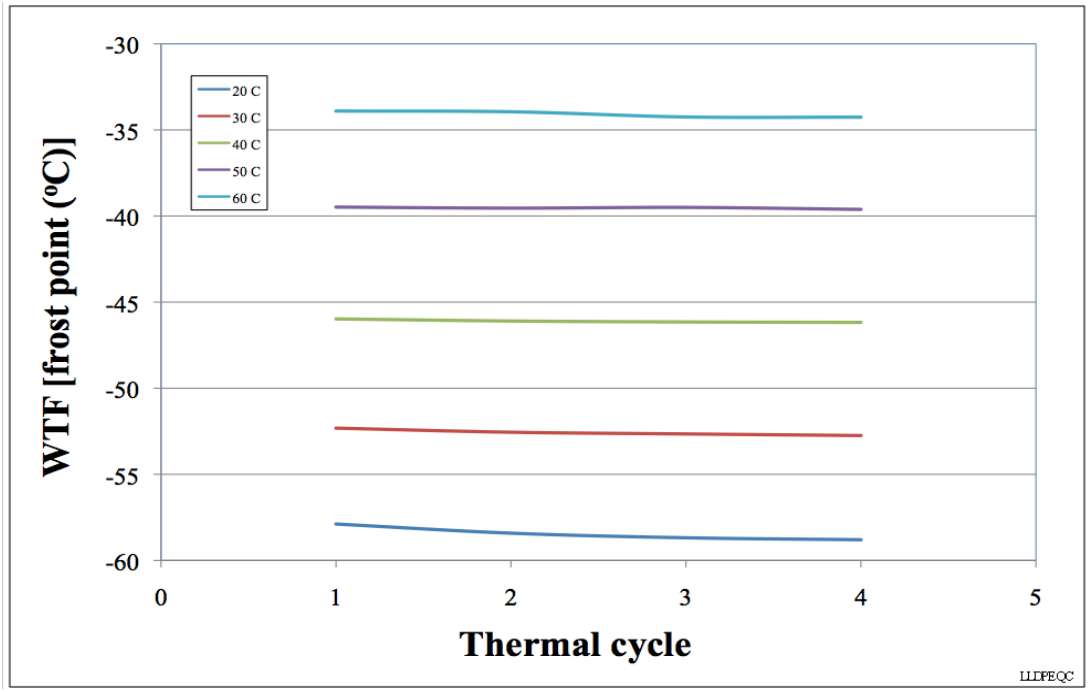

Figure 46. WTF (frost point) behavior as function of thermal cycles.

The relationship of the mass based WTF versus the frost point WTF is shown in Figure 47.

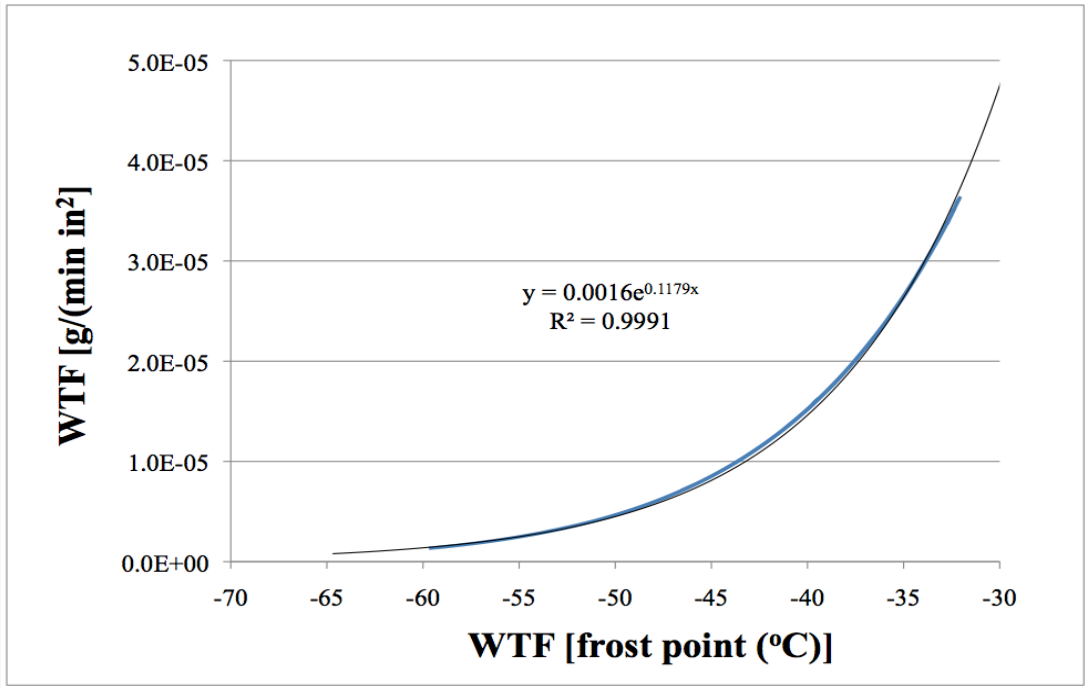

Figure 47, WTF [g/(min in^2)] v. WTF [frost point (^oC)]

The data presented in Figure 46 reaches a horizontal steady state behavior quickly during WTF testing. Not all of the samples equilibrated so quickly but experienced significant time delays before settling into a linear behavior as will be shown later.

The next LLDPE to be reviewed is LLDPE-QCA. The data for this sample is shown in Figure 48 through Figure 51. During the initial 60°C soak the WTF is shown to have a decreasing transmission rate leveling off to a constant rate before beginning thermal cycling. This sample showed some instability as evident in the WTF rate decline at the 50 and 60°C plateaus. Although the sample ultimately achieved a ULB of $R^2 = 0.9996$ the performance at the 50 and 60°C plateaus were somewhat unstable as evident when the WTF was plotted versus thermal cycle in Figure 51.

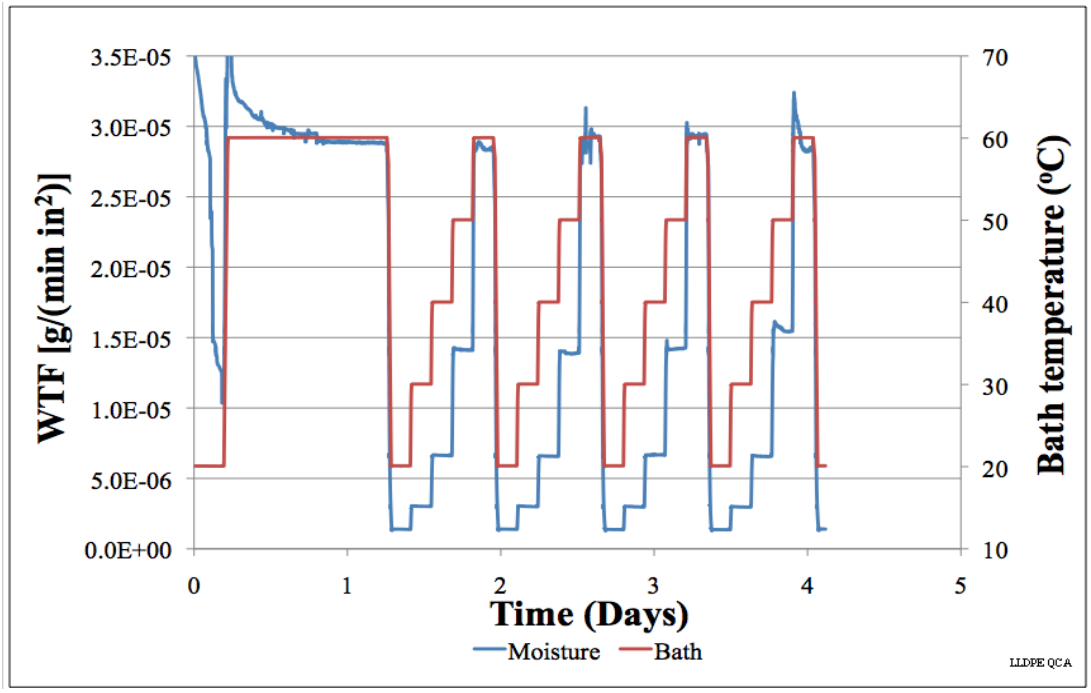

Figure 48, WTF of LLDPE QCA [g/(min in.^{2})] as function of temperature.

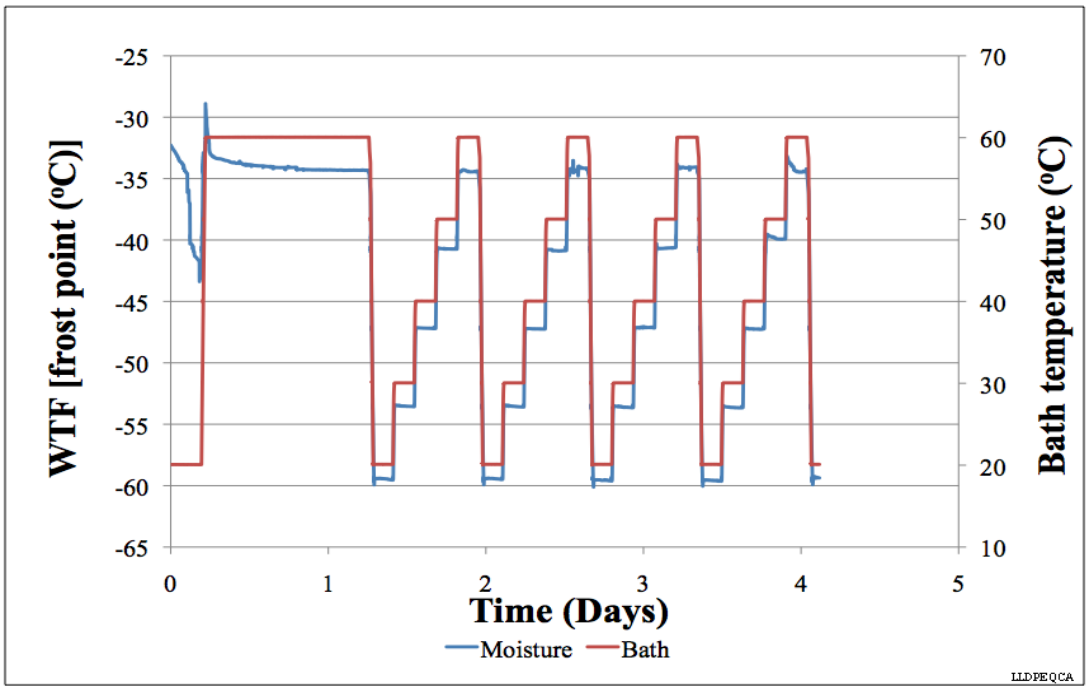

Figure 49, WTF of LLDPE QCA [frost point(°C)] as function of temperature.

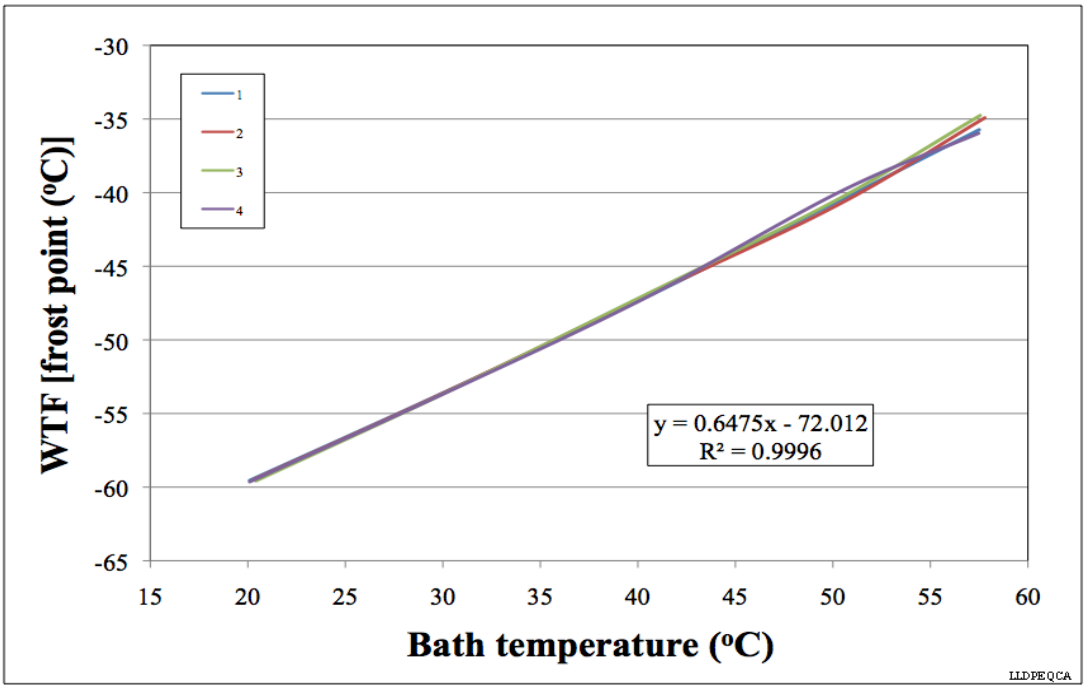

Figure 50, Linear WTF (frost point) behavior of LLDPE QCA versus temperature.

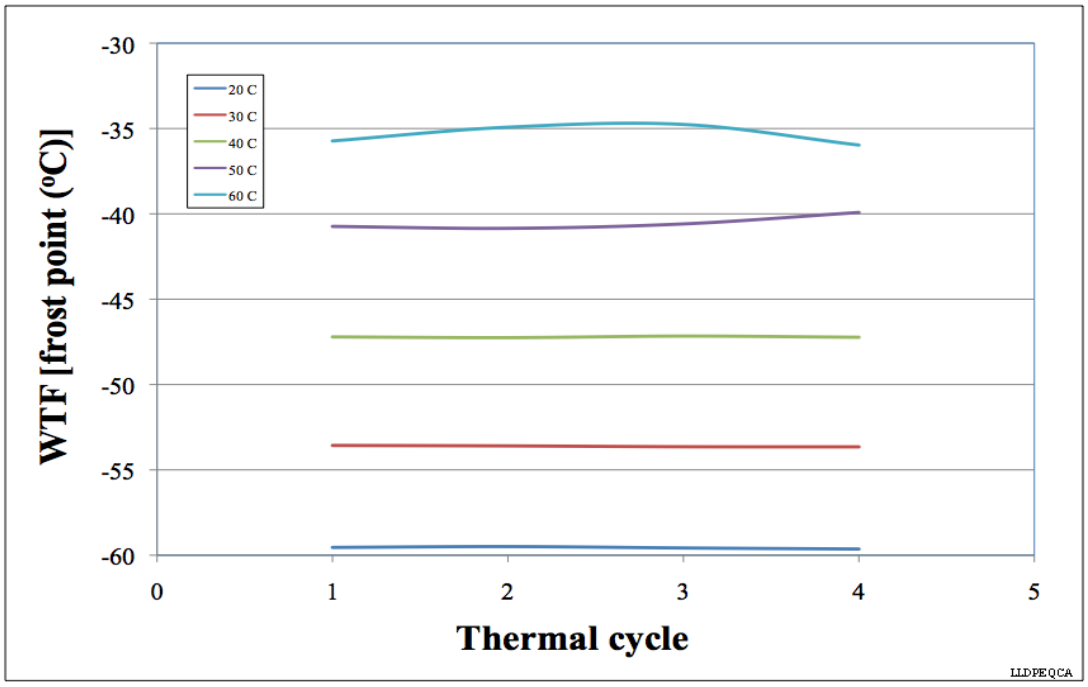

Figure 51, WTF (frost point) behavior of LLDPE QCA as function of thermal cycles.

Figure 52 through Figure 55 presents the results for the LLDPE-SC sample. A significant instability was seen in the WTF rate during the 60°C soak and at each of the temperature plateaus throughout the test. It took 8 thermal cycles before a ULB of $R^2 = 0.996$ was achieved.

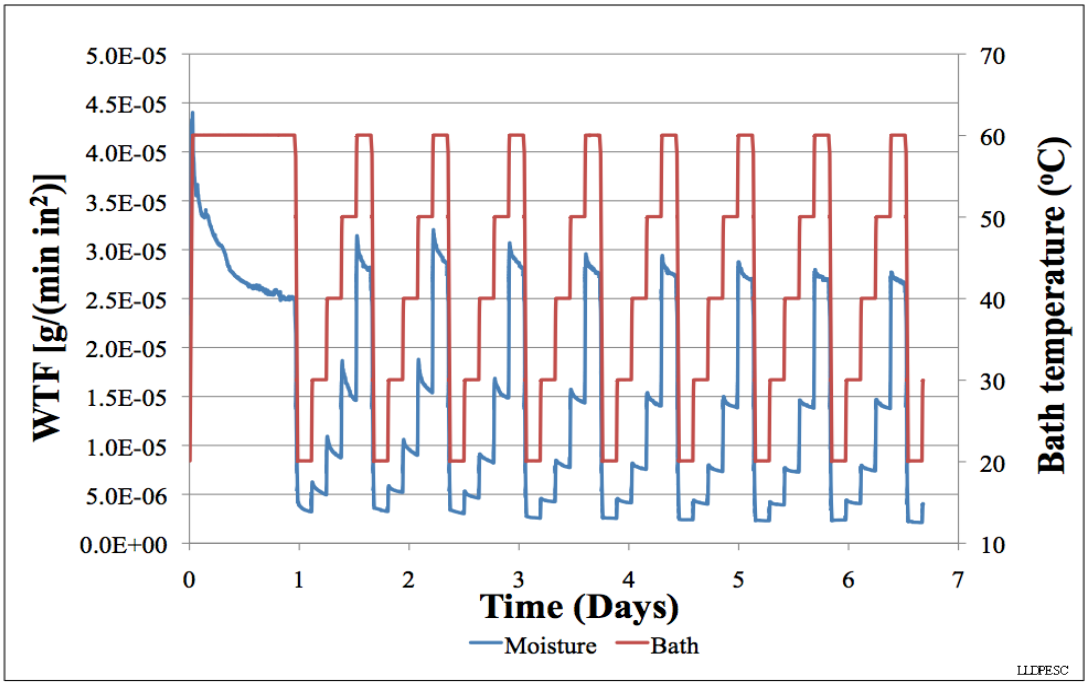

Figure 52, WTF of LLDPE SC [g/(min in.^{2})] as function of temperature.

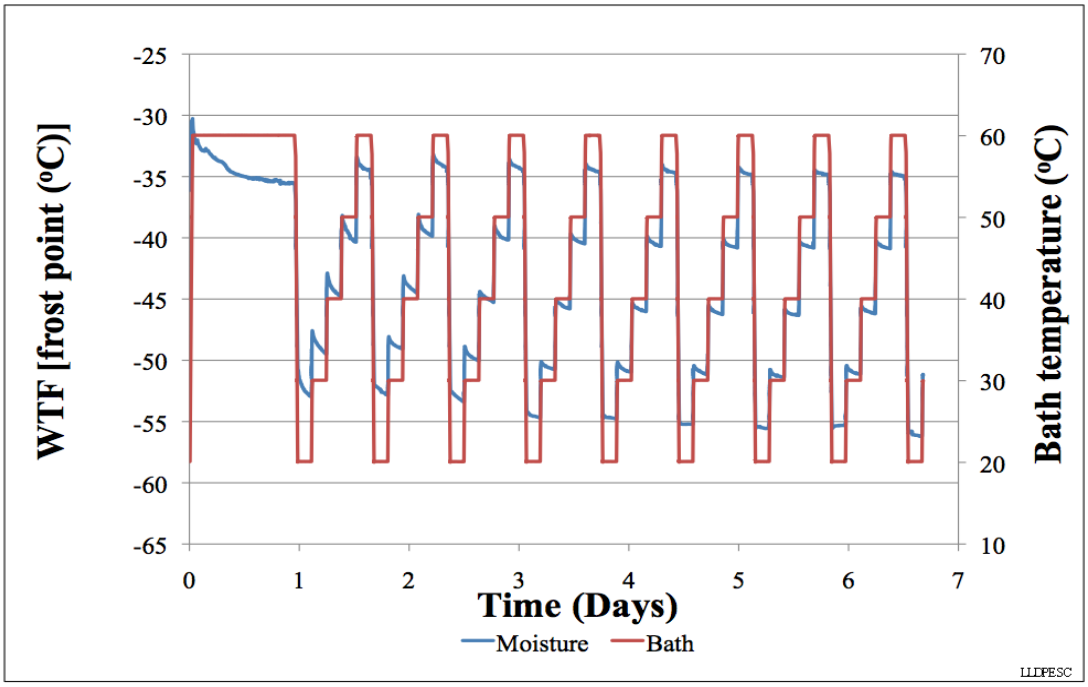

Figure 53, WTF of LLDPE SC [frost point(°C)] as function of temperature.

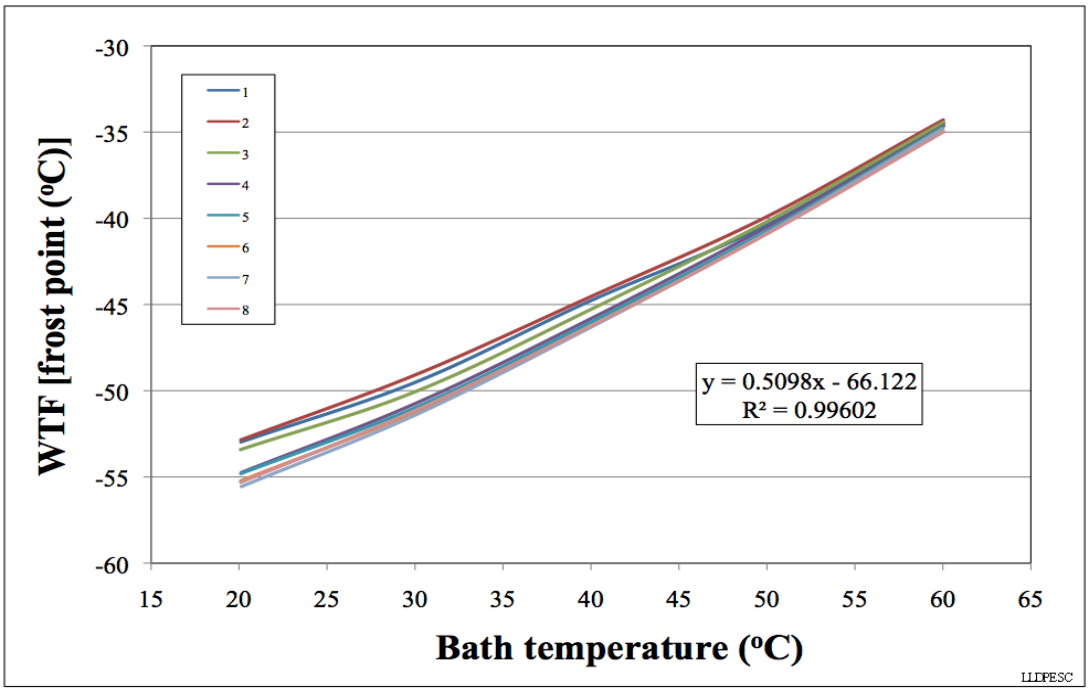

Figure 54, Linear WTF (frost point) behavior of LLDPE SC versus temperature.

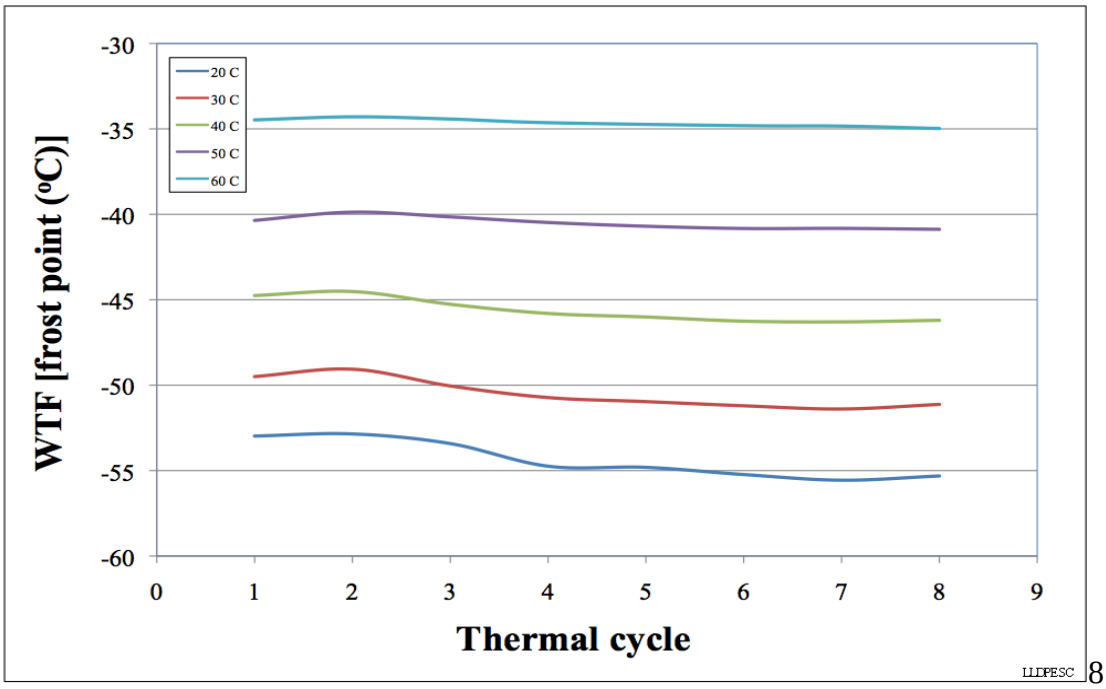

Figure 55, WTF (frost point) behavior of LLDPE SC as function of thermal cycles.

The LLDPE-SCA is the next sample to be reviewed in this series of LLDPE samples. It is shown in Figure 56 through Figure 59 and shows a rapid settling to a steady state WTF rate during the 60°C soak. This stability continued throughout the temperature plateaus and reached a ULB of R2 = 0.9998 in 5 cycles. The significance of the ULB is that the sample has stopped changing and reached steady state WTF as a function of thermal cycles. This sample has one unique quality, the WTF increased at each thermal cycle upon approach to the ULB.

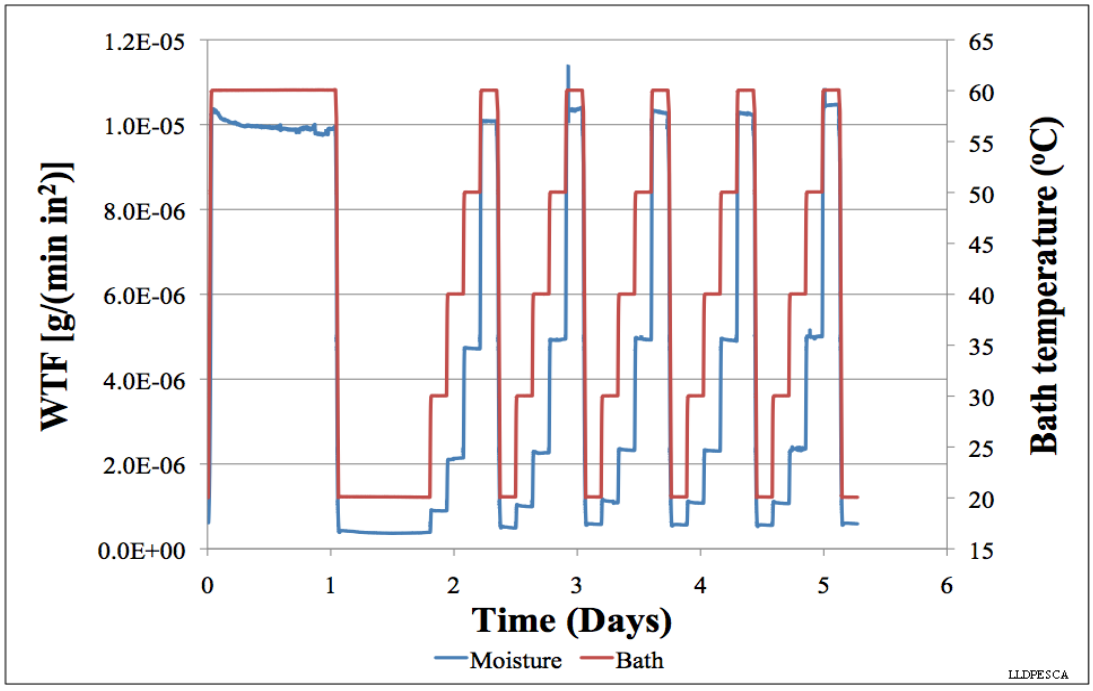

Figure 56, WTF of LLDPE SCA [g/(min in.^{2})] as function of temperature.

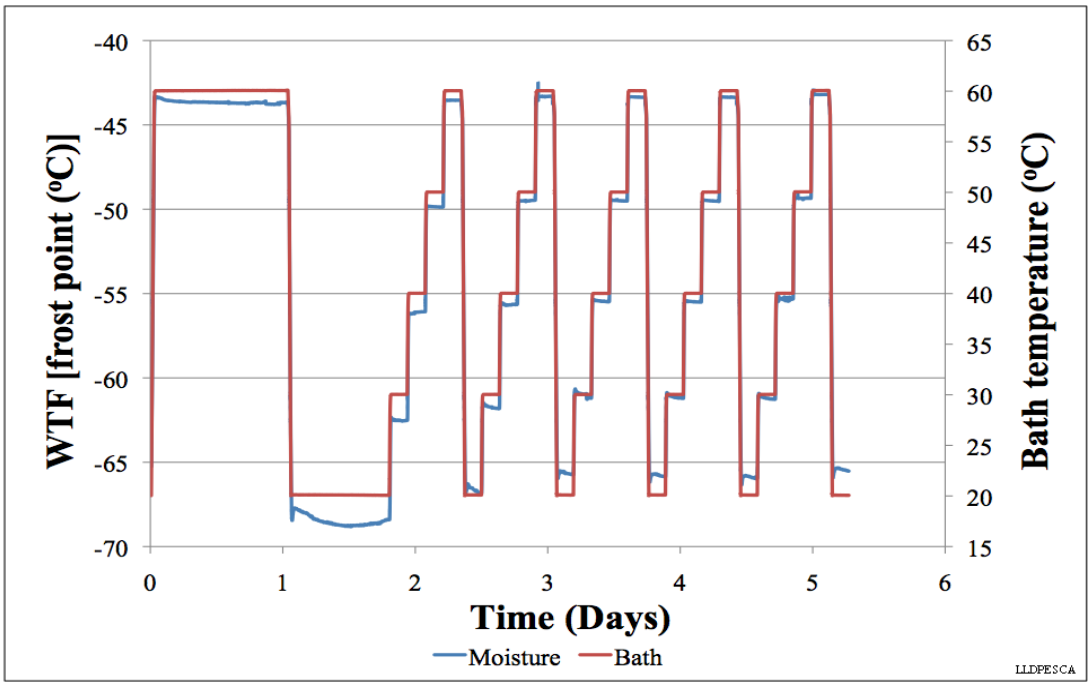

Figure 57, WTF of LLDPE SCA [frost point(°C)] as function of temperature.

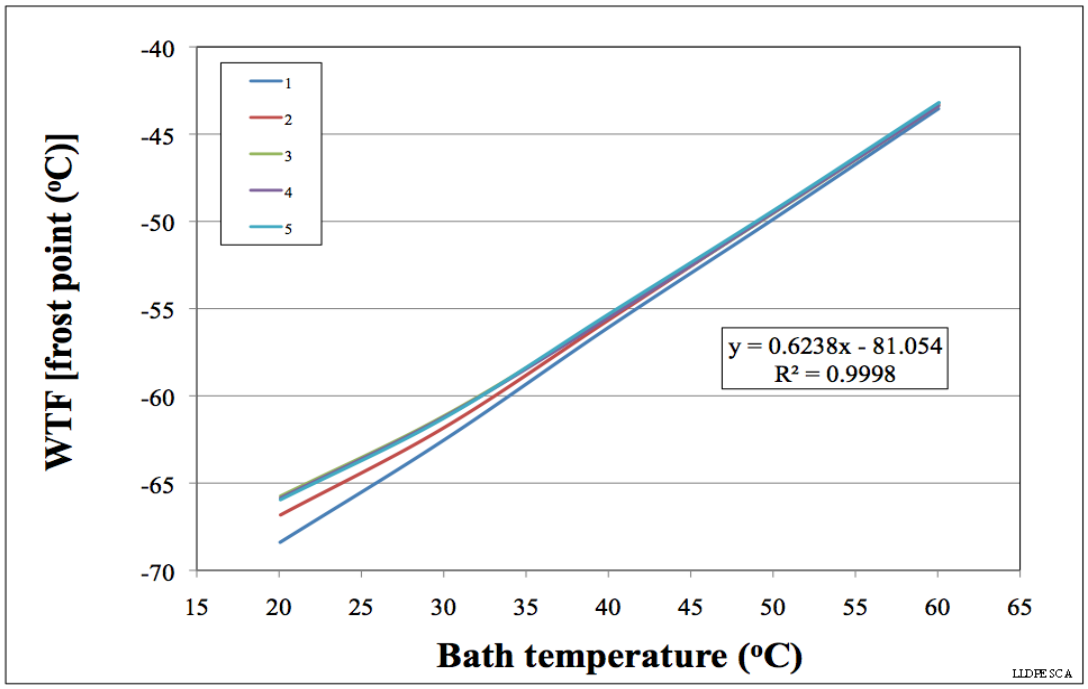

Figure 58, Linear WTF (frost point) behavior of LLDPE SCA versus temperature.

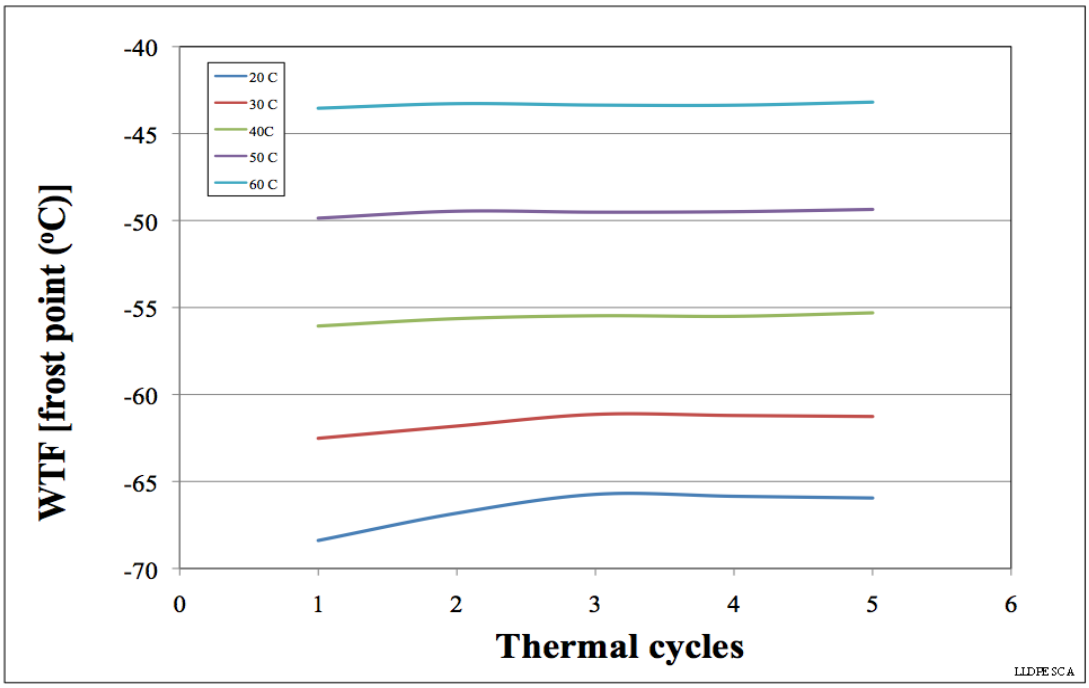

Figure 59, WTF (frost point) behavior of LLDPE SCA as function of thermal cycles.

The next material to be presented is LDPE and first sample of this material type will be the LDPE-QC shown in Figure 60 through Figure 63. During the 60°C, 24 hour soak the sample showed an unsteadiness which manifested itself by having a decreasing WTF and a spike in its rate. The decreasing slope was pronounced and persisted through the 8^{th} thermal cycle. By that time the plateau WTF was more stable and acheived ULB by the 11^{th} cycle.

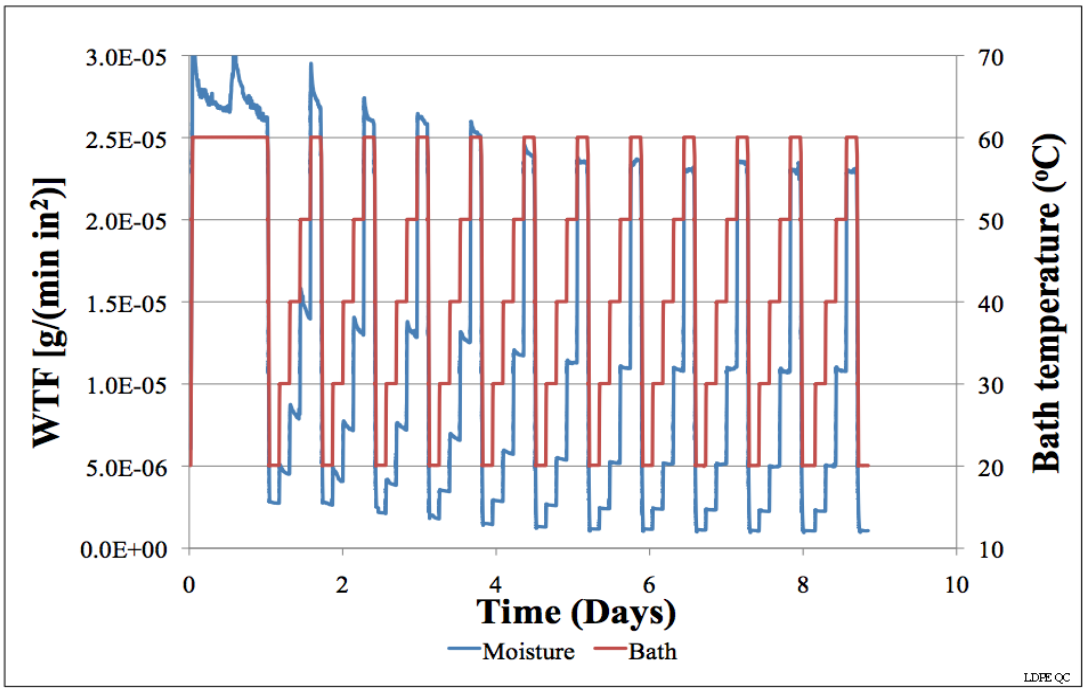

Figure 60, WTF of LDPE QC [g/(min in.^{2})] as function of temperature.

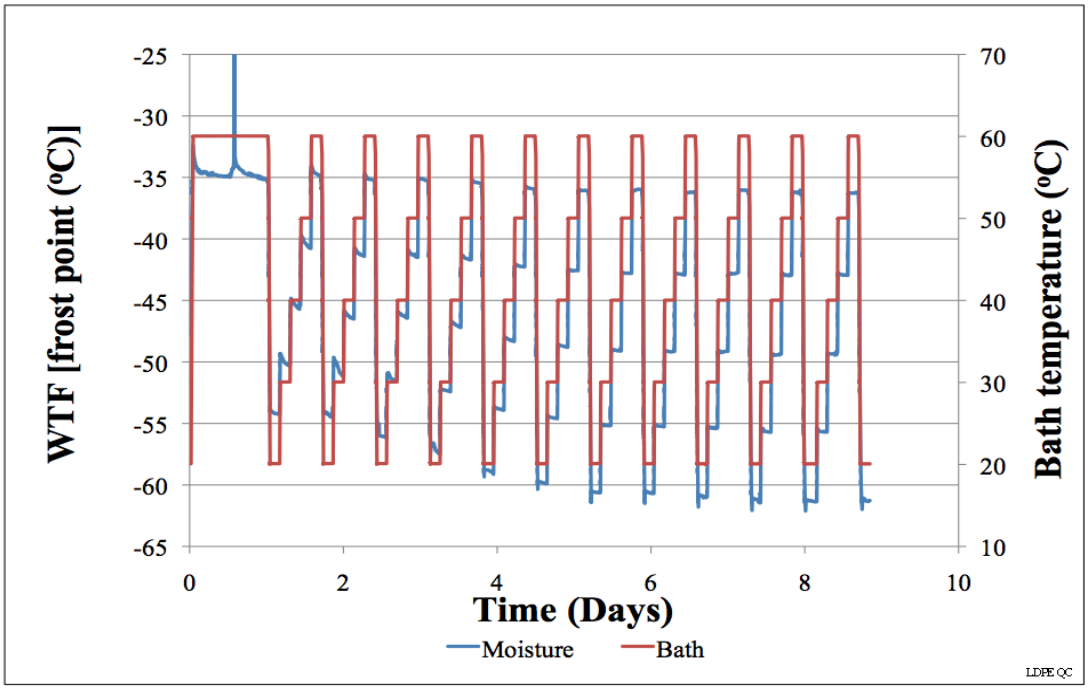

Figure 61, WTF of LDPE QC [frost point(°C)] as function of temperature.

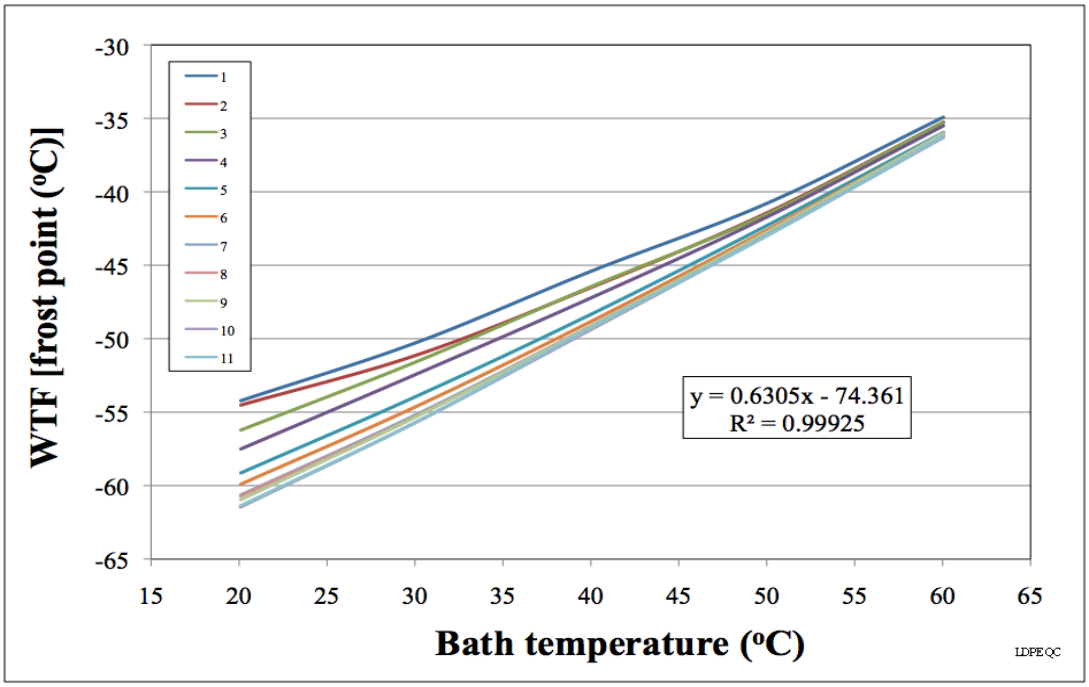

Figure 62, Linear WTF (frost point) behavior of LDPE QC versus temperature.

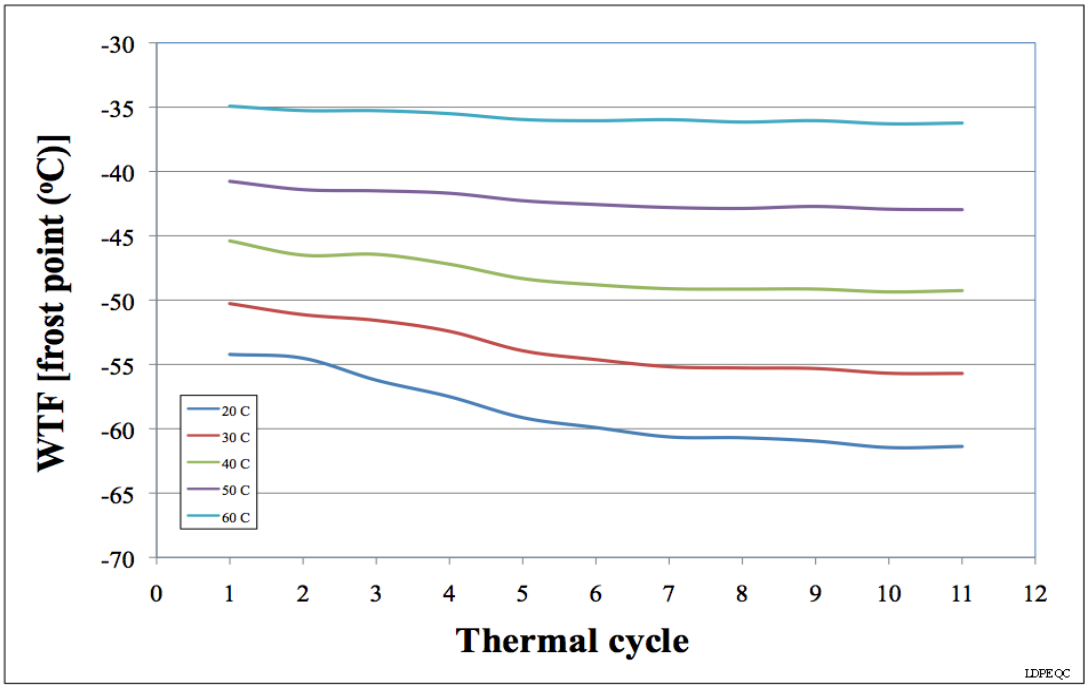

Figure 63, WTF (frost point) behavior of LDPE QC as function of thermal cycles.

LDPE-QCA is the next data set to be presented. This sample is shown in Figure 64 through Figure 67. The 60°C initial soak showed a slow response to obtaining the maximum WTF initially and then as it decreased was very choppy. The decreasing WTF and choppy behavior persisted through the 7^{th} cycle and only acheived the ULB in the 8^{th} cycle. Examination of Figure 66 shows a significant departure from the ULB in the first few cycles with the line having a pronounced curvature.

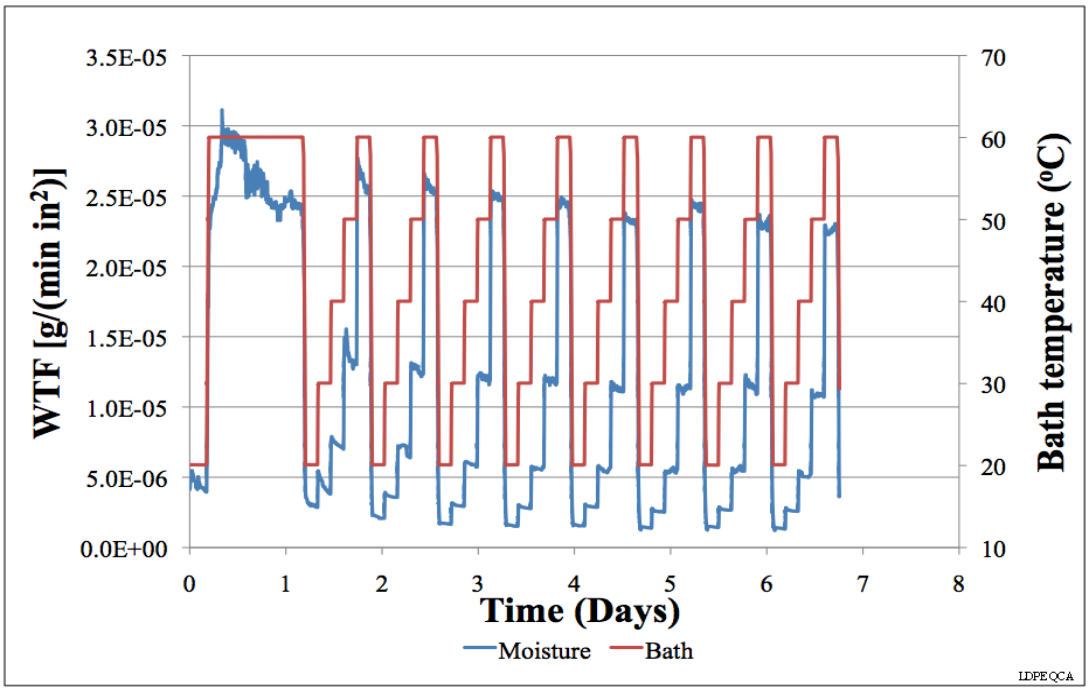

Figure 64, WTF of LDPE QCA [g/(min in.2] as function of temperature.

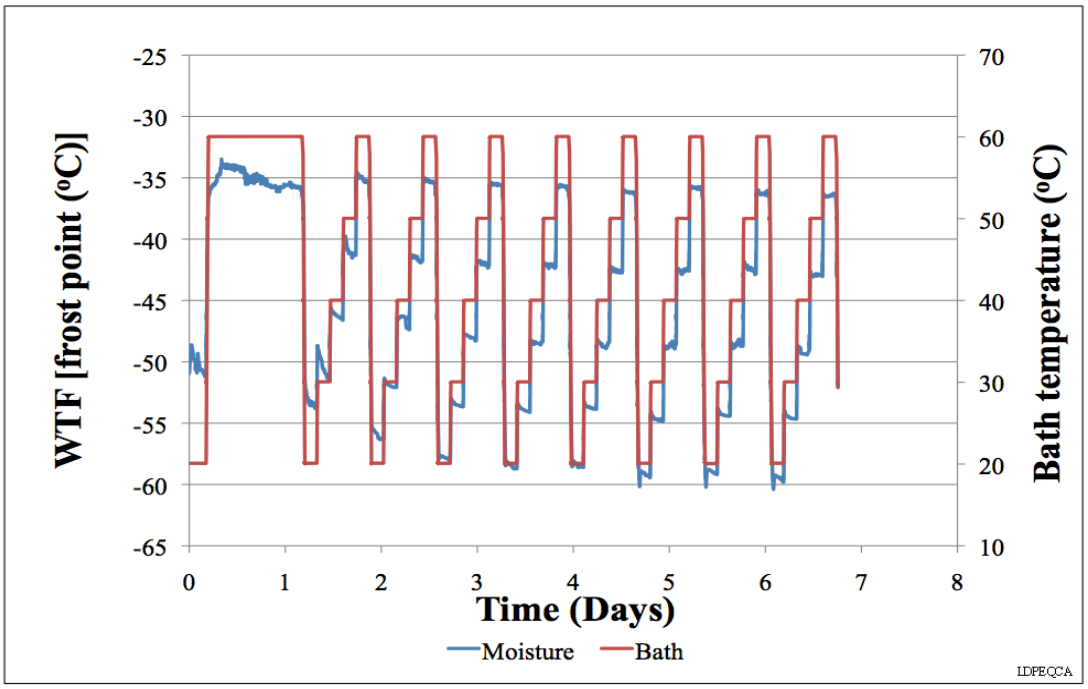

Figure 65, WTF of LDPE QCA [frost point(°C)] as function of temperature.

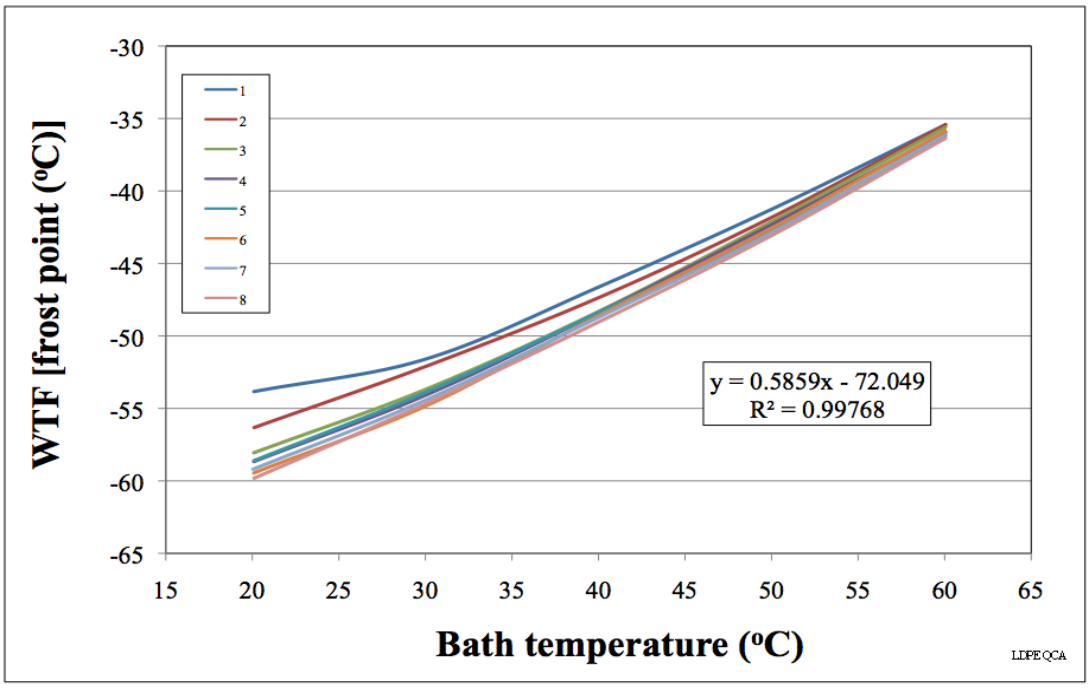

Figure 66, Linear WTF (frost point) behavior of LDPE QCA versus temperature.

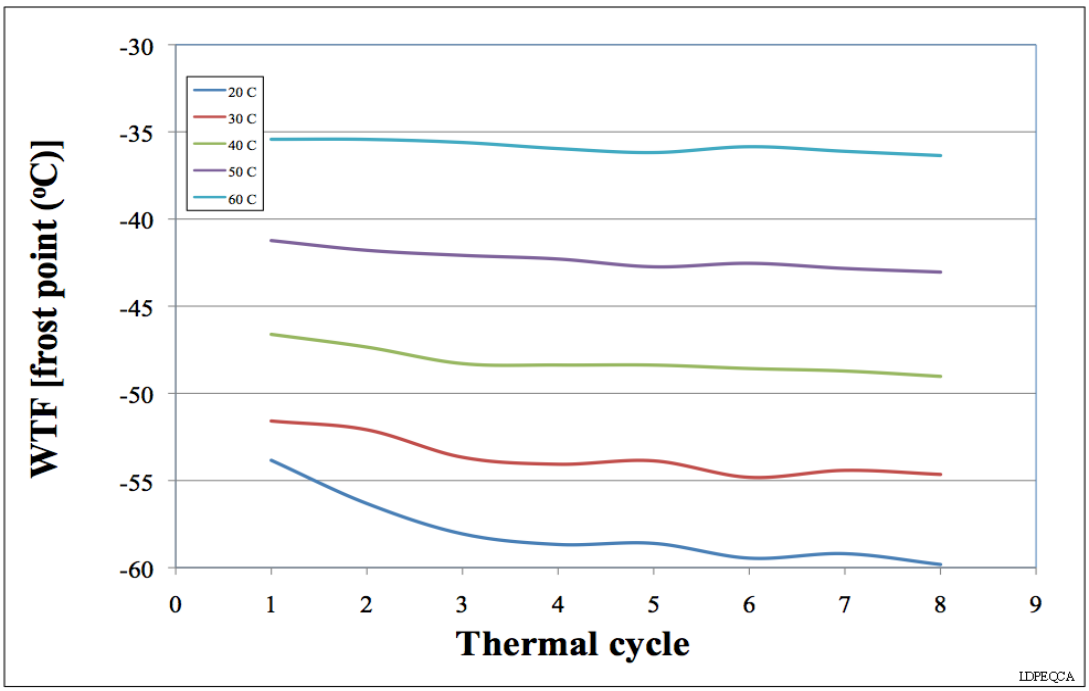

Figure 67, WTF (frost point) behavior of LDPE QCA as function of thermal cycles.

LDPE-SC is the next data set to be presented and is found in Figure 68 through Figure 71. The WTF during the 60°C soak had a pronounced decrease but achieved a stable WTF before the end of the soak. The WTF was stable at each plateau and achieved ULB of R2 = 0.9996 after 5 cycles. Inspection of Figure 71 shows that the WTF at the plateaus was nearly constant from the start.

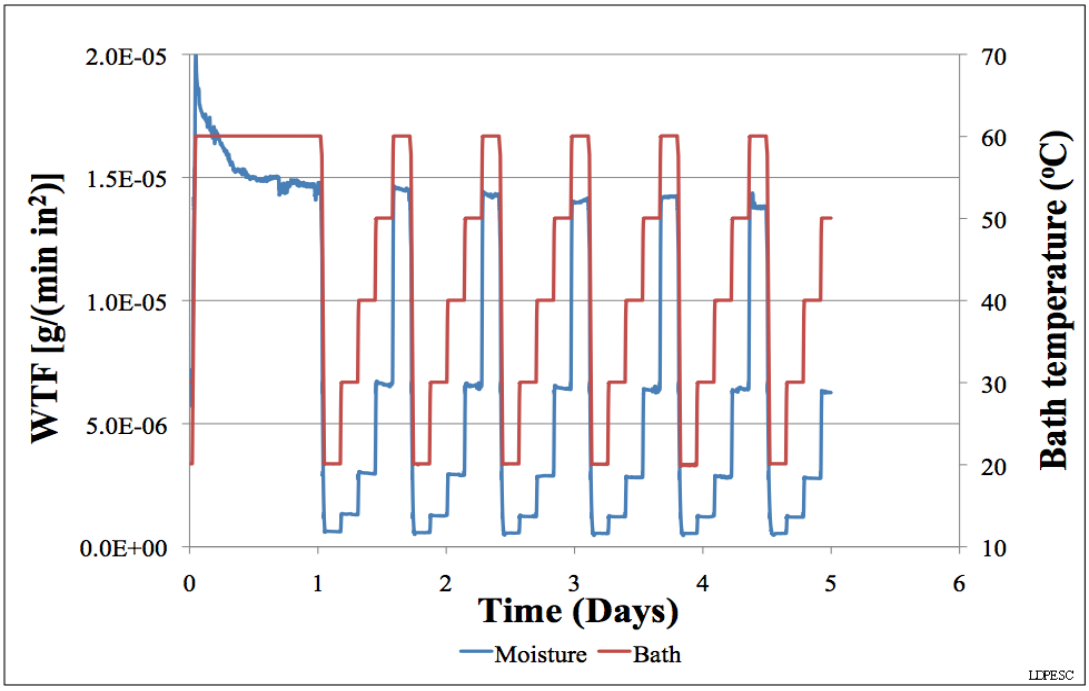

Figure 68, WTF of LDPE SC [g/(min in.^{2})] as function of temperature.

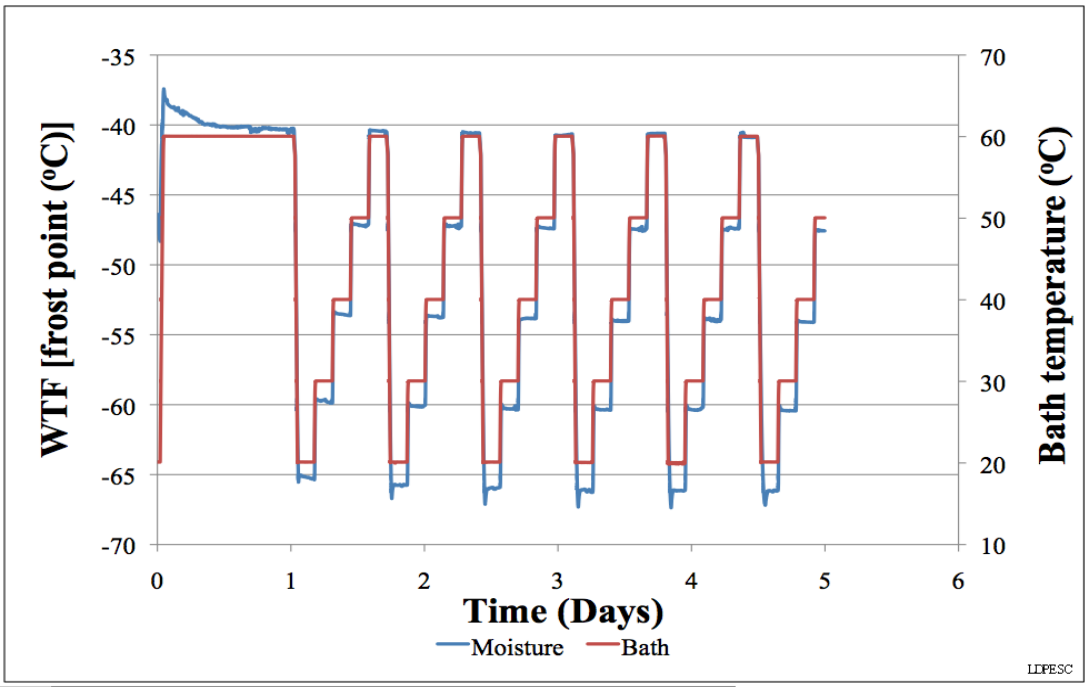

Figure 69, WTF of LDPE SC [frost point(°C)] as function of temperature.

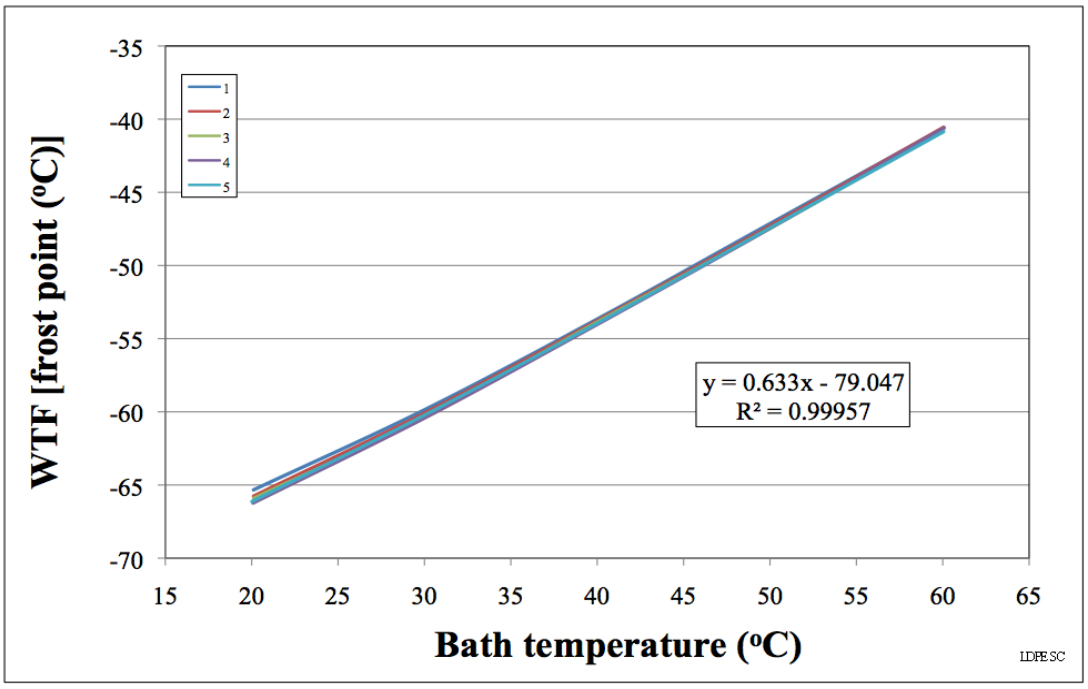

Figure 70, Linear WTF (frost point) behavior of LDPE SC versus temperature.

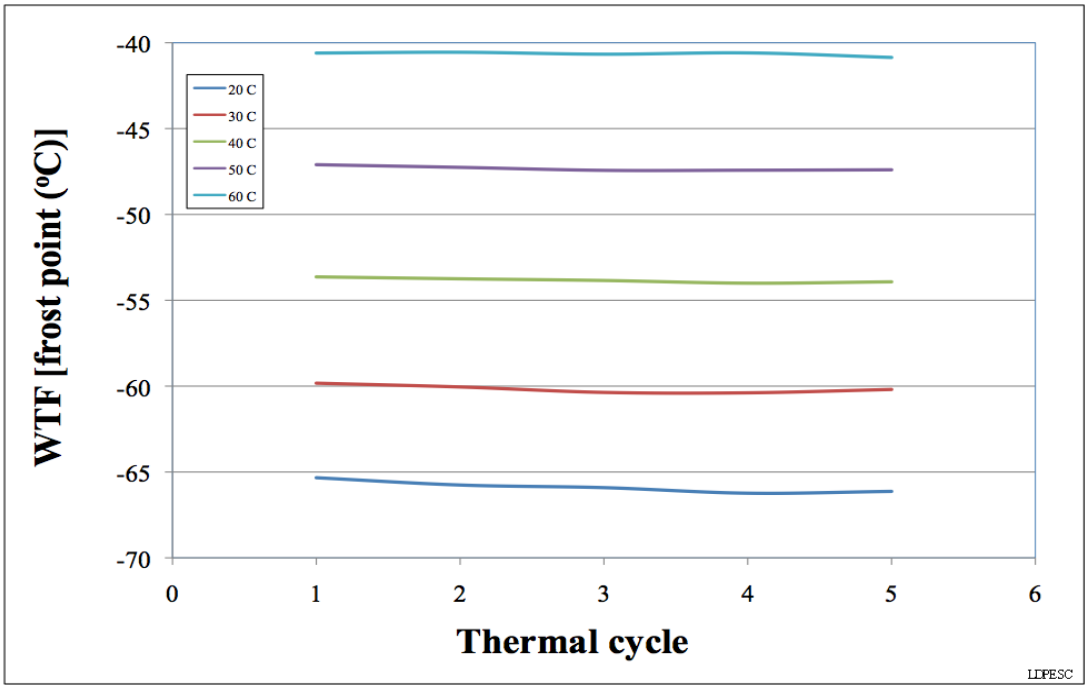

Figure 71, WTF (frost point) behavior of LDPE SC as function of thermal cycles.

The water transfer flux behavior of LDPE-SCA is presented. It appears in Figure 72 through Figure 76. This sample shows a complex and slowly stabilizing response. The WTF has a very large reduction during the 60°C soak period which occurs in the first 24 hours of the test with many spiked events. This behavior continues into the thermal cycling showing a marked reduction in WTF with each subsequent thermal cycle. This sample took 20 thermal cycles to reach linear performance and 25 thermal cycles before the ULB was reached with a correlation factor $R^2 = 0.99979$. The plot of the WTF versus bath temperature has been plotted in Figure 74 and Figure 75 to show the significant change this sample goes through during testing. For instance at the 20°C sample temperature the WTF goes from -53 to -63°C. In other words from the first thermal cycle to the last thermal cycle the amount of water vapor that migrates across the sample is significantly reduce. Figure 74 displays the first 5 and last 6 sets of cycles to demonstrate the change in WTF this sample exhibits. The last 6 cycles has been presented separately in Figure 75 to show the gradual movement to the final ULB.

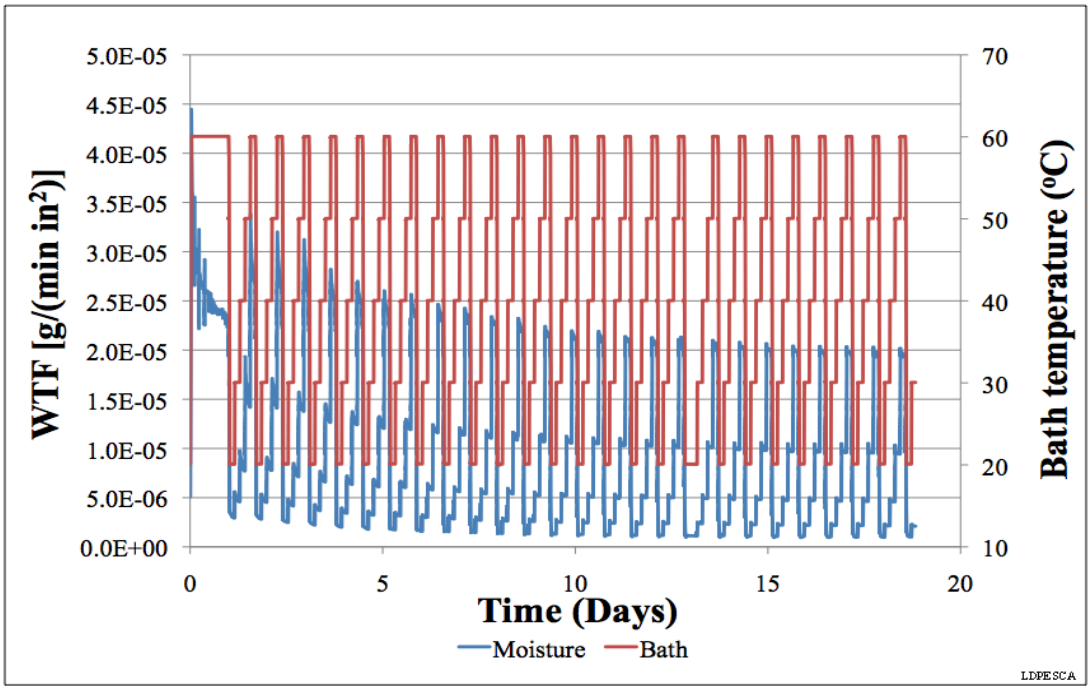

Figure 72, WTF of LDPE SCA [g/(min in.^{2})] as function of temperature.

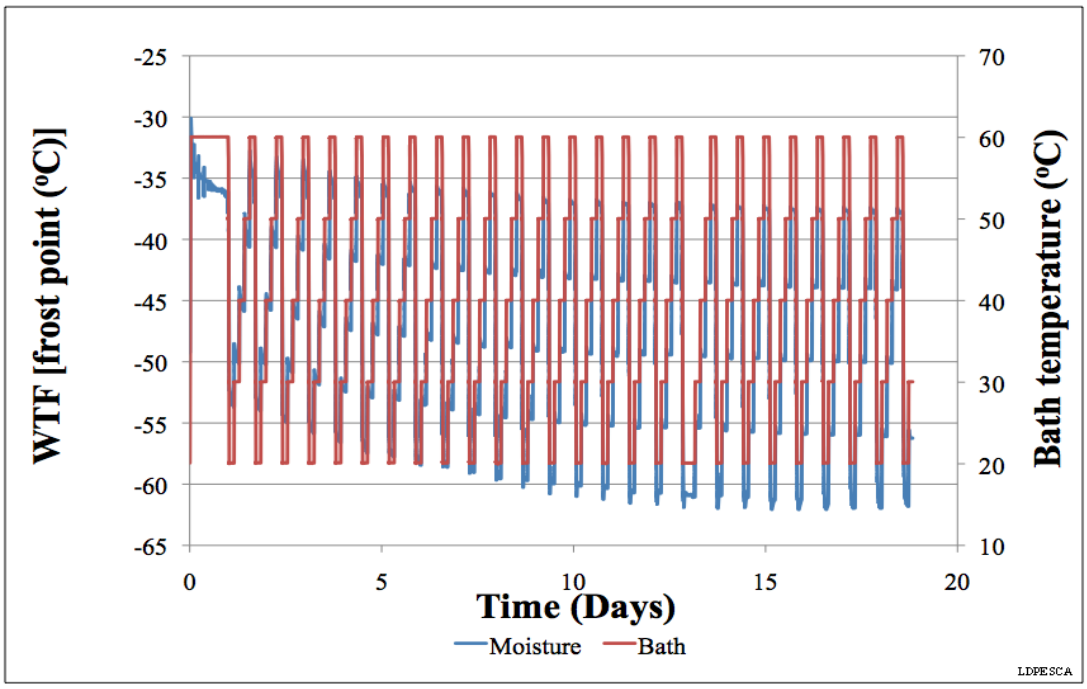

Figure 73, WTF of LDPE SCA [frost point(°C)] as function of temperature.

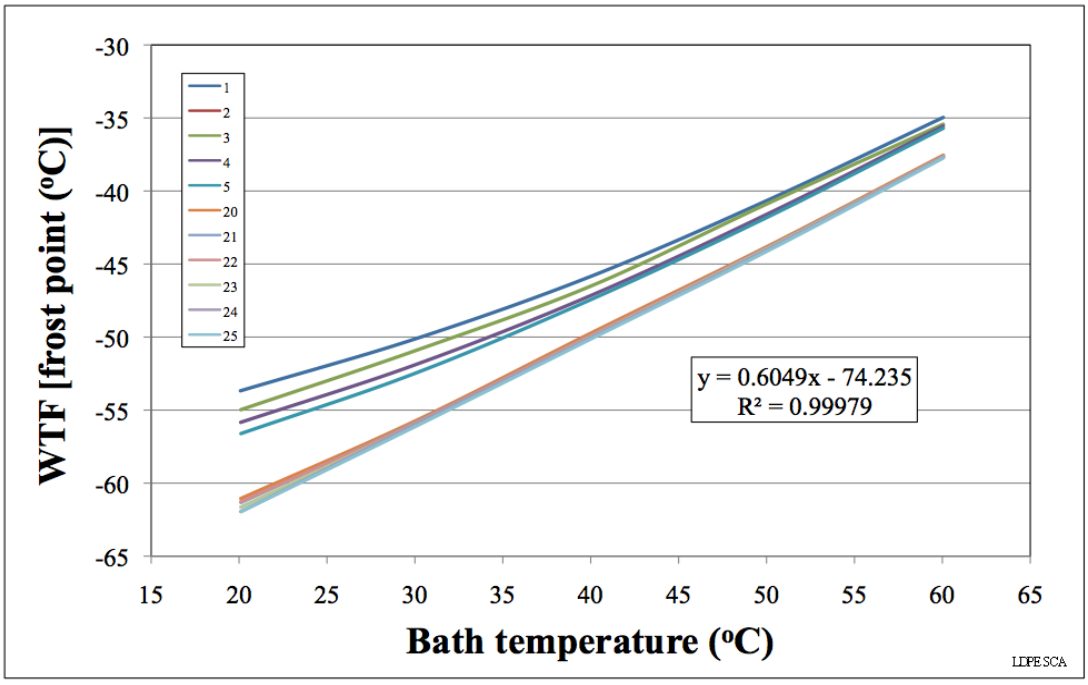

Figure 74, Linear WTF (frost point) behavior of LDPE SCA versus temperature.

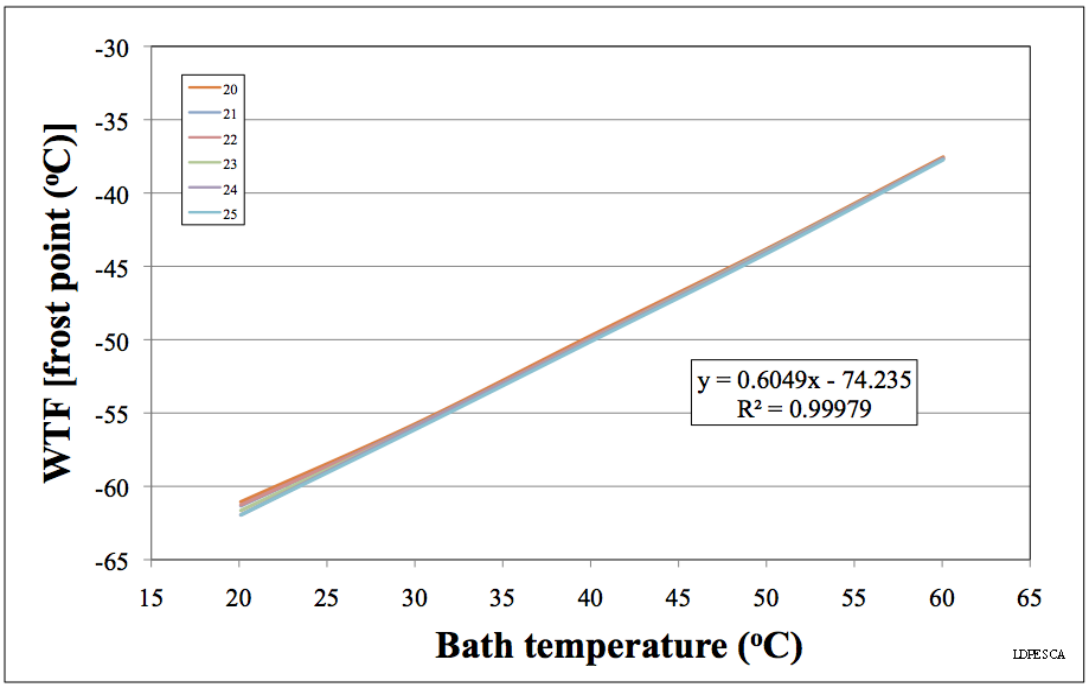

Figure 75, Final settling cycles of linear WTF (frost point) behavior of LDPE SCA versus temperature.

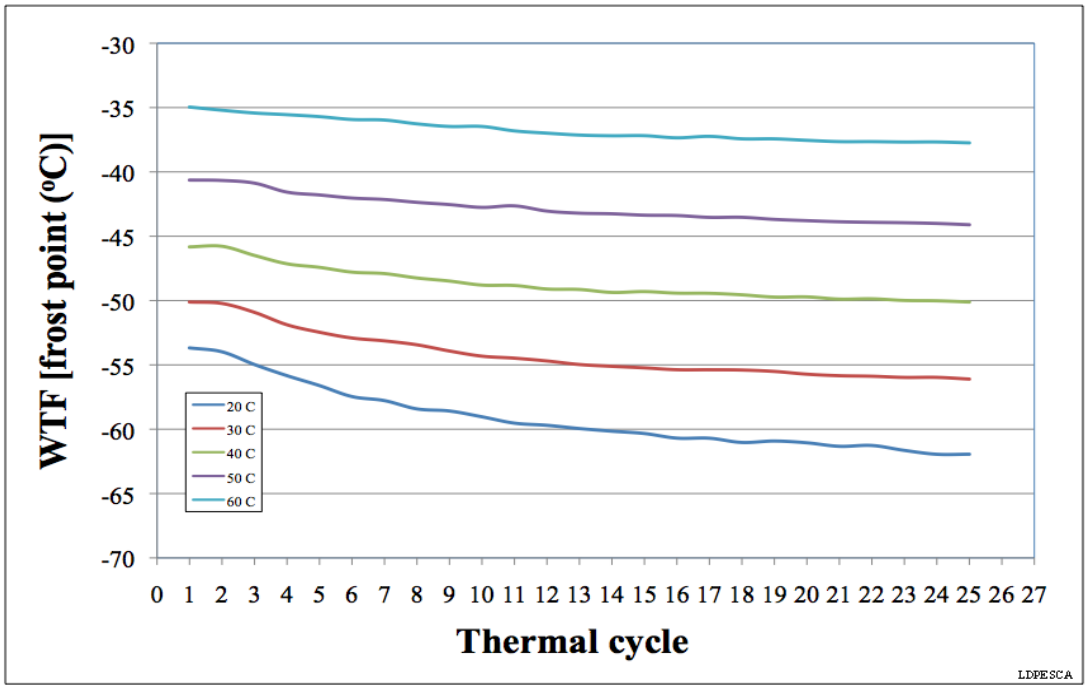

Figure 76, WTF (frost point) behavior of LDPE SCA as function of thermal cycles.

The data from testing HDPE-QC appears in Figure 77 through Figure 81. The WTF starts very high during the 60°C soak of the initial 24 hour period but drops rapidly before starting the thermal cycling. The large drops persisted into the thermal cycling with a radically unstable performance during the 3 or 4 thermal cycles. Only after the 4^{th} cycle does the sample settle and begin to have a resemblance of stable performance. The instability in performance persisted until the 23 cycle. It took 25 thermal cycles for the sample to come to steady state and obtain ULB of $R^2 = 0.99878$. The plot of the WTF versus bath temperature has been plotted twice in Figure 79 and Figure 80 to reveal the large changes in WTF from the first thermal cycle to the last. Figure 79 displays the first 5 and last 5 sets of cycles to show the large changes in the WTF over the test period. The large curvature in the first 3 WTF cycles should be noted in Figure 79. The nonlinear behavior of 20 and 21 cycles shown in Figure 80 shows that the instability was still present late in the testing. Ultimately the ULB was achieved. Figure 81 shows a plot of WTF in frost point versus thermal cycles shows the large changes in WTF from the first cycle to the 25 that the sample goes through to reach ULB.

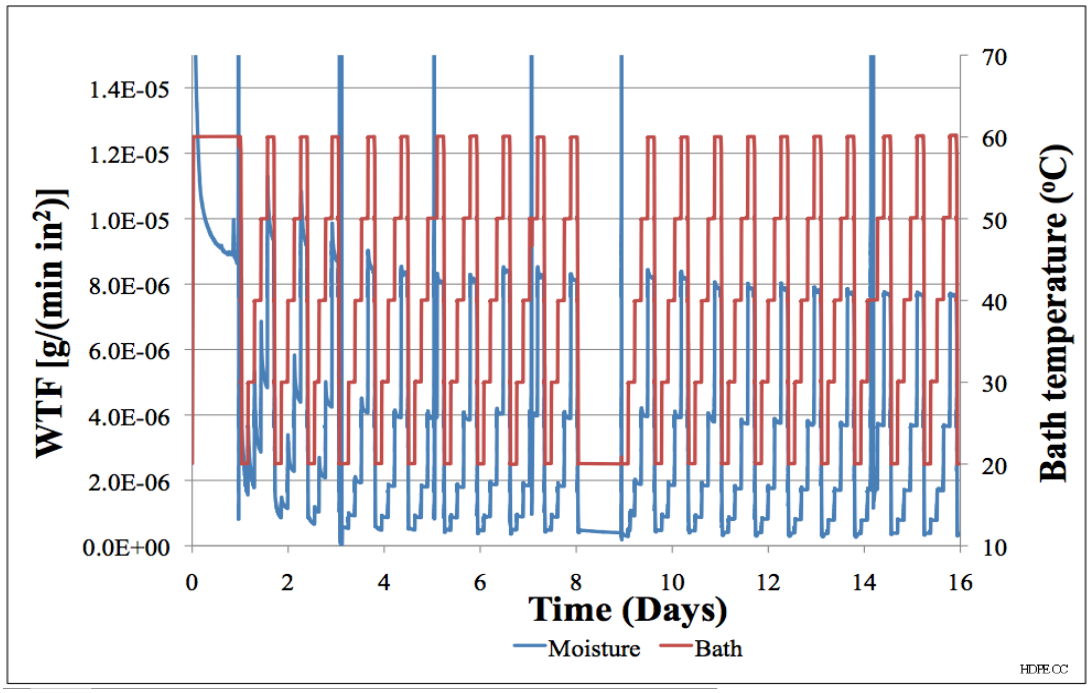

Figure 77, WTF of HDPE QC [g/(min in.^{2})] as function of temperature.

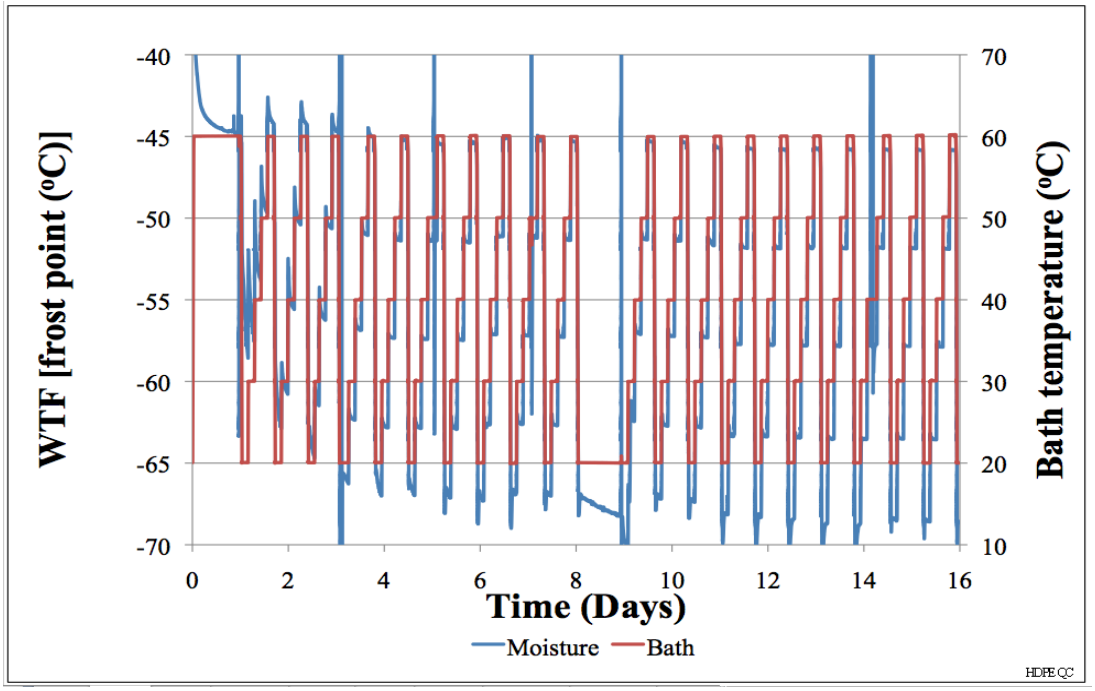

Figure 78, WTF of HDPE QC [frost point(°C)] as function of temperature.

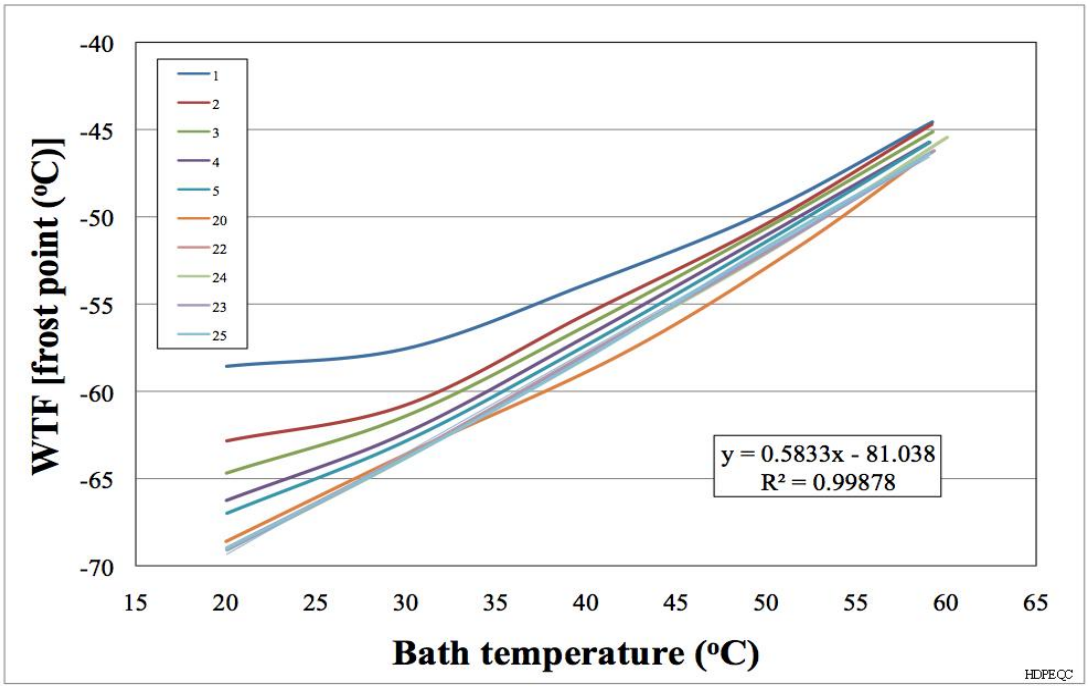

Figure 79, Linear WTF (frost point) behavior of HDPE QC versus temperature.

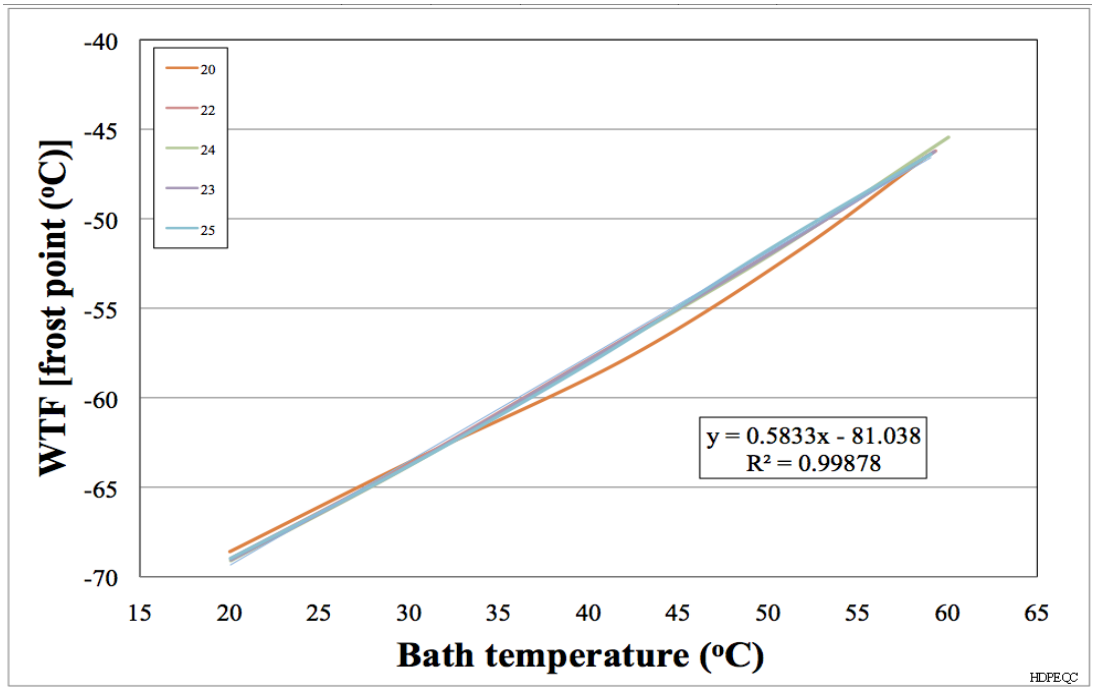

Figure 80, Final settling cycles of linear WTF (frost point) behavior of HDPE QC versus temperature.

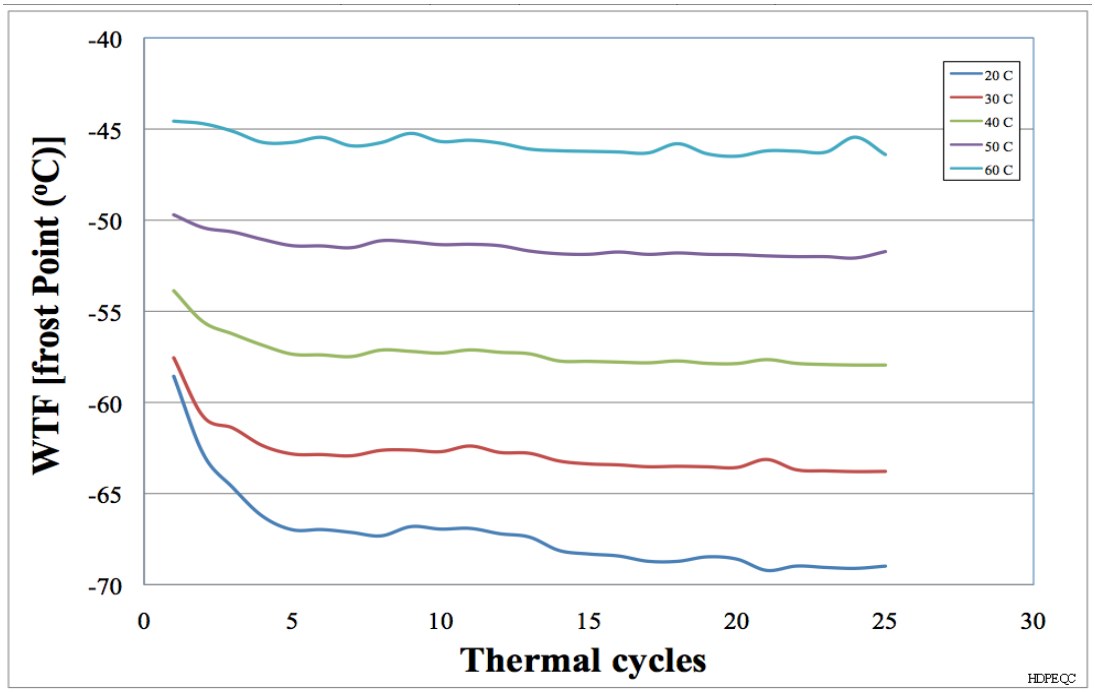

Figure 81, WTF (frost point) behavior of HDPE QC as function of thermal cycles.

The data from test of HDPE-QCA is presented in Figure 82 through Figure 86. The data shows a very unstable response during the 60°C soak and this behavior is carried into the thermal cycling. Ultimately it took 19 thermal cycles before the ULB of R2 = 0.99823 was achieved. The plot of the WTF versus bath temperature has again been plotted twice in so the large curved behavior of the earlier cycles can be clearly seen. These results show that the WTF of this sample has undergone a large change in its transport behavior.

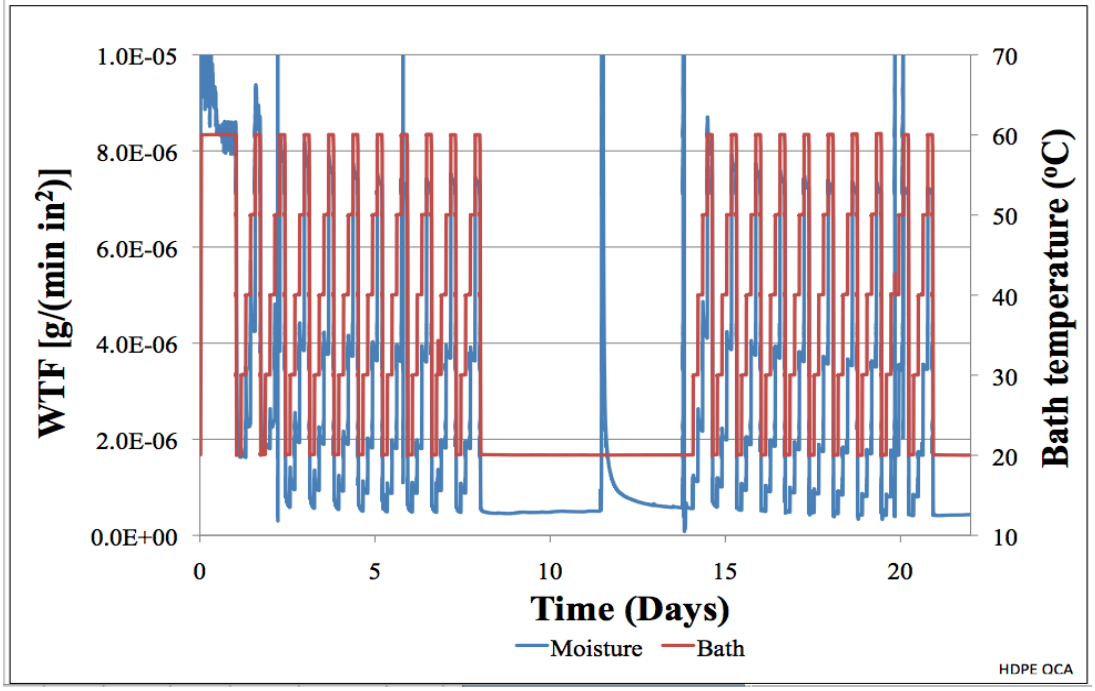

Figure 82, WTF of HDPE QCA [g/(min in.^{2})] as function of temperature.

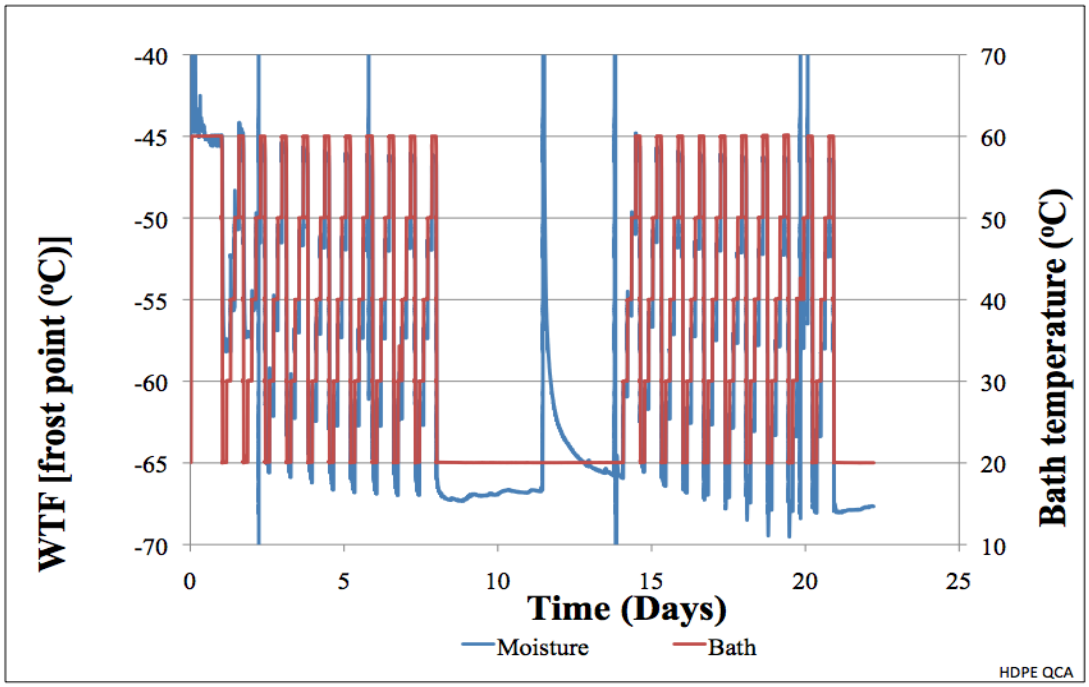

Figure 83, WTF of HDPE QCA [frost point(°C)] as function of temperature.

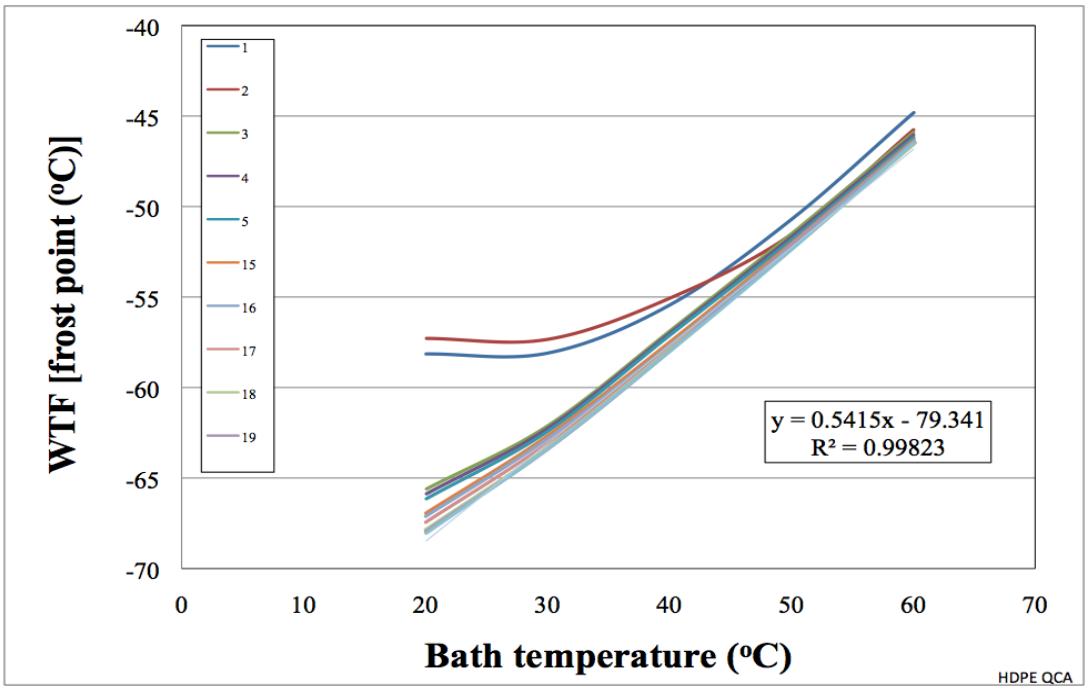

Figure 84, Linear WTF (frost point) behavior of HDPE QCA versus temperature.

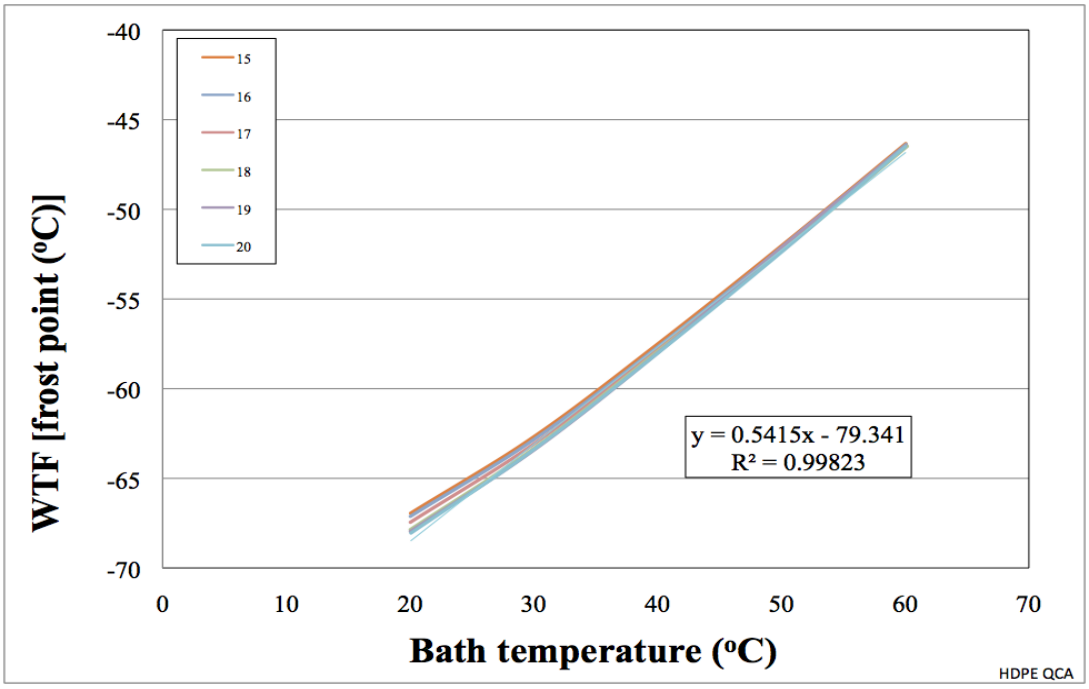

Figure 85, Final settling cycles of linear WTF (frost point) behavior of HDPE QCA versus temperature.

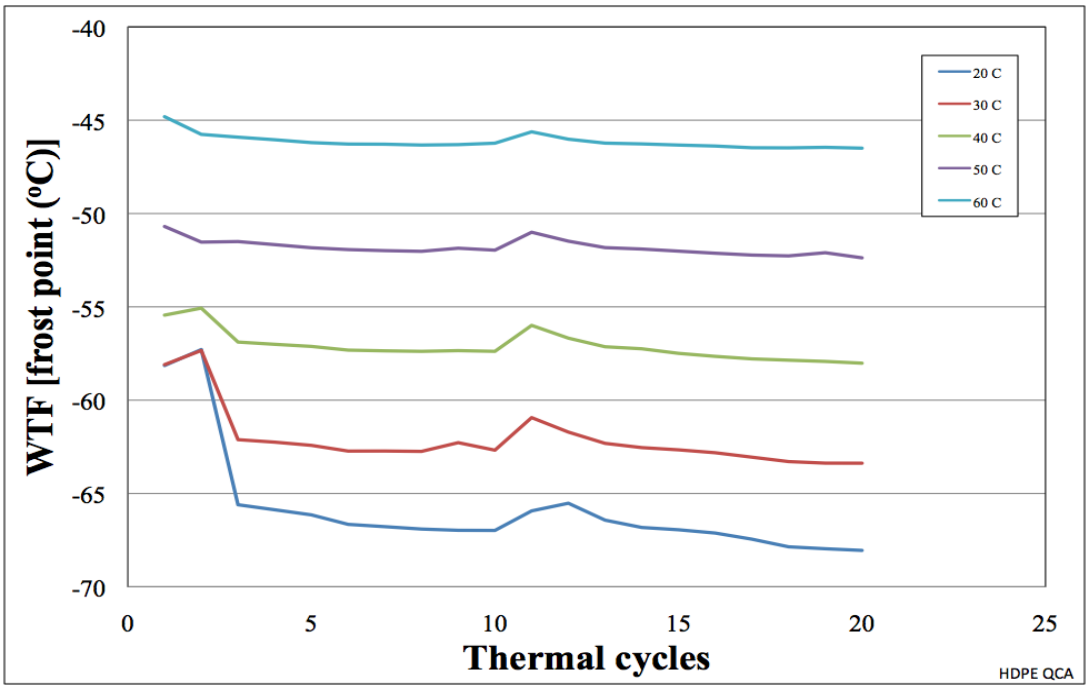

Figure 86, WTF (frost point) behavior of HDPE QCA as function of thermal cycles.

Data from test of HDPE-SC is presented in Figure 87 through Figure 90. This sample shows a very large reduction in WTF during the 24 hour 60°C soak and the behavior followed into the thermal cycling phase of the test. The WTF dropped steadily throughout the test until ULB of R2 = 0.99959 was reached after 22 cycles as shown in Figure 89. The curvature in the plot of the WTF versus bath temperature was not as great but it did extend to a higher temperature of 40°C as shown in Figure 89.

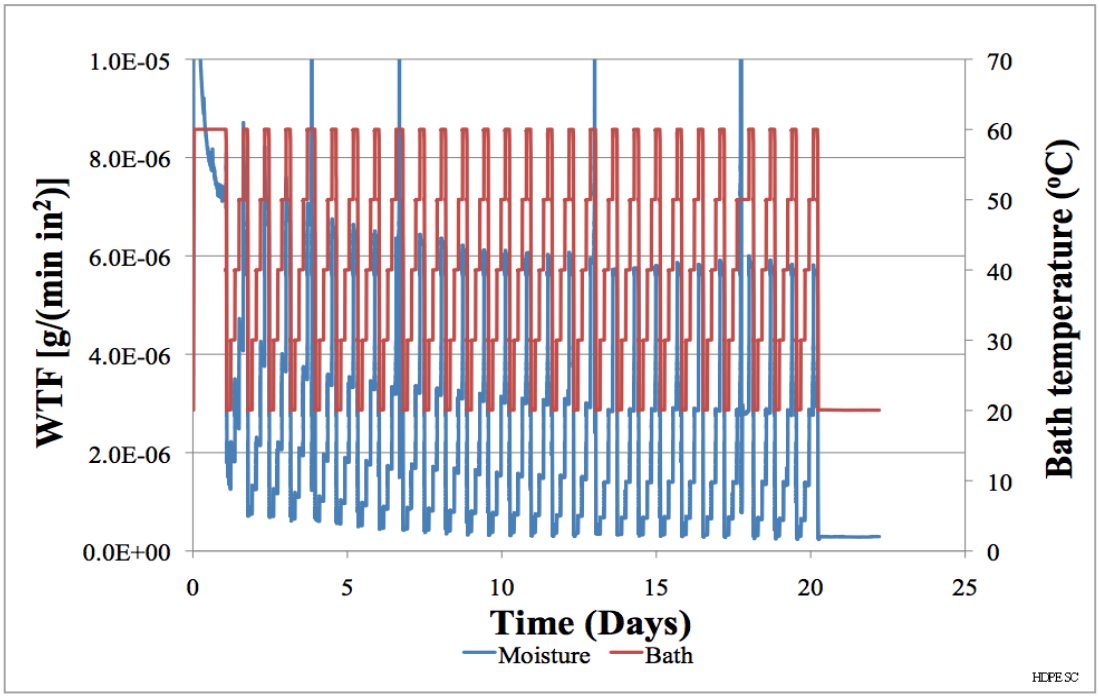

Figure 87. WTF of HDPE SC [g/(min in^2)] as function of temperature.

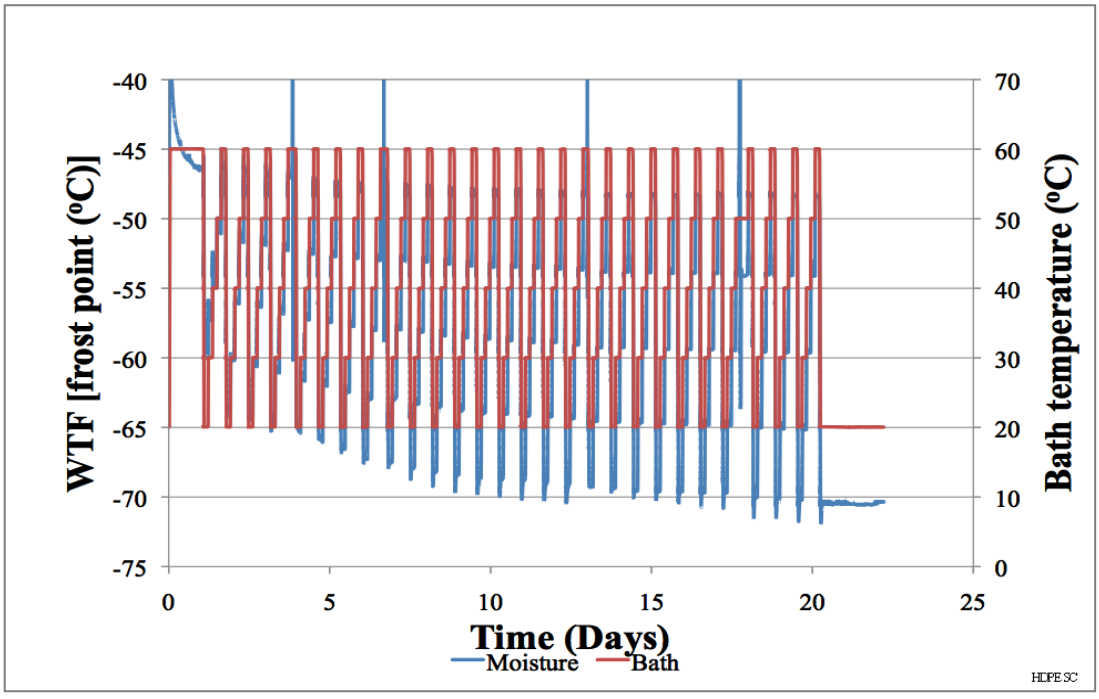

Figure 88. WTF of HDPE SC [frost point(°C)] as function of temperature.

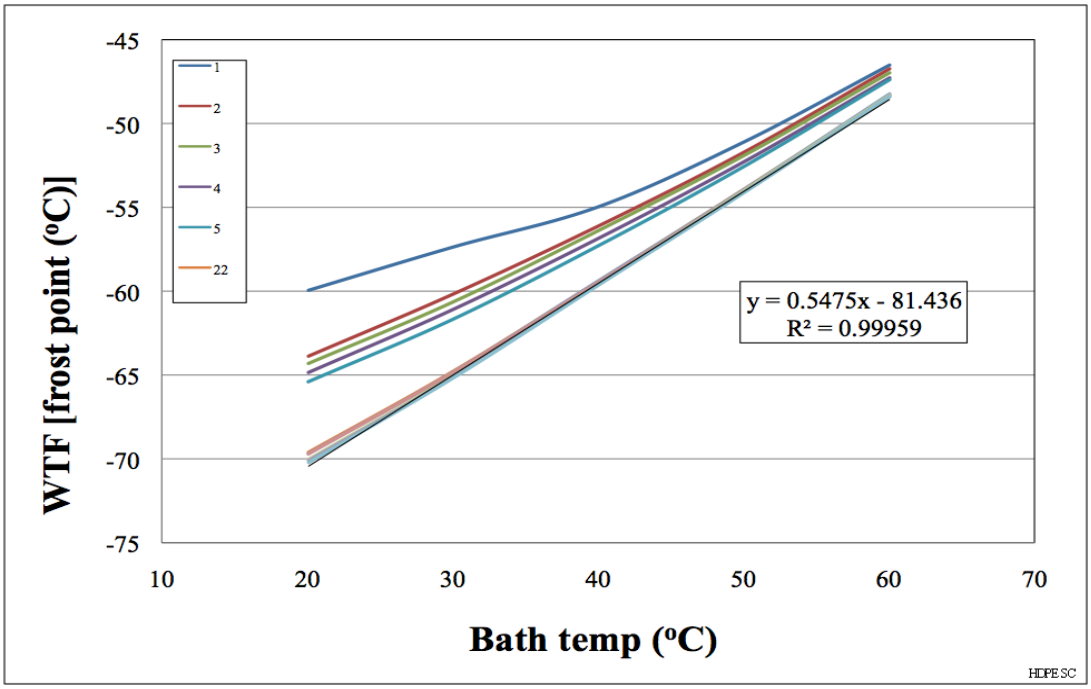

Figure 89. Linear WTF (frost point) behavior of HDPE SC versus temperature.

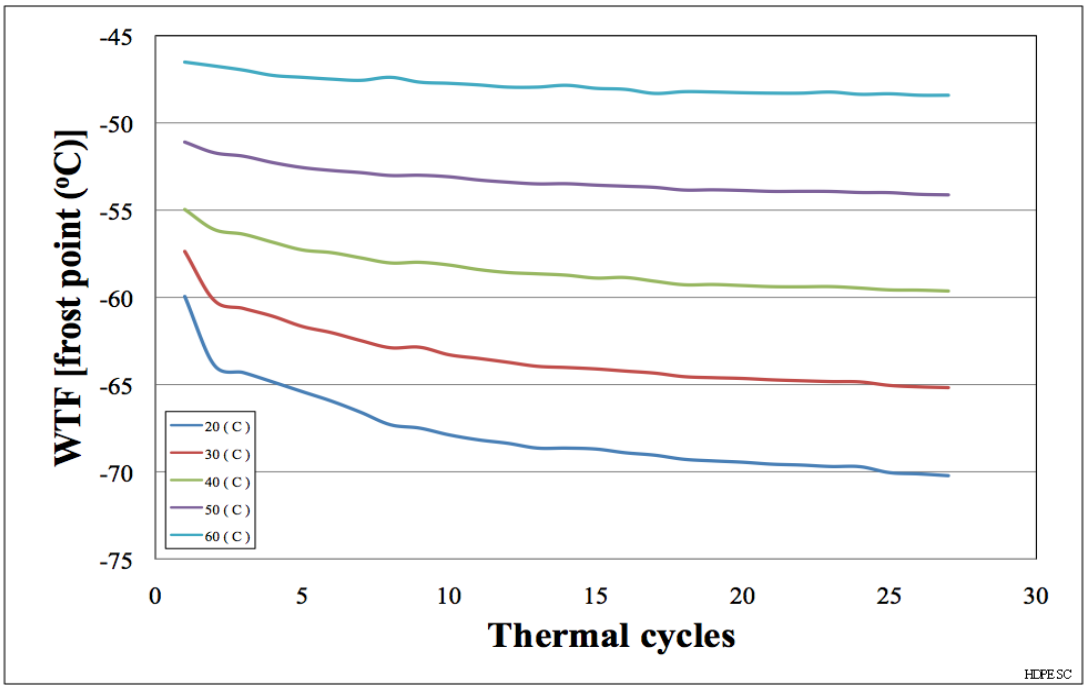

Figure 90. WTF (frost point) behavior of HDPE SC as function of thermal cycles.

The last sample to be discussed is also the last HDPE sample, HDPE-SCA. This sample is presented in Figure 91 through Figure 94. This sample shows a very large reduction in WTF during the 60°C soak and a pronounced WTF reduction at each of the temperature plateaus during the thermal cycling. It is believed that the structure formed during the slow cooling and annealing heat treatment retards this sample from coming to steady state. Unfortunately the test was terminated before ULB was reached. The plot of the WTF versus bath temperature shows a curved behavior up through the 7^{th} and final thermal cycle of the test.

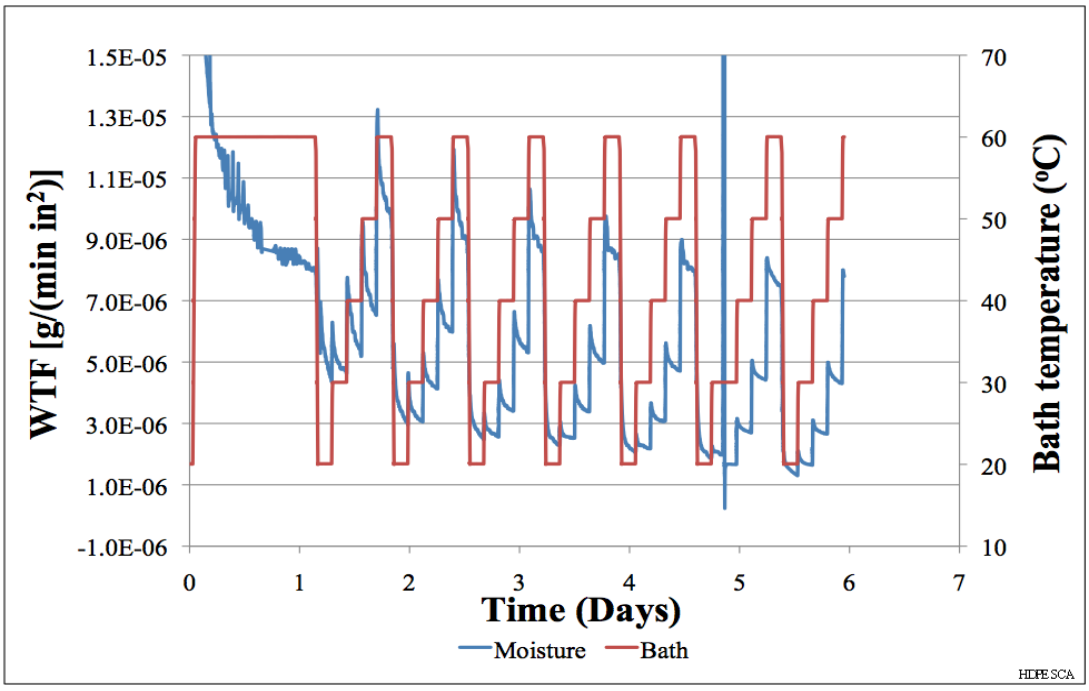

Figure 91, WTF of HDPE SCA [g/(min in.^{2})] as function of temperature.

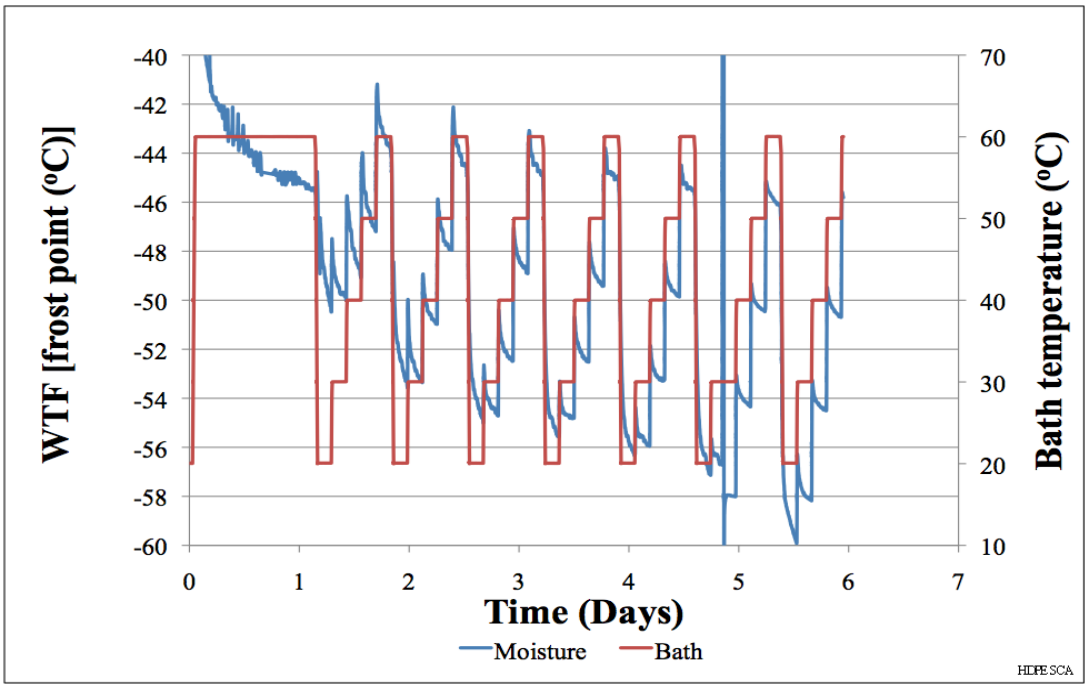

Figure 92, WTF of HDPE SCA [frost point(°C)] as function of temperature.

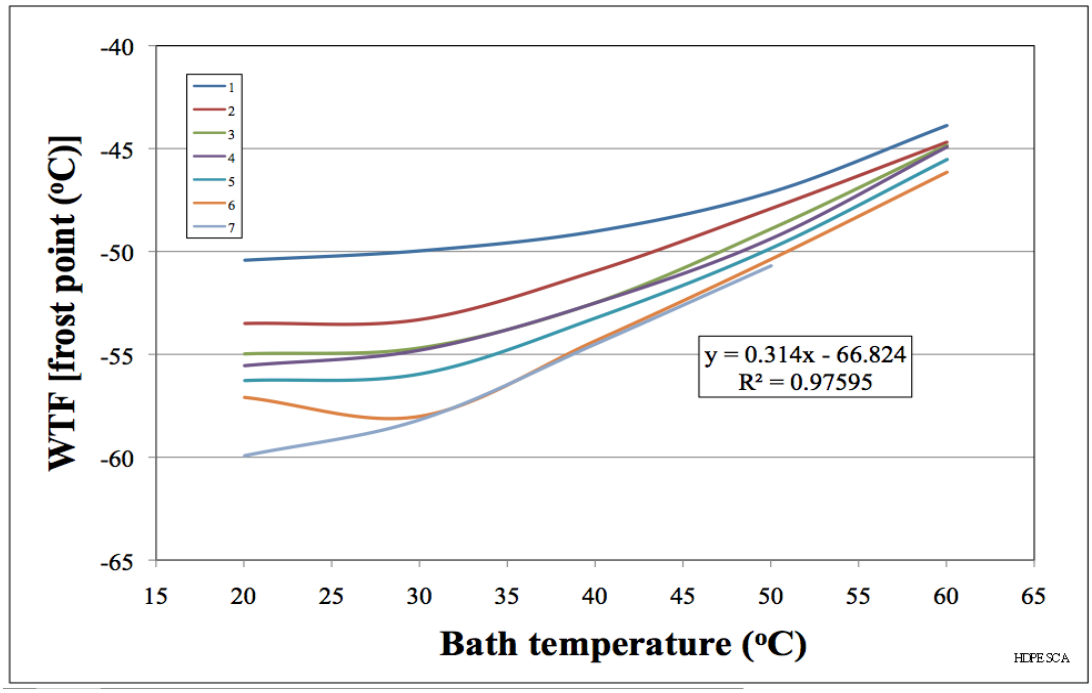

Figure 93, Linear WTF (frost point) behavior of HDPE SCA versus temperature.

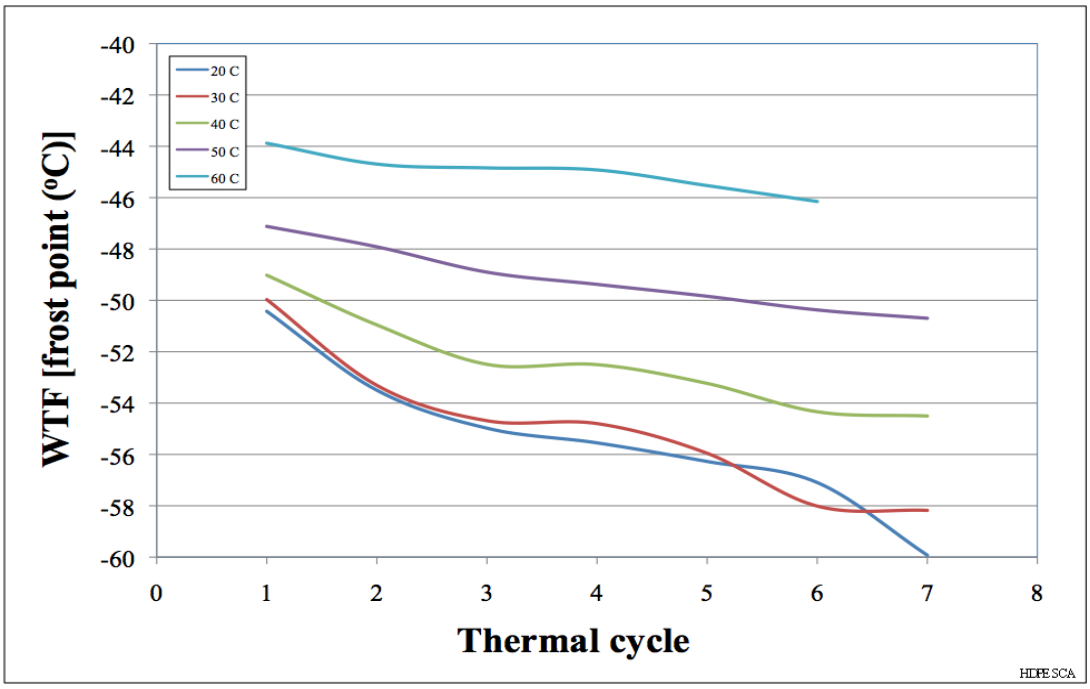

Figure 94, WTF (frost point) behavior of HDPE SCA as function of thermal cycles.

Table 2 consolidates the results from the ULB plots of all samples.

Table 2. Polyethylene ULB

Material	WTF trend toward ULB	Cycles to ULB
LDPE QC	Decrease	4
LDPE QCA	Decrease	4
LDPE SC	Decrease	8
LDPE SCA	Decrease	5
LLDPE QC	Decrease	11
LLDPE QCA	Decrease	8
LLDPE SC	Decrease	5
LLDPE SCA	Increase	25
HDPE QC	Decrease	25
HDPE QCA	Decrease	20
HDPE SC	Decrease	25
HDPE SCA	Decrease	NA

5.3 Density Gradient Column (DGC)

Once the column was established with a density span of 0.9 to 0.98, seven small strips were cut from each of the 12 polyethylene samples for a total of 84 strips. To differentiate strips of one material from another, the strips were cut into unique shapes. Shapes used were squares, triangles, and rectangles for HDPE, LDPE, and LLDPE, respectively, approximately 10 mm on their long axis. To further differentiate among the various heat treatments of each material these shapes were punched with holes. The quenched material had no holes. The quenched and annealed samples were punched with one hole. The slow-cooled samples had two holes, and the slow-cooled and annealed samples were punched with three holes.

Figure 95 shows the column with calibration beads and average sample position with the second order curve fit having a 99.8% correlations. This correlation was used to determine the samples' density and degree of crystallinity as shown in Table 3. The degree of crystallinity can be determined from the density using the expression found in

Equation 19. The relationship used to calculate crystallinity from measured density, Md, for samples used in this study if for 100 % crystalline polyethylene a density of 1.002 and 100% amorphous polyethylene a density of 0.855. Thus, the equation is

Equation 19

$$Crystallinity = \frac{Md - \rho_a}{\rho_c - \rho_a} \times 100$$

$$Crystallinity = \frac{Md - 0.855}{1.002 - 0.855} \times 100$$

Examination of the trend in density and corresponding crystallinity in Table 3 shows that a range in crystallinity has been achieved through the adjustments of processing parameters of initial cooling and annealing. It should be noted that the DGC densities reflect the overall density of the sample including the crystalline and amorphous phases. These trends show that the annealing of these thermoplastics cause rearrangement to lower energy states or higher crystalline packing and resulting in higher densities when provided sufficient cooling times. The importance of this data is that as the density, and hence the degree of crystallinity, increases the amorphous phase is consumed which is the pathway for moisture transport. The % change in crystallinity is the change relative to the quenched sample within each material.

Table 3. Polyethylene density determined by DGC

	Column position (cm)	Density	Degree of crystallinity	% Change in crystallinity
LDPE QC	27.80	0.928	49.6	0
LDPE QCA	33.55	0.933	52.8	6
LDPE SC	34.40	0.933	53.2	7
LDPE SCA	35.28	0.934	53.7	8
LLDPE QC	21.38	0.922	45.9	0
LLDPE QCA	31.81	0.931	51.8	13
LLDPE SC	32.58	0.932	52.2	14
LLDPE SCA	32.42	0.932	52.2	14
HDPE QC	49.98	0.945	61.2	0
HDPE QCA	67.72	0.957	69.2	13
HDPE SC	74.26	0.961	71.8	17
HDPE SCA	77.50	0.962	73.1	19

Figure 95 shows the overall relationship of the samples and density beads but does not show the effects of the processing methods on the samples' densities. Thus, Figure 96 was created to emphasize the relative change of each sample within a material type and the effects of the processing methods on their densities. The desire was to create a series of samples with a range of crystallinities for each material type. Figure 96 shows how effective each method was in controlling the crystallinity resulting crystallinity for any given material.

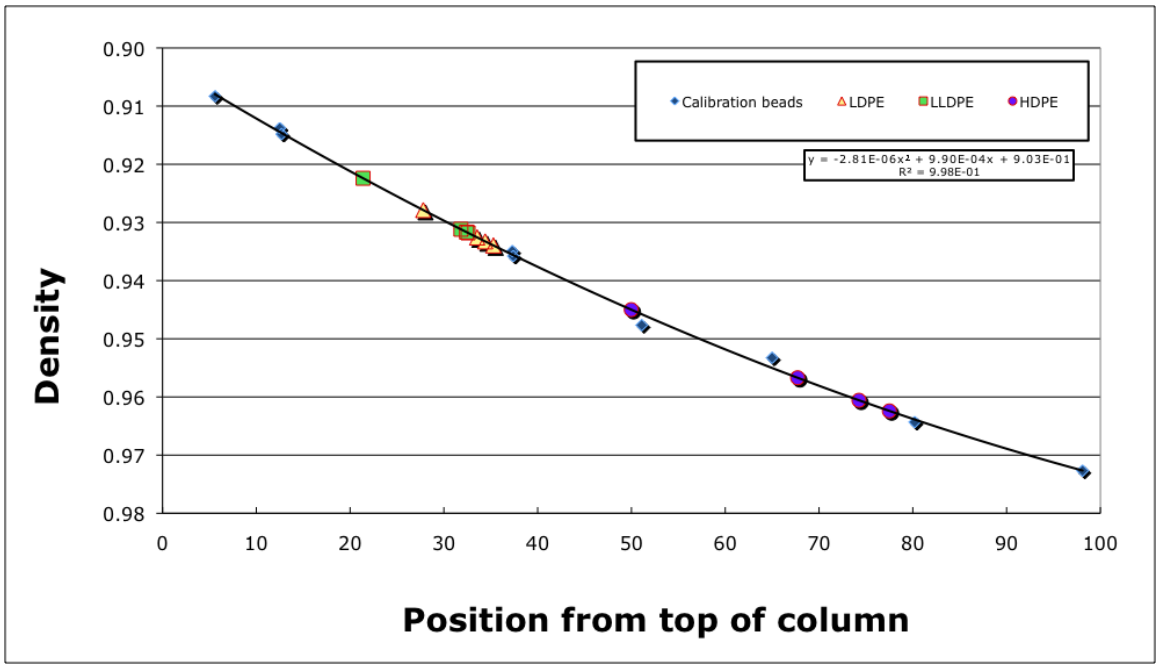

Figure 95. DGC with calibration beads and samples.

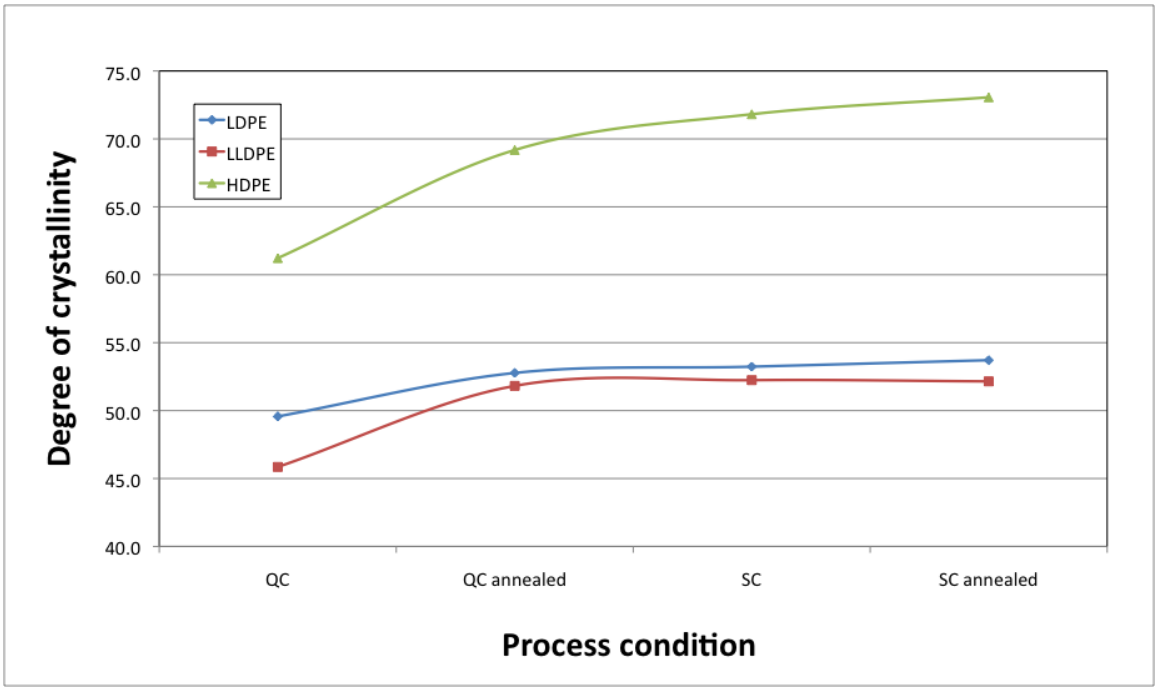

Figure 96. Effects of processing on density.

Another way of evaluating the efficacy of the processing method to changing the overall degree of crystallinity is to see the percent change within a group. In each group of samples the quenched material has the lowest degree of crystallinity and is the basis of comparison, and the change in density is expressed in percent change. These data are shown in Figure 97 where it is clear that the quenched and annealed samples have the biggest percent change with the LDPE changing by 6%, and the LLDPE and HDPE each having 13% change. The slow cooled condition for the LDPE and the LLDPE only produced a 1% increase over the quenched and annealed conditioned whereas the HDPE produced a 4% increase over its quenched and annealed condition. All three materials saw very small changes from their slow cooled conditions to their slow cooled and annealed condition.

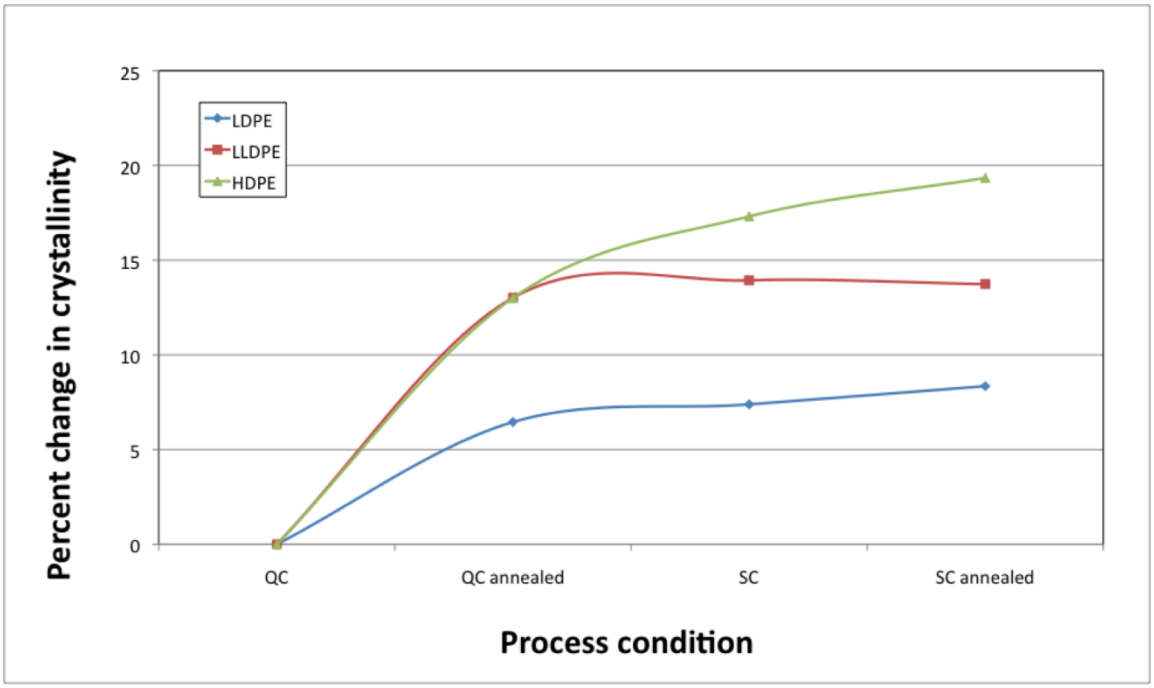

Figure 97. Percent change in degree of crystallinity as function of processing method.

5.4 Determination of Degree of Crystallinity by Differential Scanning Calorimeter

The degree of crystallinity of each material was determined by DSC. Figure 98 shows the DSC thermograms of slow cooled LDPE, LLDPE, and HDPE. The degree of crystallinity was determined by the ratio of the enthalpy of fusion for the sample compared with 288 J/g as the heat required to melt 100% crystalline sample of polyethylene. The data in Table 3 shows the degree of crystallinity for two heating passes. The first pass measures the crystallinity produced by the pressing and heat treatment during fabrication, and the second pass is after the sample was cooled in the DSC, negating the effects of thermal history. Ideally, if all vestiges of the previous processing were erased through the melting process, there should be a relative consistency within a given type of polyethylene on the second pass. As indicated by the variability in the values, on the second pass high melting temperatures or slower cooling would have been needed to completely erase the effects of the original processing. The higher temperatures and longer hold times would have provided the thermal driving force to allow for chain rearrangement and sufficient time needed for the chain movement.

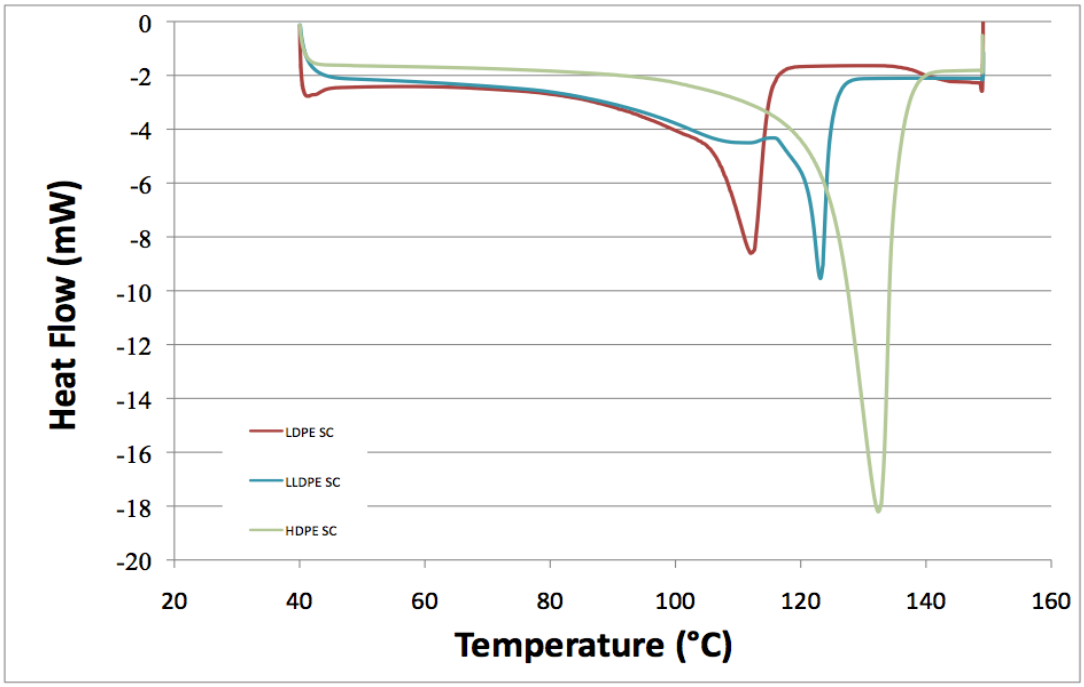

Figure 98. DSC thermograms of slow cooled LDPE, LLDPE and HDPE

Table 4. Degree of crystallinity LDPE, LLDPE, and HDPE determined by DSC

	Pass 1 Degree of Crystallinity
LDPE-QC	40.80
LDPE-QCA	51.94
LDPE-SC	46.22
LDPE-SCA	46.60
LLDPE-QC	32.6
LLDPE-QCA	43.05
LLDPE-SC	43.66
LLDPE-SCA	40.38
HDPE-QC	58.57
HDPE-QCA	68.77
HDPE-SC	69.63
HDPE-SCA	73.29

5.5 Crystal size distribution

Additional information that is extracted from the DSC scans includes the crystal size as measured in thickness and crystal size distribution.[72] The equations to determine crystal size and crystal size distribution use the power supplied by the DSC as a function of sample temperature. The equation, for crystal thickness, l, is

Equation 20

$$l = \frac{2\sigma_e 10^3}{\Delta H_m \rho_c \left(1 - \frac{T_m}{T_m^o}\right)}$$

and the equation, Equation 21, for the crystal size distribution, g(l), is

Equation 21

[72] C. P. Stephens, R. S. Benson, and M. Chipara, "Radiation induced modifications in ultra-high molecular weight polyethylene," *Surface and Coatings Technology* 201, no. 19–20 (2007).

$$g(l) = KP(T)\left(T_m^o - T\right)^2 nm^{-1}$$

where, K, is equal to

$$K = \frac{r_c}{2s_e T_m^o M a_m 10^{19} \left(\frac{dT}{dt}\right)}$$

The constants for the previous equations are:

heat of fusion per unit mass of a perfect crystal, $\Delta H_m = 288\ kJ/kg$,
DSC power output, $P(T)$ in mW,
crystalline density, $r_c = 967\ kg/m^3$,
mass of the sample, M in kg,
and the mass fraction crystallinity, a_m,
Basel surface energy, $s_e = 90\ mJ/m^2$,
melting temperature of an infinite crystal, $T_m^o = 418.7\ K$,
melting temperature of the sample, T_m in K, and
heating rate, $\frac{dT}{dt}$ in K per second.

These data are often presented graphically with the crystal size distribution plotted versus the crystal thickness. A deconvolution of the thermogram indicated size of the major crystal components. All 12 polymer samples have been processed and compiled into material specific graphs which reveal the effects of heat treatment on the crystal makeup.

Figure 99 shows the crystal size distribution for HDPE. The HDPE-QC sample has a narrow crystal size distribution centered around 8.5 nm and upon annealing moves to a distribution centered around 15 nm with a boarder distribution. The HDPE-SC sample initially formed is centered around 14.5 and upon annealing forms a broad bi-modal distribution with the broadest peak centered at about 18.5 with a smaller peak at 11.5.

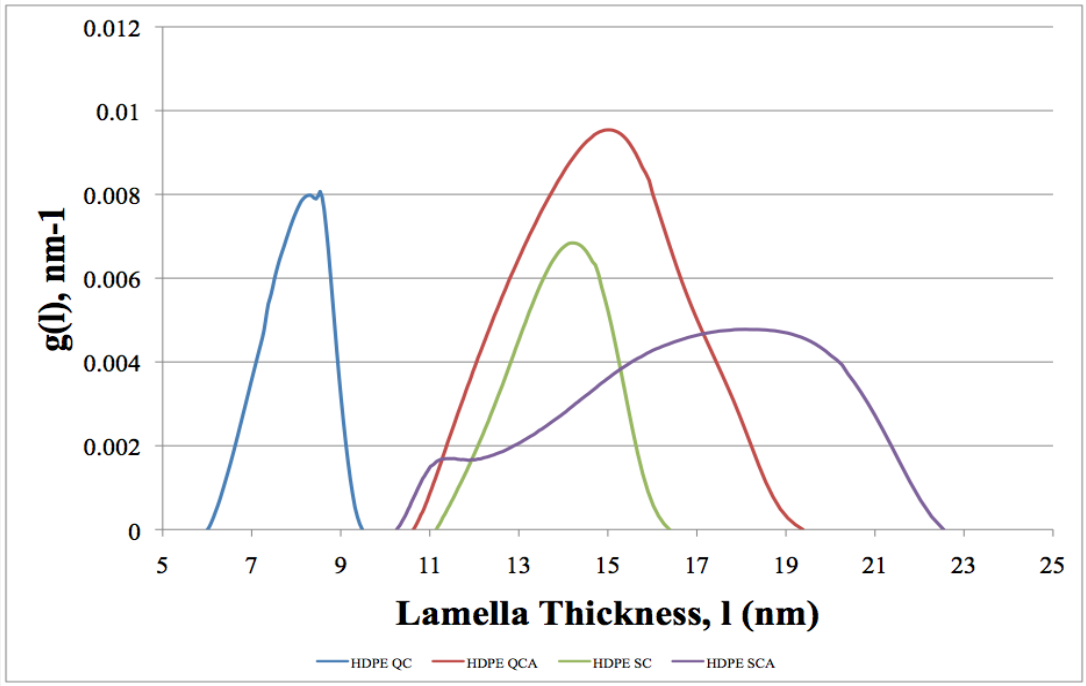

Figure 99. Crystal size distribution for HDPE.

The LDPE crystal distribution is shown in Figure 100. All of LDPE crystal distributions fall within a 3.5 nm range. The LDPE-QC is centered at 8.25 nm and upon annealing broadens and moves to 7.5 nm. The LDPE-SC is centered at 8 nm and upon annealing increases the distribution at 8 nm and forms a second peak centered at 6.5 nm indicating formation of a bi-modal distribution.

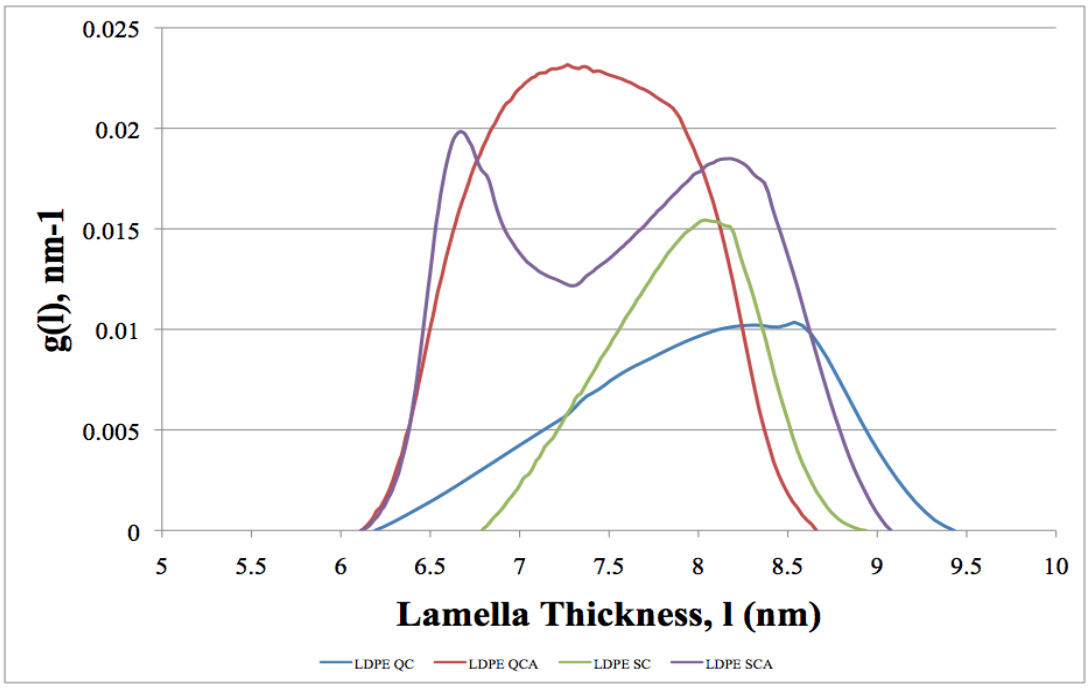

Figure 100. Crystal size distribution for LDPE.

The LLDPE crystal size distribution is shown in Figure 101. The crystal distribution of LLDPE-QC is very broad, almost 6.5 nm in width, with the main peak centered at 11.75 nm. Upon annealing the crystal size distribution shifts. The larger peak remains unaffected at 11.75 nm but the smaller crystal size at 9.25 nm increases by a factor of about 7. The LLDPE-SC has a distribution center around 12 nm but once annealed forms a bi-modal distribution centered at 12.25 and 8.75 nm indicating the formation of a bi-modal distribution through the formation of the smaller crystals.

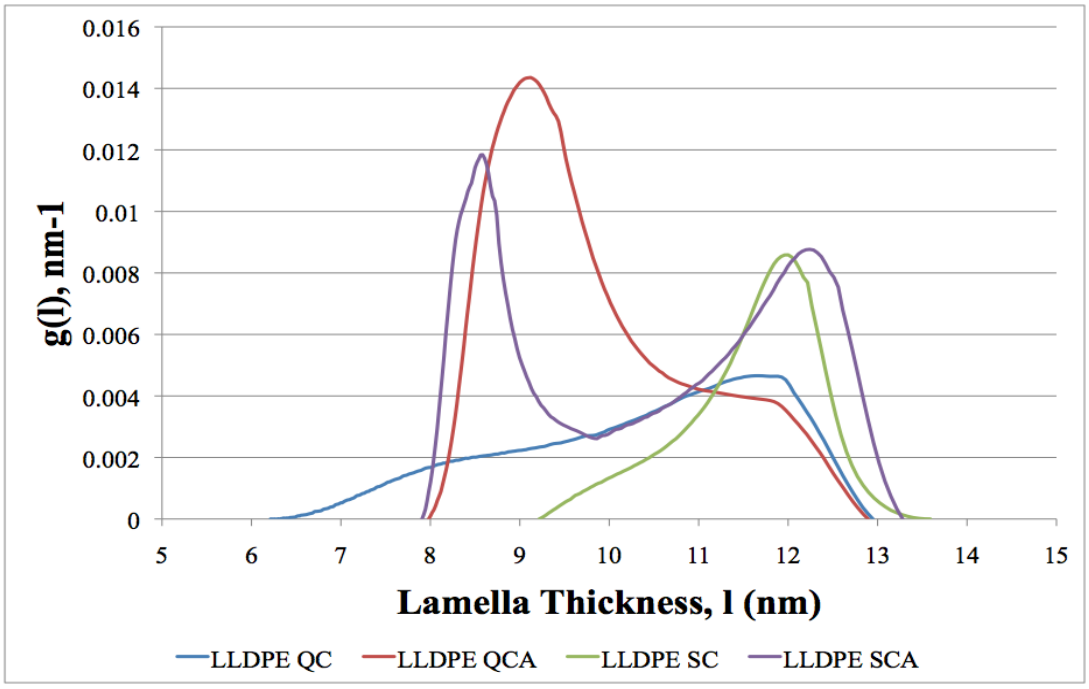

Figure 101. Crystal size distribution for LLDPE.

5.6 Small-Angle X-ray Scattering

Small -angle X-ray scattering (SAXS), was used to determine the long period of the crystalline phase. The *long period* is the spacing of the crystals and is calculated from Q_{max} obtained from SAXS. The equation used to calculate the spacing, Equation 22, follows:

Equation 22

$$L = \frac{2p}{Q_{\max}}.$$

Figure 102 through Figure 104 shows the SAXS data for LDPE, LLDPE, and HDPE respectively. Q_{max} is taken as the center of the peak and as Figure 102 shows Q_{max} progressively moves to lower values in the order of QC, QCA, SC, and SCA. Since L is a reciprocal function of Q_{max}, as Q_{max} gets smaller the long period increases.

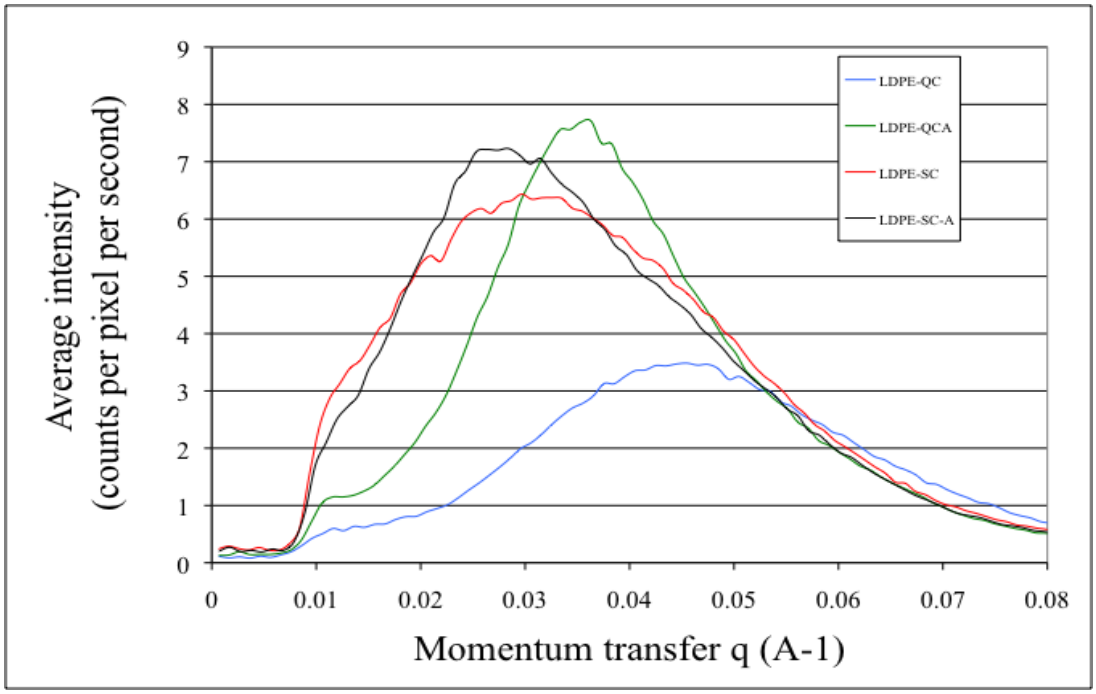

Figure 102. SAXS spectra of LDPE QC, QCA, SC, and SCA.

The same order of increasing long period was followed with the LLDPE as shown in Figure 103 indicating that the long period increases in the order of QC, QCA, SC, and SCA. Thus the crystal spacing increases with each consecutive process.

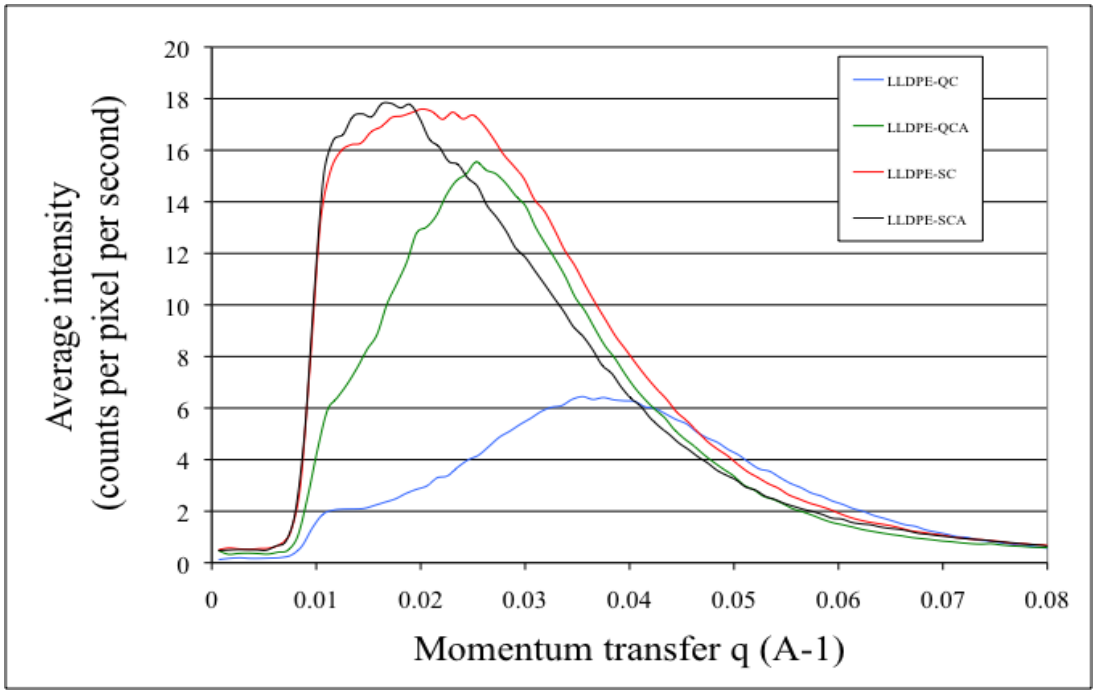

Figure 103. SAXS spectra of LLDPE QC, QCA, SC, and SCA.

The same order of increasing long period was followed in the HDPE samples.

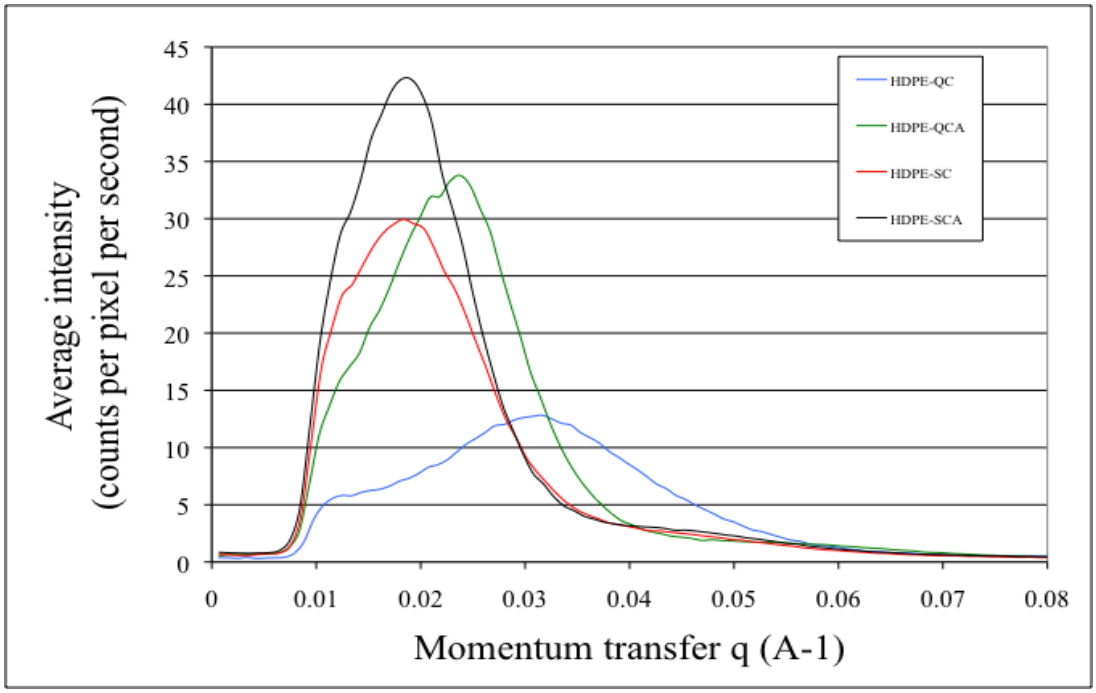

Figure 104. SAXS spectra of HDPE QC, QCA, SC, and SCA.

A more rigorous curve fit method was used for finding the center of the peak, Figure 105. With this method a better fit to the overall curve could be generated.

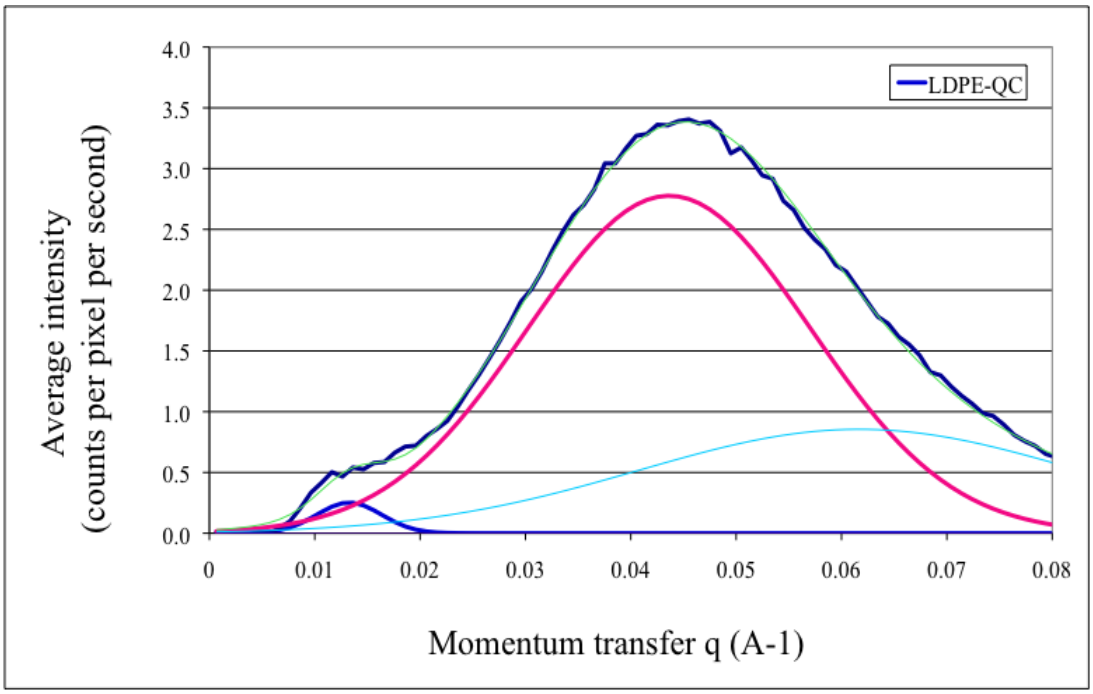

Figure 105. Determination of peak center by curve fitting.

Results from SAXS tests are compiled in Table 5 below with the calculated long period.

Table 5. Long period determined by SAXS.

	(q) = A-1	Long period (A)	% change in Long period
LDPE-QC	0.046	144.0	0.0
LDPE-QCA	0.035	178.0	23.6
LDPE-SC	0.031	210.8	46.4
LDPE-SCA	0.027	224.4	55.8
LLDPE-QC	0.037	169.8	0.0
LLDPE-QC-A	0.026	244.5	44.0
LLDPE-SC	0.020	299.2	76.2
LLDPE-SC-A	0.016	365.3	115.1
HDPE-QC	0.032	202.7	0.0
HDPE-QCA	0.024	269.7	33.1
HDPE-SC	0.018	342.4	68.9
HDPE-SCA	0.018	339.6	67.5

The long period as a function of processing method is shown in Figure 106 and as percent change in Figure 107. As Figure 106 shows the long period has an almost linear increase as a function of processing method for all 3 materials with the exception of HDPE-SCA which is essentially unchanged from the SC.

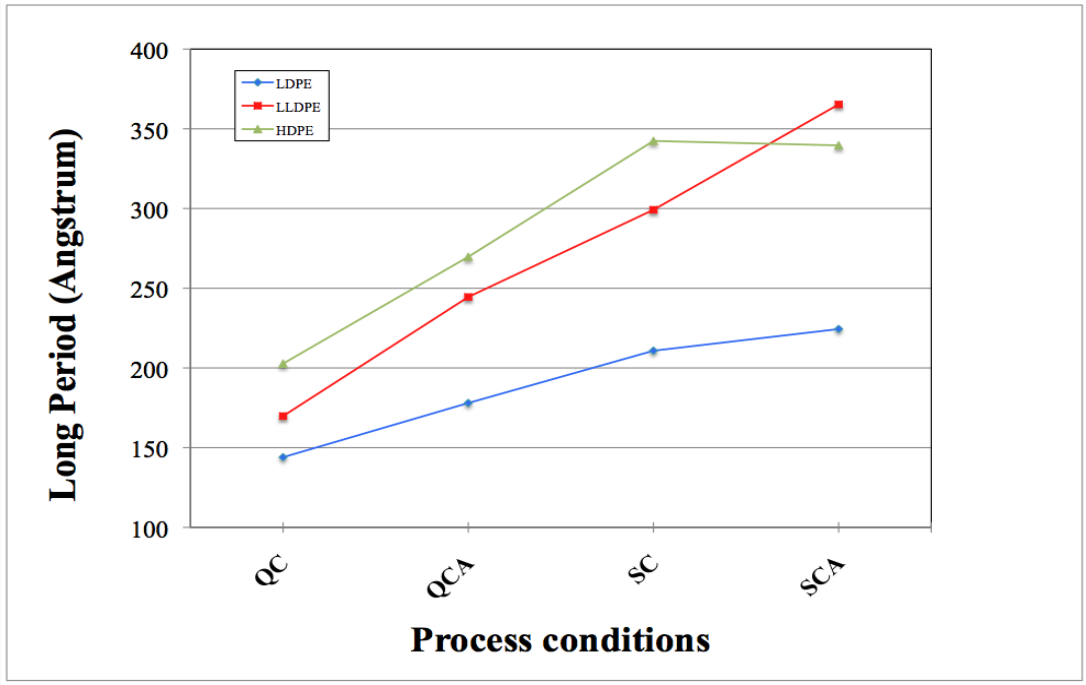

Figure 106. Long period as function of processing conditions.

The percent change as shown in Figure 107 allows for comparison of the degree of change across all 3 materials for the same processing conditions. It shows the efficacy of the processing method to increase the size of the crystal formation.

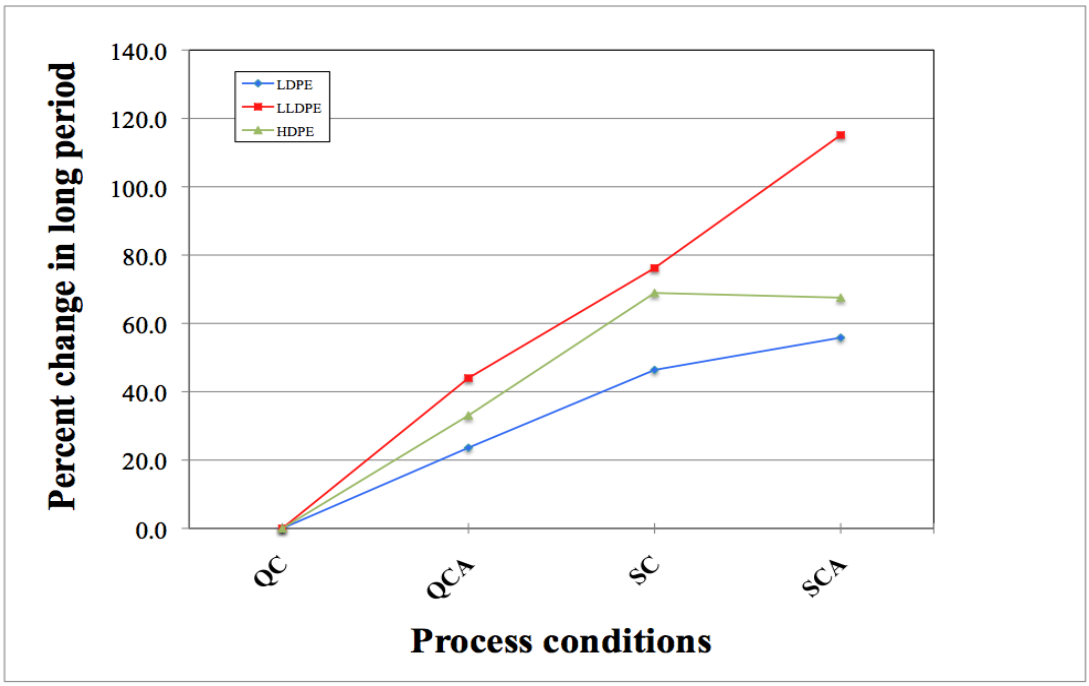

Figure 107. Percent change in long period as function of processing condition.

5.7 Wide-Angle X-ray Diffraction

Wide-angle X-ray diffraction (WAXD) data were taken. The amorphous peak is found at 2-Theta angle 20 degrees and the crystalline peaks at 21.6 and 24.3. The areas under each peak are used in Equation 17 to determine the degree of crystallinity.

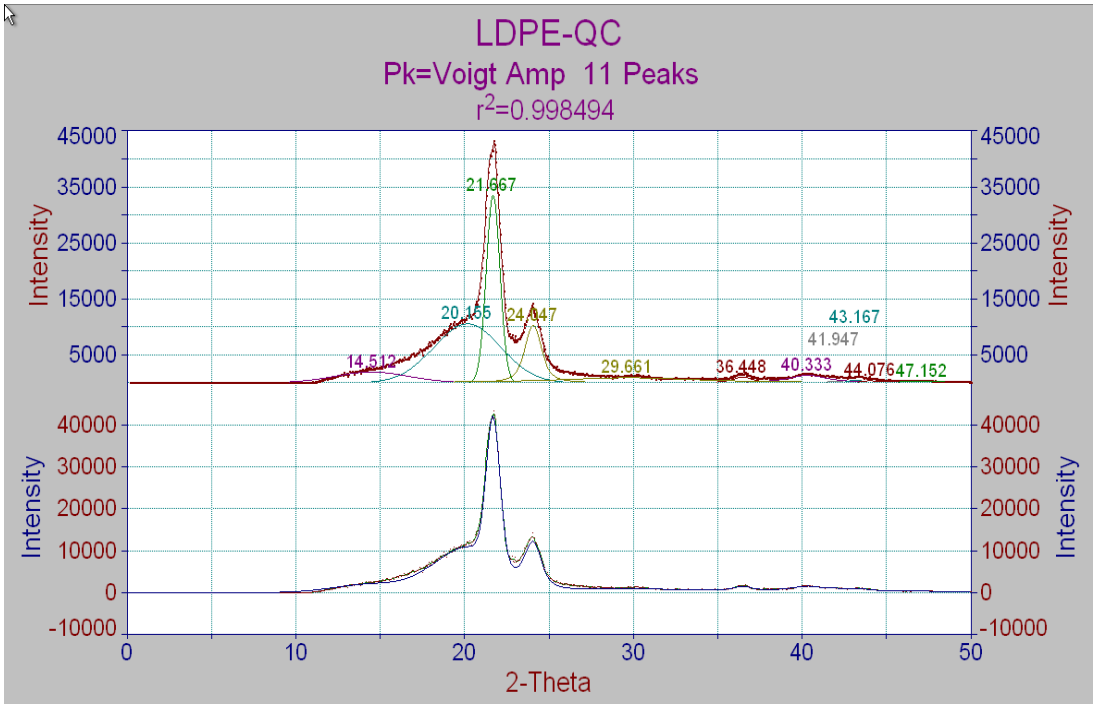

Figure 108. WAXD data for LDPE-QC

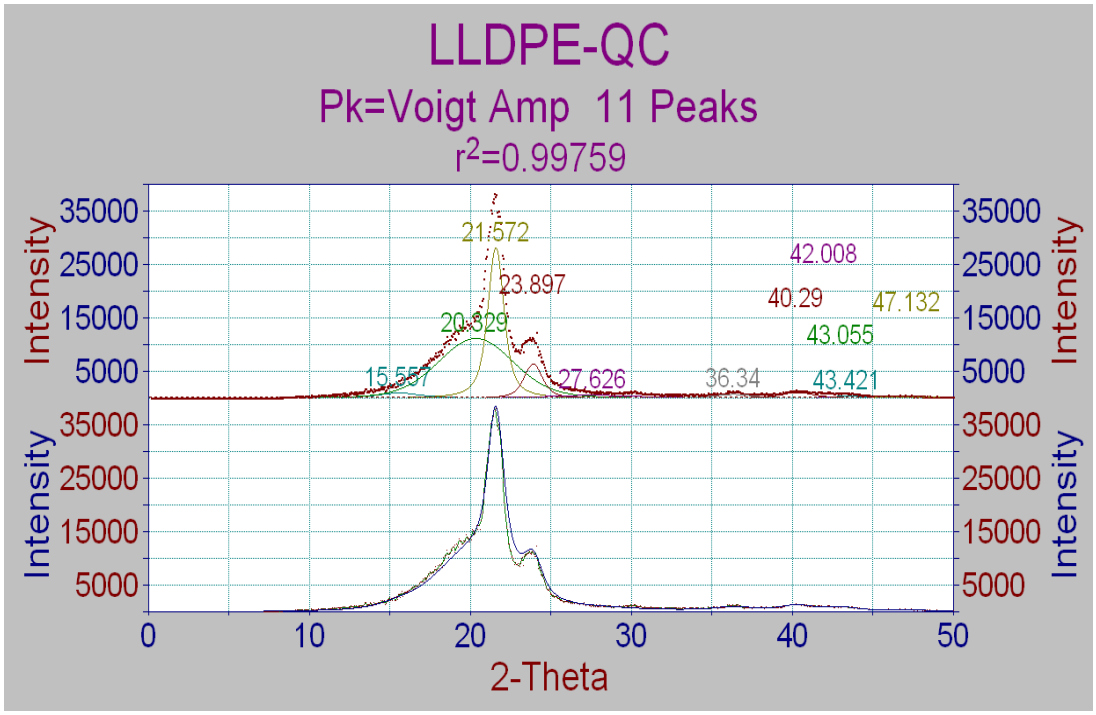

Figure 109. WAXD data for LLDPE-QC

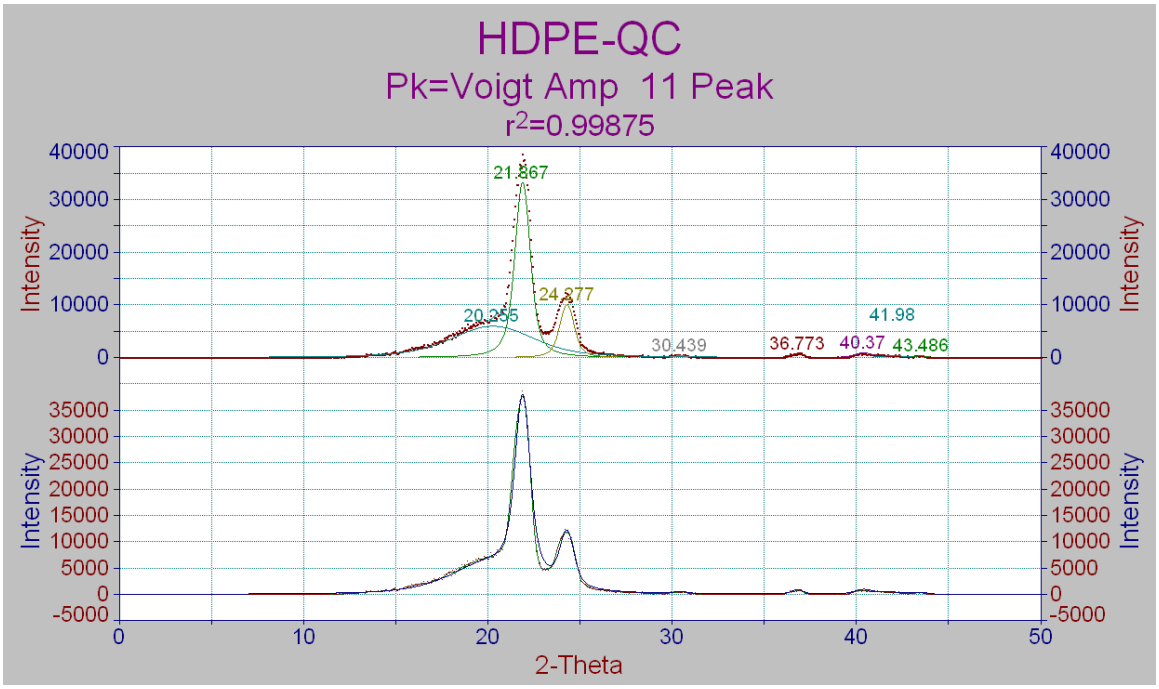

Figure 110. WAXD data for HDPE-QC

5.8 Variable Temperature Wide-Angle X-ray Diffraction

Variable temperature wide-angle X-ray diffraction (VT-WAXD) data were taken at temperatures from 20 to 60°C in 5°C increments on all samples. From these measurements lattice parameters *a*, *b*, and *c* were determined at each temperature using 110, 200, and 011 plane reflections at 2θ angles of 21.6, 24.3, and 39.75, respectively. Mark lists the lattice parameters as *a*=0.74069 nm, *b*=0.49491 nm, *c*=0.25511 nm.[73] These lattice parameters were then used to calculate the changes to the crystal lattice and how they impact the change in the crystal's volume as a function of temperature.

[73] James E. Mark, *Physical properties of polymer handbook* (New York: Springer, 2006).

Table 6 shows data generated from the measured values for LDPE-QC. A review of the data shows the largest change of the a-lattice parameter was 0.0034 nm, or 0.46%; b-lattice parameter was 0.0096 nm, or 2.04%; and the c-lattice parameter was 0.0023, or 0.86%. Data tables for the remaining samples can be found in Appendix C.

The LDPE-QCA data found in shows it to have changes in the a-lattice parameter of 0.0039 nm, or 0.52%; b-lattice parameter of 0.0116 nm, or 2.46%; and the c-lattice parameter of 0.0027, or 1.03%.

The LDPE-SC sample, found in , had lattice changes in the a-lattice parameter of 0.0057 nm, or 0.76%; b-lattice parameter of 0.0238 nm, or 5.03%; and the c-lattice parameter of 0.0028, or 1.10%.

The LDPE-SCA sample, found in , showed lattice changes in the a-lattice parameter of 0.0054 nm, or 0.72%; b-lattice parameter of 0.0139 nm, or 2.96%; and the c-lattice parameter of 0.0014, or 0.55%.

The LLDPE-QC sample, found in , had lattice changes in the a-lattice parameter of 0.0044 nm, or 0.59%; b-lattice parameter of 0.0111 nm, or 2.38%; and the c-lattice parameter of 0.0024, or 0.92%.

The LLDPE-QCA sample, found in , had lattice changes in the a-lattice parameter of 0.0037 nm, or 0.49%; b-lattice parameter of 0.0108 nm, or 2.30%; and the c-lattice parameter of 0.0023, or 0.89%.

The LLDPE-SC sample, found in , had lattice changes in the a-lattice parameter of 0.0021 nm, or 0.28%; b-lattice parameter of 0.0085 nm, or 1.81%; and the c-lattice parameter of 0.0021, or 0.79%.

The LLDPE-SCA sample, found in , had lattice changes in the a-lattice parameter of 0.0026 nm, or 0.34%; b-lattice parameter of 0.0170 nm, or 3.62%; and the c-lattice parameter of 0.0024, or 0.93%.

The HDPE-QC sample, found in , had lattice changes in the a-lattice parameter of 0.0061 nm, or 0.82%; b-lattice parameter of 0.0008 nm, or 0.16%; and the c-lattice parameter of 0.0008, or 0.33%.

The HDPE-QCA sample, found in , had lattice changes in the a-lattice parameter of 0.0052 nm, or 0.70%; b-lattice parameter of 0.0008 nm, or 0.16%; and the c-lattice parameter of 0.00010, or 0.38%.

The HDPE-SC sample, found in , had lattice changes in the a-lattice parameter of 0.0070 nm, or 0.95%; b-lattice parameter of 0.0008 nm, or 0.17%; and the c-lattice parameter of 0.0006, or 0.26%.

The HDPE-SCA sample, found in , had lattice changes in the a-lattice parameter of 0.0070 nm, or 0.94%; b-lattice parameter of 0.00112 nm, or 0.22%; and the c-lattice parameter of 0.0010, or 0.39%.

Table 6. VT-WAXD values for LDPE QC

Temp	2Θ (21.6)	2Θ (24.3)	2Θ (39.75)	a (nm)	b (nm)	c (nm)	V_c (cm^3)	ρ (kg/m^3)
25								
30	22.303	23.746	39.321	0.7495	0.4708	0.2623	9.2562E-23	1.004
35	22.131	23.763	39.383	0.7490	0.4760	0.2609	9.3022E-23	1.000
40	22.112	23.747	39.347	0.7494	0.4764	0.2612	9.3247E-23	0.997
45	22.400	23.677	39.290	0.7516	0.4674	0.2632	9.2471E-23	1.005
50	22.333	23.700	39.384	0.7509	0.4695	0.2620	9.2386E-23	1.006
55	22.164	23.680	39.365	0.7515	0.4743	0.2614	9.3170E-23	0.998
60	22.067	23.652	39.337	0.7524	0.4770	0.2612	9.3731E-23	0.992
			Change	0.0035	0.0096	0.0022	1.344E-24	
			% change	0.46	2.04	0.86		

Temp	Intensity amorphous (20.0)	Intensity 110 (21.6)	Intensity 200 (24.3)	Degree of crystallinity
25				
30	85830.8	38402.6	8419.8	0.35
35	78220.7	40318.5	12434.2	0.40
40	93429.7	43975.5	8730.3	0.36
45	99217.4	32523.4	7042.3	0.29
50	103190.0	32971.8	6744.3	0.28
55	103190.0	32971.8	6744.3	0.28
60	96363.9	35045.4	8773.7	0.31

5.9 Variable Temperature / Density Gradient Column (VT-DGC)

Since the WTF was measured over a range of temperatures, a second set of measurements was made in which the density gradient column was reconstructed to measure the change in density also as a function of temperature. Calibration beads were then added, and the column was found to be uniform, as shown by a second-order curve fit with a correlation factor of 1.000 and a linear least-squares fit having a correlation factor of 0.990.

Figure 111 shows the initial location of the samples and calibration beads at 25°C after a 12-hour equilibration period. The temperature of the column was then changed in increments of 5°C at a rate of 1°C/6 min step from 20°C to 60°C. Each time the temperature was adjusted, the column was allowed to equilibrate for 12 hours before a reading of the samples' position. The reason the column's temperature was changed so slowly was to avoid disturbing the density gradient of the fluid with convection currents. Readings were continued for a total of six thermal cycles, over 51 days. Testing was discontinued when the column become nonlinear at the top.

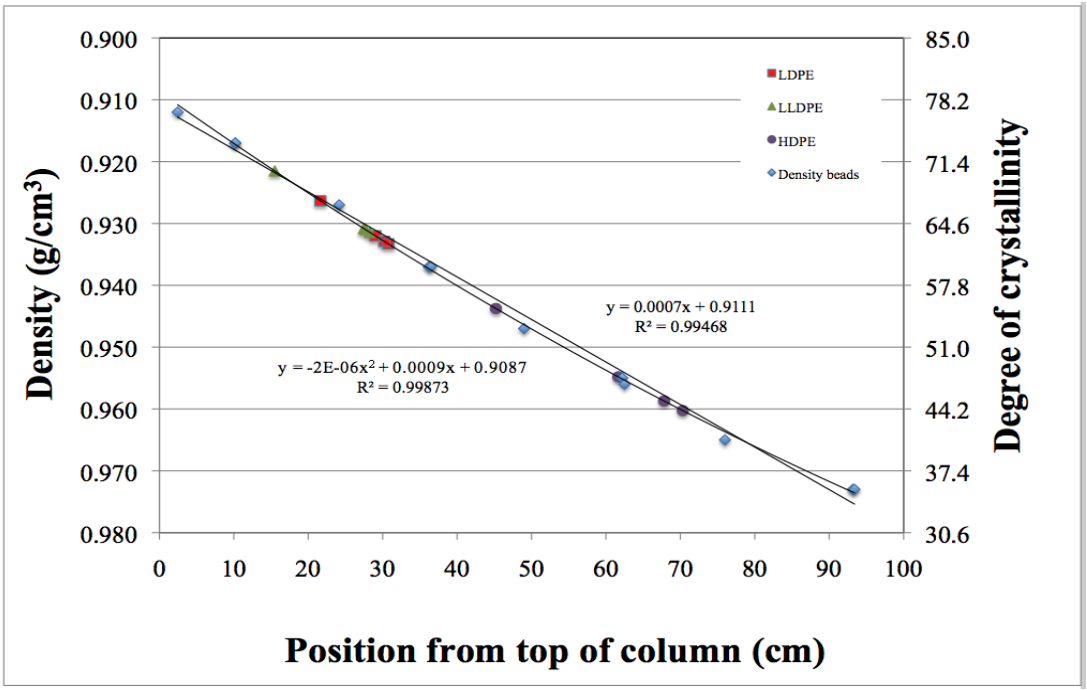

Figure 111. Initial reading of variable temperature differential gradient column at 25ºC.

The positions of all samples were recorded at 12-hour intervals and compiled in a database. Figure 112 shows HDPE quenched data for each thermal cycle and temperature. The degree of crystallinity shown is based on HDPE at 25°C; thus, it must be understood that this data is not proposing that the degree of crystallinity changes with temperature, just its density. The departure from linear behavior of the column is seen in the sixth down cycle, labeled HDPE QC 6D, at which point the test was terminated.

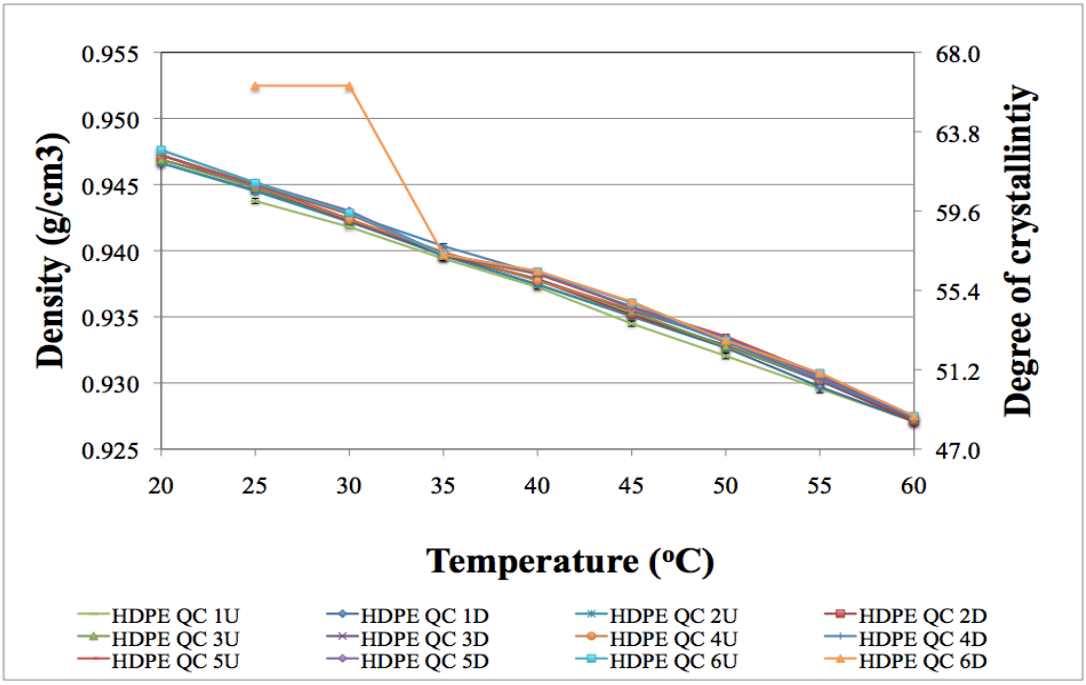

Figure 112. Thermal cycle data for HDPE QC.

To see trends across a material type with various heat treatments, data at 25°C and 60°C are shown in Figure 113 and Figure 114. In both figures the density and degree of crystallinity were essentially constant, indicating little change in structure. There are half as many data sets in the 60°C graphs as the 25°C graphs because the 25°C point is passed through twice in each cycle, once during the temperature increase and once during the temperature decrease, whereas the 60°C point is only passed through once in each cycle. Equivalent data sets for all samples are provided in Appendix B for the other samples. The density values at 25°C were chosen instead of the terminal temperature of 20°C because readings are made during decreasing and increasing heating processes to expose any hysteresis that might be stored in the material's structure. There appears to be no indication of such behavior. Table 7 and Table 8 have been provided for closer inspection of the values.

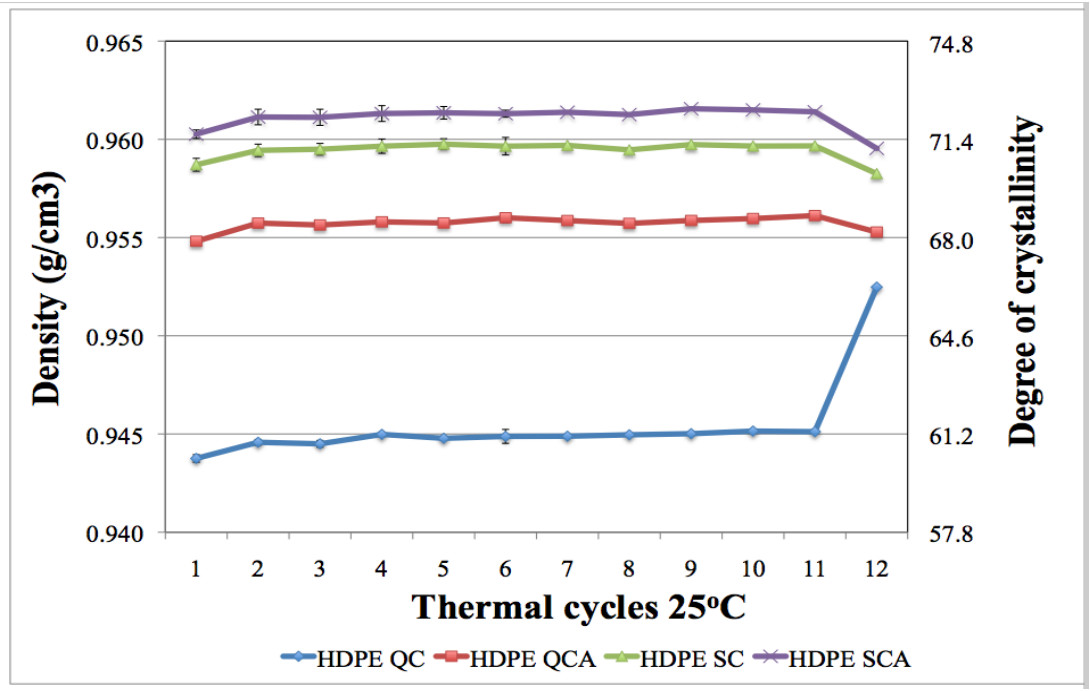

Figure 113. HDPE densities and degree of crystallinity as a function of heat treatment and thermal cycling at 25°C.

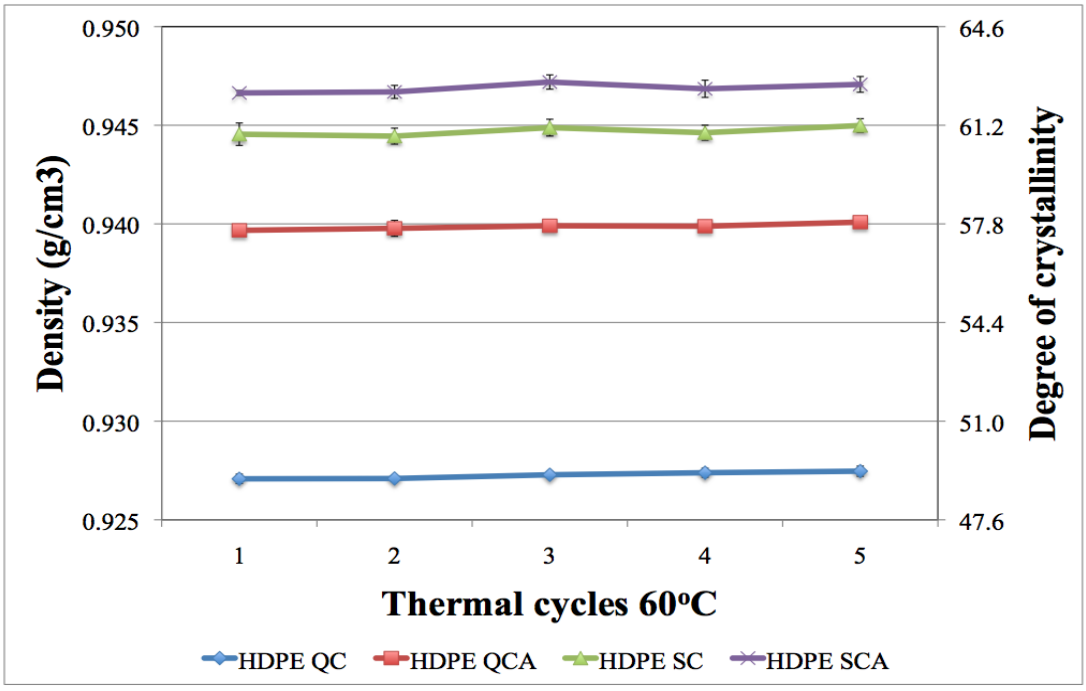

Figure 114. HDPE densities and degree of crystallinity as a function of heat treatment and thermal cycling at 60°C.

Figure 115 shows the results from all 12 samples. Error bars are provided to indicate the standard deviation for each material at each temperature. As the error bars indicate all 12 samples had similar consistent results throughout the testing. There was no evidence that any of the heat treatments of any of the materials produced any other performance. The only error bars that were not insignificant in size was the HDPE QC which indicated the deviation of the column when the test was terminated.

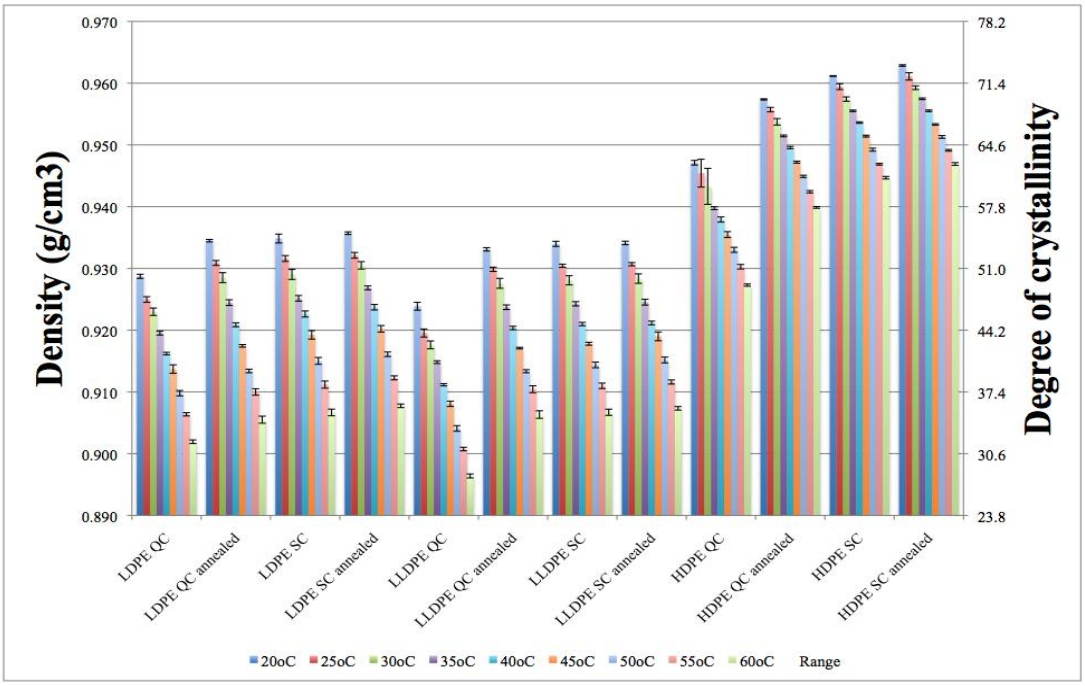

Figure 115. Collective density data for polyethylene samples with standard deviation.

Table 7. Densities and degree of crystallinities for LDPE, LLDPE, and HDPE determined by VT-DGC at 25ºC

		1U	1D	2U	2D	3U	3D	4U	4D	5U	5D	6U	6D
Density Measurements (g/cm^3) Degree of Crystallinity	LDPE QC	0.926	0.925	0.925	0.925	0.925	0.925	0.925	0.925	0.925	0.925	0.925	0.925
		48.5	47.5	47.7	47.5	47.5	47.5	47.5	47.7	47.5	47.3	47.5	47.4
	LDPE QC annealed	0.932	0.931	0.931	0.931	0.931	0.931	0.931	0.931	0.931	0.931	0.931	0.931
		52.4	51.7	51.7	51.6	51.7	51.6	51.4	51.6	51.5	51.4	51.4	51.7
	LDPE SC	0.933	0.932	0.932	0.932	0.932	0.931	0.931	0.931	0.931	0.931	0.931	0.931
		53.0	52.2	52.3	52.1	52.2	52.0	52.0	52.0	51.9	51.8	51.8	52.0
	LDPE SC annealed	0.933	0.932	0.932	0.932	0.932	0.932	0.932	0.932	0.932	0.932	0.932	0.932
		53.3	52.7	52.7	52.5	52.6	52.4	52.3	52.4	52.3	52.2	52.1	52.3
	LLDPE QC	0.922	0.919	0.919	0.919	0.919	0.919	0.919	0.920	0.919	0.920	0.920	0.919
		45.2	43.7	43.8	43.7	43.6	43.8	43.6	44.1	43.8	43.9	43.9	43.8
	LLDPE QC annealed	0.931	0.930	0.930	0.930	0.930	0.930	0.930	0.930	0.930	0.930	0.930	0.930
		51.6	50.8	51.0	50.7	50.7	50.8	50.8	51.0	50.9	50.9	50.9	51.1
	LLDPE SC	0.931	0.930	0.931	0.930	0.930	0.930	0.930	0.930	0.930	0.930	0.930	0.930
		51.7	51.3	51.6	51.3	51.3	51.3	51.2	51.2	51.3	51.1	51.2	51.3
	LLDPE SC annealed	0.931	0.931	0.931	0.931	0.931	0.931	0.930	0.931	0.931	0.930	0.931	0.931
		52.0	51.5	51.5	51.4	51.5	51.4	51.3	51.5	51.4	51.3	51.5	51.5
	HDPE QC	0.944	0.945	0.944	0.945	0.945	0.945	0.945	0.945	0.945	0.945	0.945	0.952
		60.4	60.9	60.9	61.2	61.1	61.1	61.1	61.2	61.2	61.3	61.3	66.3
	HDPE QC annealed	0.955	0.956	0.956	0.956	0.956	0.956	0.956	0.956	0.956	0.956	0.956	0.955
		67.9	68.5	68.5	68.6	68.5	68.7	68.6	68.5	68.6	68.7	68.8	68.2
	HDPE SC	0.959	0.959	0.959	0.960	0.960	0.960	0.960	0.959	0.960	0.960	0.960	0.958
		70.5	71.0	71.1	71.2	71.3	71.2	71.2	71.1	71.2	71.2	71.2	70.2
	HDPE SC annealed	0.960	0.961	0.961	0.961	0.961	0.961	0.961	0.961	0.962	0.961	0.961	0.960
		71.6	72.2	72.2	72.3	72.3	72.3	72.4	72.3	72.5	72.4	72.4	71.1

The top row of Table 7 indicates the nature of the thermal cycling when the readings were recorded. The notation gives the cycle number, 1 to 6, and whether the column was being heated up (U) or being cooled down (D). Each data set shows the density and corresponding degree of crystallinity for each material at each thermal cycle. A quick review of the data shows how stable the values are for all materials over all thermal cycles. Likewise Table 8 shows the equivalent data but at the 60°C.

Table 8. Density and degree of crystallinity for LDPE, LLDPE, and HDPE determined by VT-DGC at 60ºC

		1	2	3	4	5	6
Density Measurements (g/cm^3) Degree of Crystallinity	LDPE QC	0.901 31.5	0.902 31.9	0.902 32.0	0.902 32.1	0.902 32.0	0.902 32.0
	LDPE QC annealed	0.905 33.9	0.905 34.0	0.905 34.2	0.906 34.6	0.906 34.7	0.906 34.9
	LDPE SC	0.906 34.7	0.906 34.8	0.907 35.1	0.907 35.3	0.907 35.4	0.907 35.6
	LDPE SC annealed	0.907 35.6	0.908 35.8	0.908 35.8	0.908 36.0	0.908 36.0	0.908 36.1
	LLDPE QC	0.896 27.7	0.896 28.2	0.897 28.4	0.897 28.3	0.896 28.2	0.896 28.2
	LLDPE QC annealed	0.906 34.4	0.906 34.6	0.906 34.7	0.906 35.0	0.907 35.4	0.907 35.5
	LLDPE SC	0.906 34.7	0.906 34.8	0.907 35.2	0.907 35.3	0.907 35.5	0.907 35.6
	LLDPE SC annealed	0.907 35.3	0.907 35.5	0.907 35.5	0.907 35.7	0.907 35.7	0.908 35.9
	HDPE QC	0.927 49.0	0.927 49.0	0.927 49.2	0.927 49.2	0.927 49.3	0.927 49.3
	HDPE QC annealed	0.940 57.6	0.940 57.7	0.940 57.8	0.940 57.7	0.940 57.9	0.940 57.8
	HDPE SC	0.945 60.9	0.944 60.8	0.945 61.1	0.945 61.0	0.945 61.2	0.945 61.0
	HDPE SC annealed	0.947 62.3	0.947 62.4	0.947 62.7	0.947 62.5	0.947 62.6	0.947 62.6

5.10 Small-Angle Light Scattering (SALS)

Polyethylene samples were examined using small-angle light scattering (SALS) as a tool to probe the supermolecular crystalline structure. Those results are shown below as images of the SALS patterns for each material and its various heat treatments. Figure 116 presents four LDPE images. The LDPE-QC and LDPE-QCA images show a random H pattern. Conversely, the LDPE-SC and LDPE-SCA images show spherulitic B patterns with the annealed sample's being slightly more distinct. The next four images of LLDPE are found in Figure 117. Contrary to the LDPE this material formed spherulites when quenched and when quenched and annealed, but it did not form spherulites during SC or SCA. The HDPE samples all show signs of spherulitic structure. Inspection of the images shows a progression in organized structure from the QC => QCA => SC => SCA. Figure 118 shows the HDPE-QC and HDPE-QCA materials both with C pattern, whereas the HDPE-SC and SCA samples each show a type B pattern.

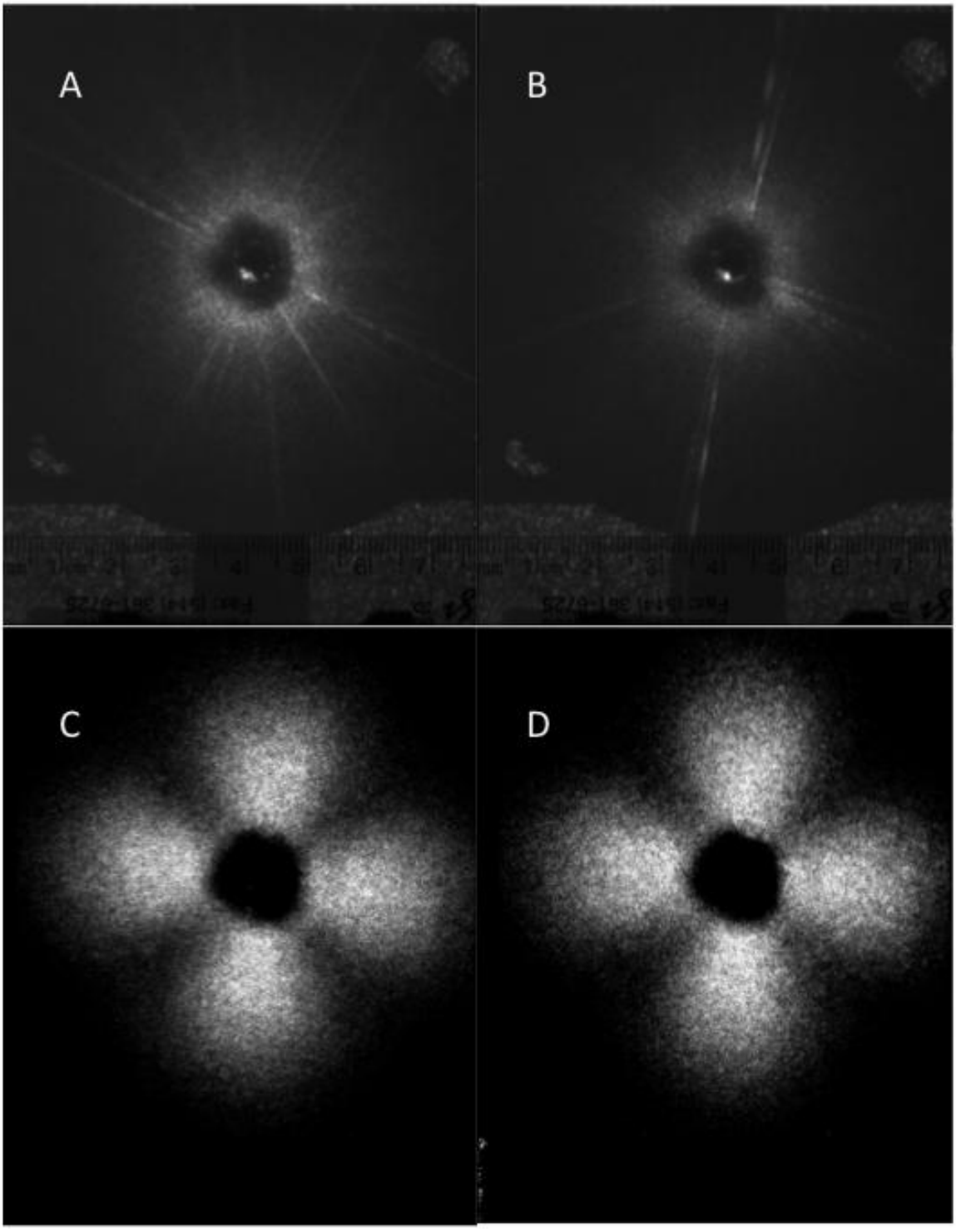

Figure 116. SALS image of (A) LDPE-QC, (B) LDPE-QCA, (C) LDPE-SC, and (D) LDPE-SCA.

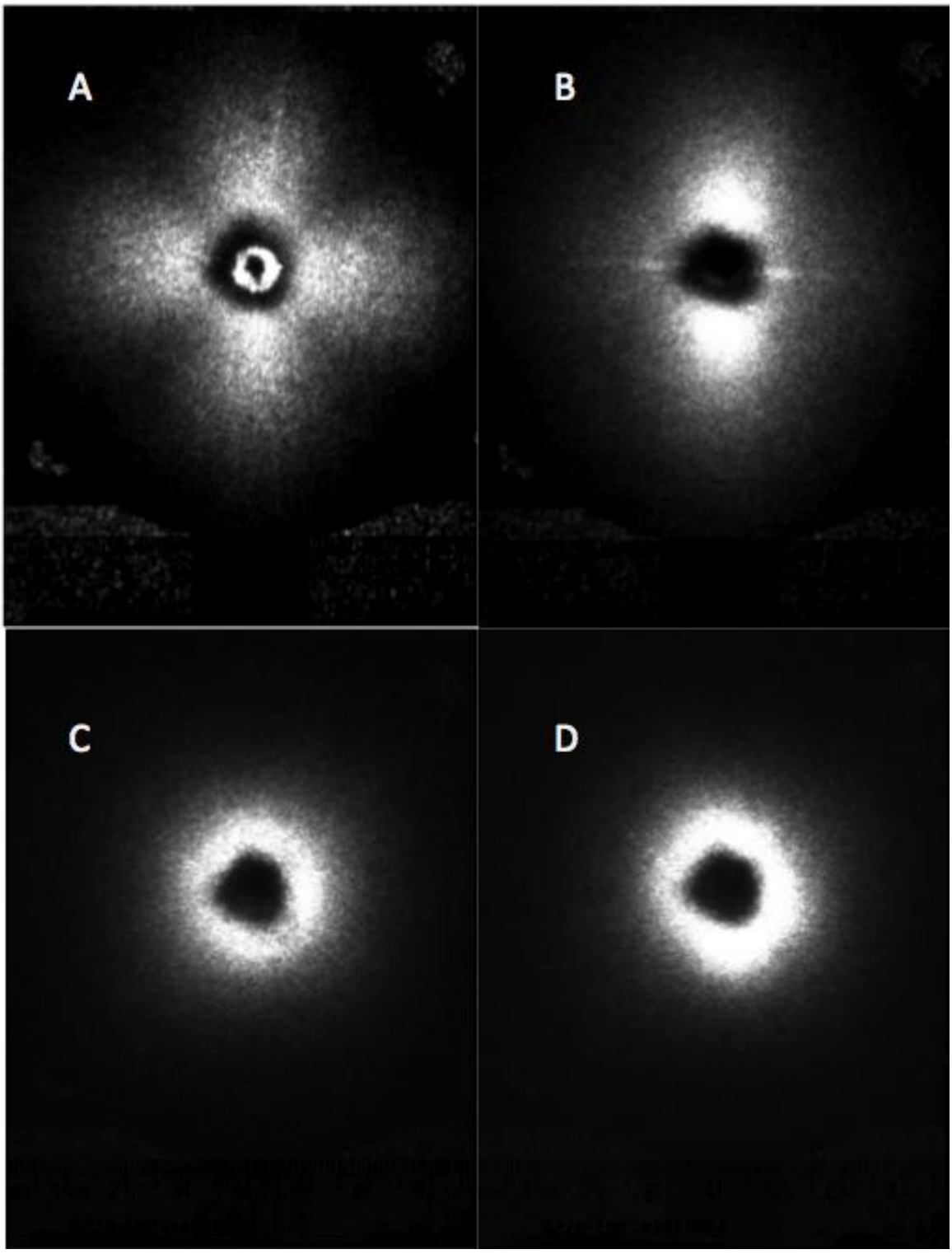

Figure 117. SALS image of (A) LLDPE-QC, (B) LLDPE-QCA, (C) LLDPE-SC, and (D) LLDPE-SCA.

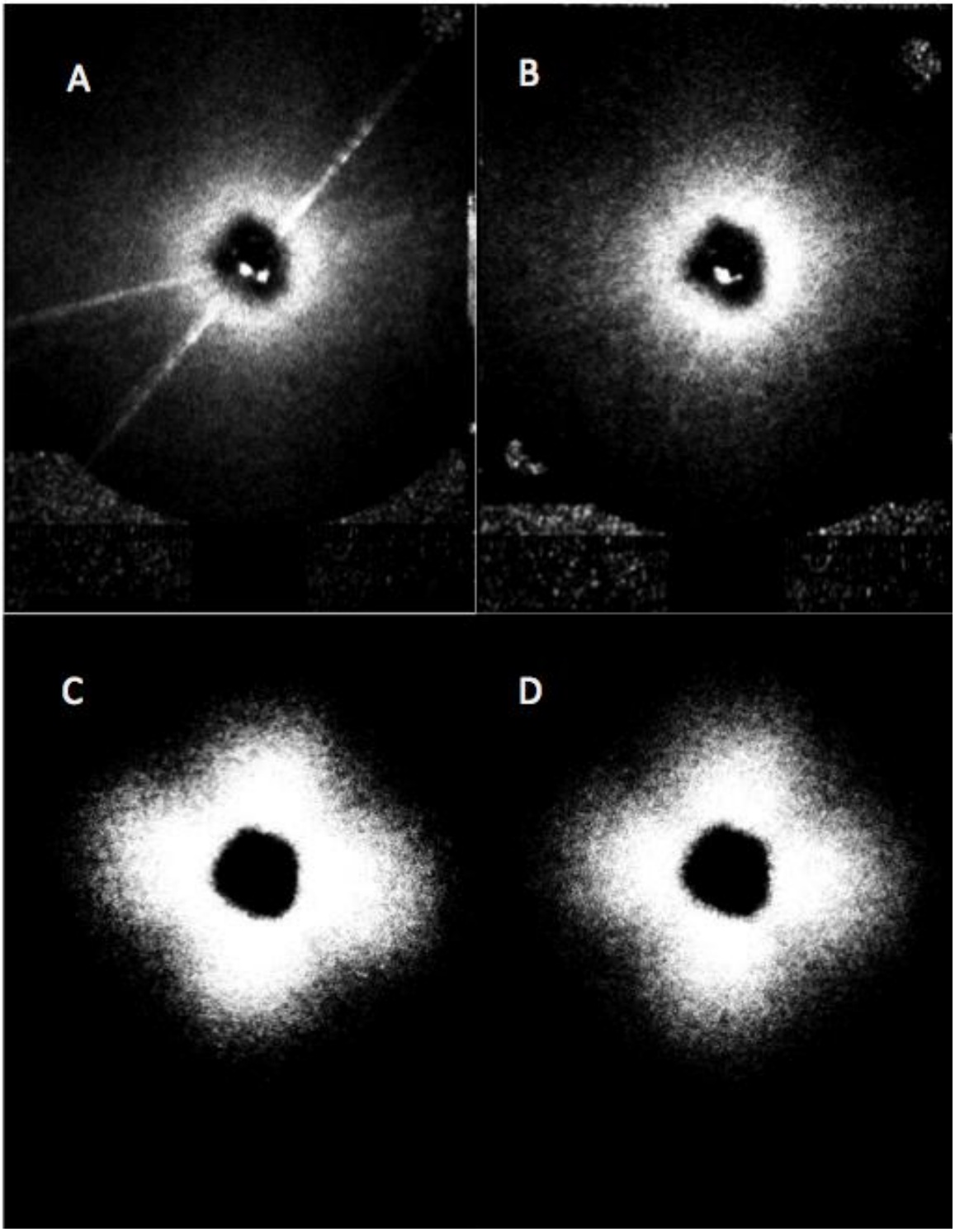

Figure 118. SALS image of (A) HDPE-QC, (B) HDPE-QCA, (C) HDPE-SC, and (D) HDPE-SCA.

Through the use of ImageJ software the images of the spherulitic structures were analyzed. The spherulites were measured to find the radial distance of the maximum intensity. The spherulite size can be found in Table 12.

5.11 Scanning Electron Microscopy

Samples of each material were etched and analyzed by scanning electron microscopy (SEM). Mandelkern and Benson have shown the spherulite pattern corresponding to the SALS pattern. They also showed that the rod and random patterns have similar SALS images and require etching and SEM imaging to differentiate between them. The etching process was able to show the rod structure of the LLDPE-QCA and SCA, as Figure 119 and Figure 120 show rod structures correspond to the H patterns in the SALS images.[74] It should be noted that the etching process removes the amorphous phase, leaving the crystalline phase.[75] [76] When the images of the QCA and SCA are compared, it is clear that the QCA possesses much larger channels of amorphous phase.

Random patterns also known as H patterns appear in the SALS images and can take several different forms as seen in the crystalline structure of the LLDPE-SC and LDPE-QC. Figure 121 and Figure 122 shows the SEM image of the etched LLDPE-SC and LDPE QC sample. These two images show the scale of the structure to vary a great extent. Both of these images show the rod-like structure of LLDPE-SC and LLDPE-QC.

[74] Roberto Benson, dissertation, 1978, Florida State University, Tallahassee, Fl.
[75] Olley and Bassett, "An improved permanganic etchant for polyolefines."
[76] Naylor and Phillips, "Optimization of permanganic etching of polyethylenes for scanning electron microscopy."

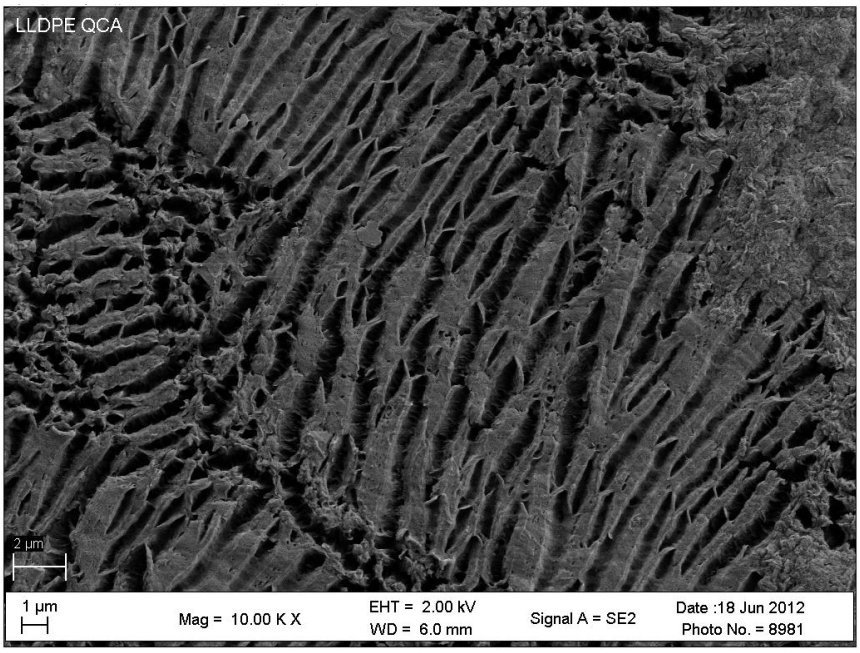

Figure 119. SEM image of LLDPE-QCA showing a rod-like pattern D.

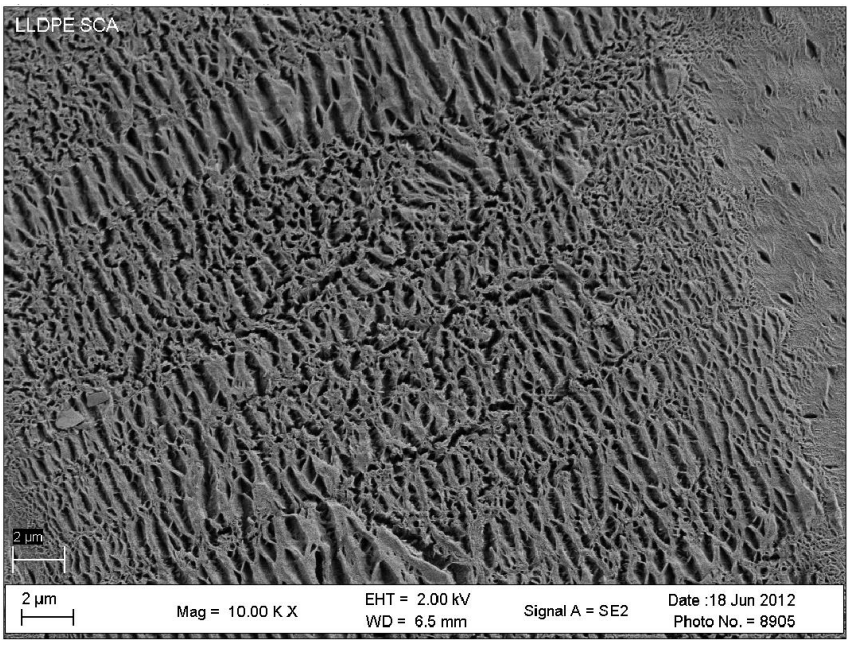

Figure 120. SEM image of LLDPE-SCA showing a rod-like pattern D.

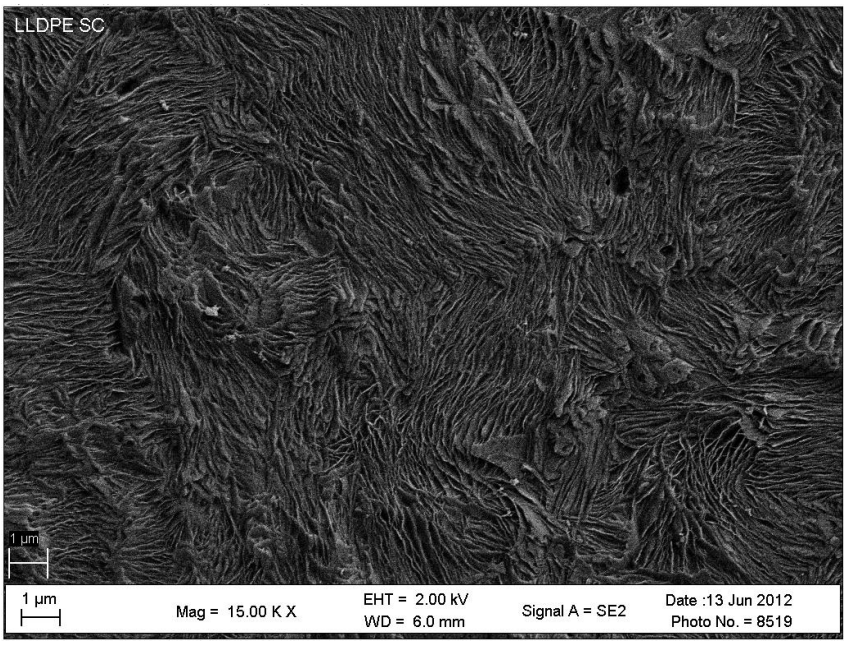

Figure 121. SEM image of LLDPE-SC showing a random-like pattern H.

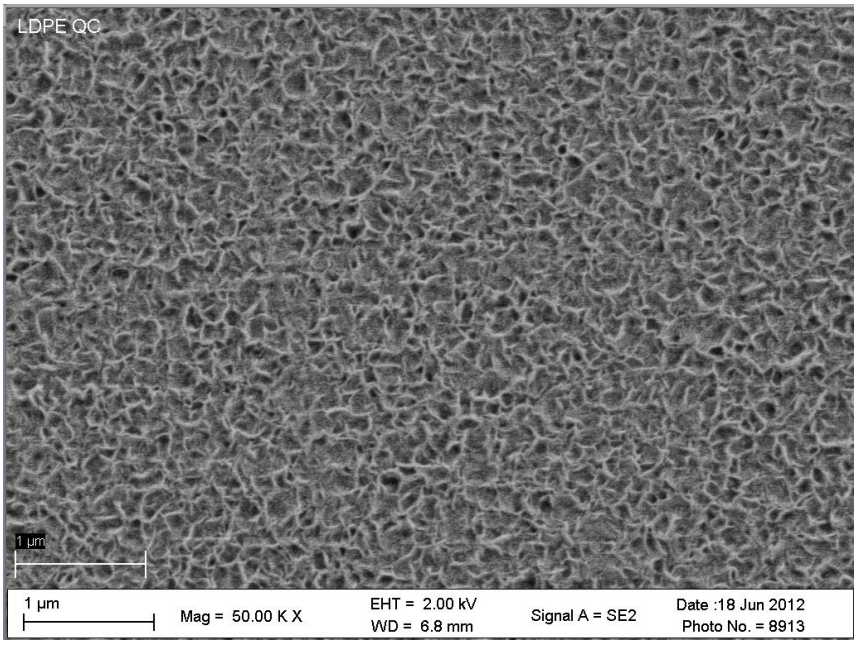

Figure 122. SEM image of LDPE-QC showing a random-like pattern H.

Chapter 6 Discussion

Since the earliest recorded observation of permeation by Nollet, researchers have been trying to understand the mechanism by which Water Transport Flux (WTF) occurs, how to predict it, and how to control it. This also is the pursuit in this study. The material selection and sample fabrication will first be discussed, followed by the WTF testing, then the polymer characterization testing, and finally the comparison of the data to determine possible correlation between the morphology and WTF.

Three polyethylenes — low density polyethylene (LDPE), linear low density polyethylene (LLDPE), and high density polyethylene (HDPE) — were each formed into thin films by melt pressing. Four samples from each material were subjected to different heat treatments. These heat treatments were quenched (QC), quench annealed (QCA), slow cooled (SC), and slow cooled annealed (SCA). Each of these samples was tested to determine their WTF. All samples were tested in a test cell, shown in Figure 11.

6.1 Water Transport Flux Through LLDPE

The LLDPE-QC water transport behavior (WTF) is shown in Figure 43 through Figure 46. The WTF rapidly responds to temperature changes from 20 to 60°C and quickly settles to a new rate at each temperature plateau. Each WTF is maintained until the next temperature change. All other samples will be compared with this one as the discussion progresses. The WTF is expressed in units of mass (g/min in^2) as a function of time as shown in Figure 43 and the same data expressed in frost point (°C) as a function of time appears in Figure 44, each plotted in blue referencing the left y-axis. Also plotted in each of these graphs is the sample temperature ranging from 20°C to 60°C in 10°C steps, drawn in red, referencing the right y-axis. These two different figures represent the same data, presented in different units. The mass WTF is more widely recognized but exponential with respect to temperature changes, as evident in the varying step size in response to the uniform temperature step size. On the other hand, when the data are plotted as frost point, the WTF step size is uniform with respect to sample temperature step size.

When the WTF is plotted as frost point versus sample temperature, as shown in Figure 44, the uniform step sizes of both frost point WTF and sample temperature produces a straight line linear relationship. As will be become more evident later this straight line linear relationship indicates

that the sample reached a steady state WTF. The data is then fitted with a least squares line showing the correlation factor to provide a measure of the linearity, as shows Figure 45. By plotting the frost point WTF and sample temperature in this manner, nonlinear behaviors from one cycle to the next become clear, as seen in the first cycle. In addition to becoming linear as the sample approaches a stable and reproducible WTF, the plot typically will move from an upwardly cupped non-linear curve with a positive slope to a straight line and moves down in WTF at all testing temperatures. This will become more prominent in later samples. The linear response has been named the *ultimate linear behavior* (ULB). This sample was tested over four thermal cycles, and by the fourth cycle the material attained ULB with the correlation factor $R^2 = 0.9996$. Referring back to Figure 44, additional signs of WTF stability in this sample is the flat response during the 24-hour 60°C soak and very flat response at each plateau temperature. It will be shown in later samples that once a sample has reached ULB that the subsequent thermal cycles are also linear and do not change in WTF.

An alternate representation of these data is in Figure 46, where the plot shows the WTF in frost point at common plateau temperatures as a function of thermal cycle. Inspection of this plot shows that the distance between each value of WTF achieves equal spacing and a horizontal profile in latter cycles. Thus, the WTF has reached a steady state. The approach to linear behavior will become more dramatic in subsequent samples and discussed in a later section.

It should be noted that most WTF data is presented as permeation rates in the literature and are provided at one testing temperature of interest to the researcher, e.g., 20°C, whereas this test method was conducted over multiple thermal cycles and a range of temperatures. Each representation provides insights into the changing WTF behavior of the material. The final WTF at ULB of all samples will be compared to literature values later.

The WTF behavior of LLDPE-QCA, is presented in Figure 48 through Figure 51. This sample responded very similarly to the LLDPE-QC in that it achieved ULB in 4 cycles, but some instability appears as overshoot before settling. The instability is manifested in a slower decay in the WTF over the 24-hour 60°C soak and some noise at each plateau temperature. The noise is more evident at the higher temperatures, and the sample eventually achieved a ULB correlation of $R^2 = 0.9996$, the same as the LLDPE-QC. Comparison of Figure 44 for the LLDPE-QC and Figure 49 for the LLDPE-QCA shows that annealing the quenched sample leads to slightly lower WTF than the QC at all tested temperatures.

The WTF behavior for LLDPE-SC is shown in Figure 52 through Figure 55. Upon inspection of these graphs, it is obvious that the sample has a dramatically different WTF response compared to LLDPE-QC. During the 24-hour 60°C soak the WTF started high and progressively dropped and did not reach a steady state rate before thermal cycling began. The WTF at each plateau temperature also showed this behavior and only achieved ULB after eight cycles. The ULB is more clearly seen in Figure 54 and Figure 55. The overall WTF of this sample is higher than either of LLDPE-QC or LLDPE-QCA. Thus, slow cooling must have caused morphological changes that result in an increased WTF and retardation in reaching the ULB. It will be shown later that this behavior in each of these samples can be explained through an evaluation of the morphology. As the morphology changes the amorphous pathway is either opened or closed promoting or restricting WTF. This is essentially a modification of the tortuosity of the amorphous pathway for water molecules or free volume.

The fourth sample of LLDPE to be discussed is the LLDPE-SCA, Figure 56 through Figure 59. This sample behaves more like the LLDPE-QC and QCA in that it rapidly achieved a constant WTF during the 24-hour 60°C soak, had a level WTF at each plateau temperature, and achieved ULB in five cycles. One significant deviation from the WTF of all three of the previous samples is that the plateau WTF started lower in the first 2 cycles and increased up to a ULB.

The ULB for all of the LLDPE samples are plotted in Figure 123. They all have similar WTF except for the LLDPE-SCA, which has a lower WTF. It should also be noted that all of the samples have similar slopes except for the LLDPE-SC, which has a slightly lower slope. As mentioned earlier it is believed all of these behaviors can be attributed to morphological changes that resulted from the heat treatments. The amorphous pathway has been modified through change in the crystalline structure or number of crystallites..

The slope and magnitude of the WTF is clearly a thermally driven response and inspection of Table 10 and Figure 101 may provide a insight into the controlling structural features. The initial population of crystals for the LLDPE-QC was centered at 11.75 nm and after annealing to produce the LLDPE-QCA the initial population was essentially unaffected but a new population of smaller crystals at 9.22 nm appeared. This smaller population is believed to increase tortuosity of the amorphous phase thus reducing WTF. On the other hand the LLDPE-SC larger crystals effect the slope and LLDPE-SCA smaller crystals the overall WTF.

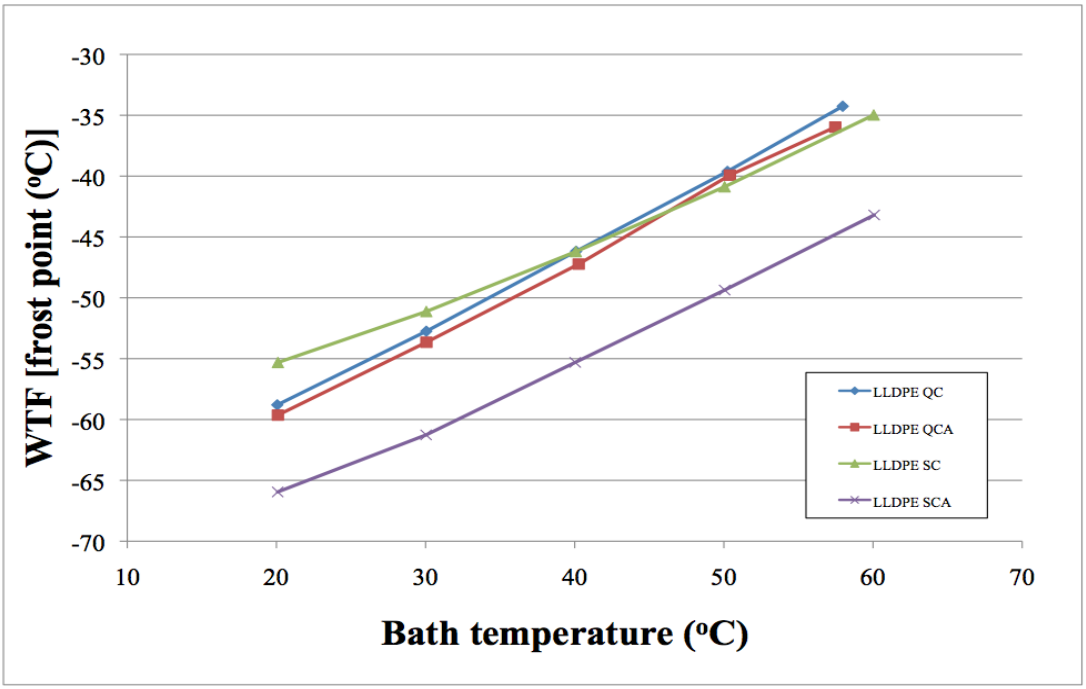

Figure 123, Comparison of WTF for LLDPE-QC, QCA, SC, and SCA

6.2 Water Transport Flux Through LDPE

The first of four LDPE samples to be discussed is the LDPE-QC, shown in Figure 60 through Figure 63. Upon inspection of figures it is immediately obvious that the WTF has a declining slope during the 24-hour 60°C soak, and the WTF at each plateau temperature also showed this behavior and only achieved ULB after 10 cycles, as shown in Figure 62 and Figure 63. These two figures show how the WTF profile as a function of sample temperature and thermal cycling goes through a significant reduction. Each thermal cycle drops until the ULB with $R^2 = 0.9993$ is achieved.

The WTF behavior of LDPE-QCA is presented in Figure 64 through Figure 67. This sample has a response similar to that of the LDPE-QC but shows a higher overall WTF. It took eight thermal cycles for this sample to achieve a ULB correlation factor $R^2 = 0.9977$. It will be shown later that these changes in WTF can be explained as a result of morphological changes caused by the heat treatments. Changes in spherulitic structure modify the amorphous path through which the water passes. In this case, the amorphous path was opened due to the transformation of the amorphous phase into the crystalline phase through the annealing process.

The third sample is the LDPE-SC, shown in Figure 68 through Figure 71. This sample presents a much more stable WTF profile with only some instability evident in the 24-hour 60°C soak. Each of the plateau WTF was very stable, and ULB was achieved after four or five thermal cycles with a correlation factor $R^2 = 0.9996$. Examination of Figure 70 shows very little change occurred between the first thermal cycle and the fifth thermal cycle. Changes in the crystalline structure created a more stable morphology whereby the amorphous pathways and crystalline structure is not influenced by the movement of water into the structure. Thus, the WTF was also more stable. This will be addressed in greater detail in later sections.

The fourth and last sample in this group is the LDPE-SCA, Figure 72 through Figure 76. The first and most obvious change in this sample is the number of thermal cycles required for the sample to reach ULB. It took approximately 25 cycles for LDPE-SCA to not only reproduce the same WTF but also show stability at each plateau. Two ULB graphs are provided in Figure 74 and Figure 75. The first graph shows both the first five cycles and the last five cycles to contrast the significant change in WTF over the duration of the testing. Ultimately, a ULB linear correlation factor $R^2 = 0.9998$ is obtained after 19 days and 25 thermal cycles.

The ULB WTF for all of the LDPE samples are plotted in Figure 124. All samples are showing very similar WTF except for the LDPE-SC, which is significantly lower.

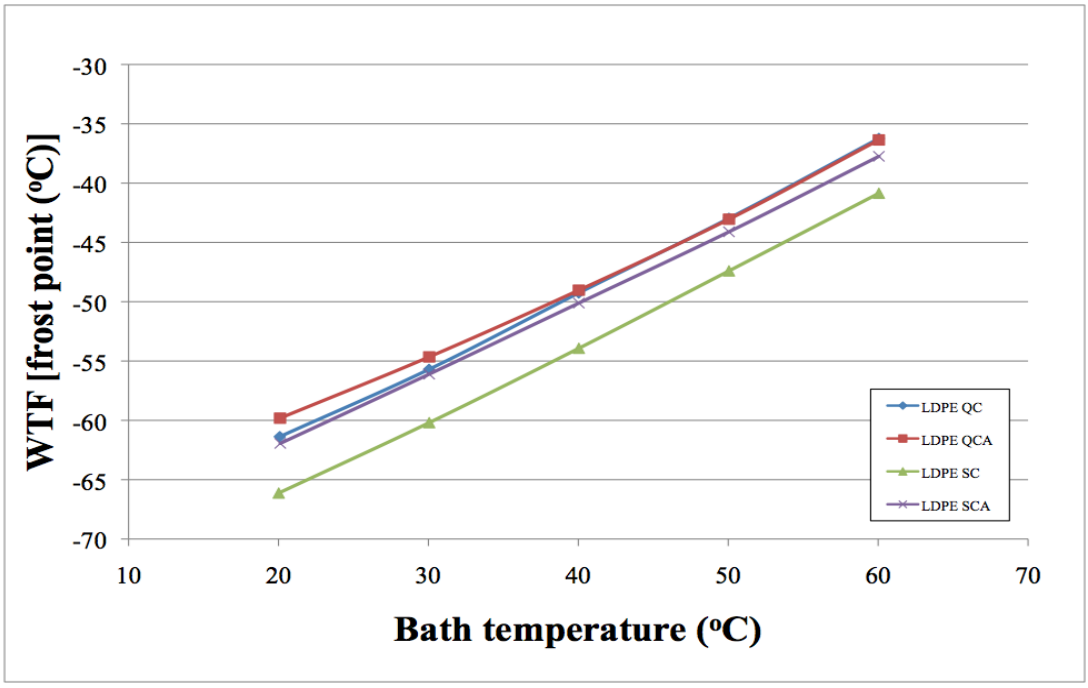

Figure 124. Comparison of WTF for LDPE-QC, QCA, SC, and SCA.

6.3 Water Transport Flux Through HDPE

The final group of samples to be discussed is the HDPE, and the first of these is the HDPE-QC. The WTF data for this sample can be found in Figure 77 through Figure 81. This sample shows a rather large reduction in WTF during the 24-hour 60°C soak. The behavior is clearly evident in Figure 77 and Figure 78 at the very beginning of the test. Keep in mind the WTF is in blue and references the left y-axis and the sample temperature is in red and references the right y-axis. The WTF declines rapidly with a very choppy response at each plateau of the first thermal cycle. The plateau WTF showed continued movement toward a stable rate with each thermal cycle. This behavior is evident in the test data shown in Figure 77 and Figure 78 and also in the plot of the WTF versus the bath temperature in Figure 79 as the change in WTF response progressing from one of a curve to a linear behavior. Figure 80 shows the reduction of the WTF for each plateau temperature as a function of thermal cycles. It eventually obtained ULB correlation factor after 25 cycles of R2 = 0.9988.

The WTF behavior of HDPE-QCA, is shown in Figure 82 through Figure 86. This sample showed a very similar response to HDPE-QC the previous sample, but of special note is the large departure from the ULB in the first few thermal cycles, as shown in Figure 84. The first 2 cycles

had a high degree of curvature showing that this sample experienced significant changes to the WTF behavior. Eventually, the sample achieved ULB after 19 thermal cycles. The high degree of curvature in the early cycles and the slow approach to ULB can be explained by the process of water clustering in the amorphous phase promoted by thermal cycling.

At the beginning of the test the amorphous phase is devoid of water and heating promotes the mobility of the water through the amorphous phase explaining the high initial WTF while simultaneously promoting solubility. As time elapses at each plateau temperature water moves into the amorphous phase approaching saturation and when the sample is cooled the individual dissolved water molecules cluster together. The waters cluster together because they are polar molecules in an otherwise non-polar amorphous phase. Reduction in WTF may be attributed to water clusters causing strain in the amorphous phase reducing chain mobility causing it to behave more like the crystalline phase. ULB is obtained once the maximum water content is achieved in the matrix. One approach to evaluate this explanation would be to perform Raman spectroscopy while conducting WTF test. This would allow for the observation of water contained within the polymer matrix and changes in the strain of the polymer matrix.

The third HDPE sample is the HDPE-SC. The WTF behavior is given in Figure 87 through Figure 90. This sample, as with the first two HDPE samples, had a significant reduction in WTF as the testing proceeded. It took approximately 25 cycles to obtain a ULB with the correlation factor $R^2 = 0.9996$.

The fourth sample in this group is the HDPE-SCA. The WTF behavior is given in Figure 91 through Figure 94. Inspection of the data shows that this sample was terminated before reaching a ULB, but 7 cycles that were recorded reveal a response very similar to the responses of the previous HDPE samples.

Figure 125 shows the ULB WTF for each of the HDPE samples. With the exception of the HDPE-SCA, which was terminated prematurely, all of the samples have very similar WTF rates and slopes. These slopes have an average of 0.5574 with a standard deviation of 0.0226. The importance of the ULB is it provides a quantification of the WTF at a steady state condition. From the graph of the individual data sets, such as the one for HDPE-QC found in Figure 85, a least squares equation is provided that allows the behavior of the material to be described as a

function of temperature once it reaches the steady state ULB. The ULB is an actual measurement of the WTF as a function of temperature. Along with the number of thermal cycles required to reach ULB the user of the information can more fully predict a materials performance. If the user is trying to select a polymer and knows the operating temperature and tolerance to water vapor exposure, he can make a more informed decision about the performance a these polymer.

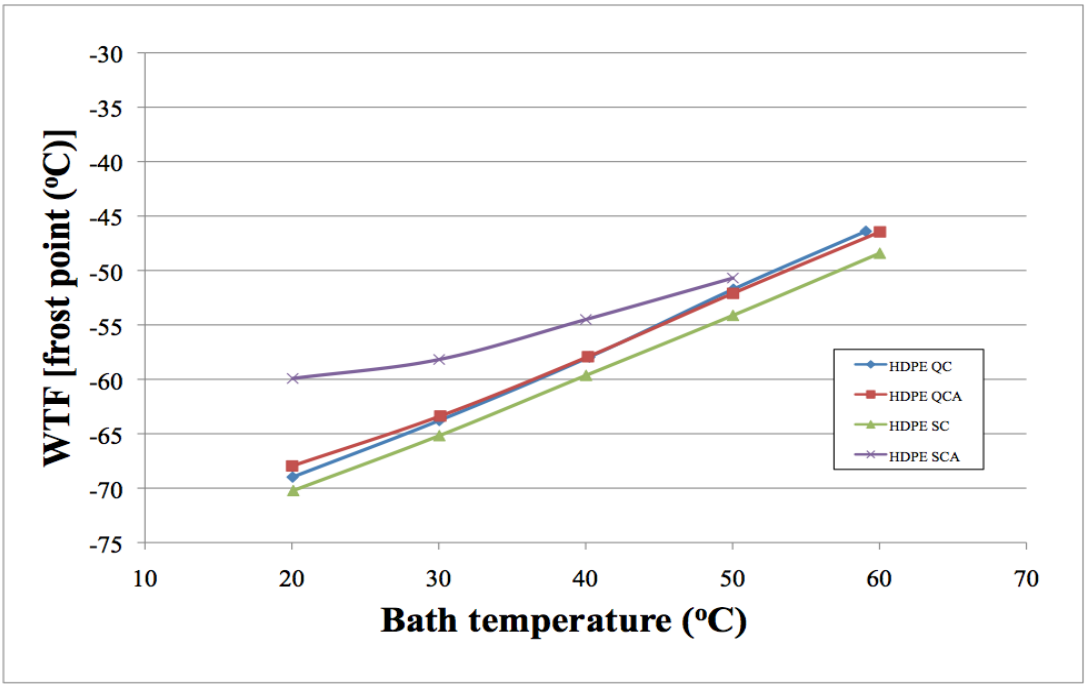

Figure 125. Comparison of WTF for HDPE-QC, QCA, SC, and SCA.

From the preceding discussion and Figure 123 through Figure 125, it can be shown that with a few exceptions the WTF is governed by the polymer species and is relatively insensitive to the processing conditions after reaching steady state ULB. For example, for the 3 HDPE samples in Figure 125 the WTF at 20°C is -69°C ± 1°C. This correlates to a WTF of 3.572x10-7 g/(min in2). It has been shown that polyethylene samples can be heat treated to cause changes in times required to reach the ULB.

Now that the WTF data of each group of polyethylene samples has been discussed, the focus shifts to comparison of these behaviors to the samples' morphology, as determined by density

gradient column (DGC), differential scanning calorimeter (DSC), wide-angle X-ray diffraction (WAXD), and small-angle light scattering (SAXS).

6.4 Comparison of Mass Based WTF to Literature Values

The mass based WTF of samples that have reached ULB have been compared to literature values. The mass based WTF values were converted to those used in the literature and plotted. The literature references present their values as g/(m^2 days) and (g mm)/(m^2 days) versus the samples density.[77] WTF values from this work at 20°C once the samples reached ULB were converted from the units used here, g/(in^2 min), using the appropriate conversion and the samples' thickness. These values are listed in Table 9 below.

Table 9, Comparison of Mass WTF to Literature Values

Material type	Density (g/cc)	WTF g/(min in^2)	g/(day m^2)	Thickness (in)	g mm/(day m^2)
LDPE-QC	0.928	1.06819E-06	2.384	0.0026	0.15503
LDPE-QCA	0.933	1.41077E-06	3.149	0.0033	0.26554
LDPE-SC	0.933	5.4368E-07	1.213	0.0027	0.08230
LDPE-SCA	0.934	1.01539E-06	2.266	0.0023	0.13125
LLDPE-QC	0.922	1.73230E-06	3.866	0.0023	0.22097
LLDPE-QCA	0.931	1.36118E-06	3.038	0.0031	0.24000
LLDPE-SC	0.932	2.20365E-06	4.919	0.0021	0.25861
LLDPE-SCA	0.932	6.03647E-07	1.347	0.0039	0.13176
HDPE-QC	0.945	3.80325E-07	0.849	0.0025	0.05369
HDPE-QCA	0.957	4.13401E-07	0.923	0.0034	0.08039
HDPE-SC	0.961	2.96992E-07	0.663	0.0020	0.03334
HDPE-SCA	N/A	N/A	N/A	N/A	N/A

Figure 126 and Figure 127 shows the comparison of the mass WTF values to those found in the literature. The agreement is reasonably good and reflects the effects of the different heat treatment within any given materials group.

[77] Liesl K. Massey and Library Plastics Design, "Permeability properties of plastics and elastomers a guide to packaging and barrier materials," Plastics Design Library : William Andrew Pub., http://www.knovel.com/knovel2/Toc.jsp?BookID=752.

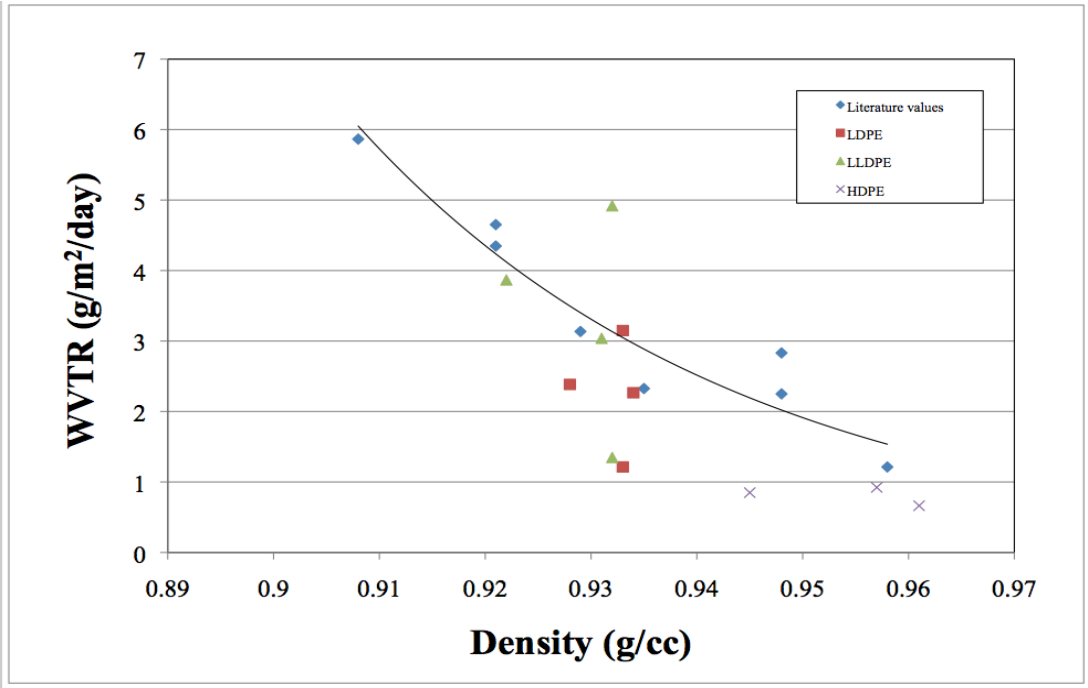

Figure 126, Comparison of WTF to Literature values (g/m^2 day)

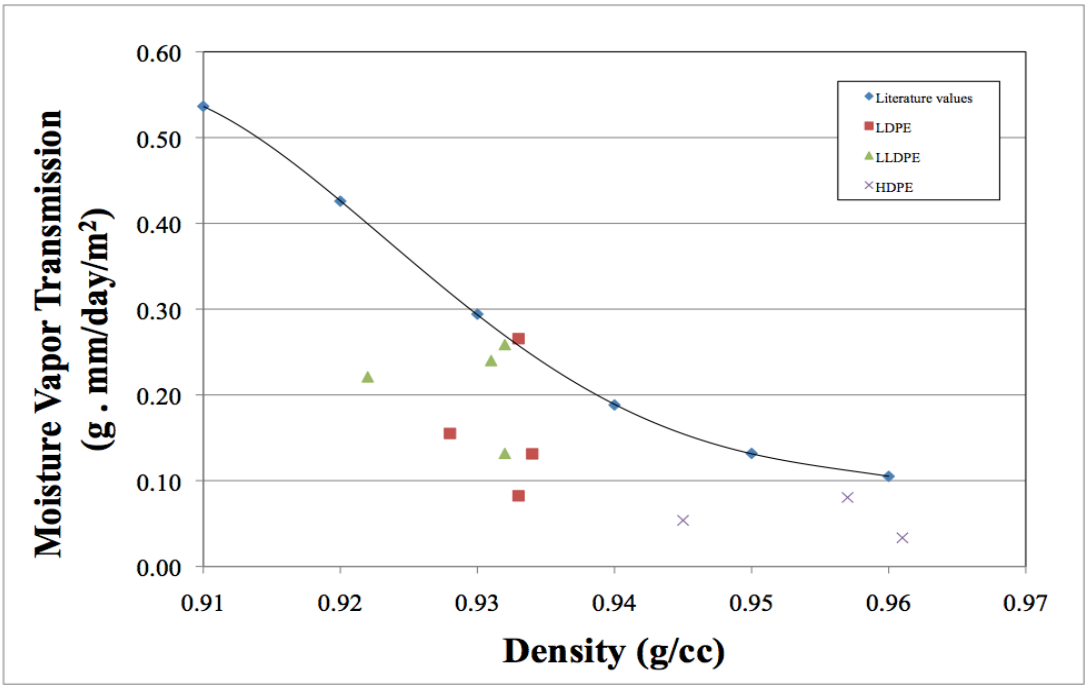

Figure 127, Comparison of WTF to Literature values (g mm/m^2 day)

6.5 Modeling of WTF behavior

After inspection of the WTF responses of the various polymers and heat treatments the question becomes how can these different responses be modeled based on the available data and theories. Depending on the materials and their heat treatments the WTF response can range from a parabolic behavior in the first thermal cycle to the linear response many thermal cycles later. The WTF appears to be a function of time, temperature, water concentration, and conductance. This suggest that two different mechanisms are involved.

Equation 23

$$WTF = f(t,T,[H2O],\mu)$$

The first mechanism is one that appears to varying in magnitude and duration in response to material type and heat treatment. Material type and heat treatment impact the samples' morphology. This mechanism initially begins high and then diminishes as either a function of time, moisture transport through the material, thermal cycling or some combination of all of these.

The second mechanism to be discussed addresses the linear frost point WTF response to sample temperature changes which all samples eventually achieve. This is best described as conductance through an interconnected series of amorphous channels. This would be analogous to conductance through a micro porous media.

With the WTF divided into a combination of 2 different responses the question becomes can these behaviors be attributed to the semi crystalline polymer structure, a response to the presents of water, or both? Beginning with what is known about polyethylene it is hydrophobic, absorbs very little water, and permits water to pass through the amorphous phase. Water does not chemically react or dissolve polyethylene so therefore the controlling mechanism must be structural. What structure could govern the movement of water and account for both of the 2 previously described WTF mechanisms?

The second mechanism, the linear WTF response to sample temperature, could be achieved by metering the flow through narrow channels. If the passages were static and did not vary in diameter or length then the flow would be simple conductance governed by concentration gradients and thermally driven kinetic motion. But this mechanism does not explain the first

behavior in which the WTF begins at a maximum and diminishes over time. This second mechanism could be thought of as a growing obstruction or modification to the path that does not completely obstruct flow just impede it. Figure 128 below provides a structure that could be used to explain both of these mechanisms.

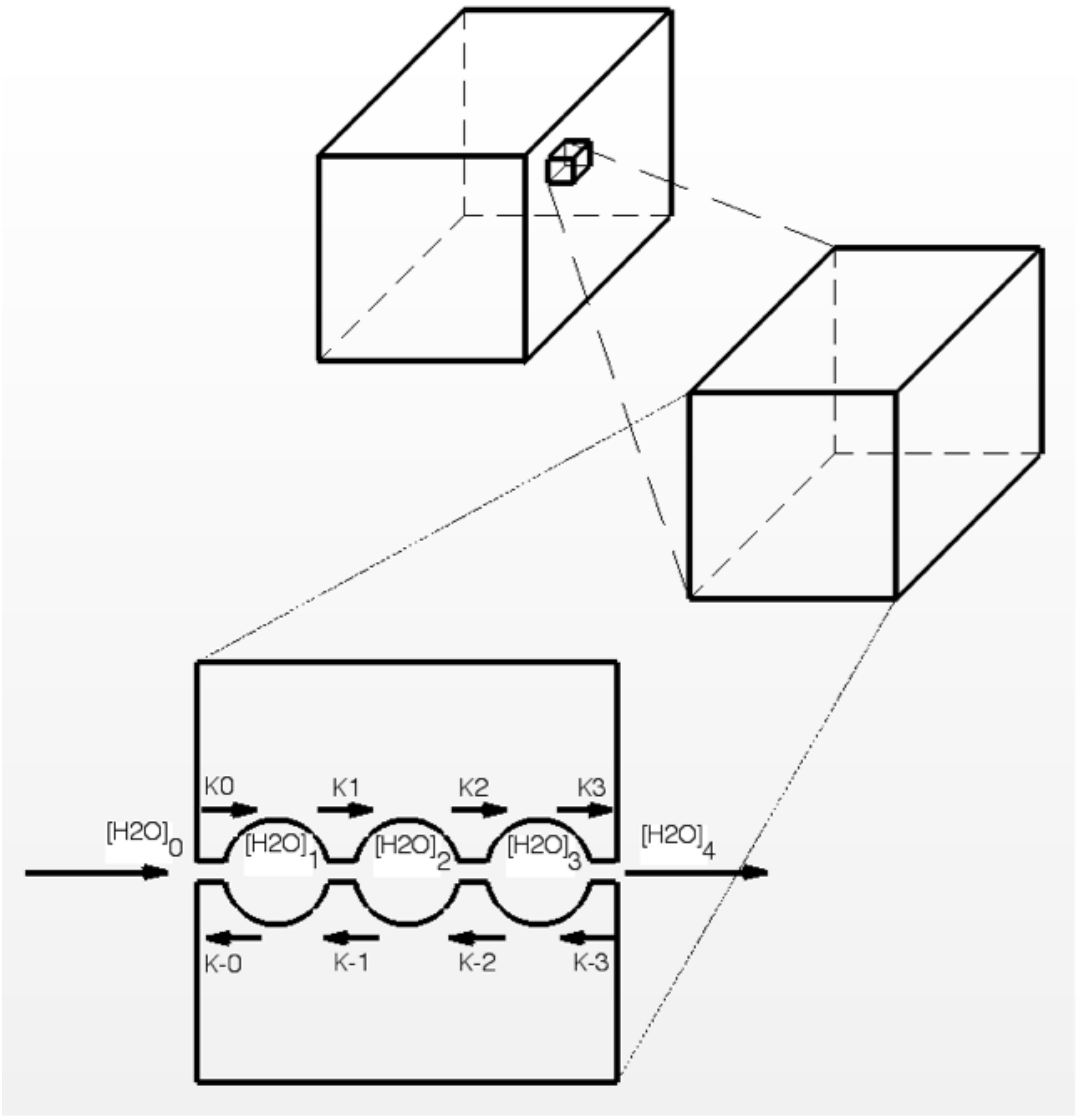

Figure 128, Diagram of flow through interconnected free volumes

The diagram shows a cross section of a differential element of the bulk polymer. In this model, 3 volumes are interconnected by water conductive amorphous paths to represent interconnected free volume voids of the polymer. At time to all of the volumes are empty, liquid water is brought into contact with the left side, and a carrier gas is passed over the right side carrying away all

waters that emerge from the polymer maintaining the exiting concentration, $[H2O]_4$, at or near zero. At this stage passage of water from the reservoir to volume 1 is a function of the supply concentration $[H2O]_0$ and the rate constant K0. The single water in volume 1 now has the same probability of progressing on to volume 2 based on the water concentration $[H2O]_1$ and the rate constant K1 as returning back to the reservoir based on the same water concentration $[H2O]_1$ but the reverse rate constant K-0. The same logic is used for movement of a single water from volume 1 to 2, 2 to 3, and 3 to 4.

As a consequence of the fill rates of each volume being concentration dependent on the previous volume an inherent delay is built into the system. Having the fill rate of each volume being concentration dependent normally means that as the concentration increases so to does the rate of filling of the next volume in the series. This is not what is seen in the WTF test data. To the contrary, the rate diminishes with time and in this case it would mean that the WTF rate would diminish with increasing volume concentrations.

The cause for the diminishing rate with increasing concentration stems from the tendency of water to hydrogen bond and two previously mentioned characteristics of the polymer. During a molecular simulation conducted by Fukuda et al. it was shown that when waters move through a polyethylene matrix they tend to cluster together due to hydrogen bonding.[78] These clusters can consist of as many as 11 waters. These water clusters reside in the amorphous phase of the polymer which is made up of tie chains, loose loops, and main chain branches. Fukuda's model showed that mobility of cluster with a higher number of waters had lower mobility than single waters. The presents of these clusters effect the structure of the surrounding polymer.

Unlike the bound chains of the crystals, the amorphous phase chains normally possess various modes of motions which permit the waters passage. As the waters coalesce into clusters they reject the hydrophobic polyethylene and strain the surrounding amorphous phase. The added strain to the amorphous chains cause them to become more aligned reducing their mobility and reducing the waters ability to move to the next volume. Additionally as waters are added to each free volume they increase the likelihood of collision between waters reducing the probability of movement to the next volume.

[78] Fukuda, "Clustering of water in polyethylene: A molecular-dynamics simulation."

Thus the combination of hydrogen bonding, molecular collision, and induced amorphous phase strain results in the reduction of water transport between internal volumes until saturation is reached in the internal volumes. At saturation in the volumes the waters' mobility is at a minimum and WTF is reduced to a thermally driven kinetic motion resulting in the linear relationship of WTF to sample temperature.

This logic was used to construct a model to simulate the response of waters moving through the polymer matrix under testing conditions of time and temperature. The first step in the model was to construct a table of test durations, sample temperatures, initial water concentrations at each volume, and associated rate constants. An equation was formulated for each volume to calculate its water concentration based on the concentration of the preceding volume, rate constant, testing duration, and temperature.

Equation 24

$$[H2O]_{i+1} = [H2O]_i \times K_i \times t_i \times T_i$$

To determine the concentration of the n^{th} volume in a series of interconnected volumes the equation becomes as shown below.

Equation 25

$$[H2O]_{i+1} = [H2O]_i \times K_i^n \times t_i^n \times T_i^n$$

Figure 129 below shows an example of the reduction of the non-linear portion of the water conduction as a function to thermal cycle and temperature.

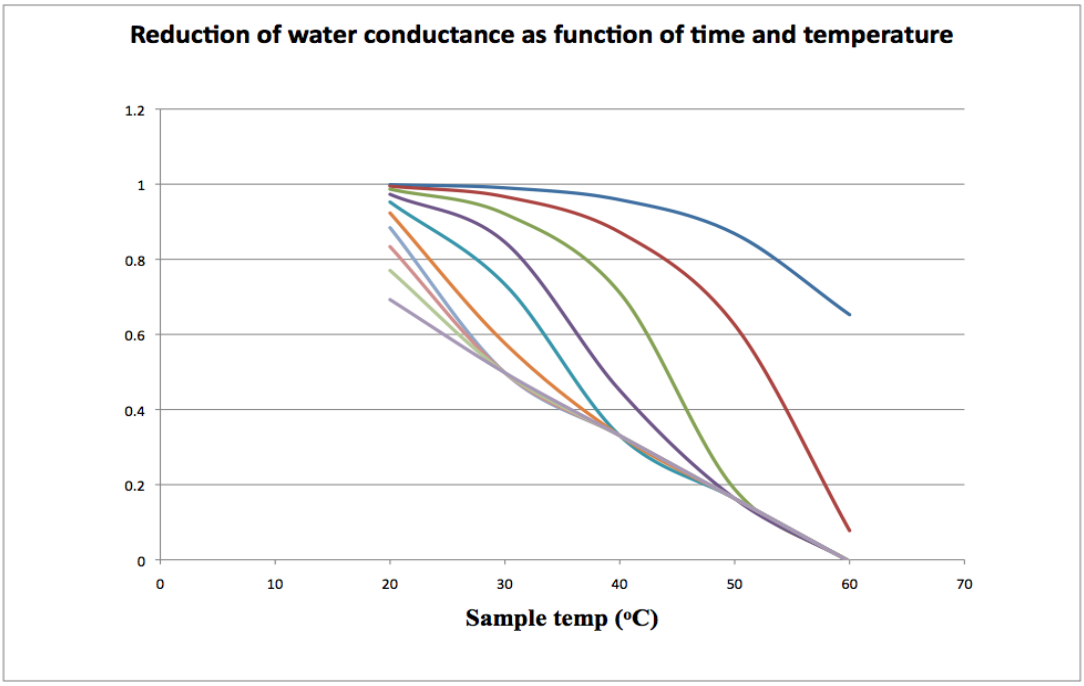

Figure 129, Non-linear portion of WTF flow

The next calculation shows that as the calculated concentration approaches saturation across the volumes the non-linear WTF based flow is projected to go to a minimum. This behavior was simulated using the natural log of the ratio of the saturation concentration versus the current concentration. As the immediate concentration approaches saturation the natural log goes to zero.

Equation 26

$$\text{Non-linear WTF} = \ln([H2O]\text{Saturation} / [H2O]_i]$$

Figure 130 below shows the reduction of the non-linear contribution to the WTF as the model is ran through multiple thermal cycles over the same time frames as the actual test.

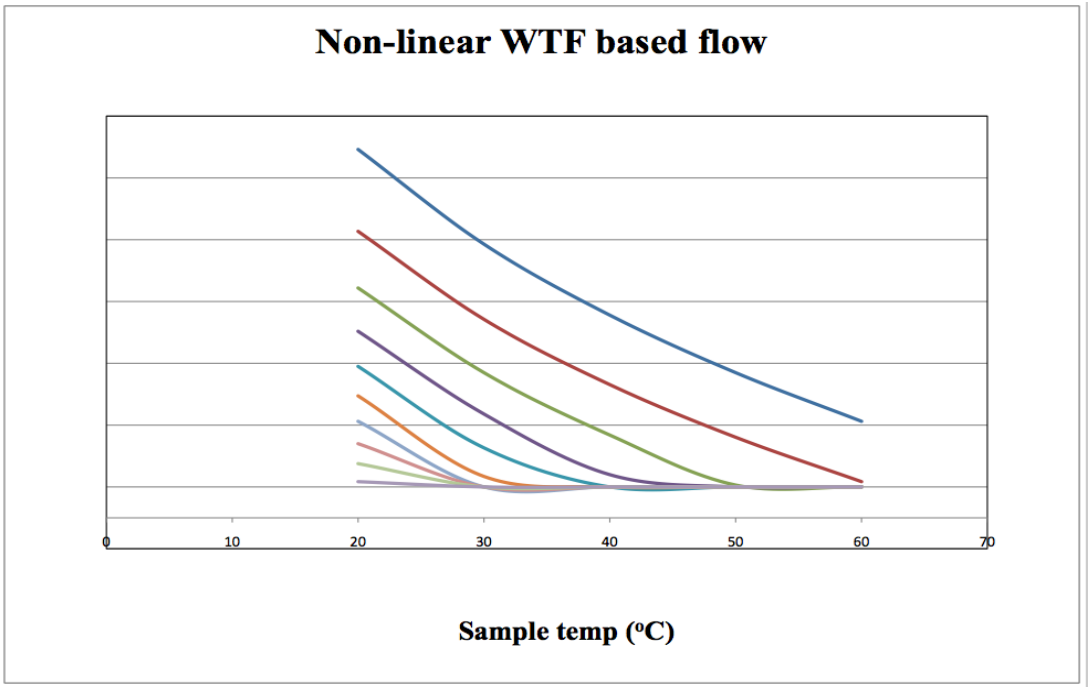

Figure 130, Non-linear contribution of WTF as function of time and temperature

The last calculation combines the Non-linear WTF (NLWTF) with a linear equation representing ULB behavior. An NLWTF coefficient (A) which represents the tortuosity of the path was added to adjust the contribution provided by the NLWTF.

Equation 27

$$\text{Simulated WTF} = A \times \text{NLWTF} + (mX+b)$$

By adjusting the rate constants and NLETF tortuosity coefficient extremely good approximations of actual WTF data can be produced. In the following simulations all rate constants were set equal to each other.

Two different materials with extremely different behaviors have been modeled. The first of these materials to be modeled is the LLDPE-QC which had a nearly linear WTF response throughout its testing. Figure 134 show a plot of the actual test response and modeled response for the LLDPE-QC. The second material to be modeled is HDPE-QCA shown in Figure 132. The first and last thermal cycles have been modeled and the large difference in these two data sets should be noted. By adjusting only the rate and tortuosity

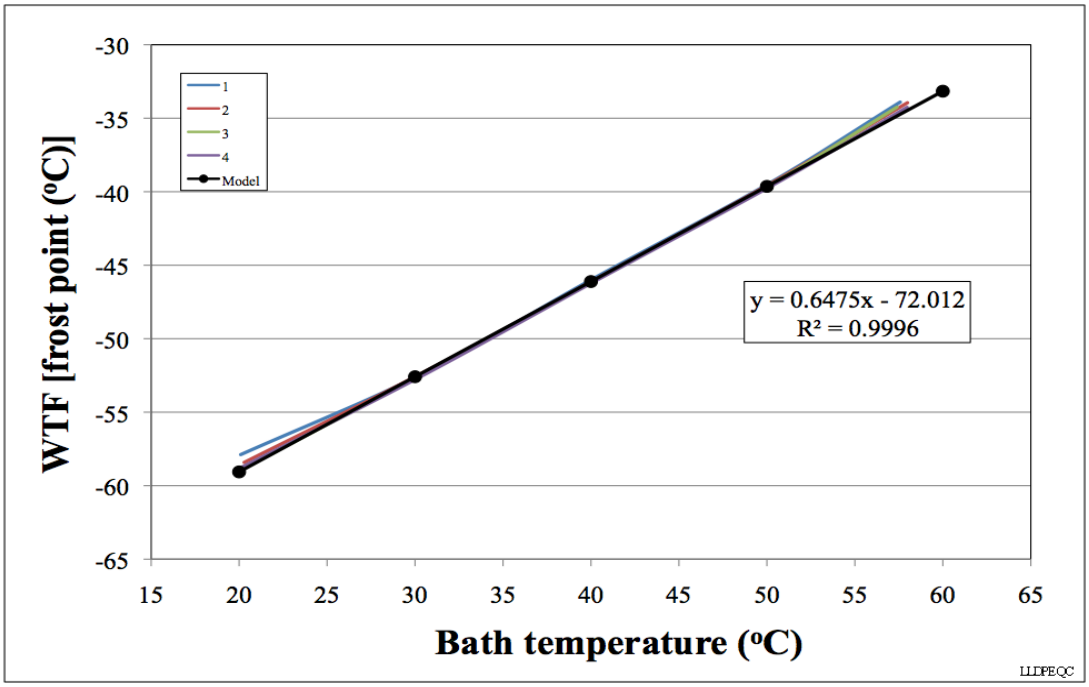

Figure 131, LLDPE-QC WTF response with modeled linear response

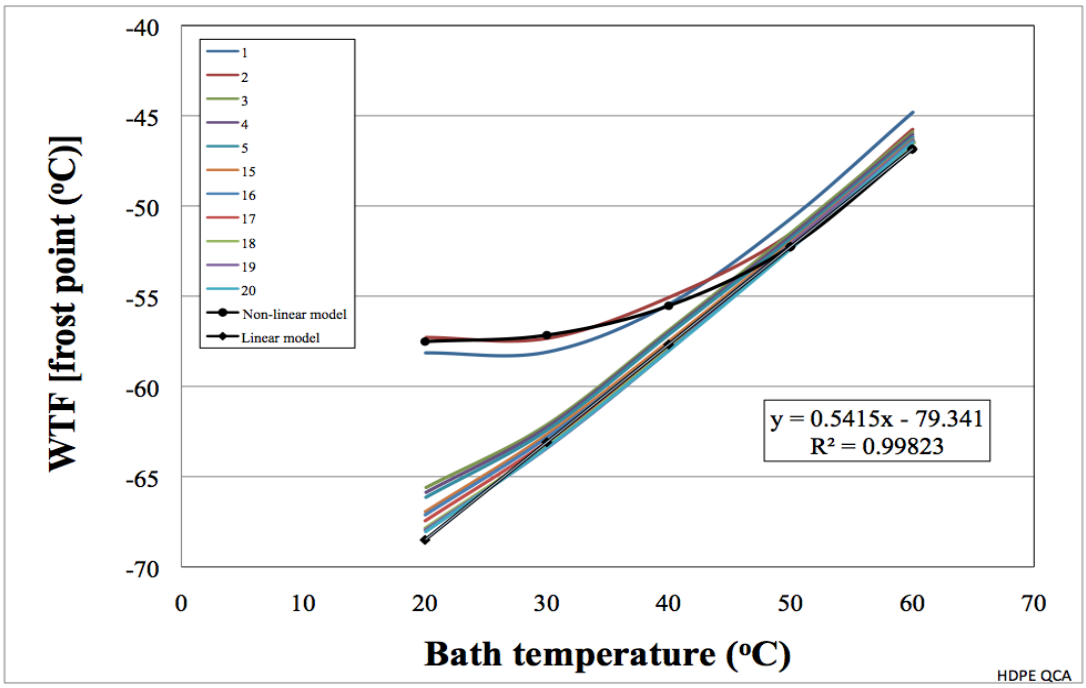

Figure 132, HDPE-QCA WTF response with non-linear and linear response modeled

6.6 Water Transport Flux as a function of crystallinity

WTF of water through polymers has long been described as primarily a movement through the amorphous phase, and the crystalline phase is essentially non-permeable. Thus, it can be expected that as the crystalline phase increases, the WTF should decrease. With this view in mind, the concern becomes the manner in how the crystallinity is characterized. Before methods for crystalline characterization are discussed, Figure 1, inspired by Mandelkern, should be reviewed; it shows that semicrystalline polymers are described as having at least three discrete zones known as crystalline, interfacial, and amorphous or interzonal. The simplest polymer characterization begins by measuring its density and interpolating between the density of 100% crystalline and 100% amorphous material. A density gradient column (DGC) was used to determine the density of all 12 samples. The DGC gives the overall density and, thus, cannot differentiate between the phase or the distribution of the phases. The crystallinity determined from the DGC densities are found in Table 10.

Figure 97 illustrates, the largest change is universally seen in all samples when the quenched samples are annealed. The quenched-and-annealed conditions for the LDPE and the LLDPE approximate the density of their slow-cooled condition, but this behavior does not hold true for the HDPE, where the slow-cooled condition provides a significant increase beyond the quenched-and-annealed state. Annealing of the slow-cooled LDPE and LLDPE samples shows only small changes, but the HDPE shows a continued increase. Thus, changes in density upon annealing indicate the possible presence of defects in the structure trending toward a more stable lower energy state of higher crystallinity. When the ULB WTF at 20°C for the polymer samples are plotted versus their degree of crystallinity, no correlation within the polymer groups of HDPE, LDPE, and LLDPE can be made, as Figure 133 shows. There is an overall trend across all of the samples that shows a decrease in WTF as a function of crystallinity.

A second method used to characterize polymers' crystalline nature is DSC. This method provides two pieces of information describing the crystalline region, the degree of crystallinity, and crystal size distribution of thickness. Figure 134 presents a plot of WTF versus crystallinity, and Figure 135 presents a chart of WTF versus crystal thickness. The crystal size distribution was calculate using Equation 21. Neither of these plots shows any correlation between WTF and crystallinity within any given polymer group, but both plots do show a trend of reduced WTF with increasing crystallinity across all polymer groups. Thus, the generally accepted rule of thumb that WTF is

governed by crystallinity is shown to be grossly correct, but high-resolution measurement systems like the method used in this study show it to not hold true within a given polymer, such as these shown.

Table 10. WTF as function of crystallinity from DGC and DSC

Polymer	WTF (C) @ 20C	WTF (g) @ 20C	DGC degree of crystallinity	DSC degree of crystallinity	DSC 1st crystal thickness (nm)	DSC 1st crystal area	DSC 2nd crystal thickness (nm)	DSC 2nd crystal area
LLDPE QC	-58.8	1.505E-06	45.9	32.60	8.92	0.0002	11.75	0.0040
LLDPE QCA	-59.6	1.350E-06	51.8	43.05	9.22	0.0140	11.79	0.0030
LLDPE SC	-55.3	2.378E-06	52.2	43.66	11.98	0.0003	11.08	0.0000
LLDPE SCA	-66.0	5.539E-07	52.2	40.38	8.75	0.0095	12.25	0.0050
LDPE QC	-61.4	1.054E-06	49.6	40.80	8.49	0.0120		
LDPE QCA	-59.8	1.306E-06	52.8	51.94	7.53	0.0270		
LDPE SC	-66.1	5.444E-07	53.2	46.22	8.20	0.0120		
LDPE SCA	-61.9	9.758E-07	53.7	46.60	6.71	0.0090	8.28	0.0140
HDPE QC	-69.0	3.572E-07	61.2	58.57	8.49	0.0090		
HDPE QCA	-68.1	4.111E-07	69.2	68.77	15.16	0.0260		
HDPE SC	-70.2	2.970E-07	71.8	69.63	14.47	0.0130		
HDPE SCA	N/A	N/A	73.1	73.29	11.66	0.0010	18.46	0.0150

** The thicknesses and areas within the inset box were determined by deconvolution of the DSC thermogram*

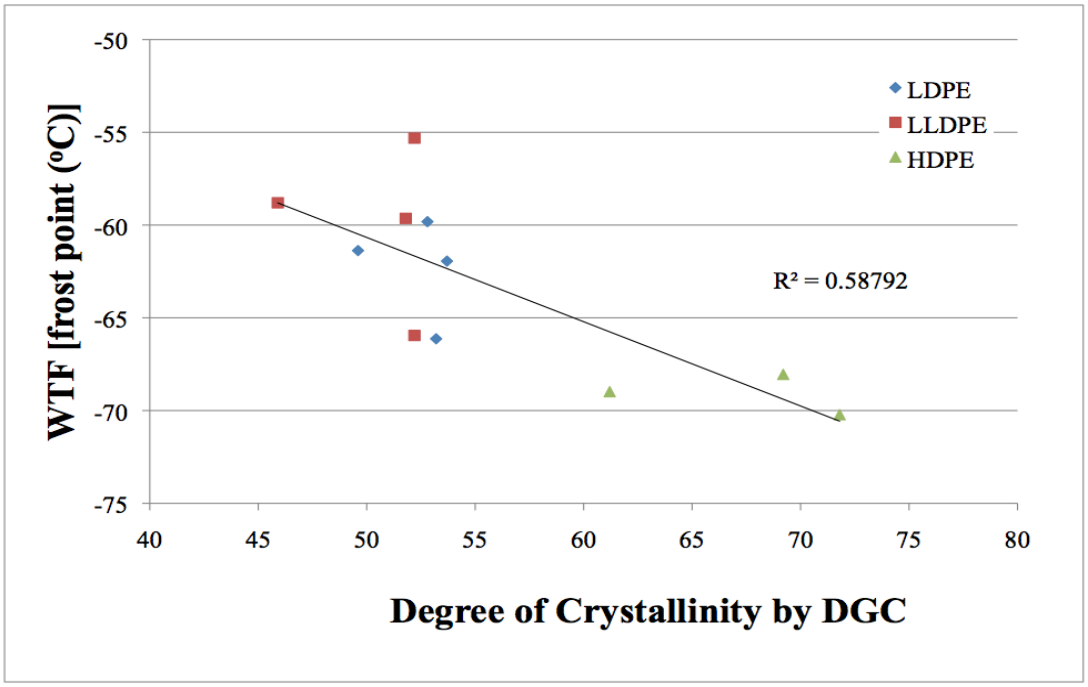

Figure 133. WTF in frost point (°C) as function of degree of crystallinity by DGC.

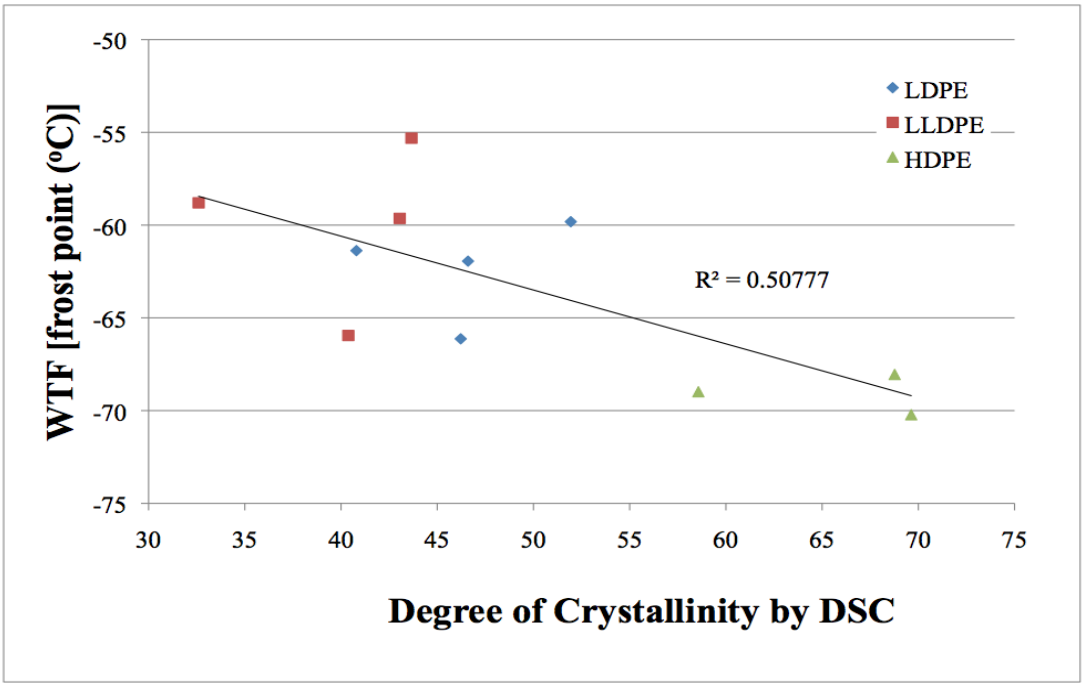

Figure 134. WTF in frost point (°C) as function of degree of crystallinity by DSC.

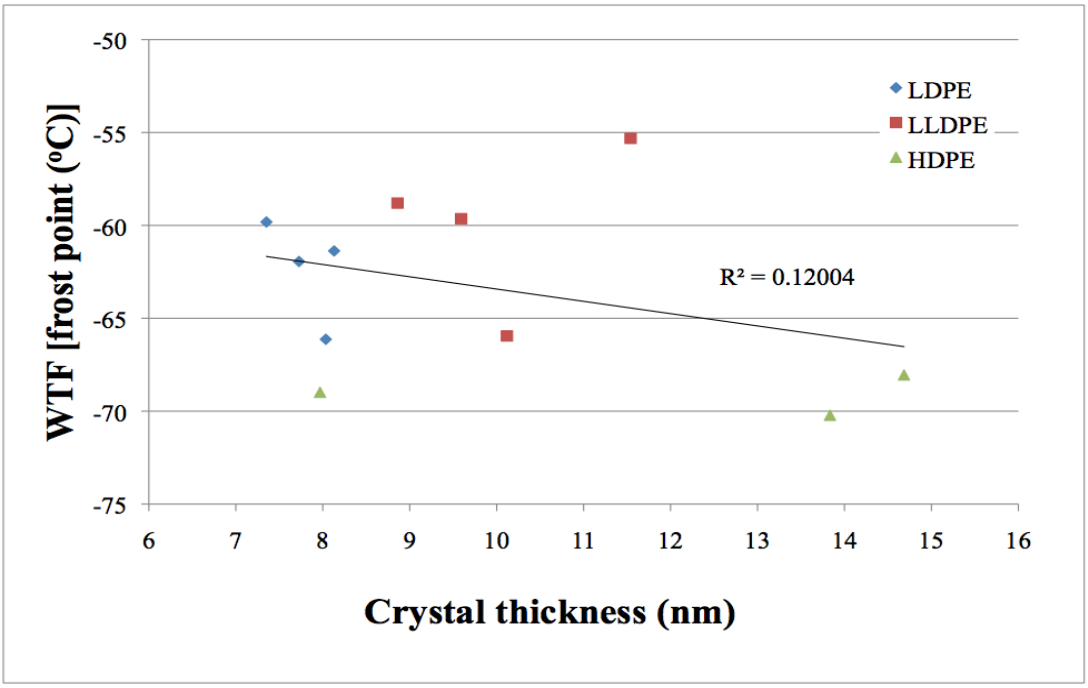

Figure 135. WTF in frost point (°C) as function of crystal thickness by DSC.

A third method used to characterize polymers' crystalline nature is WAXD. As opposed to the degree of crystallinity as determined by DSC, the WAXD degree of crystallinity includes the crystalline phase and interfacial phase. The WTF has been plotted versus the WAXD degree of crystallinity in Figure 136. Again, no clear relationship emerges within any of the three materials, but a general relationship can be seen between the WTF and overall degree of crystallinity.

The fourth method used to characterize polymers' crystalline nature is SAXS. This method provides the long spacing, the distance from one crystal to the next. It should be noted that the long period includes the crystalline, interfacial, and amorphous regions. The WTF has been plotted versus the long period in Figure 137. No clear relationship can be discerned for any polymer group or across all groups of polymers.

The thickness of the amorphous region can be obtained by taking the difference between the WAXD degree of crystallinity and the SAXS long period. The WTF is plotted versus the

amorphous region, as Figure 138 indicates. No relationship emerges between the WTF and the amorphous region within any given materials group or over all of the samples.

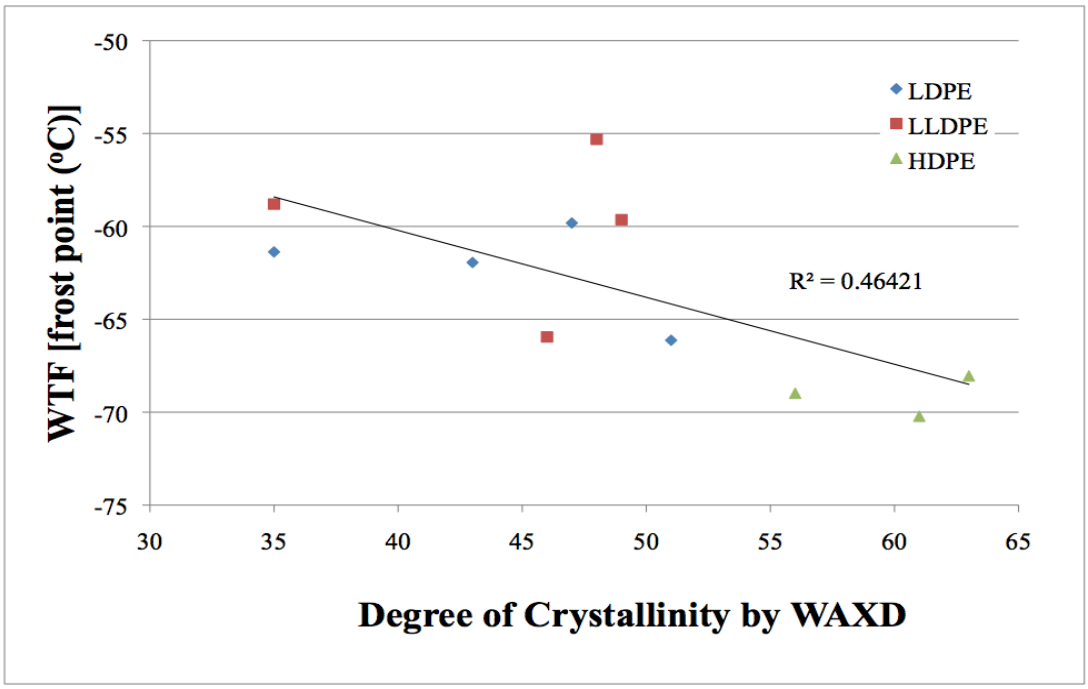

Figure 136. WTF in frost point (°C) as function of degree of crystallinity by WAXD.

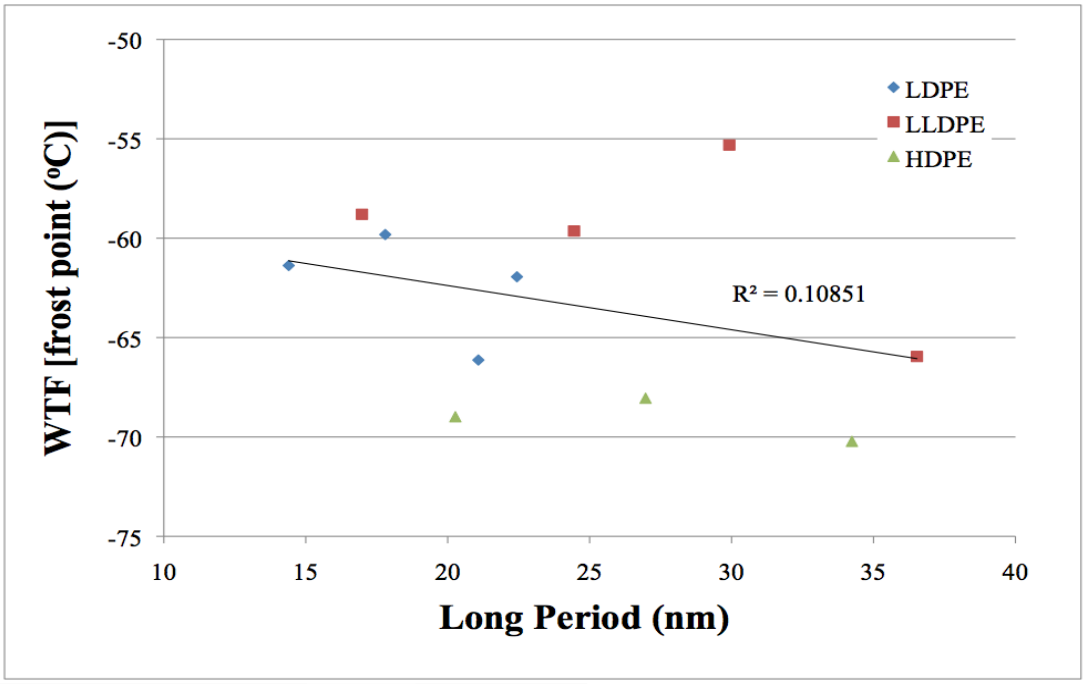

Figure 137. WTF in frost point (°C) as function of long period by SAXS.

Table 11. WTF as function of crystallinity from WAXD and long period from SAXS

Polymer	WTF (C) @ 20C	WTF (g) @ 20C	WAXD Degree of crystallinity	SAXS long period (nm)	Amorphous thickness (nm)
LLDPE QC	-58.8	1.505E-06	0.35	17.0	11.0
LLDPE QCA	-59.6	1.350E-06	0.49	24.5	12.5
LLDPE SC	-55.3	2.378E-06	0.48	29.9	15.6
LLDPE SCA	-66.0	5.539E-07	0.46	36.5	19.7
LDPE QC	-61.4	1.054E-06	0.35	14.4	9.4
LDPE QCA	-59.8	1.306E-06	0.47	17.8	9.4
LDPE SC	-66.1	5.444E-07	0.51	21.1	10.3
LDPE SCA	-61.9	9.758E-07	0.43	22.4	12.8
HDPE QC	-69.0	3.572E-07	0.56	20.3	8.9
HDPE QCA	-68.1	4.111E-07	0.63	27.0	10.0
HDPE SC	-70.2	2.970E-07	0.61	34.2	13.4
HDPE SCA			0.59	34.0	13.9

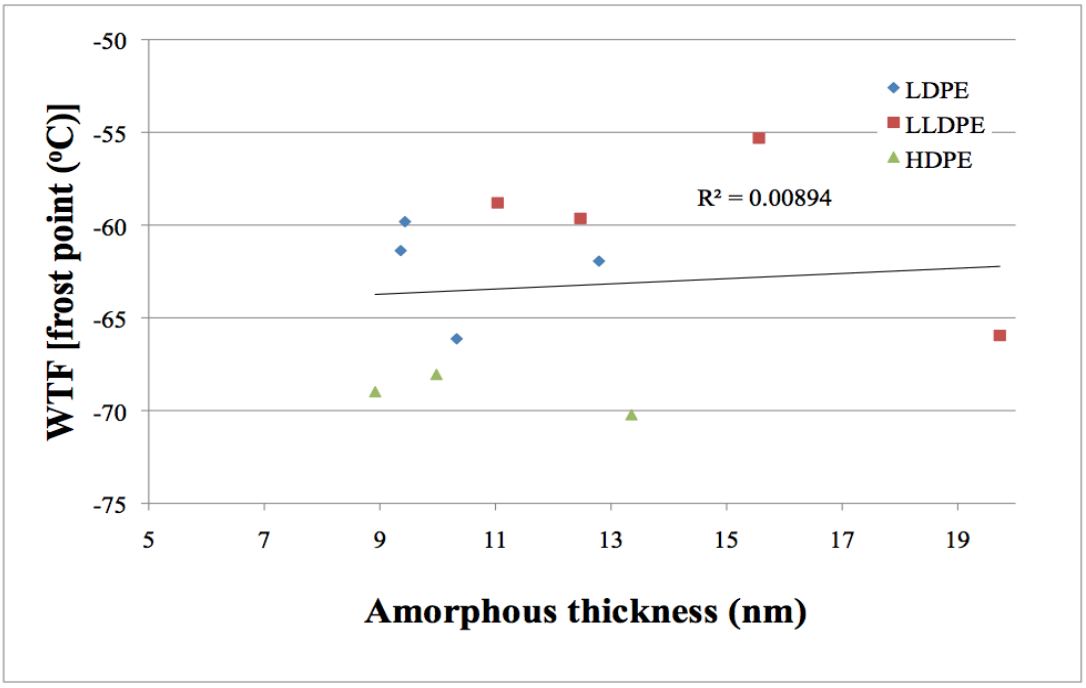

Figure 138. WTF in frost point (°C) as function of amorphous thickness (nm).

6.7 Changes in WTF resulting from thermally induced morphological variations

Three of the four preceding investigatory methods DGC, WAXD, and SAXS used to probe the crystalline structure were all conducted at one temperature, nominally 20°C. Although there has not been any direct correlation shown between the WTF and the testing results, it was thought that they may hold information with regard to the transient state of the morphology that controls changes in WTF leading to the ULB. To investigate these thermally controlled morphological mechanisms two additional tests were conducted in which the temperature was varied: variable temperature DGC (VT-DGC) and variable temperature WAXD (VT-WAXD). Both of those methods required a long-term commitment of equipment and laboratory personnel to conduct these two extensive investigations. It was believed that changes in the WTF in the form of rate decays at the plateau, and WTF rate decay over multiple thermal cycles may be attributable to thermally driven structural changes of otherwise seemingly identical samples.

6.7.1 VT-DGC

The data from the VT-DGC will be the first of these two tests to be examined. Figure 112 through Figure 114 show the VT-DGC data for HDPE, and Figure 115 shows a collective of data for all samples. The WTF data for HDPE showed the largest decay curves at the plateau and overall approaching the ULB, but there appears to be no evidence in the density data of a similar response. It appears that there is very little if any change in the density as a function of thermal cycling for this material. The collective data in Figure 115 shows there is essentially no change in the density for any of the materials that could explain the decay in WTF. This observation implies very little if any change in the density of the crystalline and amorphous phases.

6.7.2 Small Angle Light Scattering (SALS)

Another method used to probe the structure of the samples is SALS. This technique shows the supermolecular structure resulting from coalescence of crystals. There are three prominent structures of interest to this study namely random, rod like, and spherulites. The spherulitic structure is ranked from a highly organized “A” structure to a loosely organized “C” structure, as shown in Figure 31. Each sample was tested and produced one of these three patterns to varying

degrees. Table 12 lists the material type with heat treatment, resulting pattern and spherulite radius where applicable.

Table 12. SALS patterns and spherulite sizes

Polymer	SALS spherulite Image	Spherulite maximum radius (R=um)
LDPE-QC	Random pattern "H"	
LDPE-QCA	Random pattern "H"	
LDPE-SC	Spherulite pattern "A"	3.87
LDPE-SCA	Spherulite pattern "A"	3.66
LLDPE-QC	Spherulite pattern "A"	4.82
LLDPE-QCA	Spherulite pattern "C"	6.29
LLDPE-SC	Random pattern "H"	
LLDPE-SCA	Rod pattern "D"	
HDPE-QC	Spherulite pattern "C"	NA
HDPE-QCA	Spherulite pattern "C"	NA
HDPE-SC	Spherulite pattern "B"	5.34
HDPE-SCA	Spherulite pattern "B"	5.66

Previous work by Mandelkern et. al. showed that a variety of structures can be produced for linear and branched polyethylene depending on the molecular weight, quenching temperature, and degree of branching.[79] They related these variables in a 3-D graphic producing an envelope showing spherulitic and non spherulitic structure formations. They also noted that whether the cooling conditions were isothermal or nonisothermal the data merged together well. These test results are in keeping with their findings and will be discussed as the individual data sets are reviewed.

The first of these materials to be considered is LDPE, as shown in Figure 116. Only two patterns were formed, random H pattern for LDPE QC and for QCA and spherulitic B pattern for both the SC and SCA samples. These results are in agreement with the Mandelkern work. The quenched samples fall outside of the envelope indicating non-spherulite structure and the slow cooled samples inside the envelope indicating spherulite structure. These structures show that the

[79] L. Mandelkern, M. Glotin, and R. A. Benson, "Supermolecular structure and thermodynamic properties of linear and branched polyethylenes under rapid crystallization conditions," *Macromolecules* 14, no. 1 (1981).

randomly distributed branched structure of the LDPE molecules does not possess sufficient time or energy to rearrange when quenched to form spherulites, nor is there sufficient time or energy for the rearrangement to occur when the quenched structure is annealed. Conversely, when the material is slow cooled, it is clear that sufficient time and energy are supplied and a well-defined spherulite forms. Likewise, during annealing, sufficient time and energy are provided, thus resulting in a refinement of the spherulite. From these observations it can be said that the predominate structure is formed during the initial solidification, and annealing refines that structure.

These results are in keeping with Mandelkern et al. results. They observed that H type patterns are always produced upon low temperature quenching. They also showed that quenching at high temperatures, which is equivalent to the nonisothernal slow cooled conditions used here, that spherulites formation is seen. They also noted that confirmation of the non-spherulitic pattern require additional analysis by other methods. SEM was used to verify the structure as the image in Figure 122 shows for the LDPE QC.

The second material to be considered is LLDPE, as shown in Figure 117. Spherulites were produced of the A type when quenched diminishing to a C type spherulite upon annealing. The slow cooled and slow cooled annealed samples produced random H and rod D type structure respectively. When these structures were compared to the 3-D envelope from Mandelkern the structures did not match.[80] This is attributed to Mandelkern's branched polyethylene being made from ethylene-butene copolymer or hydrogenated polybutadiene with only one sample having a comparable molecular weight. The material used in this study was made using 2.3% 1-octene co-monomer which gives 23 branches / 1000 carbons. Another study by Defoor et al. focused the morphology of crystals from the melt of 1-octene LLDPE with narrow molecular weight fractions and varying branching content.[81] They melted their samples at 150°C and used only one cooling rate of 5°C/min. Although this cooling rate is closer to the quenching rate used in this study it could be considered an intermediate cooling rate between the quenching and slow cooling used here.

---

[80] Ibid.

[81] F. DeFoor et al., "Molecular, thermal, and morphological characterization of narrowly branched fractions of 1-octene linear low-density polyethylene. 3. Lamellar and spherulitic morphology," *Macromolecules* 26, no. 10 (1993).

Defoor's material had an inverse relationship of branching to molecular weight ranging from 28.2 (CH_3/1000 C) and Mw 49,300 to 2.9 (CH_3/1000 C) and Mw 269,000. Their SALS study showed clear spherulitic formation for the material with comparable branching content but the molecular weight was much lower. For the material with comparable molecular weight but much lower branching content almost no evidence of the spherulite formation was seen. The study shows that the formation of spherulites is heavily dependent on branching content and molecular weight with the tendency to form spherulites favored by increasing branching content and decreased by increasing molecular weight. They describe during the formation of the crystals the branches are rejected to the interface of the crystal resulting in a thinning of the lamella thickness with increasing branch rejection. It is reasonable to conclude that slower cooling rates would allow for the formation of thicker lamellae formation diminishing the possibility of spherulite formation in the slow cooled and annealed samples of this work.

The third material of consideration is HDPE. It formed a C pattern spherulite upon quenching and maintained the structure through annealing. Although a small refinement of the spherulitic pattern is seen, no structurally significant change is evident within the SALS pattern. When the sample was slow cooled, a B pattern spherulite was formed, and only a minimal change was seen during the annealing process evident in the image. This sample's behavior more parallels the behavior of the LDPE than it does the LLDPE in that the initial structure is carried through the annealing process. These results agree very well with those of Mandelkern et al.[82] They note that for linear polyethylene the higher the quench temperature the more highly organized the spherulites become.

After a review of the preceding WTF data, it is clear that the WTF, overall, does decrease with increasing crystallinity, as has been widely discussed in the literature, but these data also show that within any given material type crystallinity is not the sole governing factor. The SALS data shows that each of these three different polymers have different responses to quenching and annealing during formation. The data also shows that the initial structure formed from the melt determines the potential path that any subsequent thermal processing can take. With this new perspective on the structural changes within a given material the WTF data was reexamined.

[82] Mandelkern, Glotin, and Benson, "Supermolecular structure and thermodynamic properties of linear and branched polyethylenes under rapid crystallization conditions."

6.7.3 Effect of Annealing on Water Transfer Flux

Keeping in mind that the structure of the polymer initially formed from the melt is the dominant factor, the WTF are re-plotted to show changes in rate between the quenched and annealed condition for each material and initial heat treatment. The first material, Figure 139, is the LDPE with the QC and QCA heat treatments. In this LDPE both the amorphous thickness and WTF increase. This same trend continues for the SC and SCA heat treatments, shown in Figure 140. The same increase in WTF is seen in the HDPE QC and QCA material in Figure 141. The first departure from these positive trends is seen in Figure 142 with the HDPE SC and SCA sample, where the amorphous thickness decreases but, unfortunately, no WTF data is available because the sample was terminated prematurely during testing. The next material that departs from the clear relationship of increasing amorphous thickness equating to an increase in WTF is the LLDPE. Figure 143 shows the amorphous thickness of the QC and QCA samples increasing but a clear decrease in the WTF rate. This same trend holds for the SC and SCA sample seen in Figure 144. It is believed that these behaviors have not been previously observed because the instrument used for these tests lack sensitive. The newly designed instrument used in this study is more sensitive and able to provide information on WTF arising from subtle structural changes.

The question now becomes what morphological features affect the WTF. Reflecting back to the SALS data both the LDPE and HDPE found in Figure 116 and Figure 118 respectively showed that the supermolecular structure formed from the melt shows little change upon annealing, but the LLDPE found in Figure 117 showed clear structural changes. The SALS image show structure that are three orders of magnitude larger in size than the crystals examined by the other methods. Thus, the structural changes that appear to be governing the WTF are both small scale on the order of the crystal size and super molecular on the order of spherulites. To probe changes that result from these structural changes the DSC crystal size distribution data is considered.

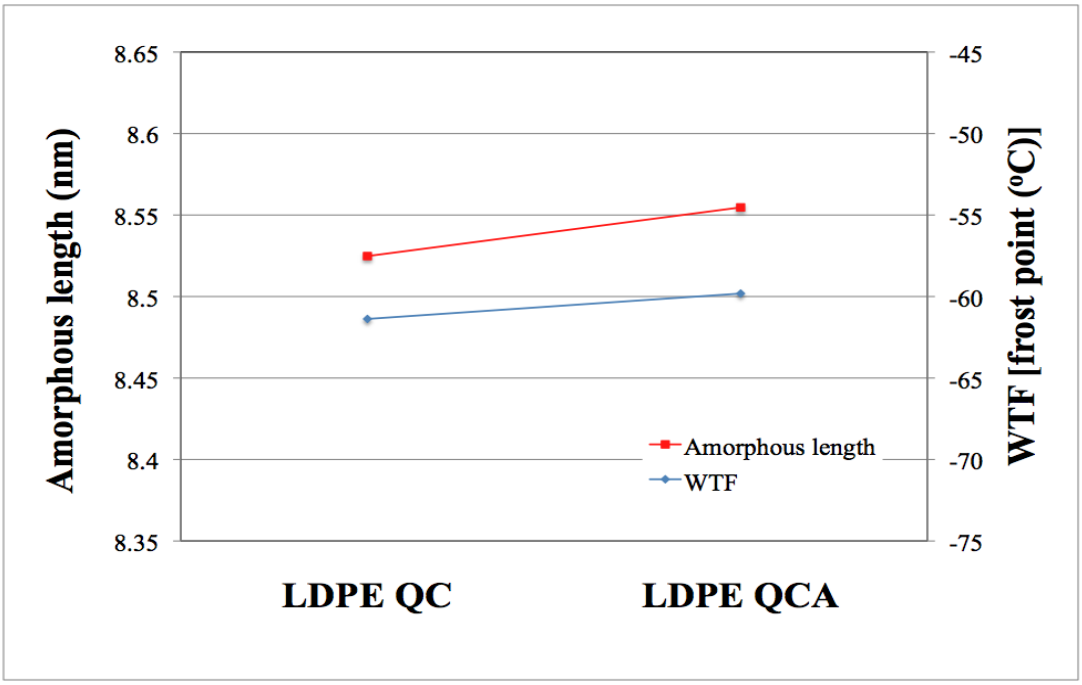

Figure 139. WTF of LDPE QC and QCA versus amorphous thickness.

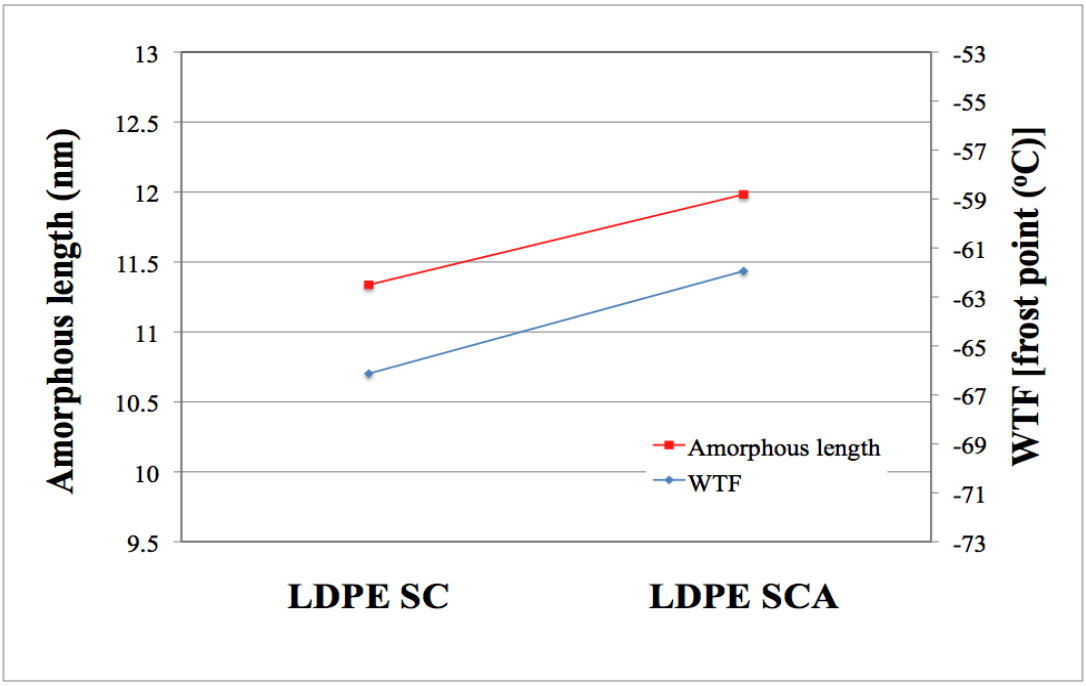

Figure 140. WTF of LDPE SC and SCA versus amorphous thickness.

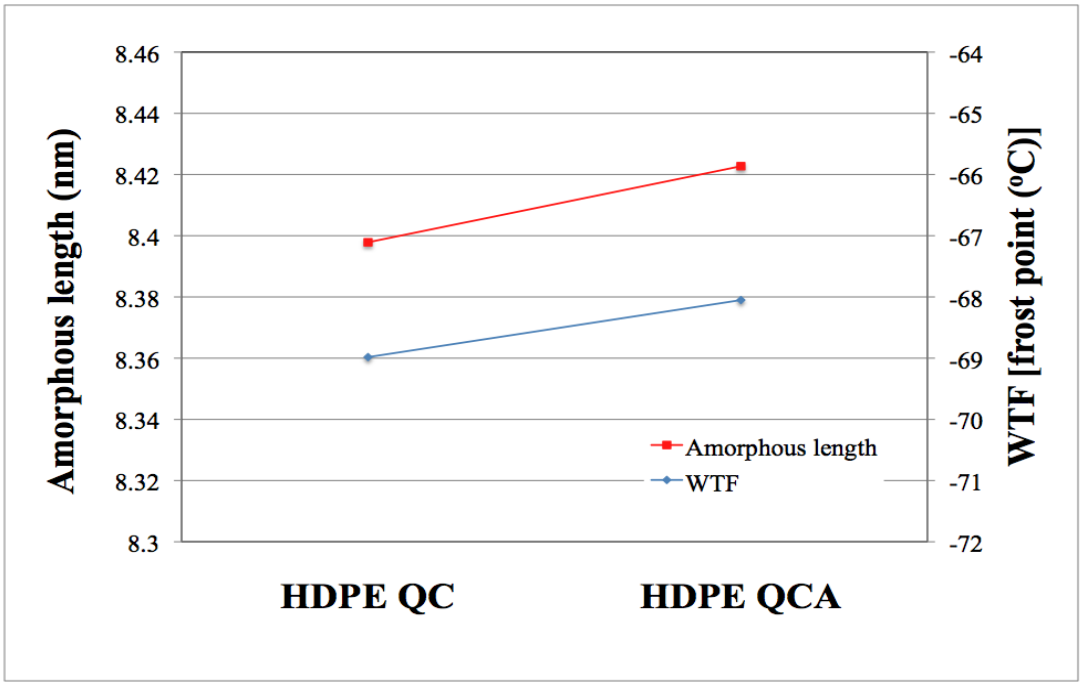

Figure 141. WTF of HDPE QC and QCA versus amorphous thickness.

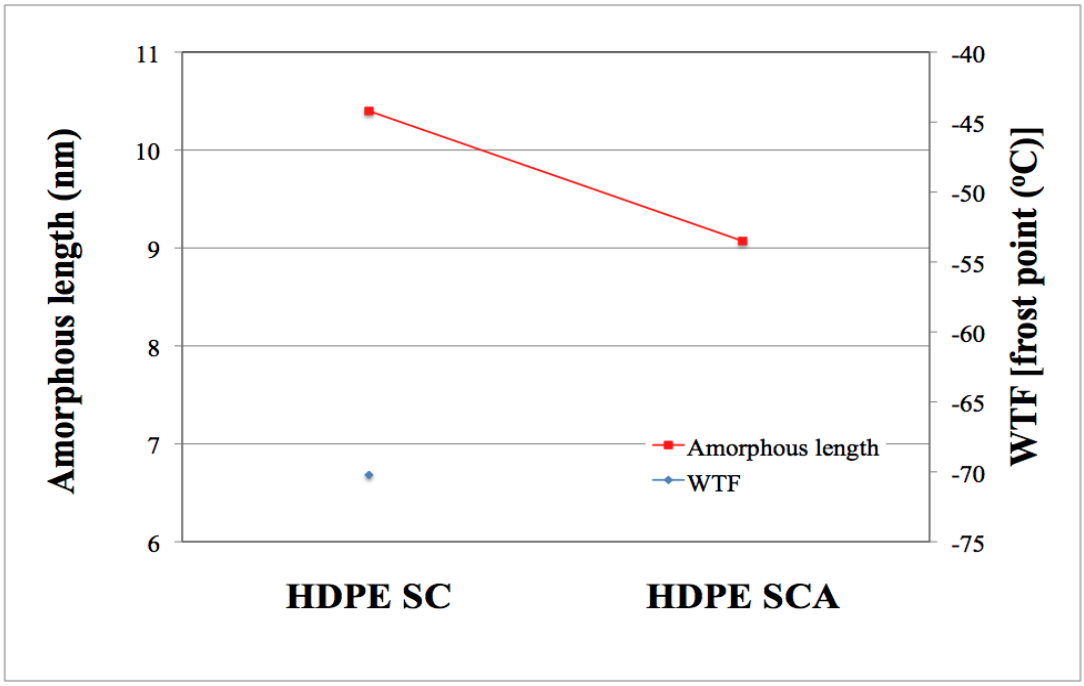

Figure 142. WTF of HDPE SC and SCA versus amorphous thickness.

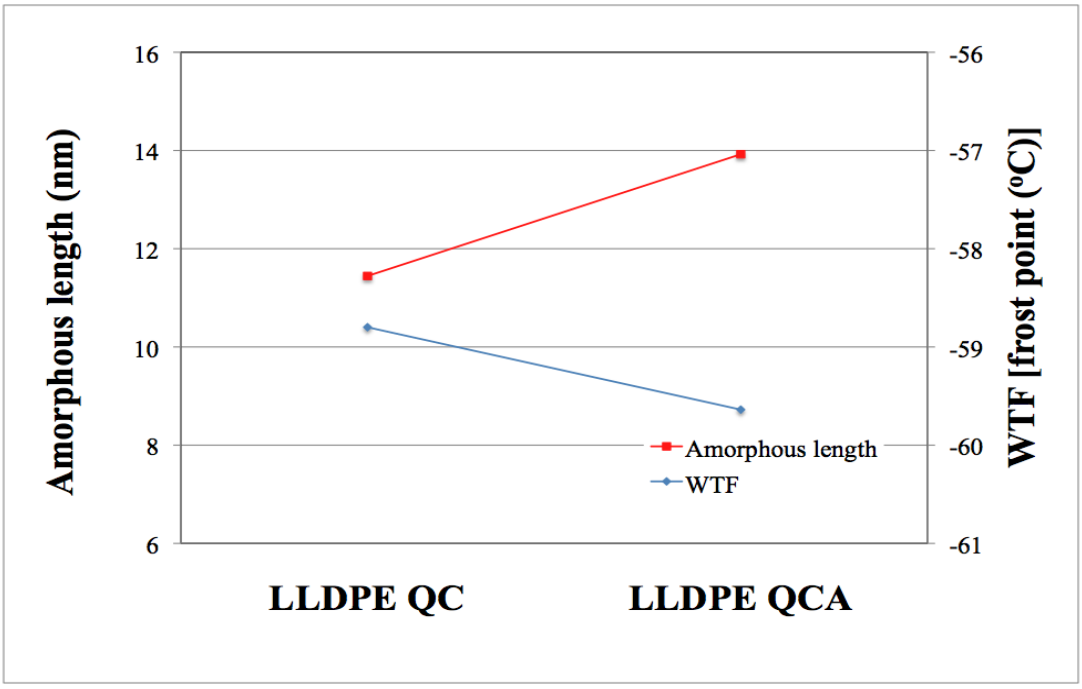

Figure 143. WTF of LLDPE QC and QCA versus amorphous thickness.

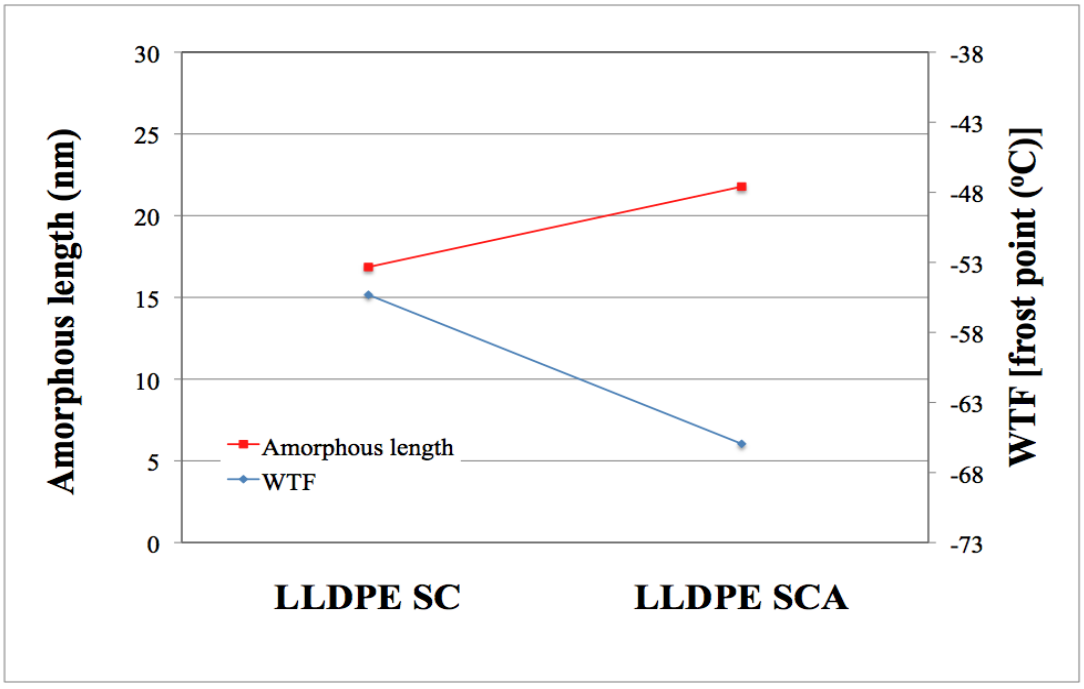

Figure 144. WTF of LLDPE SC and SCA versus amorphous thickness.

The preceding data has shown that the WTF is initially controlled by the structure formed from the melt and secondly by the changes that result from annealing. Figure 99 through Figure 101 shows the distribution of crystal sizes produced by all 12 samples. Some of these data sets show a single size distribution, while others show a bimodal distribution. It is believed that the amorphous phase is incorporated either into the initially formed crystalline structure or new crystals are nucleated and grow in the amorphous phase creating the bimodal distribution and hindering WTF. It is believed that the conversion of the amorphous phase to crystalline phase changes the tortuosity of the path within the amorphous phase that the water moves through.

Figure 99 shows the distribution for the HDPE sample. The QC sample has a narrow distribution, ~±1.5 nm, centered around 8.5 nm, and when annealed the range spreads to, ~±4.0 nm, centered around 15 nm. Obviously, the size and quantity of crystals have increased, but only a single size distribution is seen. The SC sample has a distribution, ~±2.0 nm, centered around 14.5 nm, and when annealed the distribution becomes bimodal. The first of these peaks has a narrow distribution, ~±1.0 nm, centered around 11.5 nm, and the second peak has a very broad distribution, ~±6.0 nm, centered around 18.5 nm. Essentially this data is showing that the existing crystal are growing at the expense of the amorphous phase. As the crystals grow the density increases and the amorphous thickness increases reducing tortuosity in the amorphous phase allowing the increase in WTF.

Figure 100 shows a data set for LDPE. The QC sample has the broadest crystal size distribution of all the LDPE samples. The range is ~±1.5 nm, centered around 8.25 nm. The QCA curve is more symmetric and centered at ~7.5 nm with a range of ~±1.25 nm. The SC curve was centered at ~ 8 nm with a range of ~±1.25 nm. When the SC sample was annealed, the primary peak at 8 nm increased in size and also formed a second peak at ~6.5 nm. The relative amounts of each group can be found in Table 10.

The crystal size distribution data for the LLDPE appears in Figure 101. The QC sample has the broadest distribution. The distribution curve is nonsymmetrical, and the most intense region is at ~11.75 nm and ranges from 6.25 to 13 nm. When the QC was annealed to form the QCA, the curve drastically changed. It became bimodal. The primary curve at 11.79 was slightly reduced, but a whole new peak was formed, centered at ~9.25 nm, which was four times the area of the original curve showing the growth of a large population of a much smaller crystal morphology.

The SC sample was also nonsymmetrical with two peaks centered at ~11 and 12 nm. When it is annealed, a dramatic bimodal distribution is produced. This new distribution has two distinct centers, the first is at ~8.75 nm and the second at ~12.25 nm. In each of the LLDPE annealed samples a bimodal distribution is formed, and the majority of new crystal growth is approximately half the size of the original crystal structure. This growth of the smaller crystals, without a significant reduction of the original primary crystal, is believed to be the controlling structure responsible for reducing the WTF of the annealed LLDPE samples by changing the tortuosity within the amorphous phase. It is also believed to be the cause for the change in the SALS patterns. Figure 145 shows the effect of annealing on the morphology and tortuous path.

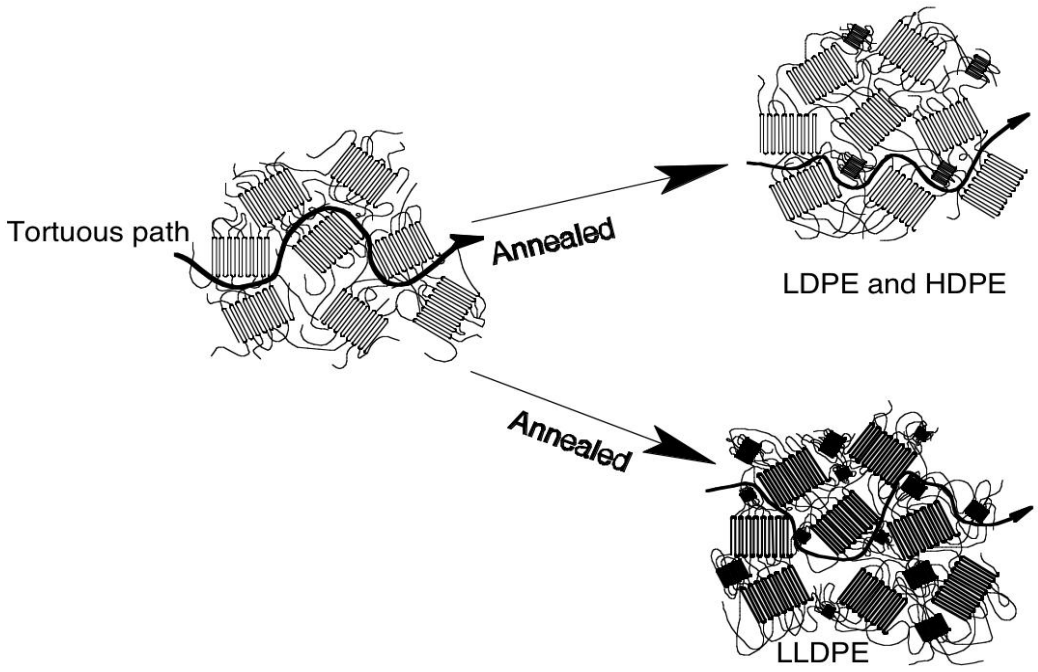

Figure 145, Schematic representation of the effect of annealing on the morphology and tortuous path

Monge et al evaluated annealed LLDPE and studied the effects of annealing on gas diffusivity using positron lifetime spectroscopy.[83] They concluded similar results. They showed that annealing results in changes to size distribution of free volume holes. They also concluded that annealing changes the free volume fraction. They stated that the gas impedance factor, in other

[83] M. A. Monge et al., "Annealing-Induced Enhancement of the Gas Diffusivity in Coextruded LLDPE Films Investigated by Positron Lifetime Spectroscopy," *Macromolecules* 35, no. 21 (2002).

words tortuosity, can be controlled through control of the size distribution of free volume holes of the amorphous phase by annealing. Their data shows by an independent method the structural control of an analogous behavior to the WTF results.

Chapter 7: Conclusions

In conclusion, the pursuit of this work was to evaluate if polymers could be made with a specific WTF behavior. The approach was to test the long-held belief that water moves through the amorphous phase of semi-crystalline polymers but is blocked by the crystalline phase, thus setting up a tortuous path restricting the flow. Polyethylene was chosen as the semi-crystalline polymer because it is a thermoplastic known to form a range of crystallinities through adjustment of the thermal processing during formation. Samples were melt pressed from LDPE, LLDPE, and HDPE. There were four different heat treatments – quenched, quenched and annealed, slow cooled, and slow cooled annealed – used to generate a series of 12 samples with a range of crystallinities. The crystallinity of LLDPE samples ranged from 32.6 to 43.66, LDPE from 40.80 to 51.94, and HDPE 58.57 to 73.29, as measured by DSC under the processing conditions of QC, QCA, SC, and SCA.

Several important observations were made when the frost point data were plotted versus time, sample temperature, and thermal cycle. The first observation was the time it took for the film to achieve a constant and reproducible WTF as a function of not only the chosen polymer but also the processing heat treatment. In most cases the instability in WTF was manifested as a decay in the rate during the initial 60°C thermal soak, at the thermal cycle plateau temperatures, and persisted over multiple thermal cycles. A test to see if the sample has reached steady state was found to be a plot of the frost point WTF versus the bath temperature. In all cases once steady state has been reached, the plot produces a straight line with correlation factors typically of R^2=0.999. This linear response has been named the ultimate linear behavior (ULB).

Two key pieces of information obtained from the ULB is the least squares fitted line which is the WTF as a function of sample temperature and the number of cycles it took to reach steady state is a measure of time delay as a function of heat treatment. In most cases all of the samples for a given polymer group produced the same WTF but the time delay was significantly different. This method has shown the ability to differentiate the subtle differences caused by various heat treatments.

Once the samples achieved steady state, the ULB permeation rate at 20°C were plotted versus degree of crystallinity as determined by DGC, DSC, and WAXD for all 12 polyethylene samples, showing correlation factors of 0.59, 0.51, and 0.46, respectively. Similar plots of WTF versus

crystal thickness, long period, and amorphous thickness showed correlation factors of 0.12, 0.11, and 0.01, respectively. None of these comparisons showed a high degree of agreement. An alternate approach to analyze the data was considered: The WTF data were examined on the basis of the polymer's initial solidification from the melt rather than as if all 12 samples were a homogeneous set only with different degrees of crystallinities.

When the WTF and amorphous thickness were plotted as a function of heat treatment for each polymer, a clear pattern emerged. For all of the LDPE and HDPE samples the amorphous thickness increased upon annealing and so did the WTF. Likewise the amorphous thickness of the LLDPE samples increased upon annealing, but the WTF decreased. An explanation of this behavior was sought in the structure data.

The SALS images showed that the initial solidification structure persists through annealing for both the LDPE and HDPE, but in the LLDPE, annealing clearly changes the structure. Thus, the WTF change has a structural influence. Further supporting evidence of a structural cause for the WTF behavior was found in the crystal size distribution. In the LDPE, annealing caused a shift in crystal size to slightly smaller crystal formation, and the SCA sample showed some indication of a bimodal distribution. In the HDPE annealing caused a shift in crystal to slightly larger crystal formation, again with some indication of a bi-modal distribution in the SCA sample. The LLDPE had a vastly different response to annealing. This material responded to annealing by developing a strong bi-modal crystal distribution. In both the QC and SC samples annealing caused a growth of a new population of smaller crystals with almost no change in the initial crystal formation.

This WTF and crystal size data along with the SALS images strongly suggests that the structure *does* control the WTF. The initial solidification structure establishes an amorphous path with a tortuosity. Tortuosity describes the twist, turns, and narrowing of the amorphous path through which the water moves. Annealing of the LDPE and HDPE causes refinement of the existing crystal structure by incorporation of the amorphous phase into the existing crystal phase. This incorporation reduces the tortuosity by opening the amorphous path through the conversion of the amorphous phase into the crystalline phase. In the LLDPE a different mechanism is followed with the formation of new crystals in the interstitial spaces. This consumes the amorphous phase and increases the tortuosity by placing new crystals in the amorphous pathway, constricting flow.

It is possible to form polymer barriers with predictable WTF. A polymer would have to be chosen and then the initial solidification conditions defined. This would determine the possible WTF behaviors that could be achieved by subsequent heat treatments.

Bibliography

Barrer, Richard M. *Diffusion in and through Solids*. The Cambridge Series of Physical Chemistry. Edited by E. K. Rideal London: Cambridge University Press, 1941.

Bigelow, S. Lawrence, and Adelaide Gemberling. "Collodion Membranes." *Journal of the American Chemical Society* 29, no. 11 (1907): 1576-89.

Boddeker, K. W. "Commentary - Tracing Membrane Science." [In English]. *Journal of Membrane Science* 100, no. 1 (Mar 1995): 65-68.

Campion, R. P., and Industries Materials Technology Institute of the Chemical Process. *Permeation through Polymers for Process Industry Applications* [in English]. St. Louis; [Great Britain]: Materials Technology Institute of the Chemical Process Industries, 2000.

Cussler, E. L. "Diffusion Barriers." *Diffusion Fundimentals* 6 (2007): 72.1 - 72.12.

DeFoor, F., G. Groeninckx, H. Reynaers, P. Schouterden, and B. Van der Heijden. "Molecular, Thermal, and Morphological Characterization of Narrowly Branched Fractions of 1-Octene Linear Low-Density Polyethylene. 3. Lamellar and Spherulitic Morphology." *Macromolecules* 26, no. 10 (1993/05/01 1993): 2575-82.

Donnan, F.G. "Theorie Der Membranegleichgewichte Und Membranpotentiale Bei Vorhandensein Von Nicht Dialysierenden Elektorlyten. Eing Beitrag Zur Physikalisch-Chemischen Physiologie (Theory of Membrane-Equilibria and Membrane Potentials in the Presence of Non-Dialysing Electrolytes. A Contribution to Physical-Chemical Physiology)." *Zeitschrift für Elektrochemie und angewandte physikalishche Chemie* 17 (1911).

Dutrochet, R.J.H. "Nouvelles Observations Sur L"Endomose Et L"Exosmose Et Sur La Cause De Ce Double Phénomène (New Observations on Endosmosis and Exosmosis, and on the Cause of This Dual Phenomenon)." *Annnales de Chimie et de Physique* 35 (1827): 393-400.

Failla, M. D., J. C. Lucas, and L. Mandelkern. "Supermolecular Structure of Random Copolymers of Ethylene." *Macromolecules* 27, no. 6 (1994/03/01 1994): 1334-37.

Fick, A. "Über Diffusion, Poggendorff's Annalen Der Physik Und Chemie." *The London, Edinburgh, and Dublin Philosophcal Magazine and Journal of Science* X (1855): 30-39.

Foskett, Laurence W., Norman B. Foster, William R. Thickstun, and Rex C. Wood. "Infrared Absorption Hygrometer." *Monthly Weather Review* 81, no. 9 (1953/09/01 1953): 267-77.

Fukuda, Mitsuhiro. "Clustering of Water in Polyethylene: A Molecular-Dynamics Simulation." *The Journal of Chemical Physics* 109, no. 15 (1998): 6476-85.

———. "Solubilities of Small Molecules in Polyethylene Evaluated by a Test-Particle-Insertion Method." *The Journal of Chemical Physics* 112, no. 1 (2000): 478-86.

Fukuda, Mitsuhiro, and Satoru Kuwajima. "Molecular-Dynamics Simulation of Moisture Diffusion in Polyethylene Beyond 10 Ns Duration." *The Journal of Chemical Physics* 107, no. 6 (1997): 2149-59.

Graham, T. "Notice of the Singular Inflation of a Bladder." *Quarterly Journal of Science*, no. II (1829): 88-89.

Hallman, Jr Russell Louis, and Michael John Renner. "Fluid Permeability Measurement System and Method." Babcock & Wilcox Technical Services Y-12, LLC, USA . 2008.

Joo, J. C., K. Nam, and J. Y. Kim. "Estimation of Mass Transport Parameters of Organic Compounds through High Density Polyethylene Geomembranes Using a Modifield Double-Compartment Apparatus." *Journal of Environmental Engineering-Asce* 131, no. 5 (May 2005): 790-99.

Knudsen, M. "Die Gesetze Der Molekularströmung Und Der Inneren Reibungsströmung Der Gase Durch Röhren (the Laws of Molecular Flow and of Inner Friction Flow of Gases through Tubes)." *Annalen der Physik* 28 (1909).

Kober, Philip Adolph. "Pervaporation, Perstillation and Percrystallization.1." *Journal of the American Chemical Society* 39, no. 5 (1917): 944-48.

Mandelkern, L. "The Crystalline State." *American Chemical Society* Physical Properties of Polymers (185.

———. "Morphology of Semicrystalline Polymers, Characterization of Materials in Research — Ceramics and Polymers, J. J. Burke and V. Weiss, Eds., Syracuse University Press, Syracuse, N. Y., 1975." *Journal of Polymer Science: Polymer Letters Edition* 15, no. 10 (1975 1977): 635-36.

Mandelkern, L., M. Glotin, and R. A. Benson. "Supermolecular Structure and Thermodynamic Properties of Linear and Branched Polyethylenes under Rapid Crystallization Conditions." *Macromolecules* 14, no. 1 (1981/01/01 1981): 22-34.

Mandelkern, Leo. *Crystallization of Polymers. Vol 2, Vol 2* [in English]. Cambridge: Cambridge University Press, 2004.

———. "Relation between Properties and Molecular Morphology of Semicrystalline Polymers." *Faraday Discussions of the Chemical Society* 68 (1979): 310-19.

Mark, James E. *Physical Properties of Polymer Handbook* [in English]. New York: Springer, 2006.

Massey, Liesl K., and Library Plastics Design. "Permeability Properties of Plastics and Elastomers a Guide to Packaging and Barrier Materials." Plastics Design Library : William Andrew Pub., http://www.knovel.com/knovel2/Toc.jsp?BookID=752.

Mitchell, J.K. "On the Penetrativeness of Fluids." *The Journal of the Royal Institution of Great Britian*, no. IV (1831): 101-18.

Monge, M. A., J. P. G. Villaluenga, A. Muñoz, T. Leguey, and R. Pareja. "Annealing-Induced Enhancement of the Gas Diffusivity in Coextruded Lldpe Films Investigated by Positron Lifetime Spectroscopy." *Macromolecules* 35, no. 21 (2002/10/01 2002): 8088-92.

Montgomery, C.D., J.M. Googin, and L.R. Phillips. "Moisture Monitor Testing and Calibration." In *Other Information: Orig. Receipt Date: 31-DEC-63*, Medium: X; Size: Pages: 26, 1963.

Naylor, K. L., and P. J. Phillips. "Optimization of Permanganic Etching of Polyethylenes for Scanning Electron Microscopy." *Journal of Polymer Science: Polymer Physics Edition* 21, no. 10 (1983): 2011-26.

Nollet, and John Colson. *Lectures in Experimental Philosophy*. London: Printed for J. Wren ... 1752.

Nollet, J.A. "Recherches Sur Les Causes Du Bouillonnement Des Liquides (Investigations on the Causes for the Ebullition of Liquids)." *Histoire de l'Académie Royale des Sciences* (1752): 57-104.

Olley, R. H., and D. C. Bassett. "An Improved Permanganic Etchant for Polyolefines." *Polymer* 23, no. 12 (1982): 1707-10.

Plaza, Alphonse, and Richard S. Stein. "The Scattering of Light from Polyethylene Films at Low Angles." *Journal of Polymer Science* 40, no. 136 (1959): 267-70.

Reynolds, William C. *Thermodynamic Properties in Si : Graphs, Tables, and Computational Equations for Forty Substances* [in English]. Stanford, CA: Dept. of Mechanical Engineering, Stanford University, 1979.

Rhodes, Marion B., Daniel A. Keedy, and Richard S. Stein. "The Use of a Laser as a Light Source for Photographic Light Scattering from Polymer Films." *Journal of Polymer Science* 62, no. 174 (1962): S73-S74.

Shewmon, Paul. *Diffusion in Solids* [in English]. Warrendale, Pa: TMS, 1989.

Stein, Richard S., and Marion B. Rhodes. "Photographic Light Scattering by Polyethylene Films." *Journal of Applied Physics* 31, no. 11 (1960): 1873-84.

Stephens, C. P., R. S. Benson, and M. Chipara. "Radiation Induced Modifications in Ultra-High Molecular Weight Polyethylene." *Surface and Coatings Technology* 201, no. 19–20 (2007): 8230-36.

Stern, S. A. "The "Barrer" Permeability Unit." *Journal of Polymer Science Part A-2: Polymer Physics* 6, no. 11 (1968): 1933-34.

van 't Hoff, J.H. "Die Rolle Des Osmotishcen Druckes in Der Analogie Zwischen Lösungen Und Gasen (the Role of Osmotic Pressure in the Analogy between Solutions and Gases)." *Zeitschrift für Physikalische Chemie* 1 (1887): 481-508.

Wunderlich, B. *Macromolecular Physics: Crystal Nucleation, Growth, Annealing*. Academic Press, 1976.

Wunderlich, Bernhard. "Chapter Vii - the Annealing of Crystals." In *Macromolecular Physics*. 348-435: Academic Press, 1976.

Appendices

Appendix A

Density Gradient Column Preparation

The density gradient column is a glass tube filled with a fluid in such a manner that the densest fluid resides at the bottom and the least dense fluid is at the top. The filling method generates a gradual change in density from the bottom to the top. This technique is ideal for determining the density of materials. Before the column can be filled, a density range must be defined such that the range includes the density of all samples to be tested. Refer to ASTM D 1505 for suggested solutions with the appropriate range. Frequently various alcohol–water mixtures are used.

Figure A.1 shows a differential gradient column including a cooling jacket to maintain the column at a constant temperature. Define the density at the bottom of the column as ρA and the density at the top as ρt. The column is filled from a doubled-walled mixer, as Figure A.2 shows. The solutions used to fill the double-walled mixer are determined on the basis of the densities chosen for ρb and ρt. Solution A, used in the inner cylinder of the mixer, has the same density as that of the bottom of the column, ρA. The mixing ratio, (xA) weight fraction, corresponding to ρA of solvent and solute may be found in *CRC Handbook of Chemistry and Physics*. The mixing ratio for solution *B*, *xB*, used in the outer cylinder of the mixer, does not correspond to the concentration of solution at the top of the column but, instead, must be adjusted to provide more solution than that needed just to fill the column. This additional solution provides for constant flow throughout the filling process and leaves a portion of the solution in the double-walled mixer once the column is full. To provide for the additional solution the density range will be expanded by 50%. This is as if the column's length and density range has been expanded, as in Figure A.3. This additional length is not actually added to the top of the column, but the concept is used to demonstrate the increase in solution volume and the corresponding continuation of the column's decreasing density gradient.

The density of the solution at the top of the extended column is determined as follows in :

Equation A. 1

$$\rho B = \rho t - (\rho A - \rho t) / 2$$

The concentration of solution B, xB, corresponding to density ρB is found using the tables found in the *CRC Handbook of Chemistry and Physics*. Interpolation may be used for greater accuracy or a curve may be fitted to the full range of densities to establish the relationship of percent solute to density.

Before determining the mass of each solution used to fill the double-walled mixer, mA and mB, the mass of the solute and solvent in the extended column will be found using the average density determined as follows in :

Equation A. 2

$$xS = (xA + xB) / 2$$

Using the average solution concentration, xS, and the *CRC Handbook of Chemistry and Physics*, the average solution density, ρS, can be found. The solution density, ρS, will now be used in the following equation, , to determine the initial mass of each solution, mA and mB, needed.

Equation A. 3

$$m = mB = mA = (1.5 \bullet Vt \bullet \rho S) / 2,$$

where Vt is the volume of the column, 1134.11 cm^3.

Both masses mA and mB will be adjusted to account for establishing flow within the system. An additional 30 mL will be added to solution A, mA, to account for filling the tubing used to convey the solution from the mixer to the column. In a similar manner an additional 4% will be added to solution B, mB, to account for the tubing that connects compartments A and B of the mixer. The following equations, presented together as , may be used.

Equation A. 4

$$mA = m + 30 \bullet \rho b$$

and

$$mB = m \bullet 1.04 \quad .$$

The mass of each component of solutions A and B are shown below in :

Equation A. 5

Solution A

m1A = mA • xA Solute
m2A = mA • (1 – xA) Solvent

Solution B

m1B = mB • xB Solute
m2B = mB • (1 – xB) Solvent

The following example calculations, in , have been provided for the construction of a DGC using isopropanol, (a.k.a. 2 propanol).

Equation A. 6

ρA = 0.9816 Density at bottom of column (same as density of solution A)
ρt = 0.8504 Density at top of column
xb = 10 wt% Corresponding concentration at bottom of column (from CRC handbook)
ρB = ρt – (ρA - ρt) / 2 Density at top of extended column (same as solution B)
= 0.8504 – (0.9816 – 0.8504) / 2
= 0.7848
xB = 100 wt% Concentration at top of extended column (from CRC handbook)
xS = (xb + xB) / 2 Average concentration of solution including extension
= (10 + 100) / 2
= 55 wt%
ρS = 0.894 Average density of column (from CRC handbook)
m = (1.5 • Vt • ρS) / 2 Initial mass of solutions A and B
= (1.5 • 1134.11 • 0.894) / 2
= 760.8 g

mA = m + 30 • ρA Corrected mass of solution A
= 760.8 + 30 • 0.9816
= 790.2 g

mB = m • 1.04 Corrected mass of solution B
= 760.8 • 1.04
= 791.2 g

Solution A

m1A = mA • xA Solute (isopropanol)
= 790.2 • 0.10
= 79.0 g
m2A = mA • (1 – xA) Solvent (water)
= 790.2 • (1 - 0.10)
= 711.2 g

Solution B

m1B = mB • xB Solute (isopropanol)
= 791.2 • 1.00
= 791.2 g

m2B = mB • (1 – xB) Solvent (water)
= 791.2 • (1 – 1.00)
= 0.00 g

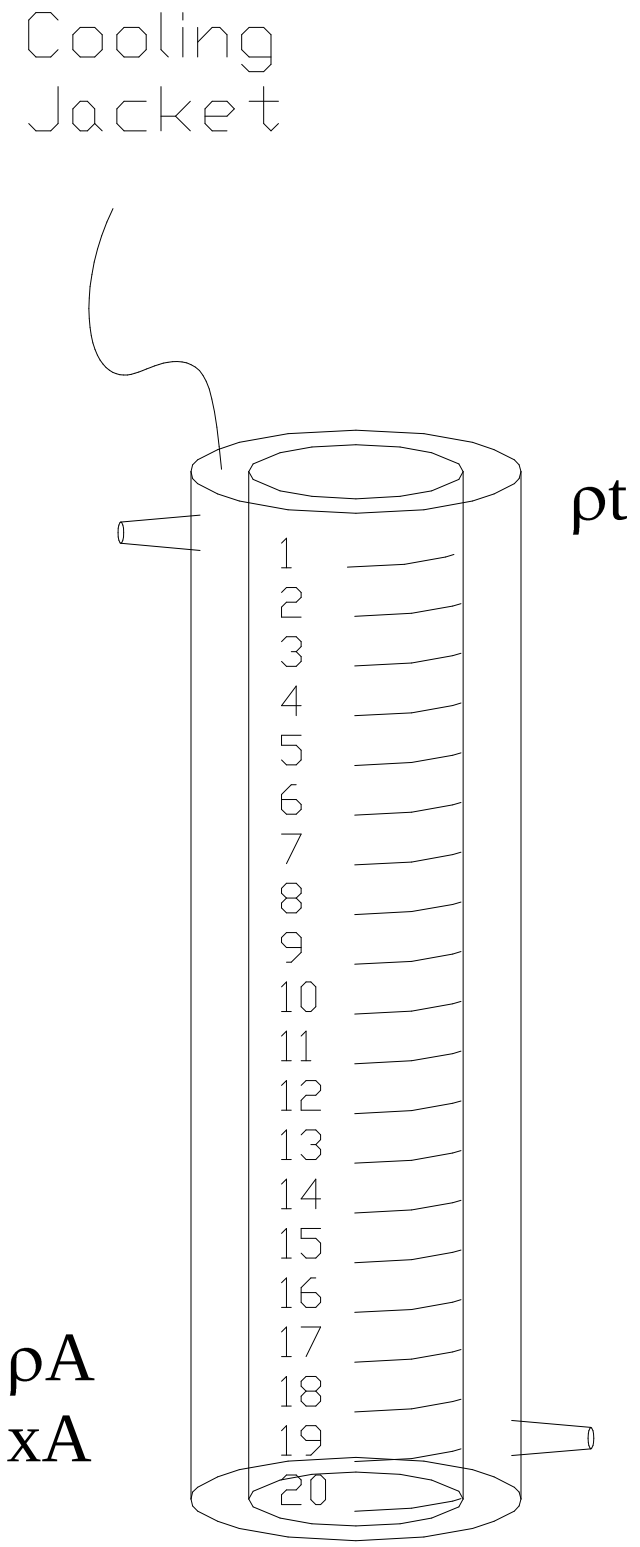

Figure A. 1. Density gradient column showing cooling jacket.

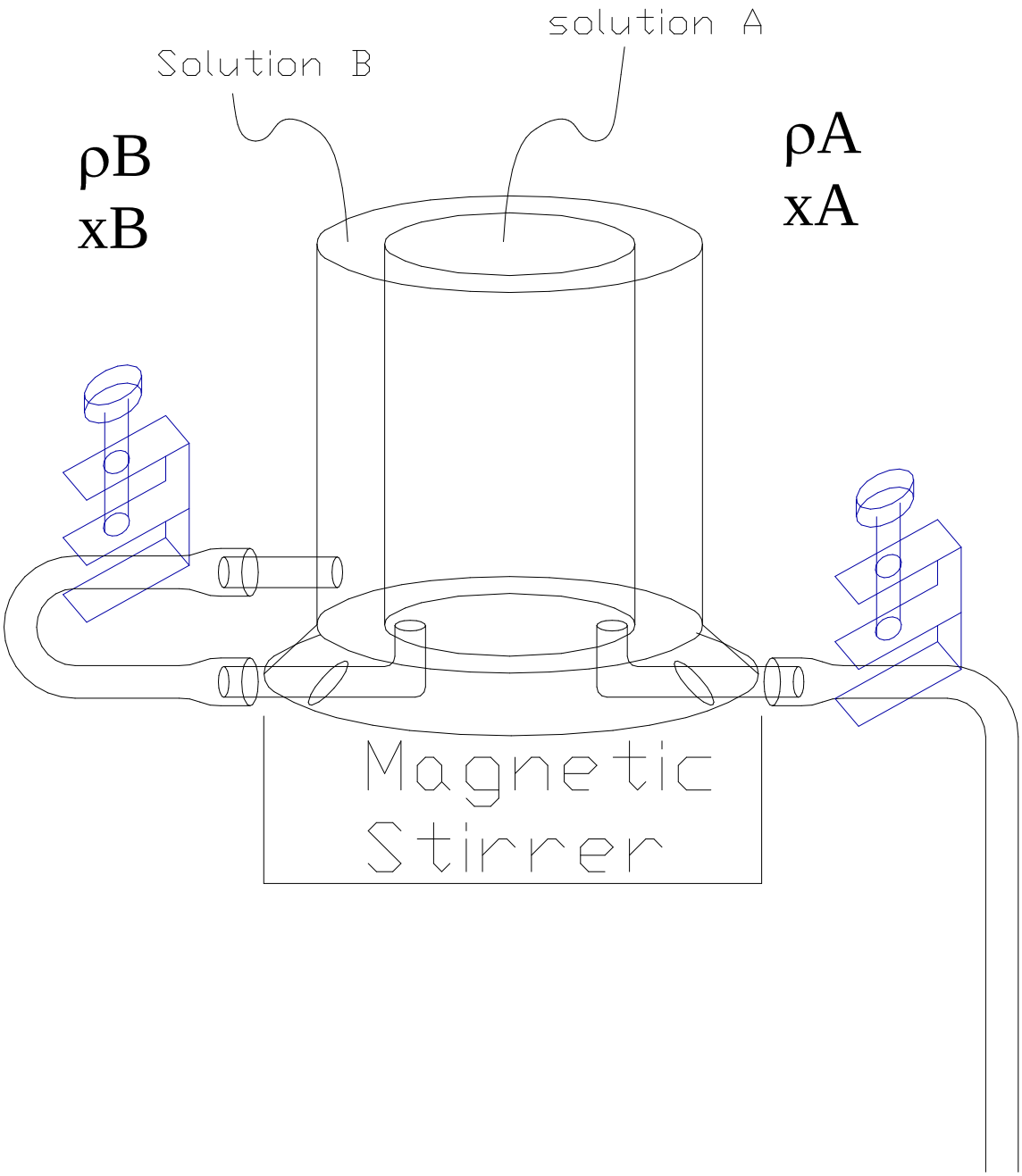

Figure A. 2. Double-walled mixer with magnetic stirrer.

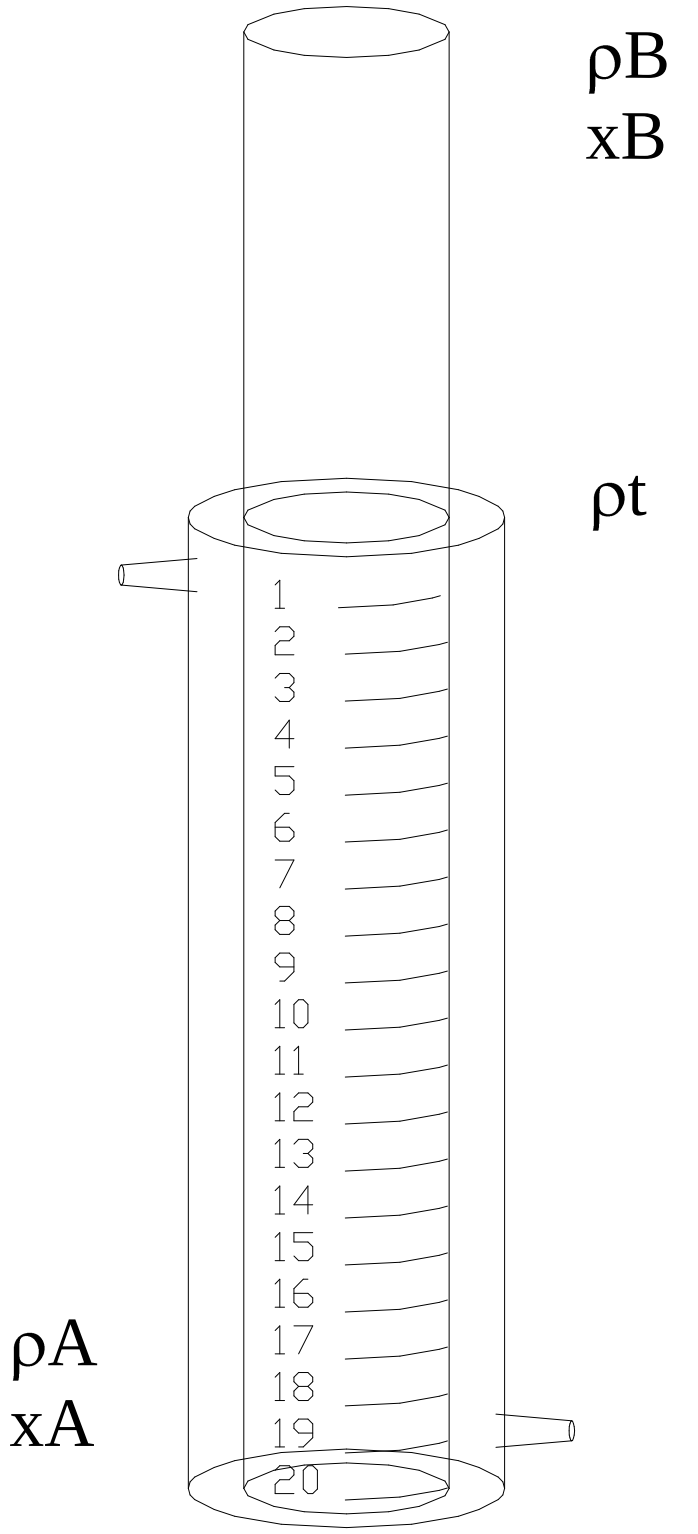

Figure A. 3. Density gradient column with 50% extension.

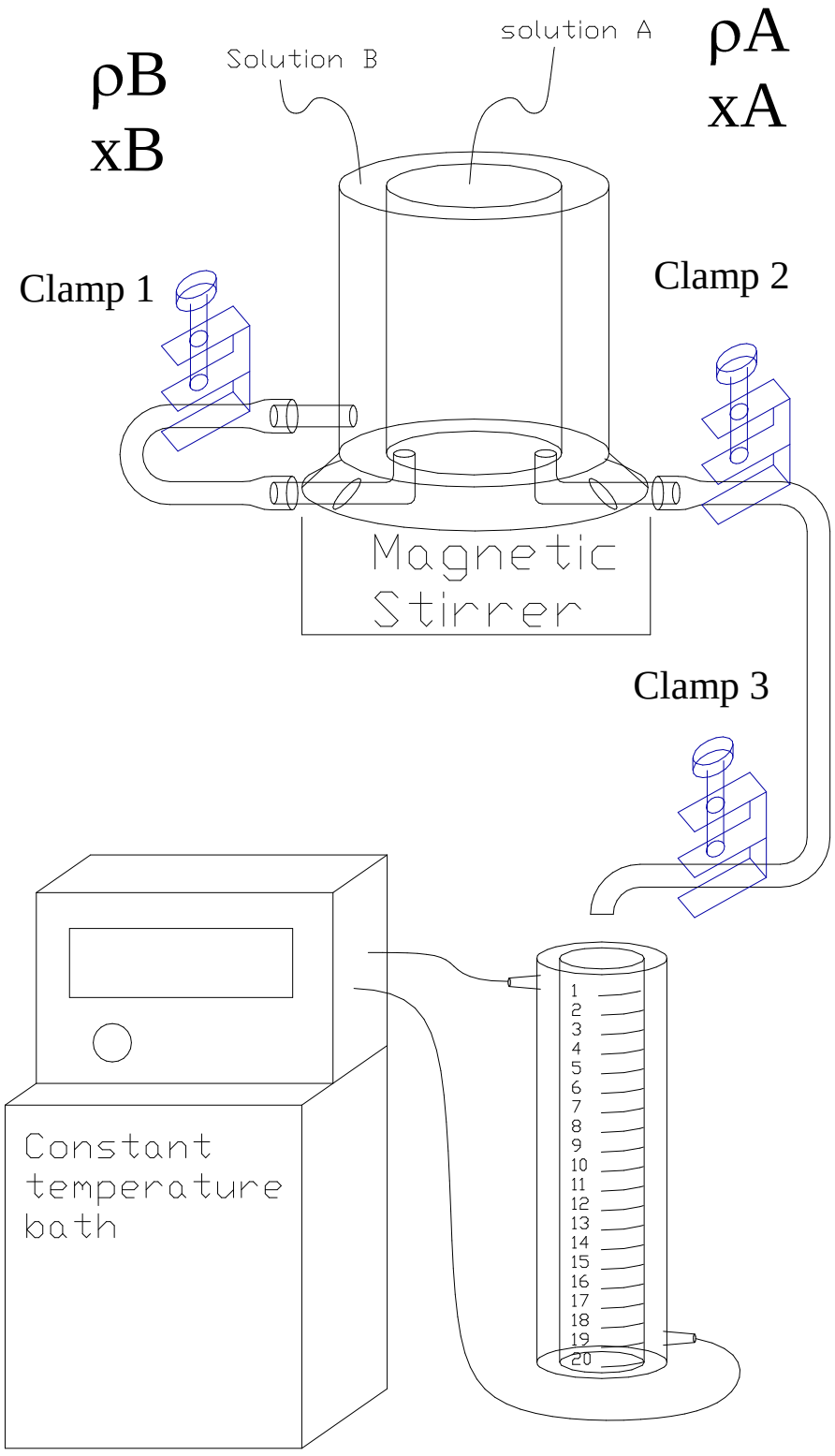

Figure A. 4. Density gradient column with double-walled mixer and constant cooling bath.

Column filling

1. Begin by weighing the solute and solvent and placing them in an Erlenmeyer flask.

2. Evacuate the solution until it boils to degas the dissolved air (if air remains in the solution, bubbles may form on samples and density gradient beads obscuring their true density)

3. Allow the temperature of the flask to equilibrate.

4. Make sure hose clamps 1, 2, and 3 are closed see Figure 4. Pour solution B, the least dense solution, into the outer cylinder of the double-walled mixer. Open clamp 1 to allow for the solution to fill the connecting tube and then close. Pour solution A, the densest solution, into the center cylinder of the mixer. Open clamps 2 and 3 to fill the hose, close clamp 3.

5. Add a stirring bar to the inner cylinder and start the stirring on low.

6. The next few steps must be performed quickly because once the filling process has started, it cannot be stopped. A 50 ml graduated cylinder and a stopwatch is needed before proceeding. 30 ml of solution are released from the filling tube through clamp 3 to establish the flow rate. The actual mixed solution will reach the end of the tube after the 30 ml has been drained.

7. Using the graduated cylinder monitor the flow rate and adjust clamp 3 to produce a 15 ml/min flow rate.

8. Place the end of the tube in the column and position the tube so the flow runs down the wall of the column. It should take about 45 seconds for the level to increase 1cm or one major division. Adjust the flow as necessary to maintain this fill rate.

9. Monitor the stirring to ensure it does not stop. This can ruin the column.

10. When the column is filled, close clamps 1 and 3. Drain the solution from the inner cylinder and retain for wetting samples later.

11. Add the appropriate density indicator beads so they are spaced throughout the column. 5 or 6 beads well spaced will yield a good indication of the columns density. Place the beads in the metal basket and lower the basket using the motor drive. Look to make sure bubbles are not trapped on the basket or beads as they are lowered. If bubbles are found raise and lower the basket and beads using the motor drive to displaced the bubbles. Once the basket reached the bottom tape the line to the side of the column to prevent accidental movement. Place a stopper in the top of the column to prevent evaporation.

12. Allow 24 hours for the column to equilibrate. Plot the position of the beads.

13. To place a sample in the column, wet it in the retained solution A. The sample is then held with tweezers slightly below the liquid level in the column and released. Depending on the size of the sample it may take 30 minutes to 6 hours to equilibrate.

Appendix B

Variable Temperature Density Gradient Column (VT-DGC) – Additional data

Table B. 1

Table 13. Densities and degree of crystallinities for LDPE, LLDPE, and HDPE determined by VT-DGC at 20ºC

		2	3	4	5	6
Density Measurements (g/cm^3) Degree of Crystallinity	LDPE QC	0.929	0.929	0.928	0.929	0.929
		50.1	50.1	49.8	50.1	50.5
	LDPE QC annealed	0.934	0.934	0.934	0.934	0.935
		54.0	54.0	53.9	54.0	54.3
	LDPE SC	0.934	0.936	0.935	0.935	0.935
		53.5	54.8	54.4	54.3	54.5
	LDPE SC annealed	0.936	0.936	0.936	0.935	0.936
		55.0	55.0	54.8	54.7	55.0
	LLDPE QC	0.923	0.924	0.924	0.924	0.925
		46.5	46.7	46.6	46.9	47.6
	LLDPE QC annealed	0.933	0.933	0.933	0.933	0.934
		52.9	53.2	53.0	53.0	53.4
	LLDPE SC	0.934	0.934	0.934	0.934	0.935
		53.5	53.8	53.6	53.5	54.2
	LLDPE SC annealed	0.934	0.934	0.934	0.934	0.935
		53.7	53.8	53.8	53.7	54.1
	HDPE QC	0.947	0.947	0.947	0.947	0.948
		62.3	62.5	62.7	62.7	63.0
	HDPE QC annealed	0.957	0.957	0.957	0.957	0.957
		69.7	69.7	69.7	69.6	69.5
	HDPE SC	0.961	0.961	0.961	0.961	0.961
		72.2	72.2	72.2	72.2	72.1
	HDPE SC annealed	0.963	0.963	0.963	0.963	0.963
		73.4	73.5	73.4	73.3	73.3

Table B. 2

Table 14. Densities and degree of crystallinities for LDPE, LLDPE, and HDPE determined by VT-DGC at 25ºC

		1U	1D	2U	2D	3U	3D	4U	4D	5U	5D	6U	6D
Density Measurements (g/cm^3) Degree of Crystallinity	LDPE QC	0.926	0.925	0.925	0.925	0.925	0.925	0.925	0.925	0.925	0.925	0.925	0.925
		48.5	47.5	47.7	47.5	47.5	47.5	47.5	47.7	47.5	47.3	47.5	47.4
	LDPE QC annealed	0.932	0.931	0.931	0.931	0.931	0.931	0.931	0.931	0.931	0.931	0.931	0.931
		52.4	51.7	51.7	51.6	51.7	51.6	51.4	51.6	51.5	51.4	51.4	51.7
	LDPE SC	0.933	0.932	0.932	0.932	0.932	0.931	0.931	0.931	0.931	0.931	0.931	0.931
		53.0	52.2	52.3	52.1	52.2	52.0	52.0	52.0	51.9	51.8	51.8	52.0
	LDPE SC annealed	0.933	0.932	0.932	0.932	0.932	0.932	0.932	0.932	0.932	0.932	0.932	0.932
		53.3	52.7	52.7	52.5	52.6	52.4	52.3	52.4	52.3	52.2	52.1	52.3
	LLDPE QC	0.922	0.919	0.919	0.919	0.919	0.919	0.919	0.920	0.919	0.920	0.920	0.919
		45.2	43.7	43.8	43.7	43.6	43.8	43.6	44.1	43.8	43.9	43.9	43.8
	LLDPE QC annealed	0.931	0.930	0.930	0.930	0.930	0.930	0.930	0.930	0.930	0.930	0.930	0.930
		51.6	50.8	51.0	50.7	50.7	50.8	50.8	51.0	50.9	50.9	50.9	51.1
	LLDPE SC	0.931	0.930	0.931	0.930	0.930	0.930	0.930	0.930	0.930	0.930	0.930	0.930
		51.7	51.3	51.6	51.3	51.3	51.3	51.2	51.2	51.3	51.1	51.2	51.3
	LLDPE SC annealed	0.931	0.931	0.931	0.931	0.931	0.931	0.930	0.931	0.931	0.930	0.931	0.931
		52.0	51.5	51.5	51.4	51.5	51.4	51.3	51.5	51.4	51.3	51.5	51.5
	HDPE QC	0.944	0.945	0.944	0.945	0.945	0.945	0.945	0.945	0.945	0.945	0.945	0.952
		60.4	60.9	60.9	61.2	61.1	61.1	61.1	61.2	61.2	61.3	61.3	66.3
	HDPE QC annealed	0.955	0.956	0.956	0.956	0.956	0.956	0.956	0.956	0.956	0.956	0.956	0.955
		67.9	68.5	68.5	68.6	68.5	68.7	68.6	68.5	68.6	68.7	68.8	68.2
	HDPE SC	0.959	0.959	0.959	0.960	0.960	0.960	0.960	0.959	0.960	0.960	0.960	0.958
		70.5	71.0	71.1	71.2	71.3	71.2	71.2	71.1	71.2	71.2	71.2	70.2
	HDPE SC annealed	0.960	0.961	0.961	0.961	0.961	0.961	0.961	0.961	0.962	0.961	0.961	0.960
		71.6	72.2	72.2	72.3	72.3	72.3	72.4	72.3	72.5	72.4	72.4	71.1

Table B. 3

Table 15. Densities and degree of crystallinities for LDPE, LLDPE, and HDPE determined by VT-DGC at 30ºC

Density Measurements (g/cm^3) / Degree of Crystallinity													
	LDPE QC	0.924	0.923	0.923	0.923	0.923	0.923	0.923	0.923	0.923	0.923	0.923	0.925
		46.6	46.1	46.3	46.3	46.2	46.1	46.3	46.0	46.0	46.0	45.9	47.4
	LDPE QC annealed	0.929	0.928	0.929	0.928	0.928	0.928	0.928	0.928	0.928	0.928	0.928	0.931
		50.2	50.0	50.0	49.9	49.9	49.7	49.8	49.7	49.7	49.7	49.7	51.7
	LDPE SC	0.929	0.929	0.929	0.929	0.929	0.929	0.929	0.929	0.929	0.929	0.929	0.931
		50.6	50.4	50.4	50.3	50.1	50.2	50.1	50.1	50.0	50.1	50.0	52.0
	LDPE SC annealed	0.930	0.930	0.930	0.930	0.930	0.930	0.931	0.930	0.931	0.931	0.931	0.932
		51.3	51.1	51.0	51.0	51.1	51.0	51.4	51.1	51.4	51.6	51.9	52.3
	LLDPE QC	0.918	0.917	0.917	0.917	0.917	0.917	0.918	0.918	0.917	0.917	0.917	0.919
		43.1	42.2	42.3	42.4	42.4	42.5	42.6	42.5	42.5	42.5	42.4	43.8
	LLDPE QC annealed	0.928	0.927	0.928	0.927	0.927	0.927	0.928	0.927	0.927	0.927	0.927	0.930
		49.4	49.3	49.3	49.2	49.1	49.1	49.3	49.1	49.2	49.3	49.2	51.1
	LLDPE SC	0.928	0.928	0.928	0.928	0.928	0.928	0.928	0.928	0.928	0.928	0.928	0.930
		49.7	49.7	49.7	49.4	49.5	49.5	49.7	49.5	49.5	49.6	49.5	51.3
	LLDPE SC annealed	0.928	0.928	0.928	0.928	0.928	0.928	0.928	0.928	0.928	0.928	0.928	0.931
		50.0	50.0	49.9	49.8	49.8	49.6	49.7	49.6	49.6	49.7	49.6	51.5
	HDPE QC	0.942	0.942	0.942	0.942	0.942	0.942	0.942	0.943	0.943	0.943	0.943	0.952
		59.0	59.4	59.3	59.5	59.4	59.3	59.4	59.7	59.7	59.9	59.8	66.3
	HDPE QC annealed	0.953	0.954	0.953	0.954	0.954	0.954	0.954	0.954	0.954	0.954	0.954	0.955
		66.7	67.0	67.0	67.1	67.0	67.1	67.1	67.2	67.2	67.2	67.1	68.2
	HDPE SC	0.957	0.957	0.957	0.957	0.958	0.957	0.958	0.958	0.958	0.957	0.957	0.958
		69.3	69.7	69.6	69.6	69.9	69.6	69.8	69.7	69.7	69.5	69.5	70.2
	HDPE SC annealed	0.959	0.959	0.959	0.959	0.960	0.959	0.959	0.959	0.959	0.959	0.959	0.960
		70.6	70.9	70.8	71.1	71.2	71.0	71.0	71.1	71.1	70.7	70.6	71.1

Table B. 4

Table 16. Densities and degree of crystallinities for LDPE, LLDPE, and HDPE determined by VT-DGC at 35ºC

		1U	1D	2U	2D	3U	3D	4U	4D	5U	5D	6U	6D
Density Measurements (g/cm³) Degree of Crystallinity	LDPE QC	0.920	0.920	0.919	0.920	0.920	0.920	0.920	0.920	0.919	0.919	0.919	0.919
		44.0	43.9	43.6	44.0	44.1	44.0	44.0	44.1	43.8	43.7	43.6	43.5
	LDPE QC annealed	0.925	0.925	0.925	0.925	0.925	0.924	0.925	0.925	0.924	0.924	0.924	0.924
		47.7	47.3	47.5	47.3	47.5	47.2	47.3	47.5	47.0	46.8	46.8	46.7
	LDPE SC	0.926	0.926	0.925	0.925	0.926	0.925	0.925	0.925	0.925	0.925	0.924	0.924
		48.1	48.0	47.7	47.7	48.0	47.7	47.8	47.9	47.5	47.3	47.2	47.2
	LDPE SC annealed	0.927	0.927	0.927	0.927	0.927	0.927	0.927	0.927	0.927	0.927	0.927	0.927
		48.9	48.6	48.7	48.7	48.9	48.8	49.0	49.3	48.6	49.0	49.1	49.1
	LLDPE QC	0.915	0.915	0.915	0.915	0.915	0.915	0.915	0.915	0.915	0.915	0.915	0.915
		40.8	40.5	40.7	40.5	40.9	40.7	40.7	40.9	40.6	40.7	40.7	40.7
	LLDPE QC annealed	0.924	0.924	0.924	0.924	0.924	0.924	0.924	0.924	0.924	0.923	0.923	0.923
		47.1	46.8	46.8	46.8	47.0	46.7	46.8	47.0	46.6	46.5	46.3	46.3
	LLDPE SC	0.925	0.924	0.925	0.924	0.925	0.924	0.924	0.925	0.924	0.924	0.924	0.924
		47.3	47.1	47.3	47.3	47.3	47.1	47.2	47.3	46.9	46.8	46.7	46.8
	LLDPE SC annealed	0.925	0.925	0.925	0.925	0.925	0.924	0.925	0.925	0.924	0.924	0.924	0.924
		47.7	47.6	47.5	47.4	47.5	47.1	47.3	47.5	47.0	47.0	46.8	46.8
	HDPE QC	0.939	0.940	0.940	0.940	0.940	0.940	0.940	0.940	0.940	0.940	0.940	0.940
		57.4	57.6	57.6	57.6	57.7	57.6	57.8	58.1	57.6	57.6	57.6	57.6
	HDPE QC annealed	0.951	0.951	0.951	0.951	0.951	0.951	0.952	0.952	0.952	0.952	0.951	0.951
		65.5	65.5	65.6	65.5	65.6	65.6	65.8	65.8	65.7	65.7	65.6	65.6
	HDPE SC	0.956	0.955	0.955	0.955	0.956	0.956	0.956	0.956	0.956	0.956	0.956	0.956
		68.4	68.2	68.3	68.3	68.4	68.4	68.4	68.4	68.4	68.5	68.4	68.5
	HDPE SC annealed	0.957	0.957	0.958	0.957	0.957	0.957	0.958	0.957	0.958	0.958	0.958	0.958
		69.6	69.7	69.8	69.7	69.7	69.6	69.8	69.6	69.8	70.0	69.8	69.8

Table B. 5

Table 17. Densities and degree of crystallinities for LDPE, LLDPE, and HDPE determined by VT-DGC at 40ºC

Density Measurements (g/cm^3) Degree of Crystallinity													
	LDPE QC	0.917	0.916	0.916	0.916	0.916	0.916	0.916	0.916	0.916	0.920	0.916	0.916
		41.9	41.6	41.8	41.7	41.7	41.6	41.5	41.7	41.5	44.0	41.5	41.4
	LDPE QC annealed	0.921	0.921	0.921	0.921	0.921	0.921	0.921	0.921	0.921	0.925	0.920	0.920
		45.2	44.9	45.0	45.0	44.9	44.9	44.9	44.7	44.6	47.3	44.5	44.5
	LDPE SC	0.923	0.922	0.922	0.922	0.922	0.922	0.923	0.923	0.923	0.925	0.924	0.923
		46.1	45.5	45.8	45.5	45.9	45.7	46.1	46.0	46.3	47.8	46.7	46.2
	LDPE SC annealed	0.923	0.923	0.924	0.923	0.923	0.923	0.923	0.924	0.924	0.927	0.924	0.924
		46.4	46.3	47.1	46.6	46.6	46.5	46.6	46.9	46.8	49.0	47.1	47.2
	LLDPE QC	0.911	0.911	0.911	0.911	0.911	0.911	0.911	0.911	0.911	0.915	0.911	0.911
		38.3	38.0	38.3	38.1	38.1	38.2	38.2	38.3	38.1	40.7	38.3	38.4
	LLDPE QC annealed	0.921	0.920	0.921	0.921	0.920	0.920	0.920	0.920	0.920	0.924	0.920	0.920
		44.8	44.5	44.7	44.6	44.5	44.4	44.3	44.4	44.3	46.8	44.2	44.3
	LLDPE SC	0.922	0.921	0.921	0.921	0.921	0.921	0.921	0.921	0.921	0.924	0.921	0.921
		45.3	44.7	44.9	45.1	44.7	44.9	44.7	45.1	44.8	47.2	44.8	44.8
	LLDPE SC annealed	0.922	0.921	0.921	0.921	0.921	0.921	0.921	0.921	0.921	0.925	0.921	0.921
		45.3	45.2	45.2	45.1	45.2	45.0	45.0	45.0	44.8	47.3	44.8	44.6
	HDPE QC	0.937	0.937	0.937	0.938	0.938	0.938	0.938	0.938	0.938	0.940	0.938	0.938
		55.9	56.1	56.1	56.3	56.4	56.3	56.3	56.6	56.6	57.8	56.7	56.8
	HDPE QC annealed	0.949	0.949	0.949	0.949	0.950	0.950	0.950	0.950	0.950	0.952	0.950	0.950
		64.0	64.2	64.3	64.2	64.3	64.3	64.4	64.4	64.4	65.8	64.4	64.4
	HDPE SC	0.953	0.954	0.953	0.954	0.954	0.954	0.954	0.954	0.954	0.956	0.954	0.954
		67.0	67.1	67.0	67.1	67.1	67.0	67.2	67.1	67.3	68.4	67.1	67.0
	HDPE SC annealed	0.955	0.955	0.955	0.955	0.955	0.956	0.956	0.955	0.956	0.958	0.955	0.956
		68.3	68.3	68.3	68.3	68.3	68.4	68.5	68.3	68.6	69.8	68.4	68.4

Table B. 6

Table 18. Densities and degree of crystallinities for LDPE, LLDPE, and HDPE determined by VT-DGC at 45ºC

		1U	1D	2U	2D	3U	3D	4U	4D	5U	5D	6U	6D
Density Measurements (g/cm³) Degree of Crystallinity	LDPE QC	0.913	0.913	0.913	0.913	0.913	0.914	0.914	0.914	0.914	0.914	0.915	0.915
		39.3	39.3	39.5	39.5	39.8	39.8	40.1	40.1	40.3	40.2	40.7	40.5
	LDPE QC annealed	0.918	0.917	0.917	0.917	0.918	0.917	0.917	0.918	0.917	0.917	0.917	0.917
		42.6	42.4	42.5	42.4	42.9	42.4	42.4	42.6	42.4	42.5	42.4	42.4
	LDPE SC	0.919	0.918	0.919	0.919	0.919	0.919	0.919	0.919	0.920	0.919	0.920	0.920
		43.2	43.1	43.4	43.2	43.5	43.5	43.8	43.7	44.1	43.9	44.4	44.5
	LDPE SC annealed	0.920	0.920	0.920	0.920	0.920	0.920	0.920	0.920	0.920	0.921	0.921	0.921
		43.9	43.9	44.1	44.2	44.3	44.2	44.4	44.5	44.5	44.6	45.0	45.0
	LLDPE QC	0.908	0.907	0.908	0.908	0.908	0.908	0.908	0.908	0.908	0.908	0.909	0.909
		36.0	35.7	35.8	36.0	36.0	36.0	35.9	36.3	36.1	36.4	36.6	36.6
	LLDPE QC annealed	0.917	0.917	0.917	0.917	0.917	0.917	0.917	0.917	0.917	0.917	0.917	0.917
		42.3	42.3	42.3	42.3	42.2	42.2	42.1	42.3	42.1	42.4	42.1	42.3
	LLDPE SC	0.918	0.918	0.918	0.918	0.918	0.918	0.918	0.918	0.917	0.918	0.918	0.918
		42.6	42.7	42.6	42.7	42.8	42.8	42.6	42.7	42.5	42.8	43.1	42.8
	LLDPE SC annealed	0.918	0.918	0.918	0.918	0.919	0.919	0.919	0.919	0.920	0.919	0.920	0.920
		43.2	43.0	42.9	43.1	43.4	43.4	43.7	43.6	43.9	43.5	44.4	44.2
	HDPE QC	0.934	0.935	0.935	0.935	0.935	0.936	0.936	0.936	0.936	0.936	0.936	0.936
		54.1	54.4	54.5	54.5	54.7	54.8	54.8	54.9	54.9	54.9	55.1	55.2
	HDPE QC annealed	0.947	0.947	0.947	0.947	0.947	0.947	0.947	0.947	0.947	0.947	0.947	0.947
		62.5	62.6	62.7	62.6	62.8	62.6	62.8	62.7	62.8	62.7	62.9	62.9
	HDPE SC	0.951	0.951	0.951	0.951	0.951	0.951	0.952	0.952	0.951	0.951	0.952	0.951
		65.4	65.5	65.6	65.5	65.6	65.6	65.7	65.7	65.6	65.6	65.7	65.6
	HDPE SC annealed	0.953	0.953	0.953	0.953	0.953	0.953	0.953	0.953	0.953	0.953	0.953	0.953
		66.7	66.9	66.8	66.9	66.9	66.9	67.0	67.0	66.8	66.9	66.9	67.0

Table B. 7

Table 19. Densities and degree of crystallinities for LDPE, LLDPE, and HDPE determined by VT-DGC at 50ºC

		1U	1D	2U	2D	3U	3D	4U	4D	5U	5D	6U	6D
Density Measurements (g/cm^3) Degree of Crystallinity	LDPE QC	0.910	0.909	0.909	0.909	0.910	0.910	0.910	0.910	0.910	0.910	0.911	0.910
		37.2	36.9	37.0	37.0	37.3	37.2	37.2	37.2	37.5	37.3	37.9	37.7
	LDPE QC annealed	0.914	0.913	0.913	0.913	0.913	0.913	0.914	0.913	0.914	0.913	0.913	0.913
		40.1	39.6	39.6	39.6	39.8	39.7	39.9	39.6	40.0	39.4	39.7	39.6
	LDPE SC	0.915	0.914	0.915	0.914	0.915	0.915	0.915	0.915	0.915	0.915	0.916	0.916
		40.6	40.5	40.6	40.4	40.7	40.6	40.9	40.8	40.9	41.0	41.6	41.5
	LDPE SC annealed	0.916	0.916	0.916	0.916	0.916	0.916	0.916	0.916	0.916	0.916	0.917	0.917
		41.4	41.3	41.3	41.4	41.4	41.5	41.5	41.5	41.7	41.7	42.0	42.1
	LLDPE QC	0.905	0.904	0.904	0.904	0.904	0.904	0.904	0.904	0.904	0.904	0.905	0.905
		33.8	33.4	33.3	33.2	33.4	33.2	33.0	33.1	33.3	33.2	33.9	33.9
	LLDPE QC annealed	0.914	0.913	0.913	0.913	0.913	0.913	0.913	0.913	0.913	0.913	0.914	0.913
		39.9	39.7	39.6	39.7	39.7	39.7	39.7	39.4	39.8	39.4	40.0	39.6
	LLDPE SC	0.914	0.914	0.914	0.914	0.914	0.915	0.914	0.914	0.915	0.914	0.915	0.915
		40.4	40.0	40.3	40.1	40.2	40.5	40.2	40.1	40.8	40.4	41.0	40.8
	LLDPE SC annealed	0.915	0.915	0.915	0.915	0.915	0.915	0.915	0.915	0.915	0.915	0.916	0.916
		40.7	40.7	40.6	40.7	40.6	40.8	40.9	40.8	41.1	41.1	41.6	41.5
	HDPE QC	0.932	0.933	0.933	0.933	0.933	0.933	0.933	0.933	0.934	0.933	0.933	0.933
		52.4	52.8	53.0	52.9	52.9	53.2	53.2	53.1	53.4	53.4	53.2	53.2
	HDPE QC annealed	0.944	0.945	0.945	0.945	0.945	0.945	0.945	0.945	0.945	0.945	0.945	0.945
		60.9	61.1	61.1	61.0	61.2	61.2	61.3	61.2	61.3	61.3	61.2	61.2
	HDPE SC	0.949	0.949	0.949	0.949	0.949	0.949	0.949	0.950	0.949	0.949	0.949	0.949
		63.7	63.9	64.0	63.9	64.2	64.1	64.2	64.3	64.3	64.2	64.2	64.2
	HDPE SC annealed	0.951	0.951	0.951	0.951	0.952	0.951	0.951	0.951	0.951	0.951	0.951	0.951
		65.2	65.4	65.5	65.3	65.8	65.6	65.6	65.5	65.5	65.5	65.5	65.5

Table B. 8

Table 20. Densities and degree of crystallinities for LDPE, LLDPE, and HDPE determined by VT-DGC at 55ºC

		1U	1D	2U	2D	3U	3D	4U	4D	5U	5D	6U	6D
Density Measurements (g/cm^3) Degree of Crystallinity	LDPE QC	0.906	0.906	0.906	0.906	0.907	0.906	0.906	0.906	0.906	0.906	0.907	0.906
		34.7	34.6	34.9	34.9	35.1	35.0	35.0	34.9	35.0	34.9	35.3	35.0
	LDPE QC annealed	0.910	0.909	0.910	0.910	0.910	0.910	0.910	0.910	0.911	0.910	0.911	0.910
		37.2	36.9	37.1	37.2	37.6	37.1	37.6	37.2	37.8	37.5	38.2	37.4
	LDPE SC	0.911	0.910	0.911	0.911	0.911	0.911	0.911	0.911	0.912	0.911	0.912	0.912
		37.9	37.7	38.0	37.9	37.8	38.1	38.3	38.2	38.5	38.4	39.1	38.7
	LDPE SC annealed	0.912	0.912	0.912	0.912	0.913	0.912	0.912	0.912	0.913	0.912	0.913	0.912
		38.8	38.6	38.9	38.9	39.2	38.8	39.0	38.9	39.2	39.0	39.4	39.0
	LLDPE QC	0.901	0.901	0.901	0.901	0.901	0.901	0.901	0.901	0.900	0.900	0.901	0.901
		31.2	31.0	31.2	31.2	31.4	31.2	31.1	31.0	30.7	30.9	31.4	31.0
	LLDPE QC annealed	0.910	0.910	0.910	0.910	0.910	0.910	0.911	0.910	0.911	0.911	0.912	0.911
		37.5	37.2	37.4	37.4	37.7	37.5	37.9	37.6	38.1	37.8	38.6	37.9
	LLDPE SC	0.910	0.910	0.911	0.911	0.911	0.911	0.911	0.911	0.911	0.911	0.912	0.912
		37.7	37.6	38.0	37.9	38.2	38.0	38.1	38.0	38.3	38.2	38.6	38.5
	LLDPE SC annealed	0.911	0.911	0.911	0.912	0.912	0.912	0.911	0.911	0.912	0.912	0.912	0.912
		38.4	38.1	38.3	38.5	38.6	38.5	38.4	38.4	38.7	38.5	38.9	38.8
	HDPE QC	0.930	0.930	0.930	0.930	0.930	0.930	0.930	0.930	0.931	0.930	0.931	0.931
		50.7	50.8	51.1	51.1	51.2	51.2	51.2	51.2	51.5	51.3	51.5	51.5
	HDPE QC annealed	0.942	0.942	0.942	0.942	0.942	0.942	0.942	0.942	0.943	0.942	0.943	0.943
		59.3	59.2	59.4	59.4	59.4	59.5	59.5	59.4	59.6	59.5	59.7	59.6
	HDPE SC	0.947	0.947	0.947	0.947	0.947	0.947	0.947	0.947	0.947	0.947	0.947	0.947
		62.4	62.2	62.4	62.5	62.5	62.6	62.5	62.6	62.6	62.5	62.5	62.6
	HDPE SC annealed	0.949	0.949	0.949	0.949	0.949	0.949	0.949	0.949	0.949	0.949	0.949	0.949
		63.9	63.9	64.0	64.0	64.0	64.1	64.0	64.1	64.0	64.0	64.2	64.1

Table B. 9

Table 21. Densities and degree of crystallinities for LDPE, LLDPE, and HDPE determined by VT-DGC at 60ºC

		1	2	3	4	5	6
Density Measurements (g/cm^3) Degree of Crystallinity	LDPE QC	0.901	0.902	0.902	0.902	0.902	0.902
		31.5	31.9	32.0	32.1	32.0	32.0
	LDPE QC annealed	0.905	0.905	0.905	0.906	0.906	0.906
		33.9	34.0	34.2	34.6	34.7	34.9
	LDPE SC	0.906	0.906	0.907	0.907	0.907	0.907
		34.7	34.8	35.1	35.3	35.4	35.6
	LDPE SC annealed	0.907	0.908	0.908	0.908	0.908	0.908
		35.6	35.8	35.8	36.0	36.0	36.1
	LLDPE QC	0.896	0.896	0.897	0.897	0.896	0.896
		27.7	28.2	28.4	28.3	28.2	28.2
	LLDPE QC annealed	0.906	0.906	0.906	0.906	0.907	0.907
		34.4	34.6	34.7	35.0	35.4	35.5
	LLDPE SC	0.906	0.906	0.907	0.907	0.907	0.907
		34.7	34.8	35.2	35.3	35.5	35.6
	LLDPE SC annealed	0.907	0.907	0.907	0.907	0.907	0.908
		35.3	35.5	35.5	35.7	35.7	35.9
	HDPE QC	0.927	0.927	0.927	0.927	0.927	0.927
		49.0	49.0	49.2	49.2	49.3	49.3
	HDPE QC annealed	0.940	0.940	0.940	0.940	0.940	0.940
		57.6	57.7	57.8	57.7	57.9	57.8
	HDPE SC	0.945	0.944	0.945	0.945	0.945	0.945
		60.9	60.8	61.1	61.0	61.2	61.0
	HDPE SC annealed	0.947	0.947	0.947	0.947	0.947	0.947
		62.3	62.4	62.7	62.5	62.6	62.6

Appendix C

Additional Data

Table C. 1

Table 22. Unit cell Parameters for LDPE QC

Temp	2Θ (21.6)	2Θ (24.3)	2Θ (39.75)	a (nm)	b (nm)	c (nm)	V_c (cm^3)	ρ (kg/m^3)
25								
30	22.303	23.746	39.321	0.7495	0.4708	0.2623	9.2562E-	1.004
35	22.131	23.763	39.383	0.7490	0.4760	0.2609	9.3022E-	1.000
40	22.112	23.747	39.347	0.7494	0.4764	0.2612	9.3247E-	0.997
45	22.400	23.677	39.290	0.7516	0.4674	0.2632	9.2471E-	1.005
50	22.333	23.700	39.384	0.7509	0.4695	0.2620	9.2386E-	1.006
55	22.164	23.680	39.365	0.7515	0.4743	0.2614	9.3170E-	0.998
60	22.067	23.652	39.337	0.7524	0.4770	0.2612	9.3731E-	0.992
			Change	0.0035	0.0096	0.0022	1.344E-24	
			% change	0.46	2.04	0.86		

Temp	Intensity amorphous (20.0)	Intensity 110 (21.6)	Intensity 200 (24.3)	Degree of crystallinity
25				
30	85830.8	38402.6	8419.8	0.35
35	78220.7	40318.5	12434.2	0.40
40	93429.7	43975.5	8730.3	0.36
45	99217.4	32523.4	7042.3	0.29
50	103190.0	32971.8	6744.3	0.28
55	103190.0	32971.8	6744.3	0.28
60	96363.9	35045.4	8773.7	0.31

Table C. 2

Table 23. Unit cell Parameters for LDPE QCA

Temp	**2Θ (21.6)**	**2Θ (24.3)**	**2Θ (39.75)**	**a (nm)**	**b (nm)**	**c (nm)**	**V_c (cm^3)**	**ρ (kg/m^3)**
25	22.184	23.817	39.368	0.7473	0.4748	0.2613	9.2697E-23	1.003
30	22.290	23.804	39.349	0.7477	0.4716	0.2620	9.2368E-23	1.007
35	21.892	23.762	39.278	0.7490	0.4832	0.2606	9.4329E-23	0.986
40	22.074	23.874	39.534	0.7455	0.4786	0.2593	9.2507E-23	1.005
45	22.050	23.766	39.412	0.7489	0.4784	0.2603	9.3256E-23	0.997
50	21.950	23.748	39.285	0.7494	0.4813	0.2609	9.4102E-23	0.988
55	22.228	23.754	39.326	0.7492	0.4730	0.2619	9.2823E-23	1.002
60	22.098	23.791	39.457	0.7481	0.4772	0.2601	9.2857E-23	1.001
			Change	0.0039	0.0116	0.0027	1.965E-24	
			% change	0.52	2.46	1.03		

Temp	Intensity amorphous (20.0)	Intensity 110 (21.6)	Intensity 200 (24.3)	Degree of crystallinity
25	59882.4	38537.5	15188.8	0.47
30	77498.4	36671.4	14512.5	0.40
35	68195.3	43415.1	16085.0	0.47
40	67316.4	49931.4	11688.5	0.48
45	65401.5	35684.2	14763.6	0.44
50	105970.0	35433.5	9556.9	0.30
55	73796.0	31851.7	12486.0	0.38
60	89568.6	33349.1	10754.1	0.33

Table C. 3

Table 24. Unit cell Parameters for LDPE SC

Temp	**2Θ (21.6)**	**2Θ (24.3)**	**2Θ (39.75)**	**a (nm)**	**b (nm)**	**c (nm)**	**V_c (cm^3)**	**ρ (kg/m^3)**
25	22.177	23.777	39.416	0.7485	0.4747	0.2609	9.2697E-23	1.003
30	22.223	23.768	39.383	0.7488	0.4733	0.2614	9.2634E-23	1.004
35	22.150	23.702	39.266	0.7509	0.4749	0.2621	9.3458E-23	0.995
40	22.132	23.707	39.385	0.7507	0.4755	0.2610	9.3163E-23	0.998
45	21.996	23.717	39.303	0.7504	0.4796	0.2610	9.3939E-23	0.990
50	21.423	23.636	39.195	0.7529	0.4971	0.2593	9.7029E-23	0.958
55	21.934	23.674	39.320	0.7517	0.4812	0.2606	9.4274E-23	0.986
60	21.881	23.596	39.248	0.7542	0.4822	0.2611	9.4932E-23	0.979
			Change	0.0057	0.0238	0.0028	4.3947E-24	
			% change	0.76	5.03	1.10		

Temp	Intensity amorphous (20.0)	Intensity 110 (21.6)	Intensity 200 (24.3)	Degree of crystallinity
25	48200.9	32875.9	16877.0	0.51
30	50200.0	35731.2	14030.0	0.50
35	58110.3	35981.7	18193.7	0.48
40	52944.9	37244.1	16792.0	0.51
45	70305.2	36524.6	15763.2	0.43
50	75410.7	47905.5	13004.7	0.45
55	64581.0	33753.3	17744.0	0.44
60	56836.1	30919.2	18224.3	0.46

Table C. 4

Table 25. Unit cell Parameters for LDPE SCA

Temp	2Θ (21.6)	2Θ (24.3)	2Θ (39.75)	a (nm)	b (nm)	c (nm)	V_c (cm^3)	ρ (kg/m^3)
25	22.326	23.746	39.298	0.7495	0.4701	0.2626	9.2540E-23	1.005
30	22.274	23.731	39.355	0.7500	0.4715	0.2619	9.2618E-23	1.004
35	22.330	23.731	39.367	0.7500	0.4699	0.2621	9.2362E-23	1.007
40	22.235	23.661	39.247	0.7521	0.4721	0.2627	9.3289E-23	0.997
45	22.234	23.671	39.309	0.7518	0.4722	0.2622	9.3081E-23	0.999
50	22.072	23.660	39.290	0.7522	0.4769	0.2616	9.3827E-23	0.991
55	21.866	23.574	39.161	0.7549	0.4824	0.2617	9.5318E-23	0.975
60	21.825	23.583	39.187	0.7546	0.4838	0.2613	9.5390E-23	0.975
			Change	0.0054	0.0139	0.0014	3.0276E-24	
			% change	0.72	2.96	0.55		

Temp	Intensity amorphous (20.0)	Intensity 110 (21.6)	Intensity 200 (24.3)	Degree of crystallinity
25	68123.8	34336.4	17827.1	0.43
30	60883.2	35787.9	18451.1	0.47
35	64952.0	34360.2	18467.4	0.45
40	59594.3	35281.2	17897.2	0.47
45	61875.2	35880.5	18872.8	0.47
50	60860.0	34338.1	18697.4	0.47
55	64640.1	37777.2	15946.9	0.45
60	63420.6	36742.1	18958.5	0.47

Table C. 5

Table 26. Unit cell Parameters for LLDPE QC

Temp	2Θ (21.6)	2Θ (24.3)	2Θ (39.75)	a (nm)	b (nm)	c (nm)	V_c (cm^3)	ρ (kg/m^3)
25	22.372	23.678	39.320	0.7516	0.4683	0.2628	9.2486E-23	1.005
30	22.315	23.610	39.201	0.7537	0.4694	0.2636	9.3255E-23	0.997
35	22.185	23.631	39.254	0.7531	0.4733	0.2625	9.3553E-23	0.994
40	22.089	23.624	39.235	0.7533	0.4761	0.2622	9.4021E-23	0.989
45	22.020	23.563	39.214	0.7552	0.4777	0.2621	9.4540E-23	0.983
50	22.021	23.540	39.192	0.7559	0.4775	0.2623	9.4670E-23	0.982
55	21.982	23.538	39.216	0.7560	0.4786	0.2619	9.4765E-23	0.981
60	21.958	23.542	39.287	0.7559	0.4794	0.2612	9.4643E-23	0.982
			Change	0.0044	0.0111	0.0024	2.2790E-24	
			% change	0.59	2.38	0.92		

Temp	Intensity amorphous (20.0)	Intensity 110 (21.6)	Intensity 200 (24.3)	Degree of crystallinity
25	73638.9	29074.7	11263.8	0.35
30	82573.4	32166.3	11522.2	0.35
35	78104.2	31139.2	16717.2	0.38
40	81632.0	29764.4	12224.4	0.34
45	80461.1	24530.7	7668.5	0.29
50	92119.9	31452.4	13927.8	0.33
55	102860.0	30934.5	13291.8	0.30
60	75653.7	29770.7	17469.4	0.38

Table C. 6

Table 27. Unit cell Parameters for LLDPE QCA

Temp	2Θ (21.6)	2Θ (24.3)	2Θ (39.75)	a (nm)	b (nm)	c (nm)	V_c (cm^3)	ρ (kg/m^3)
25	22.306	23.749	39.315	0.7494	0.4707	0.2624	9.2558E-23	1.005
30	22.060	23.741	39.309	0.7496	0.4779	0.2612	9.3589E-23	0.993
35	22.281	23.713	39.252	0.7505	0.4712	0.2629	9.2947E-23	1.000
40	22.228	23.723	39.304	0.7502	0.4728	0.2621	9.2972E-23	1.000
45	22.095	23.710	39.293	0.7506	0.4766	0.2616	9.3579E-23	0.994
50	22.054	23.696	39.315	0.7510	0.4777	0.2612	9.3724E-23	0.992
55	21.932	23.707	39.326	0.7507	0.4815	0.2605	9.4170E-23	0.987
60	22.011	23.632	39.235	0.7531	0.4785	0.2618	9.4322E-23	0.986
			Change	0.0037	0.0108	0.0023	1.7638E-24	
			% change	0.49	2.30	0.89		

Temp	Intensity amorphous (20.0)	Intensity 110 (21.6)	Intensity 200 (24.3)	Degree of crystallinity
25	28144.7	18015.2	8704.5	0.49
30	53155.6	35002.4	18453.1	0.50
35	45041.6	31472.3	13811.7	0.50
40	53361.0	31744.8	14726.8	0.47
45	57626.4	31360.1	15157.0	0.45
50	59890.0	31195.8	15322.4	0.44
55	54949.5	32377.1	16605.8	0.47
60	65356.9	30211.8	13037.5	0.40

Table C. 7

Table 28. Unit cell Parameters for LLDPE SC

Temp	**2Θ (21.6)**	**2Θ (24.3)**	**2Θ (39.75)**	**a (nm)**	**b (nm)**	**c (nm)**	**V_c (cm^3)**	**ρ (kg/m^3)**
25	22.245	23.750	39.375	0.7494	0.4725	0.2616	9.2620E-23	1.004
30	22.300	23.709	39.318	0.7506	0.4706	0.2624	9.2687E-23	1.003
35	22.084	23.751	39.388	0.7493	0.4773	0.2607	9.3229E-23	0.997
40	22.190	23.684	39.225	0.7514	0.4736	0.2627	9.3474E-23	0.995
45	22.119	23.709	39.363	0.7506	0.4759	0.2611	9.3277E-23	0.997
50	22.099	23.690	39.262	0.7512	0.4763	0.2619	9.3713E-23	0.992
55	22.111	23.704	39.354	0.7508	0.4761	0.2612	9.3348E-23	0.996
60	22.007	23.691	39.363	0.7512	0.4791	0.2606	9.3790E-23	0.991
			Change	0.0021	0.0085	0.0021	1.1693E-24	
			% change	0.28	1.81	0.79		

Temp	Intensity amorphous (20.0)	Intensity 110 (21.6)	Intensity 200 (24.3)	Degree of crystallinity
25	53232.1	29756.0	19724.0	0.48
30	68725.5	30065.1	17162.9	0.41
35	55278.6	34887.8	19026.0	0.49
40	103640.0	29978.6	12965.8	0.29
45	65557.0	29649.4	18276.5	0.42
50	71562.1	30310.1	17860.6	0.40
55	68442.7	28846.3	17897.6	0.41
60	77019.4	29100.8	18520.2	0.38

Table C. 8

Table 29. Unit cell Parameters for LLDPE SCA

Temp	2Θ (21.6)	2Θ (24.3)	2Θ (39.75)	a (nm)	b (nm)	c (nm)	V_c (cm^3)	ρ (kg/m^3)
25	22.345	23.722	39.302	0.7502	0.4694	0.2627	9.2517E-23	1.005
30	21.916	23.699	39.288	0.7509	0.4820	0.2608	9.4375E-23	0.985
35	21.767	23.674	39.219	0.7517	0.4864	0.2606	9.5294E-23	0.976
40	21.917	23.701	39.300	0.7509	0.4819	0.2607	9.4330E-23	0.986
45	22.043	23.712	39.307	0.7505	0.4782	0.2612	9.3750E-23	0.992
50	21.838	23.675	39.300	0.7517	0.4842	0.2603	9.4736E-23	0.981
55	21.806	23.640	39.251	0.7528	0.4849	0.2606	9.5121E-23	0.977
60	21.923	23.676	39.314	0.7517	0.4815	0.2606	9.4330E-23	0.986
			Change	0.0026	0.0170	0.0024	2.7768E-24	
			% change	0.34	3.62	0.93		

Temp	Intensity amorphous (20.0)	Intensity 110 (21.6)	Intensity 200 (24.3)	Degree of crystallinity
25	55520.0	31420.4	16198.0	0.46
30	50017.0	39402.4	18270.3	0.54
35	49228.5	38227.5	17503.9	0.53
40	53308.4	37119.0	17001.7	0.50
45	58910.3	32273.1	18641.2	0.46
50	54371.7	37842.9	18149.2	0.51
55	79049.6	30552.3	13156.1	0.36
60	69789.1	33646.5	14431.3	0.41

Table C. 9

Table 30. Unit cell Parameters for HDPE QC

Temp	2Θ (21.6)	2Θ (24.3)	2Θ (39.75)	a (nm)	b (nm)	c (nm)	V_c (cm^3)	ρ (kg/m^3)
25	21.515	23.878	39.976	0.7454	0.4962	0.2532	9.3662E-23	0.993
30	21.514	23.855	39.907	0.7461	0.4961	0.2538	9.3928E-23	0.990
35	21.499	23.826	39.902	0.7470	0.4963	0.2538	9.4083E-23	0.988
40	21.470	23.774	39.896	0.7486	0.4968	0.2538	9.4372E-23	0.985
45	21.461	23.751	39.877	0.7493	0.4969	0.2539	9.4532E-23	0.984
50	21.464	23.745	39.867	0.7495	0.4967	0.2540	9.4561E-23	0.983
55	21.450	23.682	39.929	0.7515	0.4966	0.2535	9.4614E-23	0.983
60	21.454	23.700	39.859	0.7509	0.4966	0.2541	9.4746E-23	0.981
			Change	0.0061	0.0008	0.0008	1.0846E-24	
			% change	0.82	0.16	0.33		

Temp	Intensity amorphous (20.0)	Intensity 110 (21.6)	Intensity 200 (24.3)	Degree of crystallinity
25	43295.3	42576.0	12495.4	0.56
30	45336.6	38750.2	12112.6	0.53
35	48628.7	38761.2	12232.8	0.51
40	45948.1	39119.6	12464.4	0.53
45	42504.1	42261.8	13147.9	0.57
50	43097.0	41140.0	12981.1	0.56
55	49518.7	37138.5	12102.0	0.50
60	47008.6	40105.7	12715.4	0.53

Table C. 10

Table 31. Unit cell Parameters for HDPE QCA

Temp	2Θ (21.6)	2Θ (24.3)	2Θ (39.75)	a (nm)	b (nm)	c (nm)	Vc (cm3)	ρ (kg/m3)
25								
30								
35	21.554	23.897	39.875	0.7448	0.4951	0.2541	9.3724E-23	0.992
40	21.531	23.847	39.949	0.7464	0.4954	0.2535	9.3749E-23	0.992
45	21.529	23.828	39.960	0.7469	0.4953	0.2535	9.3777E-23	0.991
50	21.512	23.789	39.992	0.7481	0.4955	0.2532	9.3866E-23	0.991
55	19.442	21.483	36.272	0.8274	0.5476	0.2777	9.4258E-23	0.986
60	21.490	23.736	39.990	0.7498	0.4958	0.2532	9.4112E-23	0.988
			Change	0.0052	0.0008	0.0010	5.3417E-25	
			% change	0.70	0.16	0.38		

Temp	Intensity amorphous (20.0)	Intensity 110 (21.6)	Intensity 200 (24.3)	Degree of crystallinity
25				
30				
35	28317.5	35714.8	12592.6	0.63
40	39049.5	33034.4	12717.6	0.54
45	42914.5	32919.1	12151.4	0.51
50	35734.1	34639.4	15187.1	0.58
55	38269.2	38370.2	12142.2	0.57
60	35313.3	37581.6	14842.2	0.60

Table C. 11

Table 32. Unit cell Parameters for HDPE SC

Temp	2Θ (21.6)	2Θ (24.3)	2Θ (39.75)	a (nm)	b (nm)	c (nm)	V_c (cm^3)	ρ (kg/m^3)
25	21.562	23.945	39.863	0.7433	0.4953	0.2542	9.3596E-23	0.993
30	21.555	23.924	39.810	0.7440	0.4953	0.2546	9.3835E-23	0.883
35	21.525	23.864	39.810	0.7458	0.4958	0.2546	9.4130E-23	0.988
40	21.519	23.853	39.887	0.7462	0.4959	0.2540	9.3965E-23	0.989
45	21.516	23.824	39.857	0.7471	0.4957	0.2542	9.4141E-23	0.988
50	21.498	23.771	39.839	0.7487	0.4958	0.2543	9.4412E-23	0.985
55	21.491	23.750	39.871	0.7494	0.4959	0.2541	9.4413E-23	0.985
60	21.474	23.717	39.848	0.7504	0.4961	0.2542	9.4643E-23	0.982
			Change	0.0070	0.0008	0.0006	1.0471E-24	
			% change	0.95	0.17	0.26		

Temp	Intensity amorphous (20.0)	Intensity 110 (21.6)	Intensity 200 (24.3)	Degree of crystallinity
25	25330.9	29021.0	9864.0	0.61
30	28121.7	29333.3	9222.8	0.58
35	28039.6	29878.8	9837.6	0.59
40	29843.5	29664.0	9983.4	0.57
45	23076.9	33085.8	9314.7	0.65
50	31991.7	30136.4	9684.4	0.55
55	30995.8	29241.1	10134.8	0.56
60	21594.7	30604.5	10641.6	0.66

Table C. 12

Table 33. Unit cell Parameters for HDPE SCA

Temp	2Θ (21.6)	2Θ (24.3)	2Θ (39.75)	a (nm)	b (nm)	c (nm)	V_c (cm^3)	ρ (kg/m^3)
25	21.574	23.970	39.827	0.7426	0.4951	0.2545	9.3583E-23	0.994
30	21.547	23.928	39.825	0.7439	0.4956	0.2545	9.3816E-23	0.991
35	21.526	23.896	39.827	0.7449	0.4960	0.2544	9.3995E-23	0.989
40	21.529	23.867	39.864	0.7457	0.4957	0.2542	9.3947E-23	0.990
45	21.523	23.855	39.906	0.7461	0.4958	0.2538	9.3887E-23	0.990
50	21.501	23.805	39.898	0.7477	0.4960	0.2538	9.4143E-23	0.988
55	21.494	23.779	39.898	0.7485	0.4960	0.2539	9.4245E-23	0.987
60	21.478	23.742	39.937	0.7496	0.4962	0.2535	9.4301E-23	0.986
			Change	0.0070	0.00112	0.0010	7.1811E-25	
			% change	0.94	0.22	0.39		

Temp	Intensity amorphous (20.0)	Intensity 110 (21.6)	Intensity 200 (24.3)	Degree of crystallinity
25	30808.0	32088.4	11658.7	0.59
30	35264.6	34152.4	12486.5	0.57
35	34982.7	32646.0	11705.4	0.56
40	30842.4	32903.3	12596.3	0.60
45	36976.4	31523.2	11350.3	0.54
50	36233.9	32974.2	11977.2	0.55
55	36174.4	33451.0	12244.0	0.56
60	37181.8	33713.5	12724.1	0.56

Vita

Russell Louis Hallman, Jr., a native of Nashville, Tennessee, obtained an associate's degree in chemical engineering technology from Nashville State Technical Institute in 1983. He earned a bachelor's degree in business from Maryville College in Maryville, Tennessee, in 1990 and a bachelor's degree in chemical engineering from the University of Tennessee-Knoxville in 1996. In 2002 he earned a master's degree in material science and in 2013 was awarded a Ph.D. in polymer engineering, also from the University of Tennessee-Knoxville. He is a member of the Tau Beta Pi engineering honor society and the Golden Key honor society.

He has worked in research and development at the Y-12 National Security Complex, Oak Ridge Tennessee, since 1984. Through his scientific and engineering efforts he has attained nine patents to date and spoken at a number of professional conferences.

1. Hallman, Russell L., Jr., Paul D. Vanatta, and Michael J. Renner. Constant Flow Rate Fluid Controller. Babcock & Wilcox Technical Services Y-12, LLC, USA . assignee. Patent US20130019956A1. 2013.
2. Ripley, Edward B., and Russell L. Hallman. Weak Magnetic Field Base Method and Apparatus for Control of Microstructure in Soldered, Brazed, Welded, Plated, Cast or Vapor Deposited Manufactured Components. Babcock & Wilcox Technical Services Y-12, LLC, USA . assignee. Patent US20120042993A1. 2012.
3. Hallman, Russell L., Jr., and Paul D. Vanatta. Intrinsically Safe Moisture Blending System. Babcock & Wilcox Technical Services Y-12, LLC, USA . assignee. Patent US8262280B1. 2012.
4. Ripley, Edward B., and Russell L. Hallman. Filler for Decreasing Metal Whisker Formation Lead-Free Soldering. Babcock & Wilcox Technical Services Y-12, LLC, USA . assignee. Patent US20110079630A1. 2011.
5. Seals, Roland D., Edward B. Ripley, and Russell L. Hallman. Toughened and Corrosion- and Wear-Resistant Composite Structures and Fabrication Methods Thereof. Babcock & Wilcox Technical Services Y-12, LLC, USA . assignee. Patent US20090282949A1. 2009.

6. Hallman, Russell Louis, Jr. Controlled Differential Pressure System for an Enhanced Fluid Blending Apparatus. Babcock & Wilcox Technical Services Y-12, LLC, USA . assignee. Patent US7494114B1. 2009.
7. Hallman, Jr Russell Louis, and Michael John Renner. Fluid Permeability Measurement System and Method. Babcock & Wilcox Technical Services Y-12, LLC, USA . assignee. Patent US7325439B2. 2008.
8. Hallman, Russell L., Jr., and James C. Truett. Method and Apparatus for Providing a Precise Amount of Gas at a Precise Humidity. Lockheed Martin Energy Systems, Inc., USA . assignee. Patent US6182951B1. 2001.
9. Powell, George Louis, and Russell Louis Hallman, Jr. Apparatus for and Method of Performing Spectroscopic Analysis on an Article. Lockheed Martin Energy Systems, Inc., USA . assignee. Patent US5895918A. 1999.

In addition to his engineering pursuits, Hallman has been a small-business owner for 15 years. He also is interested in and enjoys teaching various subjects. A scuba diving instructor since 2006, he teaches seven advanced scuba diving specialties in addition to basic open-water scuba instruction. He also organized and taught a small-engine repair course at Nashville State Technical Institute and a certified weld inspectors course for Pellissippi State Technical Institute in Knoxville.